Dark Matter and the Assembly History of Massive Galaxies and Clusters

Thesis by

Andrew B. Newman

In Partial Fulfillment of the Requirements

for the Degree of

Doctor of Philosophy

California Institute of Technology

Pasadena, California

2013

(Defended February 4, 2013)

Acknowledgments

When I applied to Caltech, I thought I wanted to work on the CMB, and it seemed best to be in the physics department to do that. When I applied to physics and visited Caltech, I took a break to wander over to Robinson Hall and meet some astronomers. Richard Ellis happened to be in his office, door ajar. This was very lucky for me. I left amazed by the breadth of interesting projects he was working on and his pure excitement about everything. (I also got a reprint of the *Nature* cover by Richard Massey, which looked really cool.) That enthusiasm was the main reason I came to Caltech. Being Richard's student is truly a privilege. I'm thankful that he's been such an excellent mentor, always supportive and available to talk or read a paper draft, and inspiring in his depth and versatility as a scientist. Richard taught me to focus on the important things: keep the big picture in mind, always work on questions that are interesting, and remember to have fun doing it.

I owe so much to Tommaso Treu for his guidance over the last five years. Tommaso was always there to talk, brainstorm, encourage me, and give great advice (and not only about science—also where to eat in seemingly any city!). Throughout he's been unfailingly positive. Looking back, I realize how much of my perspective on science comes from him. I've thoroughly enjoyed the humor and hospitality of Tommaso and his wife, Stefania Tutino, and look forward to staying in touch. Thank you both.

Thanks to my thesis committee of Chuck Steidel, John Johnson, Andrew Benson, and Chris Hirata for reading my thesis and for their comments and advice. Chuck, Chris, and Annika Peter, in particular, have always had an open door, and I'm grateful to have benefitted from their insight. I've been fortunate to draw upon the experience and friendship of several former students and post-docs in the Ellis empire. Kevin Bundy and Dave Sand, especially, helped me in many ways. (You're the man, Dave!) Richard Massey and Johan Richard patiently taught me about lensing in my first year. I would be remiss not to recognize Armin Rest, Stella Kafka, and Buell Jannuzi, who patiently took the time to form my first real encounter with astronomy as an undergraduate.

To Tucker "Danger" Jones, Matt "Protein" Schenker, and Sirio "Mere Pending Silver" Belli: it's been fun, and trips to Hawaii were even better with you guys. May you always be upgraded. I've had the ideal officemates in Walter Max-Moerbeck, Ben Montet, Joey Richards, and Shriharsh Tendulkar. I owe thanks to Tim Morton, Vera Gluscevic, Laura Perez, Sarah Miller, Oliver King,

Michelle Selvans, and Sonja Graves for their friendship and dinners.

Surely there is no better computer staff in astronomy than Patrick Shopbell, Anu Mahabal, and José Calderon. Thank you for your tireless work and assistance. Judy McClain has been steadfastly cheerful and kind, besides being amazingly efficient; thank you, Judy. I will certainly miss the daily warmth and humor of Efrain Hernandez. Needless to say, this thesis would be impossible without the staff of the Keck Observatory, particularly Greg Wirth and Marc Kassis, who have always shown supreme dedication, professionalism, and friendliness.

My extended family has always provided encouragement and never seemed to think it was too strange that I spent almost six years in California studying distant galaxies (including spectral lines familiar to my grandfather from identifying aluminum impurities). I can never thank my parents and my sister Emily enough for their love and support throughout graduate school and long before, even though they would probably have preferred that I moved less far away. And to Gwen—how could I have known what an adventure these years would be? I'm so grateful and lucky to enjoy your constant love and kindness that brighten each day. Now let's take a vacation!

Abstract

In Part I of this thesis we study the distribution of dark matter and baryons in a sample of seven massive, relaxed galaxy clusters by combining multiple observational tools. Our aim is to make comprehensive mass profile measurements and compare these to the form of the universal density profile derived in numerical cold dark matter (CDM) simulations. By joining weak and strong gravitational lensing observations with resolved stellar kinematic data within the central brightest cluster galaxy (BCG), we constrain the density profile over the wide dynamic range of $3 - 3000$ kpc in radius for the first time. We first compare lensing- and X-ray-derived mass measures to constrain the line-of-sight geometry of the clusters in our sample. We then show that the logarithmic slope of the *total* density profile – comprising both stars and dark matter – agrees closely with numerical simulations containing *only dark matter* down to radii of $\simeq 7$ kpc, despite the significant contribution of stellar material on such small scales. Our unique stellar kinematic data allow us to constrain two-component models of the stellar and dark matter distributions in the cluster cores. We find a mean logarithmic slope for the dark matter density of $\langle\beta\rangle = 0.50 \pm 0.10$ (random)$^{+0.14}_{-0.13}$ (systematic) at small radii, where $\rho_{\rm DM} \propto r^{-\beta}$. This is significantly shallower than a canonical CDM cusp having $\beta = 1$. Alternatively, a cored dark matter profile with $\langle \log r_{\rm core}/{\rm kpc}\rangle = 1.14 \pm 0.13^{+0.14}_{-0.22}$ provides an equally good description. The mean mass-to-light ratio of the stars in the BCGs, derived from lensing and dynamics, is found to be consistent with estimates from stellar population synthesis modeling provided that a Salpeter initial mass function (IMF), or one with a similarly high mass-to-light ratio, is adopted. We find some evidence for a correlation between the inner dark matter profile and the size or luminosity of the BCG, which suggests a connection between the inner dark matter distribution and the assembly history of stars in the central galaxy. We discuss physical processes that might account for the small-scale dark matter distribution that we observe.

In Part II we turn to the assembly of stars in massive, quiescent galaxies. Many observations now indicate that the extended stellar envelopes seen in these systems today have grown over the last 11 Gyr. We present a two-pronged program aimed at understanding the remarkable growth observed in the size of their stellar distributions over this interval. First, we conducted deep spectroscopic observations of a sample of 17 spheroidal galaxies at $z = 1.05$–1.60 to derive their internal velocity dispersions from stellar absorption lines. These dynamical data provide a robust verification of

their compactness and masses, which were previously inferred photometrically. Second, in order to investigate the likely role of galaxy mergers in contributing to the observed size growth, we searched for satellites around a sample of massive, quiescent galaxies at $z = 0.4$–2. Using *HST*/WFC3 imaging from the CANDELS survey, we are able to probe faint companions with stellar masses down to 10% of that of the host galaxy. By coupling measurements of the number and stellar mass content of such companions with results from published merger simulations, we estimate the rate of size growth attributable to major and minor galaxy mergers. We compare this to the rate of size growth measured in the same large, homogeneous sample of quiescent galaxies, based on deep, high-resolution imaging in the rest-frame optical. We find that observed impending mergers might account for the size growth seen at $z \lesssim 1$, provided that a relatively short merger timescale is valid. At progressively higher redshifts, however, the estimated merger rate is outstripped by the rate of size growth. Either the merger physics is not currently well understood, or additional processes must contribute significantly to early size growth of quiescent galaxies.

In the final chapter we summarize our results and describe future prospects for elucidating the small-scale distribution of dark matter at intermediate mass scales, as well as the physical drivers of early spheroid evolution.

Contents

List of Figures

List of Tables

Chapter 1

Introduction

This thesis is broadly concerned with observing the distribution of dark matter and stars in massive galaxies and clusters of galaxies, with the goal of understanding the physical processes that govern the observed structure and its evolution. Dark matter is gravitationally dominant outside the inner luminous regions of galaxies and is fundamental to our current understanding of cosmology and galaxy formation. Although the large-scale distribution of dark matter appears to be well understood in the reigning cold dark matter (CDM) paradigm, the small-scale distribution remains much more mysterious. The sub-galactic dark matter distribution is likely to be affected by the interplay between dark and baryonic material during galaxy formation and assembly, which is poorly constrained. Additionally, the microphysical properties of the dark matter particle itself, which is of course unknown, may also play a role. The small-scale dark matter distribution is therefore of considerable interest. Part I of this thesis (Chapters 2–5) addresses this question observationally at the galaxy cluster scale. After reviewing the history of dark matter and describing current constraints on sub-galactic scales (Chapter 2), we describe observations of seven massive, relaxed galaxy clusters. Using a comprehensive set of lensing and kinematic data, we aim to measure the radial density profile of dark matter from radii of ~ 3 kpc to ~ 3 Mpc for the first time. We particularly focus on the inner regions where our data provide the best opportunity to disentangle the relative contributions of dark matter and baryons. We compare our observations with cosmological simulations – both dark matter-only and those attempting to include baryonic physics – in order to assess the universality and form of the dark matter profile, as well as its relation to the distribution of baryons.

Massive galaxies are an excellent test-bed for studying hierarchical assembly through mergers, a cornerstone of the modern cosmological model. In Part II of this thesis (Chapters 6–8), we turn to the evolution of massive, quiescent galaxies (i.e., those with low star-formation rates) over the last ~ 11 Gyr. These galaxies have undergone major structural evolution in their stellar distribution, which has grown in half-light radius by a factor of $\simeq 4$. We aim to probe the physics driving this remarkable growth via a two-pronged approach. First, in Chapter 7, we present deep Keck spectroscopy used to derive the internal stellar kinematics of 17 such galaxies at redshifts $z =$

1.05–1.6. This is the largest comparable sample assembled in this redshift interval. We use these dynamical data to provide a robust measure of the densities and masses that were previously inferred photometrically. In Chapter 8 we turn to the role of galaxy mergers in producing the observed size growth. Via an analysis of close galaxy pairs identified in *Hubble Space Telescope* Wide Field Camera 3 (*HST*/WFC3) imaging from the CANDELS survey, we estimate the rate at which massive, quiescent galaxies accrete stellar mass in mergers over $z = 0.4$–2. The depth of the WFC3 data is sufficient to identify satellites $10\times$ less massive than their hosts. By coupling these data with merger simulations, we estimate the size growth attributable to mergers of observed close companions. We additionally measure the rate of size growth in the same large, homogenous sample of quiescent galaxies, taking advantage of the area, depth, and resolution afforded by the WFC3 imaging. We then compare the two rates in order to evaluate the role of mergers in driving the observed size growth.

The motivations and historical context for these investigations are developed extensively in the introductory Chapters 2 and 6. Chapter 9 summarizes our results and describes potential directions for future progress. The remainder of the text has nearly all been previously published. Chapters 2–5 are based on:

[1] Newman, A., Treu, T., Ellis, R. S., Sand, D. J., Richard, J., Marshall, P., Capak, P., Miyazaki, S., "The Distribution of Dark Matter Over Three Decades in Radius in the Lensing Cluster Abell 611," ApJ 706, 1078 (2009)

[2] Newman, A., Treu, T., Ellis, R. S., Sand, D. J., "The Dark Matter Distribution in A383: Evidence for a Shallow Density Cusp from Improved Lensing, Stellar Kinematic, and X-ray Data," ApJL 728, L39 (2011)

[3] Newman, A., Treu, T., Ellis, R. S., Sand, D. J., Nipoti, C., Richard, J., Jullo, E., "The Density Profiles of Massive, Relaxed Galaxy Clusters: I. The Total Density Over 3 Decades in Radius," ApJ in press

[4] Newman, A., Treu, T., Ellis, R. S., Sand, D. J., "The Density Profiles of Massive, Relaxed Galaxy Clusters: II. Separating Luminous and Dark Matter in Cluster Cores," ApJ in press

Papers [1]–[2] developed the methodology for measuring the dark and stellar density profiles and applied it to two clusters, A611 and A383. The final papers [3]–[4] present results for the full sample. Since these latter papers incorporate and supersede the results of the earlier two, they comprise the bulk of the text in this thesis. However, we have merged appropriate portions of papers [1] and [2] where appropriate to detail the methodology. In summary, Part I is a merged and slightly expanded version of papers [1]–[4] that is based throughout on the most current data and analysis.

Chapters 7 and 8, which comprise Part II of this thesis, are based on:

[5] Newman, A., Ellis, R. S., Treu, T., Bundy, K., "Keck Spectroscopy of $z > 1$ Field Spheroidals: Dynamical Constraints on the Growth Rate of Red 'Nuggets'," ApJL 717, L103 (2010)

[6] Newman, A., Ellis, R. S., Bundy, K., Treu, T., "Can Minor Merging Account for the Size Growth of Quiescent Galaxies? New Results from the CANDELS Survey," ApJ 746, 162 (2012)

Chapter 7 is based on paper [5], but we have updated and expanded some of the results. In particular, the published stellar masses have been revised so that they are derived using the same methodology as in paper [6] for consistency with planned future work. The text of Chapter 8 is drawn directly from paper [6].

Since these papers benefitted from the input of several co-authors, Caltech guidelines require that their contribution to this thesis be clarified. In Part I, some of the Subaru observations were gathered by D. Sand and T. Treu before my arrival as a graduate student, as were Keck spectroscopic observations of three of the seven BCGs we study. The reduction of the Subaru data and the weak lensing analysis were performed by myself, as were the reduction and analysis of the spectra (with the exception of the reduction of A2667). C. Nipoti performed the N-body simulations described in Chapter 5. P. Capak provided the software used for the reduction of mosaic imaging (Appendix B) and patiently trained me in its use as a first-year student. In Part II, K. Bundy and P. Capak provided galaxy catalogs from which spectroscopic targets were drawn in Chapter 7. Otherwise Chapters 7 and 8 are my own work. Naturally, the interpretation benefitted from the contribution of all the co-authors, for which I am grateful.

Throughout, we consistently use a flat ΛCDM cosmology with $\Omega_m = 0.3$, $\Omega_v = 0.7$, and $h = H_0/(100 \text{ km s}^{-1}) = 0.7$. All magnitudes are in the AB system.

Chapter 2

Part I: Dark Matter in Galaxy Clusters

It is remarkable that the existence of the dominant form of matter is inferred empirically only though its gravitational effects on astronomical scales. Dark matter is the key to the formation of cosmological structures and of galaxies. The discovery of dark matter, along with the detailed observational mapping and precise theoretical understanding of its distribution, is among the greatest achievements of astronomy. In this chapter, we first briefly review the history of evidence for dark matter and the convergence to the now-standard "concordance" cosmological model, ΛCDM. After describing results from N-body simulations of structure formation, we turn to the main challenges facing ΛCDM, which lie on sub-galactic scales. In particular, we focus on the equilibrium density structure of dark matter halos. After summarizing current observations on galactic scales, we motivate the utility of galaxy clusters as a unique window into halo structure and describe earlier observational work. Discrepancies between ΛCDM and observations on small scales may be the result of the poorly-understood interplay between dark and baryonic matter during galaxy formation and assembly. Alternatively, they may reflect dark matter microphysics that becomes astronomically significant only on small scales. We review how observations of the central regions of halos can constrain these scenarios, and finally outline the specific goals of Part I of this thesis.

2.1 Historical overview of dark matter

Kapteyn (1922) and Oort (1932) used the motion of stars perpendicular to the Galactic plane to estimate the mass density in the solar neighborhood. Kapteyn (1922) recognized that sources of "dark matter" (apparently the first use of this term) could be identified by comparing the dynamically-inferred mass to that associated with visible stellar populations. He concluded:

> We therefore have the means of estimating the mass of dark matter in the universe. As matters stand at present it appears at once that this mass cannot be excessive. If

> it were otherwise, the average mass as derived from binary stars would have been very much lower than what has been found for the effective mass.

Through a similar study, Oort (1932) concluded that the local density in the Milky Way disk may exceed that in stars by a factor of two, while acknowledging that a significant amount of stellar mass could be missed by the star counts available at the time.

The first clear detection of a large quantity of invisible mass was in galaxy clusters by Zwicky (1933, 1937).[1] Using his observed radial velocities of 8 galaxies in the Coma cluster, Zwicky measured a velocity dispersion of 1019 ± 360 km s^{-1}. Under the assumption that the cluster is a gravitationally relaxed system, as its appearance seems to indicate, Zwicky proceeded to calculate the total mass using the virial theorem. He arrived at a mass 400 times higher than that attributable to luminous matter, assuming that the mass-to-light ratio of the stars is comparable to that in the solar neighborhood. Thus, Coma would fly apart in only a crossing time (~ 2 Gyr) were it not held together by a large amount of unseen gravitating mass. In these prescient articles, Zwicky both uses the term "dark (cold) matter" to refer to the invisible mass (though not, of course, with its modern meaning) and, astonishingly, argues that future observations of gravitational lensing by clusters "promises to furnish us with the simplest and most accurate determination of nebular masses," 50 years before the first examples of strong lensing by clusters were discovered (Lynds & Petrosian 1986; Soucail et al. 1987). Smith (1936) made a similar observation in the Virgo cluster and, from his high inferred mass, suggested the presence of "a great mass of internebular material."

A few years later, Babcock (1939) measured the rotation curve of M31 to a radius of about $100'$ (23 kpc with the modern distance). If the gravitating mass is distributed similarly to the light, a disk galaxy will show a nearly Keplerian decline in the rotation velocity, following $v \propto r^{-1/2}$ in its outer regions. Babcock instead observed a slowly continuing *rise* in the rotation speed. From this he inferred a substantial rise in the mass-to-light ratio with radius. His preferred explanations were obscured starlight in the outer disk or unspecified "new dynamical considerations." Babcock's measurements were improved by Rubin & Ford (1970) and Roberts (1975) using nebular velocities and 21 cm observations, respectively; the latter suggested a population of late M dwarfs located at $R \gtrsim 25$ kpc as an explantation for the missing mass. At this time, there seems to have been no connection made between the missing mass in the outskirts of spiral galaxies and that inferred in clusters of galaxies by Zwicky and Smith. Furthermore, there was no consensus on whether the missing mass was comprised of faint stars, hot gas, or some unknown species (van den Bergh 1999).

Observations soon showed that the shape of rotation curve of M31 is not peculiar, but is in fact common to a wide range of disk galaxies (Roberts 1975; Rubin et al. 1980). Kinematic measurements in spheroidal galaxies remained ambiguous as to whether the mass-to-light ratio rises with radius as seen in spirals (Faber & Gallagher 1979 provide a review), except in some cD galaxies that showed a

[1] I rely on translated segments of Zwicky's 1933 article in German given by van den Bergh (1999).

rising velocity dispersion (e.g., Dressler 1979). Evidence mounted around the same time that X-ray emission seen in galaxy clusters is thermal bremsstrahlung emission from hot gas (e.g., Bahcall & Sarazin 1977). Under the assumption that the gas is nearly isothermal and in hydrostatic equilibrium, the total gravitating mass could be inferred. Such calculations revealed a massive, extended dark component around M87 in Virgo (Mathews 1978). The relative velocities of galaxy pairs also pointed to massive dark "coronae" (e.g., Einasto et al. 1974). The totality of the observational evidence favored a cosmological mean matter density $\Omega_m \approx 0.2$, with a large uncertainty (Ostriker et al. 1974).

Theoretical arguments also supported the presence of extended, massive, nearly spherical dark "halos." Their significance in explaining the dynamical stability of thin disk galaxies was identified by Ostriker & Peebles (1973). White & Rees (1978) postulated that dark matter comprises $\sim 80\%$ of the mass of the universe and forms structure through hierarchical gravitational collapse (following Press & Schechter 1974), while the concentrated luminous parts of galaxies are formed through gas cooling within the potential wells set by this dark matter – the essence of the modern galaxy formation paradigm.[2] White (1977) showed that the "missing mass" in clusters cannot all be associated with individual galaxies, since dynamical friction would then lead to a much higher degree of mass segregation than is observed: most of the dark matter must be more smoothly distributed between the galaxies.

The baryon density derived from big bang nucleosynthesis (BBN) and the observation of interstellar deuterium in the 1970s was only $\Omega_b \approx 0.01$ (Wagoner 1973; Rogerson & York 1973). Given that $\Omega \gtrsim 0.2$ was favored, this indicated that the dark matter could not be primarily baryonic, if deuterium is indeed produced only in the early universe.[3] In the early 1980s, improving upper limits on the anisotropy of the cosmic microwave background (CMB) showed that the density fluctuations present at recombination were too weak to be amplified gravitationally into non-linear structures by the present day, if they were dominated by a species coupled to photons (Zeldovich et al. 1982).

In the early 1980s there was initially great enthusiasm for neutrino dark matter: neutrinos could begin collapsing before recombination, since they were not coupled to the radiation field; they had the virtue of being known to exist; and Soviet physicists believed they had measured their mass (Lubimov et al. 1980). Neutrinos have highly relativistic velocities that allow them to diffuse out of all but the deepest potential wells. In such a "hot" dark matter scenario, superclusters are the first objects to collapse, whereas small objects cannot directly collapse and must form via fragmentation of larger systems. However, White et al. (1983) used N-body simulations to show

[2]While they considered low-mass or remnant stars the most likely explanation, they allowed for the possibility of black holes or massive neutrinos as comprising the dark matter.

[3]Due to the destruction of deuterium within stars, the Galactic [D/H] measure is a lower limit; this leads to an *upper* limit on the baryon density. The BBN constraint was later put on firmer footing through observations of high-redshift quasar absorption systems that are chemically unevolved compared to the Galactic disk (Songaila et al. 1994).

that in galaxies in a neutrino-dominated universe cluster on much larger scales than permitted by observations, particularly data from the Center for Astrophysics (CfA) redshift survey (Davis & Peebles 1983). Bond et al. (1982) and Blumenthal et al. (1982) discussed structure formation with weakly-interacting ∼keV mass dark matter particles ("warm" dark matter), motivated by the gravitino expected in supersymmetry theories, while Peebles (1982) considered more massive weakly-interacting particles: "cold" dark matter (CDM) with negligible thermal velocities. Cold dark matter provided the best fit to the available observations (Blumenthal et al. 1984), and it could remain consistent with the flat universe favored by inflation models (a cosmological constant was not yet considered likely), if galaxy formation was "biased" toward high-density peaks (Davis et al. 1985).

COBE measurements (Wright et al. 1992) of the CMB anisotropy further constrained the cosmological model, but remained consistent with unbiased flat CDM, a mix of cold and neutrino dark matter, or CDM with a cosmological constant (ΛCDM). Using CMB data alone there is a degeneracy between spatial curvature and the expansion history. Distances to supernovae, whose intrinsic luminosities are calibrated from the shapes of their light curves, independently constrained the latter and revealed an accelerating expansion: this demands $\Lambda > 0$ (Riess et al. 1998; Perlmutter et al. 1999). The Hubble Key Project anchored the local distance ladder by measuring H_0 to 10% (Freedman et al. 2001). As CMB experiments advanced, the first peak in the spectrum of temperature anisotropies was located by the Boomerang and Maxima balloon-borne experiments. Its angular size implied a flat universe ($\Omega = 1$ within $< 10\%$; Lange et al. 2001; Jaffe et al. 2001). The much higher sensitivity and resolution achieved by the Wilkinson Microwave Anisotropy Probe (WMAP) uncovered further peaks in the power spectrum, producing precise constraints on the cosmological parameters (Spergel et al. 2003). Together these observations led to the now standard cosmological model of a flat universe seeded by nearly scale-invariant adiabatic density fluctuations, in which the mass-energy is dominated by vacuum energy ($\Omega_v = 0.73$) and the matter is dominated by cold dark matter ($\Omega_{\rm cdm} = 0.23$, $\Omega_b = 0.05$; Komatsu et al. 2011).

Galaxy clusters played a central role in the discovery and characterization of dark matter. As described above, dark matter was first clearly identified by Zwicky in clusters, and the giant central galaxies found in clusters were the first ellipticals shown clearly to have halos with high mass-to-light ratios. The abundance of clusters and their spatial clustering has long been used as a sensitive cosmological probe, particularly of the matter density Ω_m and the amplitude of density fluctuations σ_8 (Bahcall & Soneira 1983; Bahcall & Cen 1992; Eke et al. 1996; Allen et al. 2004, 2008). The baryon fraction in clusters has also been an important benchmark (e.g., White et al. 1993), as clusters are generally thought to be large enough to "fairly sample" the matter budget. As described in Section 2.5, several observational probes (dynamics, lensing, X-ray emission) allow the internal structure of the dark matter in clusters to be mapped in detail and compared to CDM

simulations (e.g., Tyson et al. 1998). Finally, clusters provide an opportunity to search for spatial segregation between dark and baryonic material, since both the mass and the majority of the baryons (though their thermal X-ray emission) can be traced in detail. The "Bullet Cluster" provided a dramatic example of a merging cluster in which the mass and baryon fluid are clearly offset, directly demonstrating that most of the dark matter is in a nearly collisionless form (Clowe et al. 2006).

We are now in the era of increasingly precise cosmological constraints powered by large surveys. A six-parameter ΛCDM model has proven consistent with varied observations of ever-increasing precision, including the CMB power spectrum (e.g., Komatsu et al. 2011), galaxy clustering and acoustic oscillations (Anderson et al. 2012), redshift space distortions (Reid et al. 2012), galaxy cluster abundances (Vikhlinin et al. 2009), the clustering of gas in the Lyα forest (Seljak et al. 2005; Viel et al. 2008), weak lensing (Refregier 2003; Kilbinger et al. 2012), and other probes.

2.2 Dark matter particle candidates

These observations probe the distribution of dark matter and its evolution on supergalactic scales. Astrophysically, meeting these constraints requires a particle that:

1. is produced with the measured mass density,
2. is not baryonic, to preserve big bang nucleosynthesis,
3. is electrically neutral, hence is "dark" and decouples from the photon fluid prior to recombination,
4. does not interact too strongly with itself, due to limits on DM–DM collisions from the Bullet Cluster and the asphericity of cluster cores (see below),
5. is dynamically cold enough that small-scale density fluctuations, seen in the Lyα forest or weak lensing observations, are not overly suppressed by the particles' random motions.

No known particle satisfies these criteria. Cosmological dark matter thus requires an extension to the standard model, and many candidate particles that meet the above requirements have been suggested. The most favored is a weakly interacting massive particle (WIMP) whose density is set by "freeze-out" in the early universe, when its annihilation rate falls below the background expansion rate. The relic mass density automatically matches to the observed dark matter density if its annihilation cross-section is on the order of the weak interaction (the "WIMP miracle"). Furthermore, the lightest particle in supersymmetric extensions of the standard model, such as a neutralino (reviewed by Jungman et al. 1996), is a "natural" dark matter candidate in the sense that its existence is independently motivated by the gauge hierarchy problem (Why is the Higgs mass so much less than the Planck mass scale?).

Although WIMPs are the leading candidate, numerous other possibilities are viable. The flavor oscillations exhibited by solar neutrinos require physics beyond the standard model. New species of "sterile" neutrinos, so named because they have no non-gravitational couplings, could explain this puzzle and supply the needed dark matter. If sterile neutrinos are the dark matter, the mass is constrained to be $\gtrsim 0.5$ keV by the Tremaine & Gunn (1979) limit on the phase-space density – much more massive than the standard model neutrinos. Sterile neutrinos are the prototype warm dark matter candidate and are associated with small-scale power suppression, but the degree depends on the mass and production mechanism (e.g., Abazajian et al. 2001; Abazajian & Koushiappas 2006; Boyarsky et al. 2009). Another "natural" particle candidate is an ultralight axion, which was proposed to solve the strong CP problem in quantum chromodynamics. Its mass is $\lesssim 10$ meV (Feng 2010), although it is extremely cold if produced in a condensate, as expected, rather than thermally. It is also possible that dark matter exists within an entire "hidden" sector whose constituent particles are not directly coupled to the standard model (e.g., Feng & Kumar 2008). A hidden sector appears in many models for supersymmetry breaking that arise in string theory. The hidden sector may contain its own force carriers, and the dark matter particle could have significant self-interactions. This has astrophysical implications, since dark matter could be collisional (within current observational bounds). This list of dark matter candidates includes several of the most widely discussed possibilities but is, of course, far from exhaustive. Feng (2010), on which much of the above discussion is based, reviews additional options.

Three experimental routes are being pursued to further elucidate the nature of dark matter. The first is production in a collider, such as the Large Hadron Collider. The second is direct terrestrial detection of dark matter particles by observing, for example, recoils of heavy nuclei off WIMPs (e.g., Aprile et al. 2010; Ahmed et al. 2011). The third is detection of an astrophysical signal arising from the small-scale dark matter distribution. One promising "indirect detection" signal is annihilation into gamma rays in the Galactic center (e.g., Su & Finkbeiner 2012), dwarf galaxies (Abdo et al. 2010), or the cores of nearby galaxy clusters (Ackermann et al. 2010). The shape of the dark matter density profile, which is sensitive to the temperature of the dark matter particle and any self-interaction cross-section (Section 2.6.1), can also provide important clues.

2.3 The structure of dark matter halos

The success of the ΛCDM model on larger scales – larger than individual dark matter (DM) halos – now appears overwhelming (Section 2.1; Springel et al. 2006; Frenk & White 2012). The main challenges to this model currently come from observations on smaller scales (Primack 2009). Two main discrepancies between ΛCDM and small scale observations have been claimed. The first concerns the population of dwarf galaxies. The known dwarf satellites of the Milky Way are much fewer

than the number of predicted DM subhalos (the "missing satellites problem"; e.g., Kauffmann et al. 1993; Klypin et al. 1999). Such a comparison depends on the way that luminosities are assigned to subhalos in simulations, which is complex. Gas cooling can be inhibited by photoheating from the intergalactic UV background after reionization or through feedback from the first stars to form (Bullock et al. 2000; Benson et al. 2002; Kravtsov 2010). Furthermore, many dwarf galaxies were discovered in the Sloan Digital Sky Survey, and reasonable completeness corrections imply that a large undiscovered population lies below current detection limits (Tollerud et al. 2008). When these effects are taken into account, much of the difficulty in matching the luminosity function may be relieved. However, observations of known dwarfs have advanced well beyond their luminosities. If one turns to the dynamical properties of the observed bright Milky Way satellites, none is as dense as the most massive Milky Way subhalos in simulations. This problem was given the timely moniker "too big to fail" (Boylan-Kolchin et al. 2011, 2012): it implies that the subhalos most likely to retain their gas and form stars are either dark or unlike their simulated counterparts, and no satisfactory explanation has emerged.

The second discrepancy concerns the radial density structure of DM halos. In CDM this follows a specific and universal form that is well understood in CDM-only simulations. In particular, at small radii the DM density is "cuspy" and nearly follows a slope $\rho_{\rm DM} \propto r^{-1}$. Many observations indicate that at least some halos, on mass scales from dwarf galaxies through galaxy clusters, instead have a shallower inner density slope, perhaps even a constant density "core." This is sometimes called the "cusp–core" debate (although this can be a misleading dichotomy, since intermediate slopes are possible). The focus of Part I of this thesis is measuring the dark and baryonic density profiles in a representative set of massive, relaxed galaxy clusters. To place this goal in the context of theory and observations on other mass scales, we first review the halo density profiles characteristic of CDM.

2.3.1 CDM simulations

In the limit of cold DM – i.e., negligible thermal velocities in the early universe, which applies to a WIMP thermal relic or an axion particle, for example – then the transfer function is fully specified for a given cosmology (e.g., Seljak & Zaldarriaga 1996). The transfer function converts the power spectrum of primordial density fluctuations to fluctuations present at some high redshift (typically $z \sim 100$, when the perturbations are still linear). This provides the initial conditions for N-body simulations that follow the non-linear growth of structure in an expanding universe, based only on the law of gravity. These simulations have become the basic tool for calculating the abundance and spatial clustering of CDM halos and subhalos, their assembly history, and their internal structure.

The first N-body CDM simulation with sufficient resolution to trace the internal density profile of an individual halo was conducted by Dubinski & Carlberg (1991). In a very influential set of papers, Navarro, Frenk, & White (1996b, 1997, hereafter NFW) found that the density profiles of

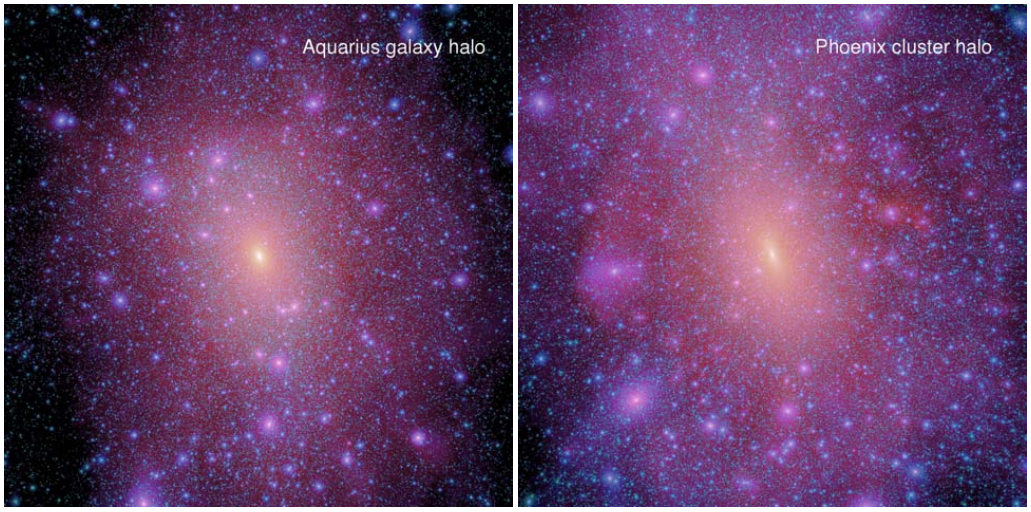

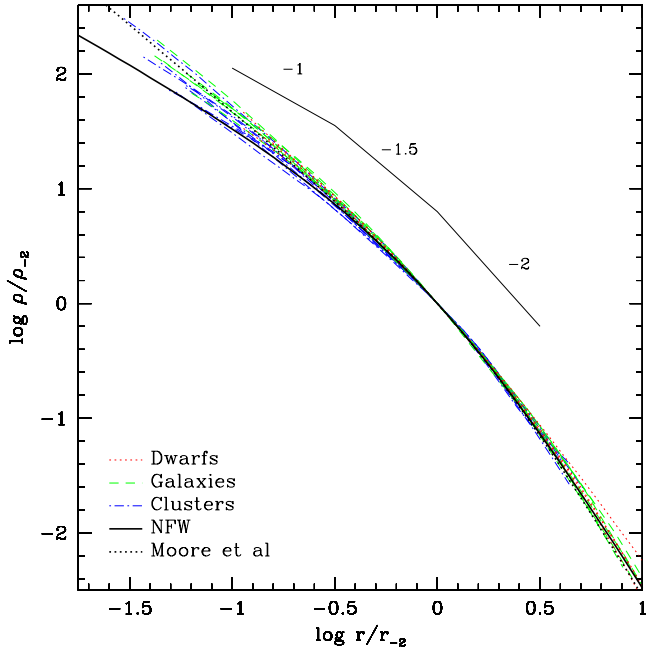

Figure 2.1: Top: State-of-the-art N-body simulations of a Mliky Way-like galaxy (left; Aquarius project, Springel et al. 2008) and a galaxy cluster (right; Phoenix project, Gao et al. 2012b). The box sides are roughly $4r_{200}$, or $\simeq 1$ Mpc and 7 Mpc for the galaxy and cluster halos, respectively. Note the smooth DM halo with an abundance of subhalos superposed ($\lesssim 10\%$ of particles are in resolved substructures) and the overall similar appearance of halos whose masses differ by a factor of $\simeq 500$. Reproduced from Frenk & White (2012). **Bottom:** The self-similarity of simulated CDM density profiles is revealed by the coincidence of the density profiles of dwarf galaxies, L_* galaxies, and galaxy clusters after a suitable rescaling of the units. Here r_{-2} denotes the radius where the local slope is $\rho \propto r^{-2}$, which equals r_s for an NFW profile, and ρ_{-2} is the corresponding density. The functional forms proposed by NFW and Moore et al. (1999) are overlaid; after rescaling, these profiles are completely fixed in this plot. Reproduced from Navarro et al. (2004).

CDM halos over a wide range of mass can be fitted by the formula

$$\rho_{\rm DM}(r) = \frac{\rho_c \delta_c}{(r/r_s)(1+r/r_s)^2}, \tag{2.1}$$

where ρ_c is the critical density of the universe, δ_c is the characteristic density of the halo, and r_s is a characteristic length scale known as the *scale radius*. In other words, by a suitable rescaling of the density and length units, CDM halos ranging from Earth- to cluster-scale masses (Diemand et al. 2005a) over all epochs fall on a "universal" density profile, which follows $\rho_{\rm DM}(r) \propto r^{-3}$ for $r \gg r_s$ and has a density cusp $\rho_{\rm DM}(r) \propto r^{-1}$ at $r \ll r_s$ (see Figure 2.1). The form of this universal profile does not depend on the spectrum of initial density fluctuations or the cosmological parameters, but appears to be a general result of hierarchical gravitational collapse of cold, collisionless material. No complete analytic derivation of the profile shape has been found.

While an NFW profile is fully specified by two parameters, several equivalent parameterizations are in common use. In addition to to δ_c and r_s, the *virial radius* r_{200} is the radius of a sphere enclosing a mean density equal to 200 times the critical density of the universe; this approximately delineates the virialized material.[4] The *virial mass* M_{200} is then the mass within r_{200}, and the *concentration* is defined as $c = r_{200}/r_s$. Furthermore, the two parameters are found to be strongly correlated, which gives rise to a *mass–concentration relation*: lower-mass halos are denser, because they typically collapsed earlier, when the universe was denser. Thus, the NFW profile is almost a one-parameter family of halos, modulo the scatter in the mass–concentration relation that arises from scatter in the halo assembly histories (e.g., Bullock et al. 2001).

Numerous simulations of ever-increasing resolution and volume have confirmed the essential findings of NFW (e.g., Moore et al. 1998, 1999; Jing & Suto 2000; Ghigna et al. 2000; Fukushige & Makino 2001; Klypin et al. 2001; Fukushige et al. 2004; Navarro et al. 2004; Diemand et al. 2005b; Gao et al. 2008; Stadel et al. 2009; Navarro et al. 2010; Gao et al. 2012b), although there has been some controversy over, and refinement of, the detailed profile shape. The NFW profile asymptotically approaches a logarithmic slope $-d\log\rho/d\log r \to 1$ (i.e., $\rho \propto r^{-1}$) as $r \to 0$. Many later studies found that the NFW form tends to slightly underestimate the density at small radii, and Moore et al. (1999) suggested an alternate functional form with $-d\log\rho/d\log r \to 1.5$.

More recent simulations have found that halo density profiles fall between the NFW and Moore et al. (1999) profiles (see Figure 2.1) and that *three*-parameter forms provide a significantly improved fit (e.g., Merritt et al. 2006; Graham et al. 2006; Gao et al. 2008; Navarro et al. 2010; Gao et al. 2012b). Common examples are the generalized NFW profile (gNFW)

$$\rho_{\rm DM}(r) = \frac{\rho_c \delta_c}{(r/r_s)^\beta (1+r/r_s)^{3-\beta}}, \tag{2.2}$$

[4] Alternate definitions are widely used, such as substituting the mean density for the critical density or varying the density contrast from 200 to a value motivated by spherical top-hat collapse models.

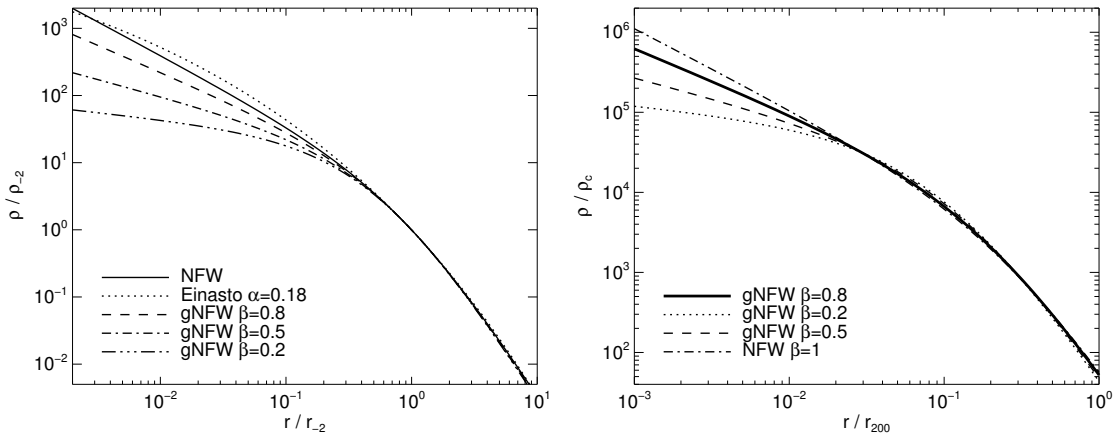

Figure 2.2: Left: The NFW and Einasto ($\alpha = 0.18$) density profiles, which provide good fits to CDM simulations, are compared to gNFW models (Equation 2.2) with varying inner density slopes. The models are normalized at r_{-2}, where the local density slope is $\rho \propto r^{-2}$. **Right:** A gNFW profile with $\beta = 0.8$ and $r_{-2} = 0.25 r_{200}$ (thick line) is approximated by profiles with different β that have been translated – i.e., their scale densities and radii adjusted – to closely match the fiducial model at $r \gtrsim 0.02 r_{200}$. This demonstrates that density measurements over wide radial intervals, both in simulations and observations, are necessary to discriminate halo models.

with an asymptotic slope $-d\log\rho/d\log r = \beta$, and particularly the Einasto (1965) profile

$$\rho_{\rm DM}(r) = \rho_{-2} \exp\left[-\frac{2}{\alpha}\left\{\left(\frac{r}{r_{-2}}\right)^{\alpha} - 1\right\}\right], \tag{2.3}$$

with a rolling logarithmic slope $-d\log\rho/d\log r = 2(r/r_{-2})^{\alpha}$. By definition, $\rho \propto r^{-2}$ locally at r_{-2}. The shape parameter is typically $0.15 \lesssim \alpha \lesssim 0.25$ for relaxed systems and varies systematically with mass and redshift; this implies that halo density profiles are *not* strictly self-similar when examined with the high resolution and statistics of present simulations.

While the Einasto profile provides statistically superior fits, the original NFW profile still provides a sufficiently accurate description of CDM N-body simulations for most purposes. The highest-resolution cluster simulations to date show that systematic deviations from the NFW profile, when averaging over many clusters, are $\Delta\rho/\rho < 10\%$ over a wide radial interval $2 \times 10^{-3} < r/r_{200} < 1$ (Gao et al. 2012b). This is comparable to the scatter between the mean density profile and those of *individual* clusters. Modern simulations also show no signs of approaching an asymptotic logarithmic slope, as the NFW profile does ($\beta \to 1$), and may continue rolling over to shallower slopes at small radii as the Einasto formula suggests. However, simulations currently cannot resolve radii where $-d\log\rho/d\log r < 1$ on average (i.e., systematically shallower than the NFW inner slope). Figure 2.2 compares the analytic NFW and Einasto profiles fit to simulations, along with gNFW profiles with varying inner slopes. The right panel demonstrates that due to the freedom to tune the density and length scales, discriminating the *shape* of the density profile (i.e., constraining a third parameter) requires measurements over a wide dynamic range extending well within $0.02 r_{200}$.

2.4 Observations on galactic scales

Numerical simulations provide a clear prediction for the density structure of CDM halos, at least in the absence of baryonic effects. Due to its clear cosmological significance, a great deal of observational effort has gone into testing this prediction, which has produced a vast and often controversial literature. As we describe below, many galaxies appear to have inner density slopes that are *shallower* than a CDM cusp. When the slope is ambiguous, the central densities are often still lower than expected from the CDM mass–concentration relation. The quality of the evidence varies with mass scale and the type of galaxy, since verifying the form of the DM profile presents several observational challenges: (1) obtaining constraints that are precise enough and that span a wide enough radial interval to discriminate between models (see Figure 2.2), (2) overcoming degeneracies inherent to individual mass probes, such as velocity anisotropy, and (3) separating the baryonic and dark mass at small radii. In this section we review the current state of observations in low-mass galaxies and $\sim L_*$ systems, reserving galaxy clusters and their central galaxies for Section 2.5.

2.4.1 Low-mass disk galaxies

It was realized very early that the kinematics of low-mass disk galaxies are not consistent with the universal CDM profile (Flores & Primack 1994; Moore 1994; Burkert 1995). Their rotation curves rise much more slowly than an NFW halo in the inner regions. These galaxies are highly DM-dominated, so the uncertainty introduced by subtracting the stellar and gas mass to isolate the halo is minimal. The impact of baryons on the DM profile is sometimes claimed to be negligible, although this is not certain (Section 2.6.2). Further H I and long-slit Hα observations broadly supported these earlier findings (e.g., Côté et al. 2000; de Blok et al. 2001; Swaters et al. 2003; Gentile et al. 2005), but possible systematic errors in the observations and interpretation remained a major concern (e.g., van den Bosch et al. 2000; reviewed by de Blok 2010). Extended two-dimensional velocity fields with higher spatial and spectral resolution in H I (de Blok et al. 2008; Oh et al. 2011) and Hα (Simon et al. 2003, 2005; Kuzio de Naray et al. 2006, 2008), along with more detailed modeling of the observational effects (Kuzio de Naray & Kaufmann 2011), have mostly alleviated these worries. While individual galaxies frequently present ambiguities, and some low-mass disks do appear to contain a CDM-type cusp (e.g., Simon et al. 2005), it seems clear that many low-mass disks with $M_B > -19$ are more consistent with a shallow DM cusp or a core than with an NFW profile, particularly when the latter is forced to follow the ΛCDM mass–concentration relation. Figure 2.3 shows the inner density slopes recently measured in a sample of low-mass disks. While there is likely a range of slopes, most galaxies appear to have flat inner density profiles relative to CDM halos.

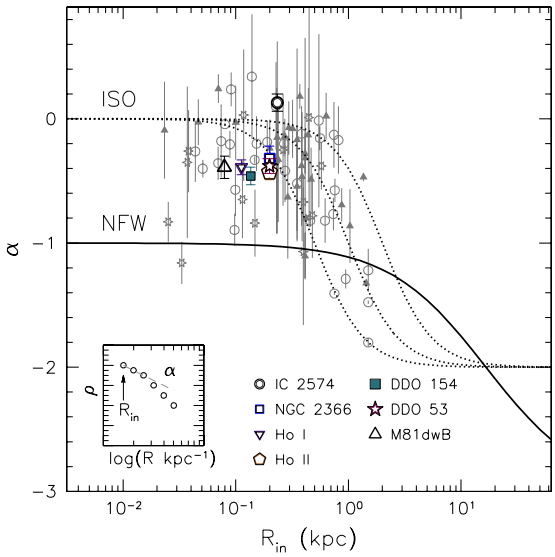

Figure 2.3: The inner density slope α, where $\rho \propto r^{\alpha}$, of DM-dominated low-mass disk galaxies is plotted against the innermost resolved radius $R_{\rm in}$. Overlaid are an NFW density profile ($\alpha \to -1$ as $r \to 0$) and a model with a constant-density core ("ISO," $\alpha \to 0$). While there may be significant galaxy-to-galaxy variation, most systems appear to reside in DM halos with inner density profiles that are flatter than canonical CDM halos. Reproduced from Oh et al. (2011).

2.4.2 Milky Way satellites

The dwarf spheroidal (dSph) satellites of the Milky Way are the most DM-dominated galaxies known. Their masses can be measured through the kinematics of individual stellar members, but this processes is more complex than the nearly circular rotation encountered in disk galaxies, owing to the unknown distribution of stellar orbits in these pressure-supported systems. While the mass enclosed within the half-light radius is relatively insensitive to the stellar orbital anisotropy and is therefore robustly constrained (e.g., Walker et al. 2009), the *slope* of the density profile is degenerate with the anisotropy in a simple Jeans analysis. While many dSph density profiles appear to be cored if one imposes isotropic orbits (Gilmore et al. 2007), the data are consistent with an NFW-type cusp if the orbits are mildly tangential *and* the concentration parameter is low (Wolf & Bullock 2012). Fitting an NFW profile that lies on the ΛCDM mass–concentration relation requires very tangential orbits ($\beta_{\rm aniso} \simeq -1.5$; Equation 2.6). Thus, it seems very likely that the central densities of dSph galaxies are lower than CDM subhalos, regardless of whether a cusp is present, and this may be related to the "too big to fail" problem discussed in Section 2.3.

When additional information is available to supplement a simple Jeans analysis, the data usually favor cored profiles over NFW-type cusps, although this has been possible so far only in a few systems. Fornax and Sculptor contain chemically and dynamically distinct subpopulations with different half-light radii; this allows robust measures of enclosed mass at two radii and thus determines a slope, which is shallower than an NFW cusp at high confidence (Battaglia et al. 2008; Walker & Peñarrubia

2011; Amorisco & Evans 2012). A flat inner mass distribution appears necessary to explain the persistence of cold substructures (Kleyna et al. 2003) and globular cluster populations (Goerdt et al. 2006) in Ursa Minor and Fornax, respectively. In some luminous classical satellites thousands of stellar velocities have been measured. Higher moments of the velocity distribution (beyond the dispersion) can be derived from these data to constrain more general dynamical models. Jardel & Gebhardt (2012) constructed Schwarzschild models of Fornax and showed that a cored model fits the velocity data much better than an NFW profile, and that the stellar orbits are mildly radially biased. On the other hand, a similar analysis of Draco indicated the presence of an NFW-type cusp, which could indicate the presence of significant scatter (Jardel et al. 2012).

2.4.3 $\sim L_*$ galaxies

Baryons (stars and cold gas) contribute very significantly to the mass budget in the inner regions of luminous disks like the Milky Way. In principle one can model the observed rotation curve using multiple mass components: a stellar contribution for which mass traces the near-infrared light, a gas contribution based on 21 cm data, and a parameterized DM halo (e.g., an NFW, cored, or power law model). In practice, isolating the central DM is very difficult in these systems due to uncertainties in the baryonic mass. Estimates of the mass in stars are particularly uncertain due to imperfect knowledge of the underlying stellar population, such as the initial mass function (IMF). This "disk–halo degeneracy" has prevented strong conclusions regarding the form of the DM profile in luminous disks (e.g., van Albada & Sancisi 1986; Dutton et al. 2005). The DiskMass project is addressing this degeneracy by quantifying the disk surface density via the vertical velocity dispersion in face-on disks (Bershady et al. 2010, 2011), while the SWELLS survey (Treu et al. 2011) combines strong lensing with gas kinematics. These programs have made important progress in quantifying the relative scaling of the stellar and DM components, but the internal distribution of DM remains fairly poorly constrained (Westfall et al. 2011; Barnabè et al. 2012; Dutton et al. 2012).

In luminous elliptical galaxies the dominance of the baryons in the central regions has also stymied a detailed mapping of the DM distribution. A robust mass decomposition requires reaching the DM-dominated regime at large radii, but unlike disks, gas kinematics are not available in gas-poor ellipticals. Alternative dynamical tracers include kinematics of globular clusters, planetary nebulae, and integrated starlight, but these observations are more difficult and often noisy. Dynamical measurements are again plagued by degeneracies associated with the orbital distribution, which can even mask the presence of a DM halo (Romanowsky et al. 2003; Dekel et al. 2005; de Lorenzi et al. 2009). Significant progress has been made in securing radially-extended, high-quality kinematic data, sometimes including higher moments of the line-of-sight velocity distribution to quantify the orbital anisotropy (Cappellari et al. 2006; Weijmans et al. 2009; Murphy et al. 2011; Thomas et al. 2011). This recently has allowed the bulk DM content (e.g., the DM fraction within r_e) and

M_*/L to be constrained more robustly, but the internal distribution of DM remains unclear.

X-ray emission (Humphrey et al. 2006; Buote & Humphrey 2012) and weak gravitational lensing (Mandelbaum et al. 2006) can also probe the DM-dominated regime. While the inferred DM profiles appear broadly consistent with a CDM halo, the resolution of these techniques is too poor to usefully constrain the inner slope. In strong lensing ellipticals, the position of the gravitational arc combined with stellar kinematic data exquisitely fixes the slope of the *total* density profile, which is nearly isothermal ($\rho_{\rm tot} \propto r^{-2}$), but the "bulge–halo degeneracy" has prevented a precise measurement of the inner DM slope β (Treu & Koopmans 2004; Jiang & Kochanek 2007). An exception is the rare *double* lens (the "Jackpot") studied by Sonnenfeld et al. (2012), who infer a *steep* $\beta = 1.7 \pm 0.2$; this may indicate that the halo has been compressed by the baryons (Section 2.6.2).

Given the difficulty of determining the detailed distribution of DM and baryons within individual ellipticals, many important insights have come from examining trends within the population. There is now strong evidence that the total dynamical mass-to-light ratio M/L rises with mass, and that this is the long-debated origin of nearly all of the "tilt" of the fundamental plane (Padmanabhan et al. 2004; Cappellari et al. 2006; Auger et al. 2010a; Napolitano et al. 2010; Thomas et al. 2011; Cappellari et al. 2012b). Furthermore, M/L rises faster than the *stellar* mass-to-light ratio M_*/L derived from population synthesis models based on a uniform IMF. This suggests that either the IMF is "heavier" or the central DM fraction is higher in more massive ellipticals. While earlier attempts were unable to break this degeneracy (e.g., Schulz et al. 2010), recent dynamical and lensing studies (Treu et al. 2010; Auger et al. 2010b; Cappellari et al. 2012a) have indicated that a variable IMF contributes strongly to this trend. We discuss these important findings further in Section 5.6.1.

2.5 Observations of galaxy clusters

Galaxy clusters are promising locations in which to map the detailed distributions of DM and baryons. Clusters are DM-dominated outside of the very central regions and are the only systems that can be individually mapped to their virial radius, using weak gravitational lensing. In selected clusters, strong lensing provides exquisite mass measurements that are independent of the dynamical state. X-ray emission from the hot intracluster medium (ICM) can also be used to derive mass profiles. The kinematics of cluster galaxies and of stars within the central giant elliptical provide powerful tools as well. Each of these techniques is valid over a specific radial interval. Weak lensing cannot reach within ~ 100 kpc. The strong lensing zone is usually confined to roughly $30 - 150$ kpc. X-ray emission is difficult to interpret within $\simeq 50$ kpc due to gas cooling and substructure, while temperature measurements become prohibitive at $\gtrsim 700$ kpc. We first review the physical basis of each of these mass probes, along with a brief summary of the associated observational results, which are described in greater detail in Section 5.6. We then turn to the utility of combining multiple

observational tools to derive comprehensive constraints on the mass distribution of clusters.

2.5.1 Gravitational lensing

Gravitational lensing refers to the deflection of light rays as they propagate through an inhomogeneous mass distribution (the lens), which leads to displacement, distortion, and magnification of images of sources located behind the lens. The fundamentals of lensing are described in detail by Schneider, Kochanek, & Wambsganss (2006) and by Treu (2010) and Kneib & Natarajan (2011) for galaxies and clusters specifically. Here we present a brief overview, and refer to Appendix A for a summary of the mathematical formalism.

Images of background galaxies located far from the cluster center are weakly distorted in shape as they pass through the cluster. This gravitational *shear* induces an additional ellipticity, which is oriented tangentially to the cluster center. Although the intrinsic (unlensed) shapes of individual sources are unknown, by averaging over many distant galaxies with uncorrelated shapes we can construct a circular source. Any measured ellipticity can then be attributed to gravitational shear. This is the basis for *weak lensing* as a mass probe. Since the typical ellipticities of galaxies can be more than 10 times larger than the shear signal sought, overcoming statistical noise requires averaging over many sources. Deep and high-resolution imaging is therefore essential.

As we move inward toward the cluster center, the gravitational shearing becomes progressively stronger. At the location of the *critical curve*, the distortion is strong enough to split the light from a background galaxy into multiple images. Physically, these images are located at extrema of the light travel time surface (Fermat's principle). There are two types of critical curves. Near the outer *tangential* critical curve, images are highly elongated in the azimuthal direction (see Figure 2.4). The angular size of this curve, known as the *Einstein radius*, can be measured with a precision of a few percent; it provides a direct geometric measure of the enclosed projected mass, provided that the distances to the lens and source are known through their redshifts. At the inner *radial* critical curve, images are instead elongated in the radial direction. While less commonly observed, this configuration is very valuable, since it constrains the *slope* of the surface density at small radii. When multiple background sources at different redshifts are strongly lensed, it is possible to reconstruct a detailed map of the inner mass distribution of the cluster.

Lensing studies have generally shown that NFW profiles provide adequate descriptions of cluster halos at radii $r \gtrsim 50$ kpc (e.g., Kneib et al. 2003; Broadhurst et al. 2005; Mandelbaum et al. 2006; Schmidt & Allen 2007; Okabe et al. 2010; Umetsu et al. 2011; Coe et al. 2012; Morandi & Limousin 2012). Several studies have questioned whether the relationship between halo mass and concentration follows that in simulations. Many lensing clusters have surprisingly high concentrations (e.g., Kneib et al. 2003; Broadhurst et al. 2008; Zitrin et al. 2011b). Interpreting this requires careful study of possible measurement biases or selection effects (Hennawi et al. 2007; Meneghetti et al. 2010a).

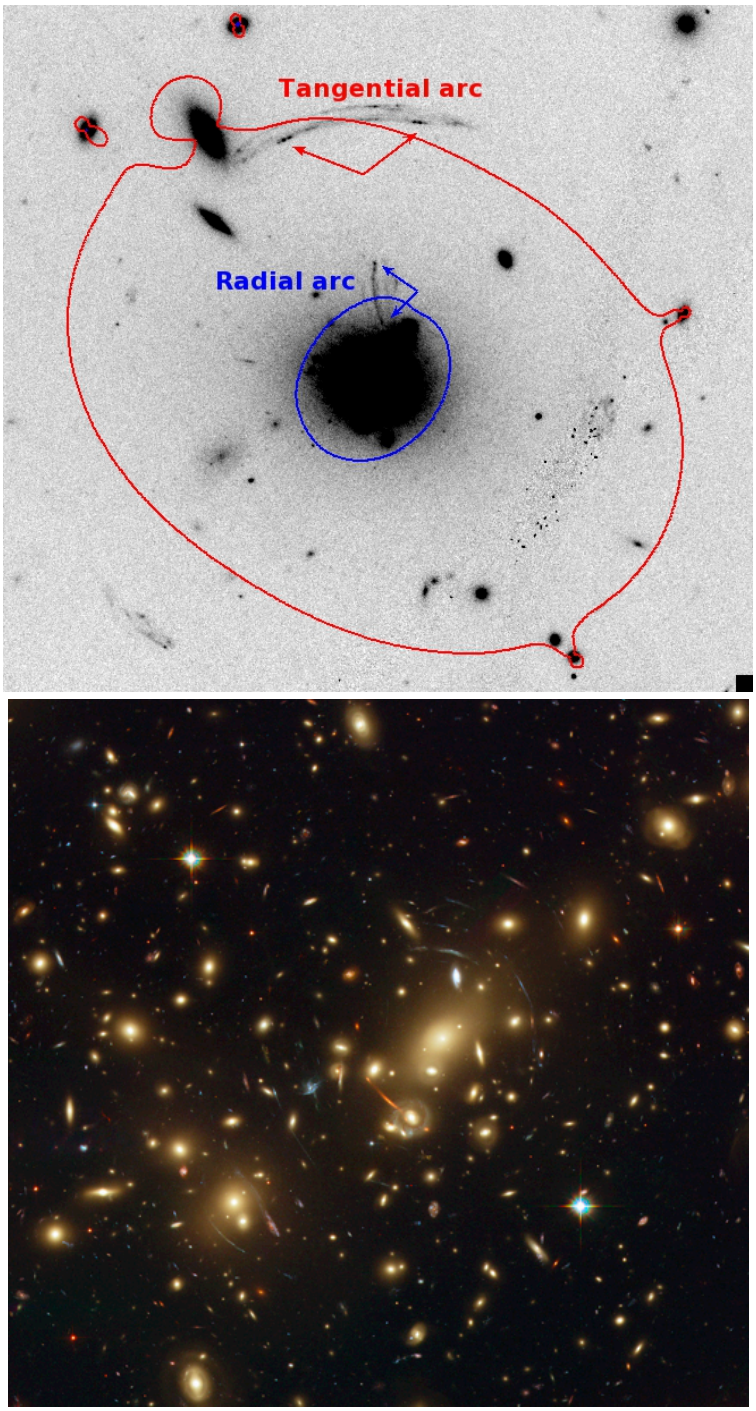

Figure 2.4: Top: Inner region of the lensing cluster MS2137, which exhibits prominent tangential and radial arcs. Each arc exhibits symmetry about the critical line, as illustrated by the corresponding features highlighted by arrows. The mass distribution imparts a slight ellipticity to the critical curves, which are also perturbed locally by galaxies. **Bottom:** *Hubble* image of a more complex lens, A1689, which is one of the most powerful lenses known. More than 100 multiple images have been identified. Reproduced from Kneib & Natarajan (2011).

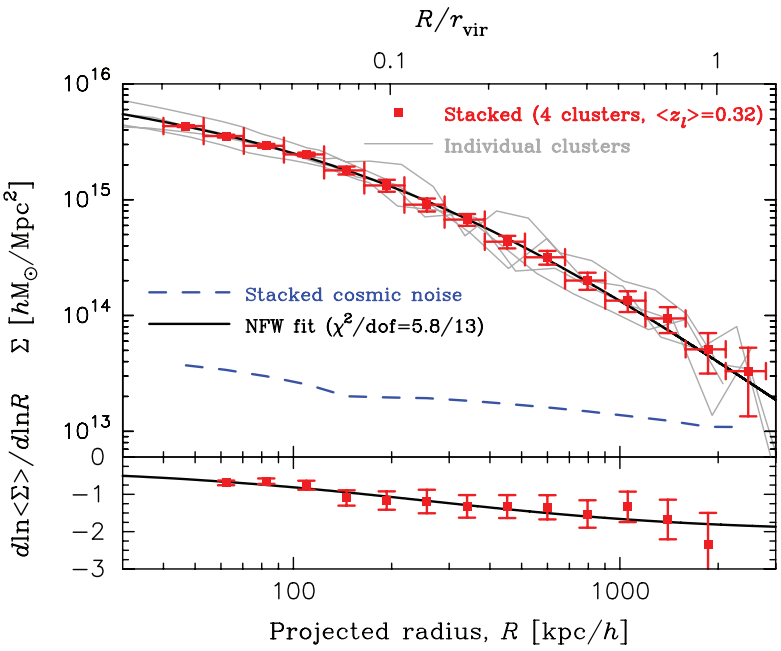

Figure 2.5: Mean surface density profile derived from strong and weak lensing measurements in four well studied cluster lenses. The NFW model (black line) fits the data very well at $R \gtrsim 50h^{-1}$ kpc. This thesis aims to measure the distribution of dark matter and baryons extending to radii one decade smaller than plotted here. Reproduced from Umetsu et al. (2011).

Measuring the *shape* of the radial density profile to test whether the NFW form (or the result of numerical simulations generally) is valid over the full range of scales – for any mass and concentration – is more challenging, but possibly more profound. Lensing alone generally cannot test for deviations from an NFW DM profile in the inner halo with much statistical power. We review results on the inner mass profile from lensing studies in more detail in Section 5.6. Figure 2.5 shows the surface density profile obtained from stacking strong and weak lensing data in four of the best-studied cluster lenses (Umetsu et al. 2011). At radii $R \gtrsim 50h^{-1}$ kpc, an NFW model fits the observations exquisitely well. However, when a more general model is considered (gNFW; Equation 2.2), the constraints on the inner slope of even the *total* density are relatively weak ($\beta = 0.89^{+0.27}_{-0.39}$). Constraints at smaller radii are necessary to provide a lever arm to measure the inner density slope and probe the innermost decade in radius now resolved in the best simulations. On these scales the stellar mass in the brightest cluster galaxy (BCG) is significant, and there has often been confusion in the literature about whether the *total* density or only that of the *dark matter* is being reported and compared to simulations. Separating the baryonic and DM contributions in the cluster core requires constraints reaching into the stellar-dominated regime, which usually are not available from lensing except in rare configurations (e.g., Limousin et al. 2007).

2.5.2 X-ray emission

Galaxy clusters have typical velocity dispersions of $\sigma \sim 1000 - 2000$ km s^{-1}, corresponding to virial temperatures of $T = \frac{1}{2} m_p \sigma^2 / k \sim 10^8$ K. At such high temperatures the cooling timescale is on the order of a Hubble time outside the innermost regions. Thus, clusters retain a hot gaseous ICM. X-ray spectroscopy can be used to measure the temperature profile $T_g(r)$ of the ICM. By deprojecting the X-ray surface brightness, the gas emissivity can be determined. Since the emission is dominated by thermal bremsstrahlung, these measurements can be used to infer the gas density $n_g(r)$. The *Chandra* observatory revolutionized X-ray studies of clusters due to its sensitivity and $\sim 1''$ angular resolution. Buote & Humphrey (2012) review the technical aspects of various methods that have been used to perform the deprojection and fit the data.

Two key further assumptions are typically made: that the gas is near hydrostatic equilibrium, which is necessary to infer the gravitating mass profile, and that the cluster is spherically symmetric, which is not a necessary assumption but simplifies the calculations. While neither of these assumptions is strictly true, and we discuss their limitations further in Section 4.3.2, they are accurate enough for many purposes. Hydrostatic equilibrium requires that

$$\frac{d\Phi}{dr} = \frac{GM(<r)}{r^2} = -\frac{1}{\rho_g}\frac{dP_g}{dr} \quad \Rightarrow \quad M(<r) = -\frac{krT_g(r)}{G\mu m_p}\frac{d\log n_g T_g}{d\log r}, \tag{2.4}$$

where we assume here that the mean molecular weight ($\mu \approx 0.6$) is known. This determines the enclosed mass profile $M(<r)$ from the observed $T_g(r)$ and $n_g(r)$.

At intermediate redshift temperature measurements are usually prohibitive at $r \gtrsim 700$ kpc. Interpreting X-ray emission within $r \lesssim 30$ kpc is often complicated by gas substructures, and observations of luminous distant clusters generally yield mass profiles that are consistent with an NFW model but only weakly constrain the inner density slope (e.g., Schmidt & Allen 2007). Lewis et al. (2003) identified the particularly relaxed, symmetric, nearby cluster A2029 as an ideal target for a detailed X-ray study and found that the *total* mass distribution is well fit by an NFW profile down to ~ 3 kpc (Figure 2.6). Even in this ideal case, the contribution of stars in the BCG could not be constrained, resulting a major uncertainty in the inner DM profile.

2.5.3 Kinematics

The mass distribution can also be constrained using kinematics. For a given mass distribution, the velocity dispersion of a population of tracer particles can be computed from the first moments of the collisionless Boltzmann equation, which are known as the Jeans equations. In the spherically symmetric case, the Jeans equation reduces to

$$\frac{1}{\nu}\frac{\partial \nu \sigma_r^2}{\partial r} + 2\frac{\sigma_r^2 - \sigma_t^2}{r} = -\frac{\partial \Phi}{\partial r} = -\frac{GM(<r)}{r}, \tag{2.5}$$

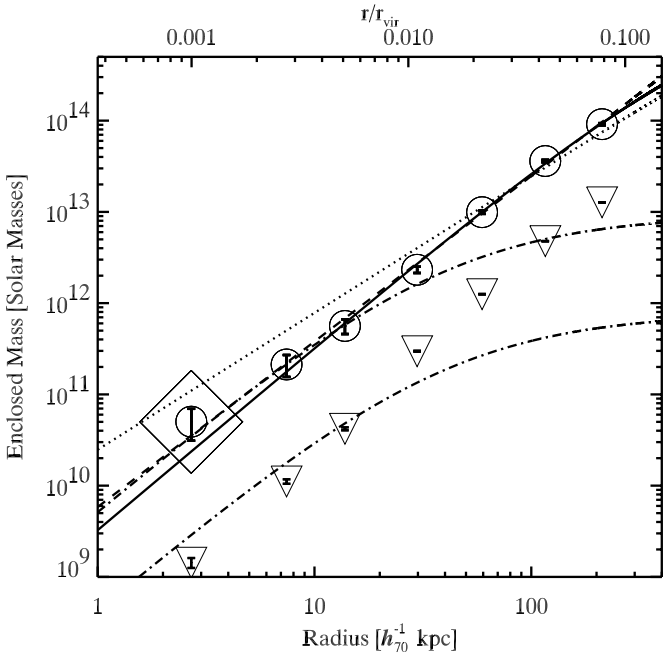

Figure 2.6: The mass profile of A2029, an unusually relaxed and symmetric nearby cluster, as measured via X-ray observations. The total and gaseous mass profiles are identified by circles and triangles, respectively. The large diamond on the first data point highlights additional systematic uncertainty. Fitted total mass profiles are NFW (solid line), power law (dashed), and Moore et al. (1999, dotted) models. The dot-dashed curves show the stellar contribution to the total mass assuming $M_*/L_V = 1$ (bottom curve) and $M_*/L_V = 12$ (top). Note that an NFW model appears to fit the *total* mass distribution well, but the uncertain stellar mass obscures the small-scale DM profile. Reproduced from Lewis et al. (2003).

where $\nu(r)$ is the number density of tracer particles, $M(< r)$ is the mass within a radius r, and σ_r and σ_t give the radial and azimuthal components of the velocity dispersion tensor. (Throughout this section we assume for simplicity there is no streaming motion, consistent with the lack of rotation exhibited by galaxies in clusters and by most BCGs; thus, $\sigma^2 = \overline{v^2}$.) The degree of orbital anisotropy is commonly characterized by the parameter

$$\beta = 1 - \frac{\sigma_t^2}{\sigma_r^2}, \tag{2.6}$$

where $\beta = 1$, 0, and $-\infty$ refer to purely radial, isotropic, and purely tangential orbits. (Where the anisotropy parameter is in danger of confusion with the inner DM slope β, we denote it by $\beta_{\rm aniso}$.) With this definition,

$$\frac{1}{\nu}\frac{\partial \nu \sigma_r^2}{\partial r} + 2\beta\frac{\sigma_r^2}{r} = -\frac{GM(< r)}{r}. \tag{2.7}$$

In practice, the observed surface luminosity of tracers $\Sigma_*(R)$ is measured and deprojected to obtain $\nu(r)$, either through an Abel integral technique or by fitting a parameterized form directly to the surface photometry. The other observable is the luminosity-weighted velocity dispersion $\sigma_{\rm los}(R)$ projected along the line of sight. For a given mass profile, one solves Equation 2.7 to obtain $\sigma_r(r)$ and then projects to obtain $\sigma_{\rm los}$. This requires two integrations, which can be reduced to a single quadrature using integration by parts:

$$\Sigma_*(r)\sigma_{\rm los}^2(R) = 2G\int_R^\infty \frac{\nu(r)M(< r)\mathcal{F}(r)}{r^{2-2\beta}}dr, \tag{2.8}$$

where $\mathcal{F}(r) = \sqrt{r^2 - R^2}$ in the isotropic limit ($\beta = 0$). Cappellari (2008) provides an expression for $\mathcal{F}$ appropriate to constant $\beta \neq 0$ involving incomplete beta functions, which we use in Chapter 4.

The most commonly-used tracers are the galaxies that are bound to the cluster, whose velocities can be easily measured in redshift surveys. Their velocity dispersion supplies an inexpensive estimate of the bulk mass of a cluster. Redshift surveys can also play a unique role in assessing the mass in the infall region on the cluster outskirts, beyond several virial radii (Rines et al. 2003). Nonetheless, the sampling noise present in even large surveys, the poor spatial resolution imposed by the need to assemble a significant number of galaxies into a bin, and the slope–anisotropy degeneracy have limited the utility of cluster galaxy dynamics to constrain the precise form of the mass profile, even when multiple clusters are stacked (van der Marel et al. 2000; Biviano & Girardi 2003).

Dynamically relaxed clusters often host a BCG in equilibrium and at rest at the bottom of the cluster potential. In this situation, a more novel application is to use the stars in the BCG as tracers of the gravitational potential down to very small radii. The orbital distribution in the central regions of giant ellipticals has been quantified in local observations and is not a major limitation (see Section 3.5.3). Figure 2.7 shows the spatially-resolved stellar velocity dispersions measured in

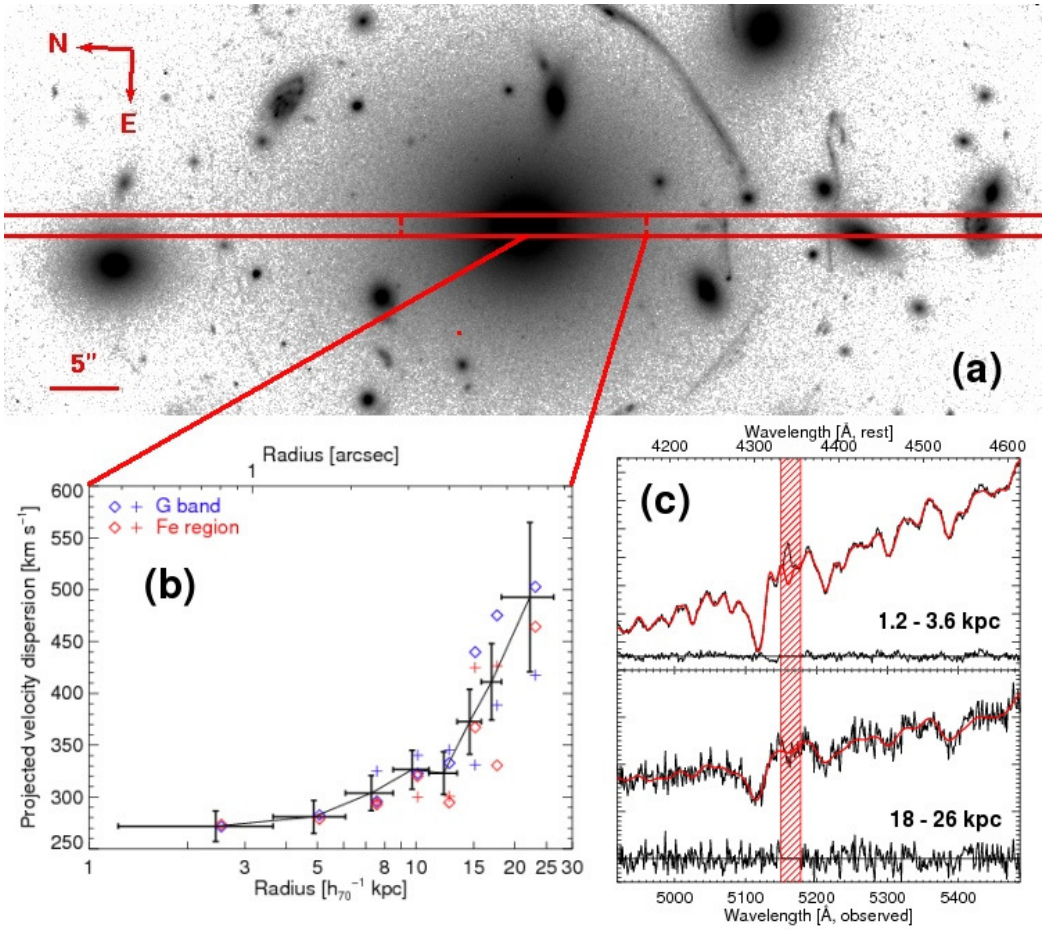

Figure 2.7: Spatially resolved stellar kinematics in the BCG of A383, based on observations described in Section 3.5. Panel (a) illustrates the position of the spectrograph slit across the BCG. The extracted spectra in the inner- and outermost spatial bins are shown in panel (c), along with fits (red) and residuals (bottom of panels). Panel (b) shows the resulting velocity dispersion profile. (Black crosses indicate the weighted mean across different spectral regions and sides of the center.)

the BCG of A383 (Section 3.5), one of the clusters that will be studied in this thesis. The velocity dispersion profile is nearly flat in the stellar-dominated regime, while its rapid rise at $R \gtrsim 10$ kpc – seen only in the central galaxies of clusters – reflects the dominance of DM at these radii. Kelson et al. (2002) and Richtler et al. (2011) studied the dynamics of two BCGs in combination with kinematic tracers (galaxies and globular clusters) at larger radii. While neither study constrained the stellar and dark mass independently through dynamics, both concluded that cored DM halos fit the data better than an NFW model for reasonable values of the stellar mass-to-light ratio M_*/L.

2.5.4 Combining mass probes

Given that clusters present multiple observational mass probes, each with its own limitations in isolation and an applicable radial range, it is clear that combining multiple tools can yield a more comprehensive picture of the mass distribution. Sand et al. (2002, 2004, 2008)[5] made an important advance on the inner DM density slope in clusters by combining strong lensing constraints with stellar kinematics, implementing the approach advocated by Miralda-Escude (1995) and Natarajan & Kneib (1996). In a sample of six lensing clusters, Sand et al. (2004) measured the angular position of the tangential arc, which precisely constrains the total mass enclosed within a typical Einstein radius of $R_{\rm Ein} \sim 60$ kpc. Half of the sample additionally presented a radial arc, thereby constraining the *slope* of the surface density at $R \sim 10 - 20$ kpc. Resolved stellar velocity dispersions within the BCG at $R \lesssim 10$ kpc were measured through Keck spectroscopy.

The left panel of Figure 2.8 shows the velocity dispersion data in one of the six clusters studied by Sand et al. (2004, S04), along with two mass models. Both models reproduce the tangential and radial arc positions, but they have differing M_*/L and DM inner slopes β. The two models present very different velocity dispersion profiles, which can easily be distinguished. Thus, the BCG kinematics supplement the lensing data by extending resolved mass constraints to small radii, thus providing a long lever arm to measure the density slope and reaching into the stellar-dominated regime, which is essential to quantify the stellar mass and break the bulge–halo degeneracy. S04 found evidence for a shallow DM density cusp with $\beta < 1$ in five of the six clusters they studied, with an ensemble mean $\langle\beta\rangle = 0.52 \pm 0.05$ (Figure 2.8, right panel).

S04 performed a simple axisymmetric lensing analysis based on the angular radii of the tangential and radial critical lines. This simplification was criticized by Bartelmann & Meneghetti (2004) and Meneghetti et al. (2007), who claimed that neglecting even a small ellipticity in the surface density would bias the inferred DM profile to shallow slopes. Gavazzi (2005) claimed that line-of-sight ellipticity could complicate the comparison between lensing and dynamical masses and suggested this as a possible source of systematic bias in the results of S04. The first concern was addressed by Sand et al. (2008, S08), who performed a full two-dimensional lens model in A383 and MS2137,

[5] D. Sand was a Caltech graduate student whose 2005 thesis was supervised by R. S. Ellis.

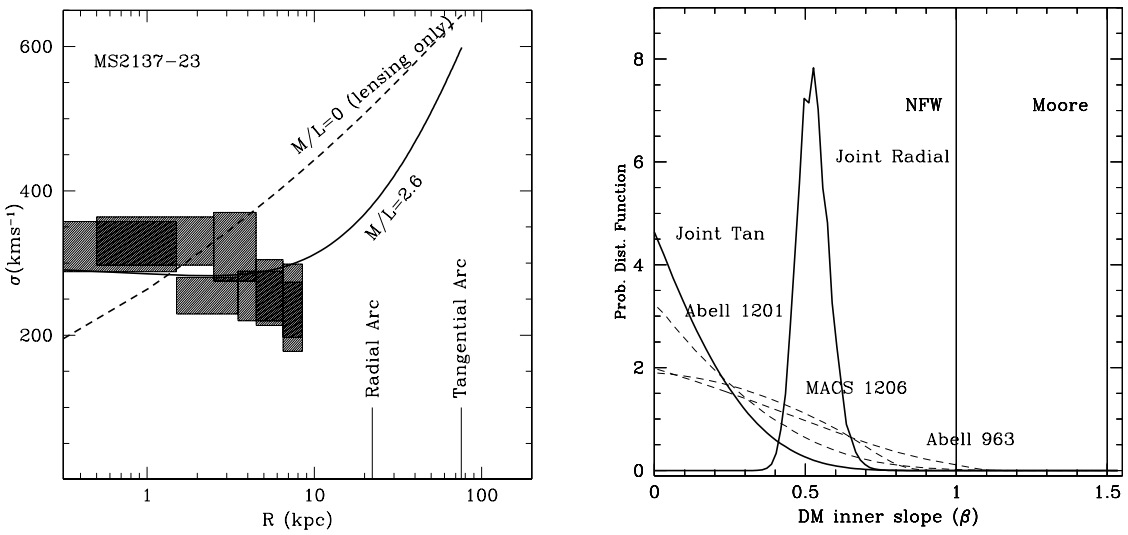

Figure 2.8: Left panel: Velocity dispersion data in MS2137, with two mass models overlaid that have varying M_*/L and β. Both match the lensing constraints, but the two have very different velocity dispersion profiles. This demonstrates how the combination of lensing and stellar kinematics can break the bulge–halo degeneracy. **Right panel:** Joint constraints on the inner DM density slope β in the subsample of S04 presenting radial and tangential arcs, and that presenting only tangential arcs. (In the latter case, only upper limits on β can be obtained.) The DM cusp is found to be significantly shallower than those seen in CDM simulations. Reproduced from Sand et al. (2004).

two of the previously studied clusters. This improved modeling did not change their essential earlier conclusions. However, S08 noted that additional data at larger radii were needed to constrain the scale radius r_s. Figure 2.9 illustrates how the inferred asymptotic inner DM slope changed when different scale radii were fixed. Whereas S04 simply set $r_s = 400$ kpc, S08 imposed a uniform prior on r_s spanning the range indicated by independent weak lensing studied and suggested by simulations. Clearly, mass probes extending beyond the strong lensing zone are needed to robustly constrain β.[6] This illustrates again the necessity of observations spanning a wide dynamic range to determine the shape of the DM profile. S08 also noted that halo triaxiality, particularly the unmodeled line-of-sight ellipticity, was a possible source of systematic error. In Section 2.7, we describe the specific ways that we make progress on these fronts in this thesis.

2.6 Implications of shallow dark matter cusps

Before turning to the specific goals of this thesis and its relation to Sand et al. (2004, 2008), we first briefly consider the implications of shallow dark matter cusps in order to motivate a more

[6]One may wonder whether degeneracies involving the *asymptotic* slope β are meaningful, since the observations essentially are sensitive to the mean slope between the gravitational arcs and the radii where stellar kinematics are measured. A more general point is that CDM density profiles have rolling slopes, and therefore, in order to compare a slope measured over a given radial interval to simulations, one needs to know how this interval relates to the key theoretical scales r_s and r_{200}. This requires data beyond $R_{\rm Ein}$.

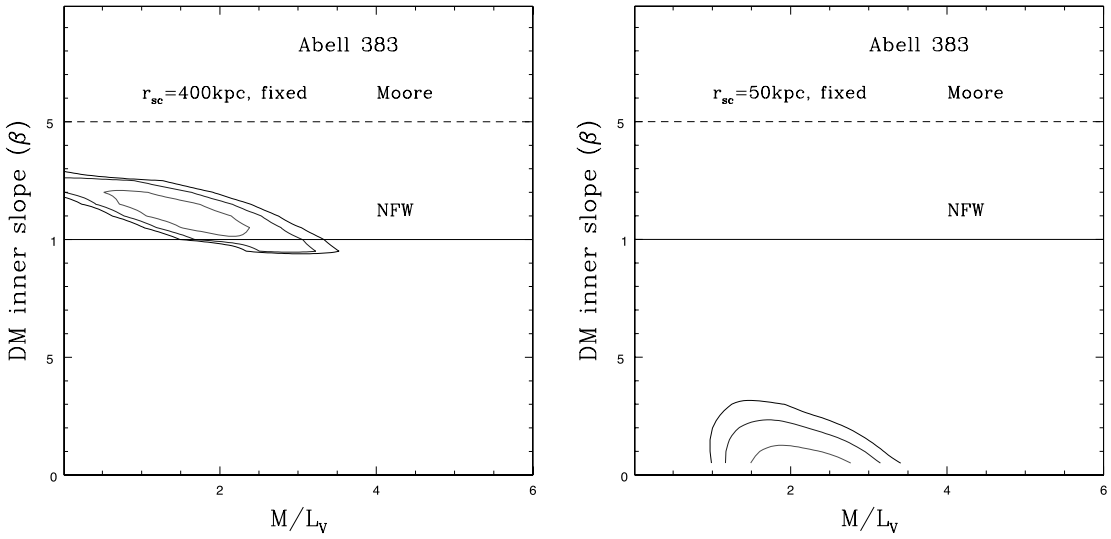

Figure 2.9: Degeneracy between the inferred DM inner density slope β and the imposed scale radius r_s. The latter is unconstrained by stellar kinematic and strong lensing data alone; data at large radii are required. Reproduced from Sand et al. (2008).

detailed study. There are two routes toward explaining small-scale discrepancies between ΛCDM and observations. On the one hand, small-scale observations are very interesting from the point of view of understanding DM, since they probe its structure in the highly non-linear regime, below the scales probed by the Lyα forest. They may provide more detailed microphysical information about DM than is accessible via large-scale observations alone. On the other hand, the effects of baryons become increasingly important on smaller scales. Although DM is gravitationally dominant on large scales and sets the sites for galaxy formation, the rich and complex baryonic physics that are involved may feed back on the DM backbone and modify its structure. The structure of real halos may inform us about the interplay between DM and baryons, which relates to the formation and assembly history of galaxies, groups, and clusters.

2.6.1 Warm or collisional dark matter

Although observations of galaxy clustering and the Lyα forest require DM to be fairly cold, there is some room for slightly warm or "tepid" DM. Introducing non-negligible thermal velocities in the early universe has two effects. First, since the random motions of particles allow them to free-stream out of shallow potential wells, the formation of low-mass halos (i.e., dwarf galaxies) is suppressed. Second, the density cusp characteristic of CDM can be washed out. Liouville's theorem shows that during dissipationless evolution of a collisionless system of particles, the coarse-grained phase space density can only decrease. For a primordial phase space density $Q_0 = \rho_0/\sigma_0^3$, this imposes a "packing limit" on warm DM. For an idealized isothermal halo with velocity dispersion σ, this translates to a

minimum core size $r_c \propto (Q_0\sigma)^{-1/2}$ (Tremaine & Gunn 1979; Hogan & Dalcanton 2000; Dalcanton & Hogan 2001). The packing limit alone cannot account for observations of both low-mass disks and clusters: the ~ 1 kpc cores claimed in dwarf galaxies would scale to completely negligible sub-kpc cores in clusters. Furthermore, DM temperatures consistent with Lyα forest observations are too cold to produce cores as large as ~ 1 kpc in dwarf galaxies. Even ignoring Lyα forest constraints, a temperature high enough to produce a large core would prevent the formation of dwarf galaxies in the first place due to the associated suppression of substructure (Macciò et al. 2012), although this "catch-22" is alleviated if mixed cold-plus-warm scenarios are considered (Macciò et al. 2013).

A "self-interacting" DM (SIDM) particle with a cross-section σ for DM-DM scattering was proposed by Spergel & Steinhardt (2000) as a way to preserve the large-scale successes of standard CDM while alleviating small-scale discrepancies with observations. Its astrophysical implications were soon explored in several simulations (e.g., Yoshida et al. 2000; Davé et al. 2001). SIDM departs from collisionless CDM only in the dense inner regions of halos, where the density is high enough for scatterings to occur within a Hubble time. There is no difference on larger scales. The cross-section is empirically limited to $\sigma/m \lesssim 1\mathrm{cm}^2\ \mathrm{g}^{-1}$ from observations of the Bullet cluster (Randall et al. 2008, Section 2.1). The other important limit comes from the observed ellipticity of the mass in cluster cores, since collisions tend to sphericalize the density. Miralda-Escudé (2002) used the ellipticity of MS2137 to place a strong limit $\sigma/m \lesssim 0.02\ \mathrm{cm}^2\ \mathrm{g}^{-1}$. Since this is far too small to have an appreciable effect on the density cusp or Galactic substructure – the original motivations for SIDM – this essentially killed interest in collisional DM for a decade. Several authors (Loeb & Weiner 2011; Vogelsberger et al. 2012) considered a cross-section that declines with velocity, which could account for dwarf cores without affecting systems with higher velocity dispersions, such as clusters. However, Peter et al. (2012) and Rocha et al. (2012) performed improved SIDM simulations extending to the cluster scale, along with more careful comparisons to observations. They showed that the earlier ellipticity constraint is greatly exaggerated, and the range $\sigma/m \approx 0.1 - 1\ \mathrm{cm}^2\ \mathrm{g}^{-1}$ is both allowed by all observations and can produce appreciable flattening of the inner DM density profile in both dwarf galaxies and clusters. Thus, SIDM appears to be a viable explanation of DM cores, although the range of parameter space that is both allowed and astrophysical relevant is rather limited. Further simulations are needed to assess whether a single σ/m can explain dwarf and cluster density profiles.

2.6.2 The impact of baryons

In reality, halos also contain baryons that could significantly modify the structure of the DM. The pioneering study of Blumenthal et al. (1986) was the first to treat systematically the effect of baryonic infall on the DM profile. Their picture follows gas that initially traces the DM distribution at early times. As the gas cools and dissipates energy, it falls toward the halo center. Provided that this occurs slowly, the response of the halo can be calculated using an adiabatic invariant of the DM orbits.

In the simplified case of circular orbits and a spherical mass distribution, the adiabatic invariant is $rM(< r)$. For a model of the initial DM+gas profile and the final distribution of baryons, it is straightforward to calculate the final DM profile. Baryon infall results in a steeper DM cusp. This process is typically known as *adiabatic contraction*, although *baryon pinching* or *loading* and other terms are also used. Many subsequent studies have produced more sophisticated models that address some of the original simplifying assumptions, such as circular orbits, and tested its predictions against hydrodynamical simulations (Gnedin et al. 2004; Sellwood & McGaugh 2005; Gustafsson et al. 2006; Pedrosa et al. 2009; Abadi et al. 2010; Sommer-Larsen & Limousin 2010). While the degree of the effect is a matter of debate, the direction is always to compress the halo. Thus, adiabatic contraction alone only exacerbates tension between CDM halos and observed flattened cusps.

The adiabatic contraction model is clearly a very simplified picture of galaxy formation. Additional baryonic effects have been proposed to *reduce* the central DM concentration. If baryons are derived to the central galaxy in "lumps" (e.g., galaxies) whose orbits decay via dynamical friction on the DM halo – as opposed to diffuse gas that radiates energy dissipatively – then the lumps transfer energy and angular momentum to the inner DM halo and could lower its central density (e.g., El-Zant et al. 2001, 2004; Nipoti et al. 2004; Romano-Díaz et al. 2008; Jardel & Sellwood 2009; Johansson et al. 2009; Del Popolo 2012). The assembly history of the galaxy – for example, the fraction of stars formed *in situ* versus delivered in mergers – may then be reflected in the DM profile (Lackner & Ostriker 2010). The effect of satellite mergers is sensitive to the density, number, and stellar/DM content of the infalling galaxies and so requires realistic simulations to quantify.

Removal of gas may also flatten the DM cusp. If this occurs slowly, the same formalism introduced to describe baryon infall can account for an "adiabatic expansion." If the removal of gas is "bursty" and the potential fluctuates on sub-dynamical timescales, then the effect on the central DM is qualitatively different, and its density may be reduced irreversibly (Pontzen & Governato 2012). Supernovae are suspected of producing cores in low-mass disks via this mechanism (Navarro et al. 1996a; Mashchenko et al. 2006; Governato et al. 2010; Oh et al. 2011; Brooks & Zolotov 2012), although this may not scale to dSph satellites (Peñarrubia et al. 2012). AGN feedback could play a similar role in clusters (Peirani et al. 2008; Martizzi et al. 2012b). Much effort has been devoted to understanding the net result of all these competing using comprehensive hydrodynamical simulations of galaxies over a range of masses (e.g., Duffy et al. 2010; Gnedin et al. 2011). Due to the difficulty of realistically treating all the relevant physics, predictions for halos with baryons remain unclear.

2.7 Goals of Part I of this thesis

Relaxed clusters that host a dominant central galaxy at the bottom of the cluster potential provide the best opportunity to measure the mass distribution over a wide range of scales and to separate

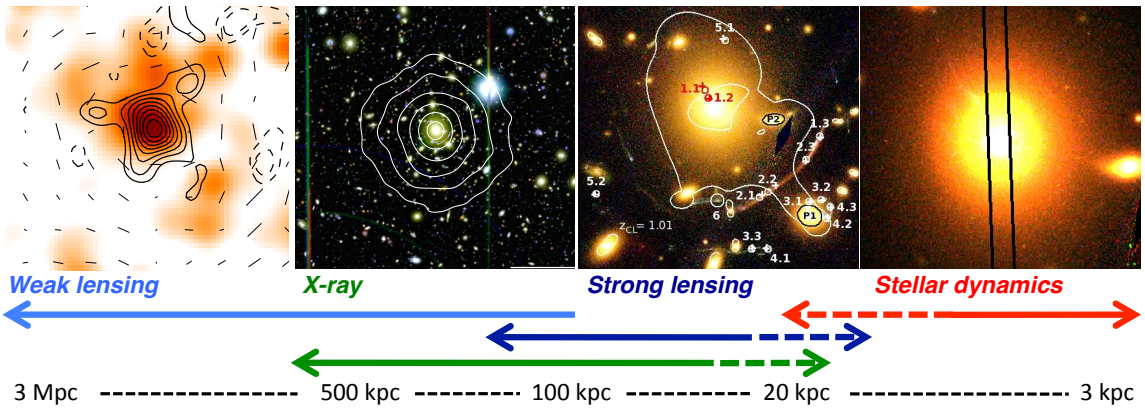

Figure 2.10: Schematic illustration of the radial coverage of the observational tools used in this thesis. By combining these data, the density profile can be constrained over nearly three decades in radial scale. Solid lines roughly indicate the typical range; dashed lines refer to more optimal cases.

the contributions of DM and baryons (BCG stars) at small radii, which is essential to discriminate between DM halo models. The goal of this thesis is to combine strong and weak lensing, X-ray, and stellar kinematic observations to constrain the radial density profile of DM and stars in a sample of seven relaxed, massive lensing clusters. Together these data provide nearly continuous coverage from $\sim 3 - 3000$ kpc (Figure 2.10). This will allow the density structure of individual halos to be measured over almost three decades in radius for the first time – a dynamic range that compares to that achieved in the best current simulations. Therefore, these observations will provide an excellent basis for detailed comparisons that test the uniformity and form of the DM profile and its relation to the distribution of baryons.

This thesis will build upon the earlier work by Sand et al. in several important ways by aiming

1. to extend the sample with full two-dimensional lens models beyond the two clusters studied by S08 to a sample of seven,

2. to incorporate several multiple image systems at different source redshifts when possible, thereby further constraining the density slope,

3. to add mass probes beyond the strong lensing zone via a weak lensing analysis, thereby addressing the degeneracy noted by S08 (Figure 2.9),

4. to obtain higher-quality, more radially-extended stellar velocity dispersion profiles in the BCGs, thereby reaching into the DM-regime where the velocity dispersion is expected to rise,

5. to quantify projection effects that were suggested as a source of systematic bias by including results from X-ray observations,

6. to study the stellar populations of the BCG by comparing their dynamically-derived stellar masses to those estimated using population synthesis models.

These data provide the best opportunity to disentangle baryons and dark matter in cluster cores, allowing us to assess the form and universality of the dark matter distribution and providing an excellent basis for detailed comparisons with numerical simulations.

Chapter 3

Weak Lensing, Strong Lensing, and Stellar Kinematic Observations

In this chapter, we first present a sample of seven massive, relaxed galaxy clusters that were selected for a combination of strong lensing, weak lensing, and stellar kinematic observations and describe their characteristics. These clusters span the redshift range $z = 0.2$–0.3 and the mass range $M_{200} = 0.4$–$2 \times 10^{15}\,\mathrm{M}_{\odot}$. We then describe the observations, reduction, and analysis of each of these data sets. In Section 3.2, we introduce the weak-lensing observations and the associated shear analysis, which probes the mass distribution from $r \simeq 100$–3000 kpc. The *Hubble Space Telescope* (*HST*) images and spectroscopic redshifts that form the basis for our strong-lensing analysis are introduced in Section 3.3, along with our interpretation of the multiple images. These data precisely constrain the projected mass on typical scales of $r \simeq 20$–100 kpc. Section 3.4 describes photometry of the BCGs, which are needed for our dynamical analysis and for comparing our measurements of the stellar mass to stellar population synthesis (SPS) models. Finally, Section 3.5 describes our unique spectroscopic data, which are used to measure the internal stellar kinematics of the BCGs from $r \simeq 3$–20 kpc. In later chapters, these data are combined to study the density distribution over $r \simeq 3$–3000 kpc.

3.1 A sample of seven massive clusters at $z = 0.2$–0.3

Our goal is to fit simple parametric models to lensing and kinematic data spanning a wide range of scales and to compare our results to simulations. This requires selecting a sample of clusters that are reasonably relaxed and symmetric, both to ensure that our models are adequate and to make clean comparisons with theory. Furthermore, our use of stellar kinematics to trace the mass distribution on small scales requires that the centers of the BCG and DM halo are well aligned. Table 3.1 introduces the sample of seven massive clusters, which range in redshift from $z = 0.19$–0.31. As we describe below, A611, A383, MS2137, A963, and A2667 are well relaxed clusters, A2390

Table 3.1. Cluster sample and alignment between BCG and mass centers

Name	$\langle z \rangle$	$N_{\rm gal}$	BCG peculiar velocity (km s^{-1})	Source of galaxy redshifts	BCG offset (kpc) from X-ray centroid	BCG offset (kpc) from Lensing center Δx	BCG offset (kpc) from Lensing center Δy	Cool core?	$L_{\rm X}$ (10^{37} W)
MS2137.3-2353	0.314	...	...	...	4†	1.2 ± 0.8	0.1 ± 0.6	Yes^{a}	11.10
A963	0.206	...	...	...	6	...	...	No^{b}	5.03
A383	0.190	26	-261 ± 187	This work	2	-2.7 ± 0.6	2.9 ± 1.1	Yes^{b}	4.12
A611	0.288	236	-67 ± 68	This work	1	-1.3 ± 0.9	4.2 ± 0.8	No^{b}	5.33
A2537	0.294	273	-325 ± 311	Braglia et al. (2009) and this work	13†	-0.4 ± 1.2	5.2 ± 1.5	No^{c}	9.37
A2667	0.233	22	438 ± 730	Covone et al. (2006)	3	-6.5 ± 3.6	4.1 ± 2.9	Yes^{b}	11.97
A2390	0.229	52	270 ± 218	Yee et al. (1996)	2	4.9 ± 6.7	-0.2 ± 3.5	Yes^{b}	14.81

Note. — Redshifts $\langle z \rangle$ are the biweight mean of $N_{\rm gal}$ cluster galaxies identified with an iterative 2.5σ clip applied. The uncertainty is provided on the peculiar velocity of the BCG [$v_{\rm BCG} = c(z_{\rm clus} - z_{\rm BCG})/(1 + z_{\rm clus})$]. For A2537 the redshift and $v_{\rm BCG}$ are given relative to the main peak (Figure 3.2). Where no redshift survey is available, the redshift of the BCG is given instead. Offsets between the BCG and the X-ray centroid measured in the central 1 arcmin are from Sanderson et al. (2009) and Richard et al. (2010), except those marked † which are original to this work. Offsets between the BCG and lensing center are discussed in Section 4.2.1; $\Delta x > 0$ and $\Delta y > 0$ denote offsets west and north of the BCG. $L_{\rm X}$ is the X-ray luminosity in the $0.1 - 2.4$ keV band within R_{500} from Piffaretti et al. (2011). Sources of cool core classification: ^{a} Donnarumma et al. (2009), ^{b} Richard et al. (2010), ^{c} Rossetti et al. (2011).

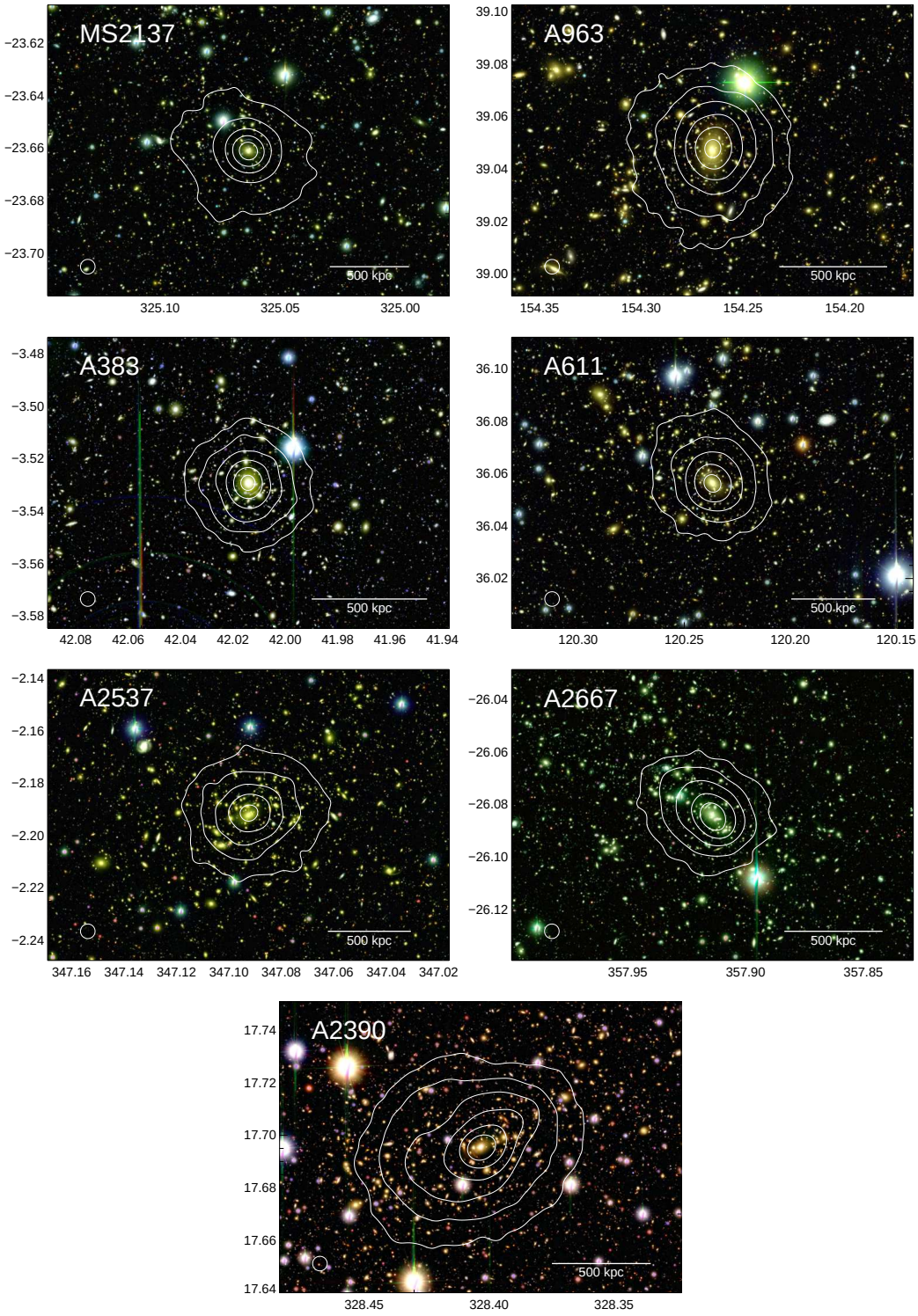

Figure 3.1: Color composites of the central regions of each cluster based on the imaging data introduced in Section 3.2.1 are displayed with an arcsinh stretch (Lupton et al. 2004). Only a small portion of the total field of view is shown. The *Chandra* X-ray emission in the $0.8 - 7$ keV band is overlaid, smoothed with a Gaussian kernel whose size (FWHM of $20''$) is indicated in the lower- eft of each panel. Contour levels are equally spaced logarithmically but are otherwise arbitrary. Axes show the R.A. and declination.

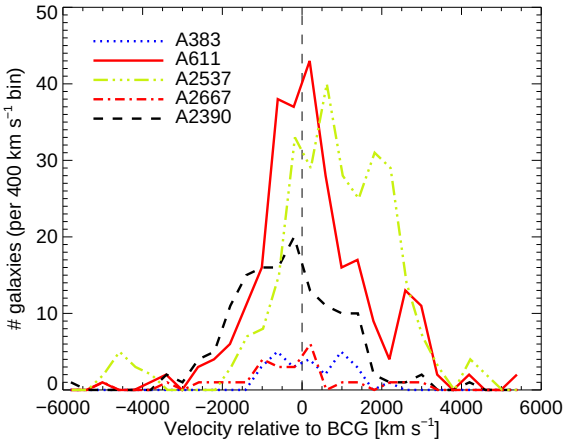

Figure 3.2: Histogram of velocities of cluster galaxies relative to the BCG, $\Delta v = c(z - z_{\rm BCG})/(1 + z_{\rm BCG})$, based on the sources listed in Table 3.1. The available data are consistent with the BCGs being at rest in the cluster potentials. A2537 has a bimodal velocity structure: the BCG coincides with the primary peak, but there is a second peak at $\Delta v \simeq 2000$ km s^{-1} as discussed in the text.

is likely only slightly perturbed, and A2537 shows signs of a more complex mass distribution.

Optical images of the central $\simeq$ 1 Mpc of each cluster are shown in Figure 3.1 with X-ray contours overlaid. The X-ray data were obtained from the *Chandra* archive[1], and point sources were removed using the `CIAO` tools. We first discuss A611, A383, MS2137, A963, and A2667, which are prototypically relaxed clusters, and reserve A2390 and A2537 for individual comments below. The X-ray emission in these five clusters is regular, symmetric, and well aligned with the BCG, and is extended along the same directions as both the BCG and the surface density in our lens models. The alignment is quantified in Table 3.1, which shows that the X-ray centroid is typically within a few kpc of the BCG, comparable to the measurement uncertainty (A. Sanderson, private communication). Similar small offsets between the BCG and center of mass are derived from lens models, which we discuss further in Section 4.2.1.

It is unlikely that we have simply selected clusters in which the BCG is offset primarily along the line of sight (l.o.s.), given that these clusters exhibit many characteristics that are known to be correlated with a relaxed state and a centrally-located BCG: a large luminosity gap between the BCG and the second rank galaxy, a low substructure fraction, and the presence of a cooling core (Sanderson et al. 2009; Smith et al. 2010; Richard et al. 2010). Furthermore, the available redshifts in the fields of A383, A611, and A2667 (see sources Table 3.1) are consistent with a unimodal velocity distribution in which the BCG is at rest in the cluster potential, as shown in Figure 3.2.

A2390 shows slightly more complicated X-ray emission that is characterized primarily by a low-level extension to the northwest on $\sim$ 200 kpc scales, in the same location as an enhancement of cluster galaxies. The extension has long been noted (Kassiola et al. 1992; Pierre et al. 1996; Frye

[1]Observation IDs 3194, 2320, 4974, 903, 2214, 4962, 9372, and 4193.

& Broadhurst 1998). As we discuss in Section 4.1.1, our strong lensing model does not demand a major additional mass concentration in this region, provided an elliptical halo is used. Further, the X-ray and galaxy distributions are regular on larger scales, the BCG is well aligned with the X-ray and lensing centers (Table 3.1), the velocity distribution of cluster galaxies is unimodal and centered on the BCG (Figure 3.2), and there is a strong cooling core (Richard et al. 2010). From this we infer that A2390 is likely to be only mildly unrelaxed.

Finally, we consider A2537, which is the most likely disturbed cluster in our sample. The X-ray emission is regular and symmetric, but centered slightly north of the BCG (13 kpc). There is no cool core (Rossetti et al. 2011). The curvature of the arcs suggests that a second mass concentration may be present to north (Section 4.1.1). Crucially, the distribution of cluster galaxy velocities appears bimodal (Figure 3.2), with the main peak centered on the BCG and a second peak at $\Delta v \simeq 2000$ km s^{-1}. Galaxies in the high-velocity tail do not appear spatially distinct from the remainder. It is possible A2537 has not fully relaxed from a merger near the l.o.s. (perhaps similarly to Cl0024+1654; Czoske et al. 2002). Throughout, we bear in mind the uncertain dynamical state of this cluster when interpreting our results.

3.2 Weak lensing

We begin our discussion of the data forming the basis of our analysis on the largest scales. These are probed by weak gravitational shear, the systematic distortion in the shapes of background sources by the cluster. Weak-lensing analyses present a number of technical challenges. Proper handling of the point-spread function (PSF) of the instrument used for the observations is essential, since it induces spurious shear of comparable magnitude to the real signal and varies across the focal plane. Additionally, galaxies located behind the cluster must be isolated in order to avoid dilution of the shear signal by unlensed cluster galaxies and those in the foreground: this requires multi-color photometry. In Section 3.2.1 we introduce the imaging data, primarily from the Subaru telescope, and its reduction. In Section 3.2.2 we briefly describe our technique for extracting the shear signal and verify our method using simulated data. Section 3.2.3 describes the photometric redshift measurements used to select background sources and tests of their validity. Finally, in Section 3.2.4 we present two-dimensional (2D) mass maps and tangential shear profiles.

3.2.1 Data reduction and catalog construction

The imaging data used in our weak-lensing analysis are listed in Table 3.2. Most observations were conducted with SuprimeCam (Miyazaki et al. 2002) at the Subaru telescope, either in a run obtained through the Caltech time share (observers D. Sand and T. Treu) or using archival data. Its $30'$ field of view is well matched to clusters at intermediate redshifts. In a few cases, additional color

information is provided from observations using IMACS at the Magellan Observatory (PI D. Sand) or via archival data from the 12K or MegaPrime cameras at the Canada–France–Hawaii Telescope (CFHT). In all clusters we obtained imaging in three to five different filters. A sample of the imaging data is shown in Figure 3.3 to illustrate the field of view, depth, image quality, and color coverage (see also Figure 3.1).

The data were reduced by the author following the procedures described in Appendix B. Briefly, we used the `IMCAT`-based pipeline developed by Donovan (2007) and Capak et al. (2007) to perform bias subtraction, flat fielding, sky subtraction (including a sophisticated algorithm suitable for the removal of large-scale scattered light patterns), astrometric and photometric registration, warping, and stacking. Object detection and galaxy shape measurements were performed in the R-band image (I in A963). Absolute astrometry was tied to the USNO-B (Monet et al. 2003) or Sloan Digital Sky Survey (SDSS) DR7 or DR8 (Abazajian et al. 2009) catalogs. In most cases photometric calibration was tied to stellar photometry from the SDSS, which has the merit of uniform and accurate calibration when including archival data taken in uncertain photometric conditions. Multi-color catalogs were created based on PSF-matched aperture photometry in each cluster using `SExtractor` (Bertin & Arnouts 1996). The full details of this procedure are given in Appendix B.

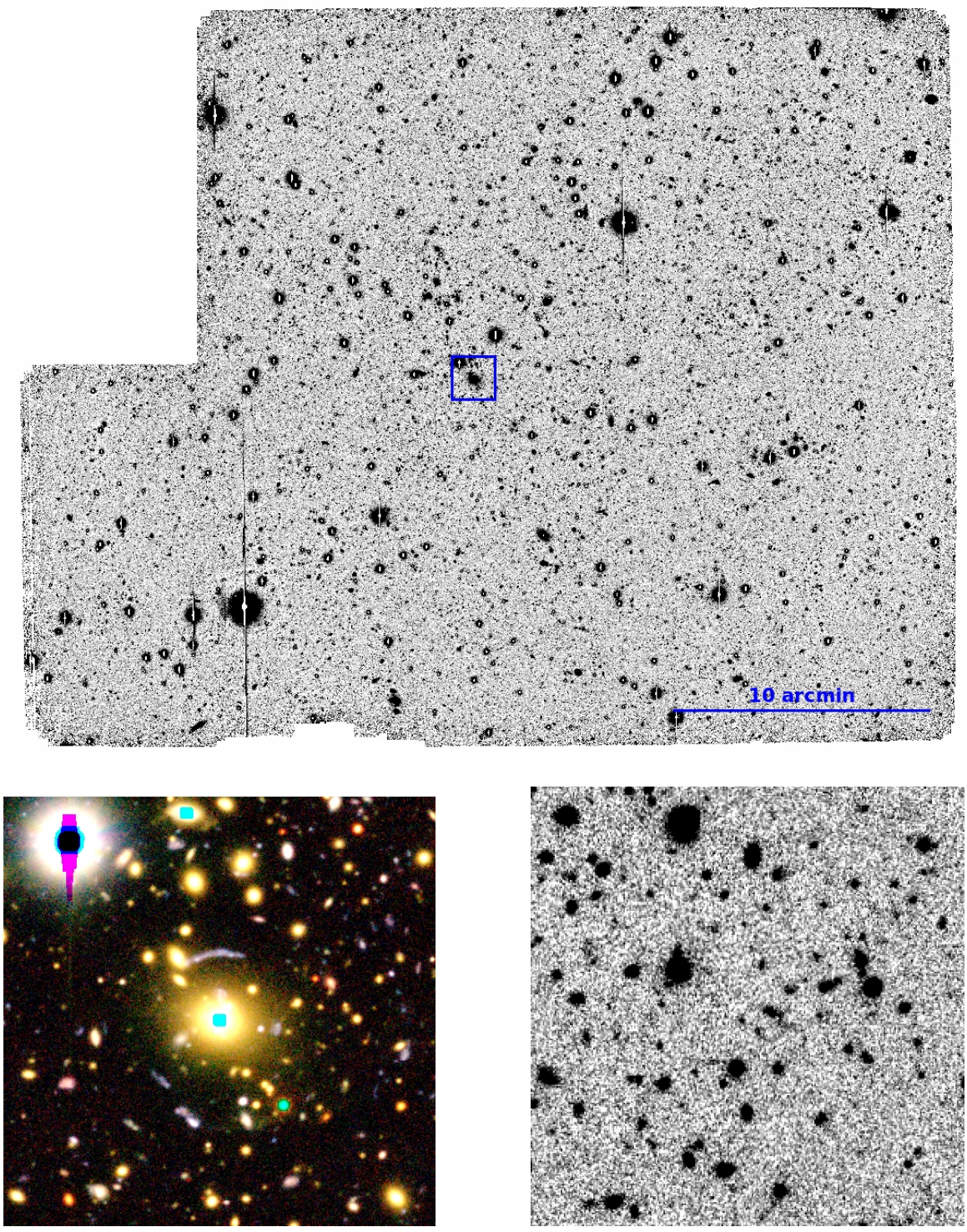

Figure 3.3: Top: R-band image centered on MS2137, as observed with SuprimeCam. (The upper-left chip was excluded due to poor CTE.) **Bottom left:** BRI composite image of the central $100'' \times 100''$, indicated by the blue rectangle in the top panel, displayed with an arcsinh stretch. Note the blue gravitational arcs. (The center of the BCG is saturated in some filters.) **Bottom right:** A $1' \times 1'$ patch in the R band located far from the cluster center, displayed with a linear stretch.

Table 3.2: Imaging observations for weak-lensing analysis

Cluster	Instrument	Filter	Dates of observation	Exposure time (ks)	Seeing (FWHM, $''$)	Depth (mag, 5σ)	$\langle D_{ls}/D_s \rangle$	$n_{\rm bkg}$ (arcmin^{-2})
MS2137	SC	B	2007-08-13	1.4	0.75	26.5		
	SC	$V^\dagger$	2007-11-14	1.2	1.01	25.8		
	SC	$\mathbf{R}^\dagger$	2007-11-13	2.4	0.68	26.2	0.563	17.8
	SC	$I^\dagger$	2007-11-14	1.9	0.95	25.4		
	SC	$z+$	2007-07-18	1.6	0.81	24.8		
A963	CFHT 12K	B	1999-11-15, 17	7.2	0.90	26.3		
	SC	V	2000-11-28	1.8	0.69	25.8		
	SC	R	2000-11-24, 25	3.4	0.69	26.1		
	SC	$\mathbf{I}$	2003-04-08	3.0	0.64	25.8	0.693	22.8
A383	MegaPrime	u^*	2003-12-20, 23 and 2004-01-21	9.2	1.21	26.1		
	SC	B	2002-09-10 and 2008-01-10	7.5	0.85	27.0		
	SC	V	2008-01-09	2.4	0.64	26.5		
	SC	$\mathbf{R}^\dagger$	2007-11-13	2.4	0.56	26.3	0.731	22.7
	SC	$i+$	2005-10-02	2.4	0.62	25.8		
	SC	$z+$	2002-09-11	1.5	0.59	24.9		
A611	SC	$B^\dagger$	2007-11-13	2.4	0.62	26.7		
	SC	$V^\dagger$	2007-11-14	1.2	0.56	26.2		
	SC	$\mathbf{R}^\dagger$	2007-11-13	2.4	0.68	26.2	0.600	18.3
	SC	$I^\dagger$	2007-11-14	2.4	0.66	25.8		
A2537	IMACS	$B^\dagger$	2009-08-23	5.0	0.99	26.0		
	SC	$\mathbf{R}^\dagger$	2007-11-13	2.4	0.56	26.4	0.600	9.9
	IMACS	$I^\dagger$	2009-08-23	4.1	0.88	25.5		

Continued...

Table 3.2 – Continued

Cluster	Instrument	Filter	Dates of observation	Exposure time (ks)	Seeing (FWHM, $''$)	Depth (mag, 5σ)	$\langle D_{ls}/D_s \rangle$	$n_{\rm bkg}$ (arcmin^{-2})
A2667	SC	$V^\dagger$	2007-11-14	1.2	0.88	26.0		
	SC	$\mathbf{R}^\dagger$	2007-11-13	2.4	0.66	26.4	0.686	14.6
	IMACS	$I^\dagger$	2009-08-23	1.7	0.91	25.2		
A2390	SC	B	2004-09-15 and 2005-11-30	2.2	0.80	26.7		
	SC	V	2004-07-18	0.8	0.63	26.1		
	SC	$\mathbf{R}$	2004-09-15	2.3	0.64	26.1	0.686	15.1
	SC	I	2004-09-18	6.3	0.74	26.1		
	SC	$z+$	2004-09-16	1.7	0.97	24.9		

Note. — SC denotes SuprimeCam, and † indicates observations conducted by the authors. The remainder were obtained from the Subaru and CFHT archives. The filter used for detection and shear measurement is in bold. Depth is measured by the median magnitude of all 5σ detections within a $2''$ diameter aperture. The surface density of sources selected for the shear analysis $n_{\rm bkg}$, along with their mean lensing distance ratio $\langle D_{ls}/D_s \rangle$, are listed.

3.2.2 Shear measurement and source selection

As described in Section 2.5.1 and Appendix A, in the weak lensing regime the induced distortion in the shape of a background source is proportional to the reduced gravitational shear g_α. Since the induced shape distortions are small (a few percent near the virial radius of a massive cluster), one must average over a number of galaxies to obtain an estimate of the local shear. Further, the atmosphere and observations induce distortions that are comparable to the signal to be measured. Thus, it is essential to account for the smearing and shearing introduced by seeing and by the instrument optics, which in general vary across the focal plane. Kaiser et al. (1995, KSB95) and Luppino & Kaiser (1997) developed a mathematical framework for measuring galaxy shapes and removing the observational distortions to isolate the gravitational component. Below we provide a brief summary of this scheme, which is fully implemented in the public `IMCAT` code that we use to conduct our analysis. Another discussion of a practical implementation of the `IMCAT` code can be found in Oguri et al. (2009).

In the KSB95 framework, the ellipticities of galaxies e_α (here α denotes the two components) are measured as weighted quadrupole moments of the light distribution: $e_1 = (Q_{11} - Q_{22})/(Q_{11} + Q_{22})$ and $e_2 = Q_{12}/(Q_{11} + Q_{22})$, where

$$Q_{\alpha\beta} = \int d^2\theta W(\theta)\theta_\alpha\theta_\beta f(\theta). \tag{3.1}$$

Here the integral is over the angular extent of the galaxy image, $f(\theta)$ is the surface brightness of the galaxy, and $W(\theta)$ is the window function. Uniform weighting ($W = 1$) produces shear estimates with divergent noise properties; thus, in practice, one chooses a window with finite extent. We take $W(\theta)$ to be a Gaussian with σ given by the `SExtractor FLUX_RADIUS` estimate of the half-light radius, denoted below by r_h.

With the raw galaxy ellipticties e_α in hand, the first correction is to remove the anisotropy of the point-spread function (PSF). This anisotropy-corrected estimate is given by

$$e'_\alpha = e_\alpha - P^{\rm sm}_{\alpha\beta} q^*_\alpha. \tag{3.2}$$

Here $P^{\rm sm}_{\alpha\beta}$ is the smear polarizability tensor, which is calculated from the second moments of the galaxy image (see equations 4.3-4.5 of KSB95), and the PSF anisotropy kernel

$$q^*_\alpha = (P^{*,{\rm sm}}_{\alpha\beta})^{-1} e^*_\alpha \tag{3.3}$$

is measured from from stellar images, which have no intrinsic ellipticity. In practice the off-diagonal elements of $P^{\rm sm}_{\alpha\beta}$ are small, and given that the measurements are noisy, we follow the usual practice of neglecting them in both the stellar and galaxy images. (Note that $P^{\rm sm}_{\alpha\beta}$ is then easily inverted.)

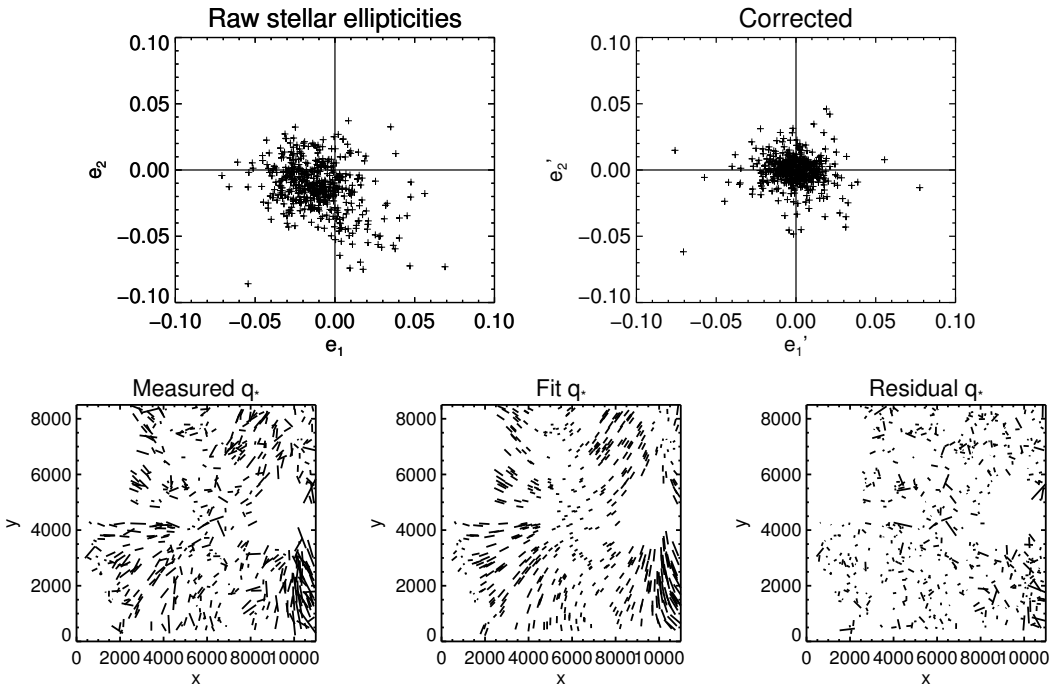

Figure 3.4: Top: Raw measured stellar ellipticities in the field of A611 (left) and those after correction for PSF anisotropy using the fitted variation of $q^*_{\alpha\beta}$ across the focal plane (right). **Bottom:** Raw stellar anisotropy kernel q^*_α measured in individual stellar images in the field of A611 (left), the fitted smooth variation using a 5th degree polynomial (center), and the residuals from the fit (right). Note the lack of a systematic trend after the smooth variation is removed.

In order to capture the variation in q_α over the focal plane, we first identify stars in our catalogs as bright, unresolved objects in the magnitude–size plane. We then fit the spatial variation of q^*_α on the detector using a two-dimensional fifth-order polynomial in the pixel coordinates. We found this to be sufficient to capture the smooth variation in the PSF anisotropy. Figure 3.4 demonstrates the quality of the PSF correction.

Hoekstra et al. (1998) showed that the correction in Equation 3.2 is improved when the weight function $W(\theta)$ used in the measurement of the stellar and galaxy images is the same. Following their suggestion, we therefore measure q^*_α for each star using a grid of Gaussian window functions whose widths span the range seen in the galaxy sample. The spatial variation of q^*_α is fitted independently for each window function. When Equation 3.2 is evaluated for a specific galaxy, we first evaluate the polynomial fit for each component of q^*_α at the spatial position of the galaxy, doing so for every window function in the grid. Finally, q^*_α is derived by interpolating these esimates to the width of window function used for the galaxy measurement (i.e., $\sigma = r_h$).

The next step is to remove the isotropic smearing effect induced by the optics and (primarily)

the atmosphere. Luppino & Kaiser (1997) showed that

$$g_\alpha = (P^{\rm g}_{\alpha\beta})^{-1} e'_\alpha \tag{3.4}$$

accounts for the isotropic distortion to produce an estimate of the local reduced shear g_α at the position of each background galaxy. Here

$$P^{\rm g} = P^{\rm sh} - P^{\rm sm}(P^{*,{\rm sm}})^{-1} P^{*,{\rm sh}} \tag{3.5}$$

is known as the "pre-seeing shear polarizability tensor" and $P^{\rm sh}$ is the "shear polarizability tensor"; each is calculated from the image second moments (see Equations 5.2-5.4 in KSB95). As before, the superscript $*$ refers to quantities measured for stellar images. The small off-diagonal elements of $P^{\rm g}$ are generally neglected. Furthermore, since estimates of $P^{\rm g}$ derived from individual faint galaxy images are very noisy, it is common to take the average of the on-diagonal elements. $P^{\rm g}_{\alpha\beta}$ is then an identity matrix times the scalar

$$P^{\rm g} = \frac{1}{2}\left({\rm tr}\ P^{\rm sh} - f_* {\rm tr}\ P^{\rm sm}\right), \tag{3.6}$$

where

$$f_* = \frac{{\rm tr}\ P^{*,{\rm sh}}}{{\rm tr}\ P^{*,{\rm sm}}}. \tag{3.7}$$

We measure f_* using stellar images and fit its variation in the focal plane in the same way as described above for q^*_α. As before, f_* is estimated for each galaxy at a matching window function width. The shear estimate for each galaxy is then

$$g_\alpha = e'_\alpha / P^{\rm g}. \tag{3.8}$$

We use estimates of $P^{\rm g}$ derived from individual galaxies, rather than fitting them as functions of various galaxy properties. We also equally weight the shear estimates derived from each galaxy, rather than weighting by some estimate of the inverse variance of the shear estimator, since we found this yielded less biased estimates in the simulations described below.

It is important to select sources for the shear analysis that are well resolved, of sufficient signal-to-noise for shape estimation, and located behind the cluster. From the `SExtractor` catalog described in Section 3.2.1, we selected galaxies for our shear analysis via the following criteria:

1. S/N > 7, where S/N is the detection significance defined in Erben et al. (2001) measured with a window function having $\sigma = r_h$,

2. $1.15 r_h* < r_h < 6$ pixels, where r^*_h is the median stellar `FLUX_RADIUS`, to avoid unresolved and

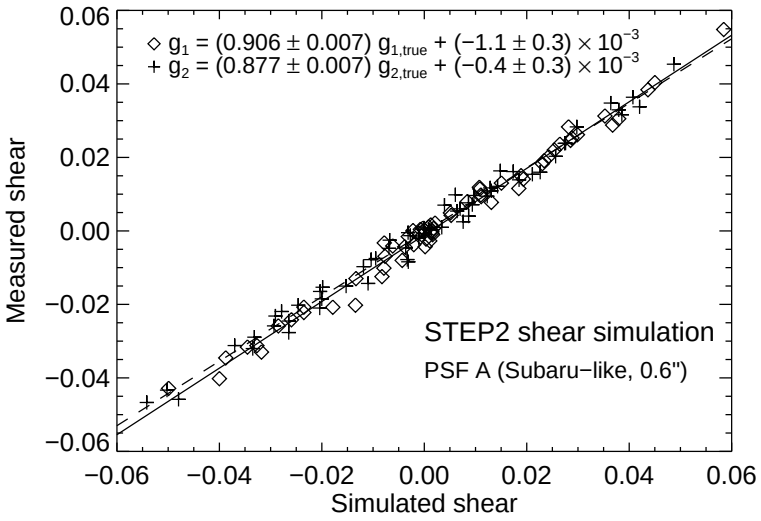

Figure 3.5: Calibration and validation of our shear measurement method using images from the STEP2 simulation, designed to mimic our typical SuprimeCam imaging. As described in Massey et al. (2007), shot noise is reduced using rotated image pairs. We determine a calibration factor $g_{\rm meas} = 0.89 g_{\rm true}$ comparable to other techniques, with a negligible additive bias. Similar results hold for other PSFs.

very large galaxies,

3. $|e| < 1$, $|g| < 1.5$, tr $P^{\rm sm} > 0$, and $0.15 < P^{\rm g} < 2$, to exclude sources with pathological moments,

4. `MAG_AUTO` > 21,

5. to eliminate blended and asymmetric galaxies, a distance of at least 6 pixels to the nearest object, a distance of at least $3(r_{h,1} + r_{h,2})$ to any other object > 3 mag brighter, and a shift of less than 1 pixel between centroids measured with and without the window function,

6. a photometric redshift selection described below.

Even within the KSB95 framework, there are a number of choices that must be made to arrive at a specific implementation. Furthermore, in common with other shear estimation methods, KSB95 is known to underestimate the shear by $\simeq 10\%$. Therefore, it is important to verify and calibrate our shear pipeline using simulated images with known shear. For this purpose we use images from the STEP2 project (Massey et al. 2007), which were designed to mimic the depth, sampling, and PSF typical of SuprimeCam data (Figure 3.5). For their PSF A (a Subaru-like PSF with FWHM = $0\farcs6$), we find a linear relation between simulated and recovered shear with a slope of 0.89, averaged between shear components. The additive bias is negligible, indicating the PSF correction is good, although these simplified simulations have a spatially-constant PSF. Very similar results hold for PSF C ($0\farcs8$), leading to a mean calibration factor $m_{\rm WL} = g_{\rm meas}/g_{\rm true} = 0.89 \pm 0.01$. We correct our

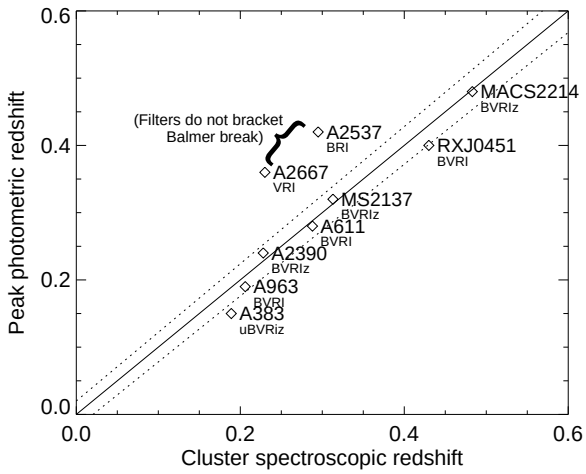

Figure 3.6: Comparison of spectroscopic cluster redshifts to the peak of the distribution (measured in $\Delta z = 0.01$ bins) of photometric redshifts of bright, red-sequence galaxies selected from the inner $\simeq 2'$ of the cluster. All clusters with 4 or more photometric bands show good agreement, with an r.m.s. scatter of $\Delta z/(1+z) = 0.02$ (dotted lines). In A2667 and A2537, the filters bracketing the Balmer break are not both available.

raw shear measurements $g_\alpha^{\rm raw}$, obtained as described above, using this calibration factor:

$$g_\alpha = g_\alpha^{\rm raw}/m_{\rm WL}. \tag{3.9}$$

The magnitude of this calibration factor is typical of other authors and methods. Although STEP2 does not extend to the shears $g = 0.2 - 0.3$ that we measure near cluster centers, the tight linearity in Figure 3.5 gives us confidence that the shear pipeline is working well and that an extrapolation of the calibration factor to higher shear is reasonable.

3.2.3 Photometric redshifts

Galaxies located between a cluster and the observer are not lensed by it. Therefore, when measuring the gravitational shear, it is essential to identify background sources. This requires multi-color photometry, which we have collected for the entire sample. This section presents the photometric redshift estimates we derived for all detected sources in order to select those located behind the clusters. We use the `BPZ` (Benítez 2000) software (version 1.99.3), with its CWWSB4 set of eight templates and the default prior, which fits redshifted galaxy templates to all the available photometry. `BPZ` provides both a marginalized redshift probability density $P(z)$ as well as a point estimator z_b. We use both and define $z_{\rm phot} = z_b$ below. For five of the seven clusters in our sample, the spectroscopic redshift and the peak $z_{\rm phot}$, as measured from bright galaxies in the cluster core, agreed with a scatter of $\sigma_{\Delta z/(1+z)} = 0.02$ (see Figure 3.6). Additionally, we obtained a large number of spectra of red galaxies in the field of A611 using Hectospec at the MMT Observatory (PI D. Sand),

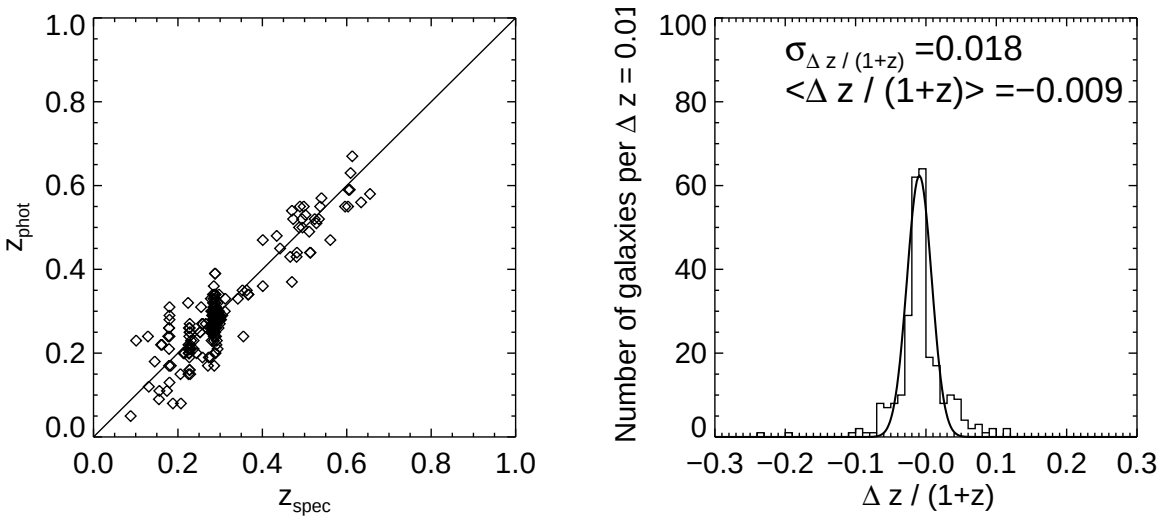

Figure 3.7: Comparison of photometric and spectroscopic redshifts for 383 red galaxies in the field of A611, as measured using Hectospec spectroscopy. The photometric redshifts are obtained without any alteration to the SDSS-based calibration. This comparison does not directly verify the utility of the photometric redshift technique as applied to our weak lensing study, which would require a complete spectroscopic sample of very faint sources, but the close agreement does suggests that the photometry is well calibrated.

and Figure 3.7 shows that the photometric redshift estimates agree well with these spectroscopic determinations. These observations support the quality of the photometric calibration described in Appendix B. The poorer results in A2667 and A2537 are not surprising, since these clusters are the only two observed through only three filters, which do not closely bracket the 4000 Å break. We describe our more conservative treatment of these clusters below.

Two criteria were used to select background galaxies. First, we required $z_{\rm min} < z_{\rm phot} < z_{\rm max}$, where we define $z_{\rm min} = z_{\rm clus} + 0.1$ and $z_{\rm max} = 2$ by default. (For the special cases of A2537 and A2667 discussed above, we conservatively take $z_{\rm min} = 0.55$ and $z_{\rm min} = 0.50$, respectively.) Second, we eliminated sources with a significant low-redshift solution by requiring that the probability that $z > z_{\rm clus} + 0.1$, determined by integrating $P(z)$, is $> 90\%$. Adopting a higher threshold generally had little effect on the resulting shear profiles, but reduced the surface density of selected sources. A2667 showed the greatest possibility of residual dilution, consistent with the more limited photometry described above, but we show in Section 4.3.2 that the shear profile is consistent with the strong-lensing and X-ray mass measurements where they overlap.

Dilution of the shear signal from cluster or foreground sources is probably the main systematic error in cluster weak-lensing analyses. Therefore, we conducted several astrophysical tests to assess the reliability of our background galaxy identification. These are illustrated in Figure 3.8 for the case of A611. First, we searched for an angular clustering signal between galaxies identified as in the cluster or the foreground, and those in several bins of higher redshift. The principle is that galaxies in widely-separated redshift intervals should not have correlated positions. Indeed, the

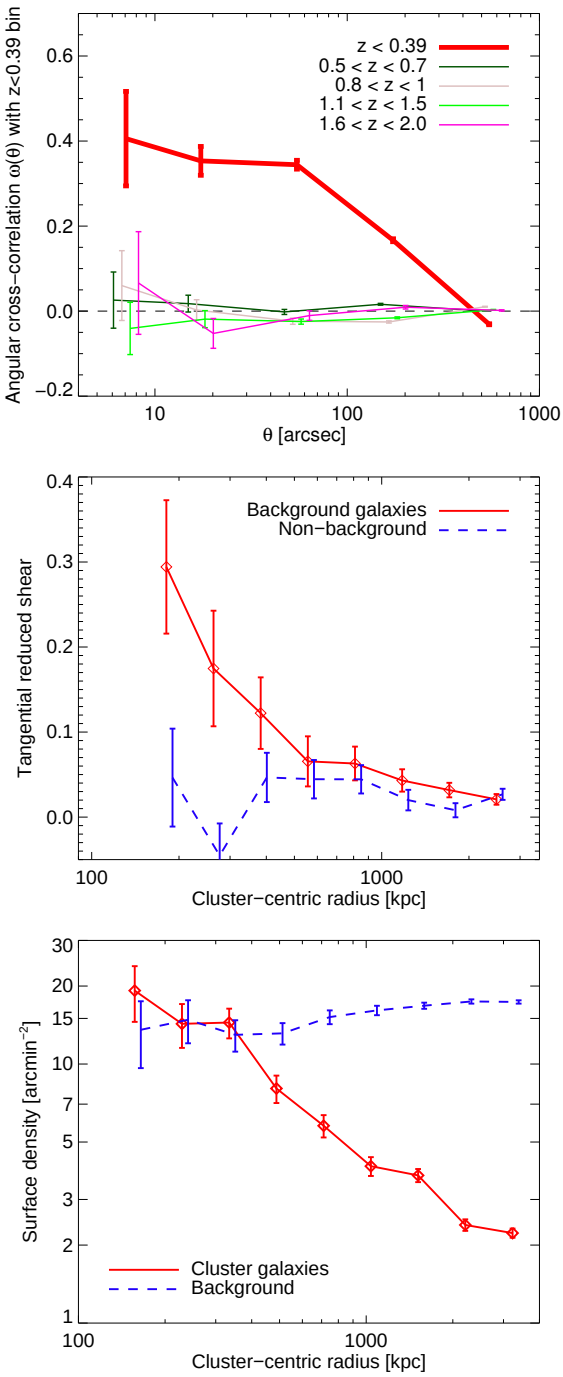

Figure 3.8: Tests of our background galaxy selection for the weak lensing analysis, demonstrated in A611. **Top:** Angular correlation between galaxies with $z_{\rm phot}$ securely below the selection threshold $z_{\rm min} = 0.39$, and those in other bins of $z_{\rm phot}$. The auto-correlation at $z < z_{\rm min}$ and the lack of any cross-correlation with other $z_{\rm min} < z_{\rm phot} < 2$ galaxies indicate low contamination. **Middle:** Tangential shear profile measured using selected background sources (red), which shows the expected rise toward the center, and using excluded foreground and cluster galaxies (blue), which shows a flat, low signal. **Bottom:** The surface density profile of galaxies with secure $z_{\rm phot}$ near the cluster redshift (red) shows the expected rise, while the density of selected background sources (blue) is flat or declining toward the center.

cross-correlation signal (top panel) is low or absent at $z < 2$, while the auto-correlation in the foreground bin is prominent. If we admit sources with $z_{\rm phot} \gtrsim 2$, a significant clustering with low-redshift sources arises from confusion between the photometrically inferred Balmer and Lyman breaks; this motivates our choice of $z_{\rm max} = 2$. Second, we examined the radial shear profile, which shows a well-defined rise toward the cluster center when using our selected background sample and a flat, marginal signal when using the remainder of sources (Fig. 3.8, middle panel), as expected if they are mostly unlensed. Finally, we investigated the surface density of sources as a function of cluster-centric radius (Fig. 3.8, bottom panel). The density of cluster galaxies rises rapidly towards the center, while that of background sources is flat or declines. These tests give us confidence that the photometric redshifts are effective at isolating lensed sources.

In our shear analysis we incorporate the individual $z_{\rm phot}$ measurements of the background sources. However, as a check of our $z_{\rm phot}$ distribution, we computed the mean distance ratio $\langle D_{ls}/D_s \rangle$ that determines the lensing efficiency (Table 3.2). We then selected galaxies from the COSMOS survey with a matching magnitude distribution in the detection band and with similar $z_{\rm min}$ and $z_{\rm max}$ cuts.[2] The $\langle D_{ls}/D_s \rangle$ determined from the 30-band $z_{\rm phot}$ in COSMOS (Ilbert et al. 2009) agreed with our determinations with a scatter of only 3%, suggesting that errors in the mean distance to the background sources have a minimal effect on our analysis.

3.2.4 Results

The mean distortion of background galaxies is a measure of the reduced shear $g = \gamma/(1-\kappa)$, where γ and κ are the shear and convergence, respectively (e.g., Schneider et al. 2006). Figure 3.9 displays the azimuthally averaged tangential component of the reduced shear for all seven clusters. In general we select galaxies with 100 kpc $< R <$ 3 Mpc for the shear analysis. At smaller radii there are few sources and contamination from cluster galaxies is most severe, while the outer limit corresponds roughly to the SuprimeCam field of view. In A2667 and A2537, where our photometry is less extensive, we require $R > 150$ kpc to account for the greater possibility of dilution at small radii. In all clusters, a smoothly rising tangential shear profile is observed, with no clear evidence for dilution from contaminating foreground sources. A significant B-mode signal, which should not arise physically and is thus often used a diagnostic of systematic errors, is not detected.

For each cluster we also produced 2D surface density maps following Kaiser & Squires (1993), which are shown in Figure 3.10. To increase the surface density of sources, we loosened the $P(z)$ selection criterion described in Section 3.2.2; this has no effect on our quantitative results, which do not rely on the 2D maps. In general mass and light are well aligned, and any other structures in the fields are detected at marginal significance. (This can be seen by noting that the dashed

[2]In detail, we increased $z_{\rm min}$ by 0.1 to account for the effects of our $P(z)$ cut that could not be directly mimicked in COSMOS. The COSMOS broadband photometry was linearly interpolated to the central wavelength of our detection band when necessary.

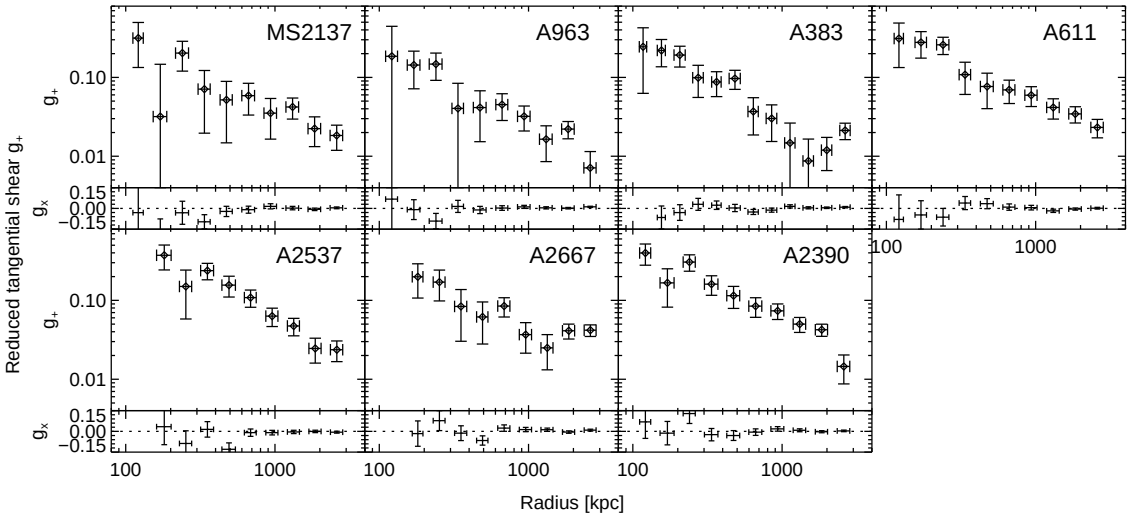

Figure 3.9: Tangential reduced shear g_+ measured in annular bins. The B-mode component $g_\times$, which should vanish in the absence of systematic errors, is also plotted and is consistent with zero. Measurements have been calibrated on simulated STEP2 data as described in Section 3.2.2. Horizontal error bars indicate the dispersion in radius within each bin. The rising signal seen at large radii in A2667 and A383 is ascribed to secondary mass peaks as discussed in the text.

contours show the mass reconstructed using the B-mode signal: all such peaks are spurious and give an indication of the number of noise peaks of a given significance expected in this field of view.) These mass maps are useful for investigating the upturn or plateau in the radially averaged shear signal seen at large radii in A383 and A2667. The upturn in A383 is likely related to substructures near the virial radius, and following N10, we therefore restrict to $R < 1.5$ Mpc in this cluster.

In A2667, the radial shear profile shows a high plateau to $R > 3$ Mpc, which is explained in the mass map by a second large mass concentration clearly detected $6'.2 = 1.4$ Mpc north of the main, strong-lensing cluster. The secondary clump detected in the lensing map is exactly aligned with an excess of bright red galaxies near the cluster redshift (Figure 3.10). The brightest of these galaxies has a redshift $z = 0.2042$ from the 2dF survey (Colless et al. 2001), corresponding to a comoving distance of 100 Mpc along the l.o.s. This suggests the second clump is slightly in the foreground of A2667. In our weak-lensing study we model both mass concentrations simultaneously, and results for the main cluster are independent of the redshift of the second peak.

3.3 Strong lensing

We now turn to smaller spatial scales and the identification of sources multiply imaged by the clusters. The angular positions of these images, along with the redshift of the lensed source, provide precise geometric constraints on the mass distribution over the radii spanned by the multiple images, which is typically $r \simeq 20$–100 kpc. When multiple background galaxies located at different redshifts

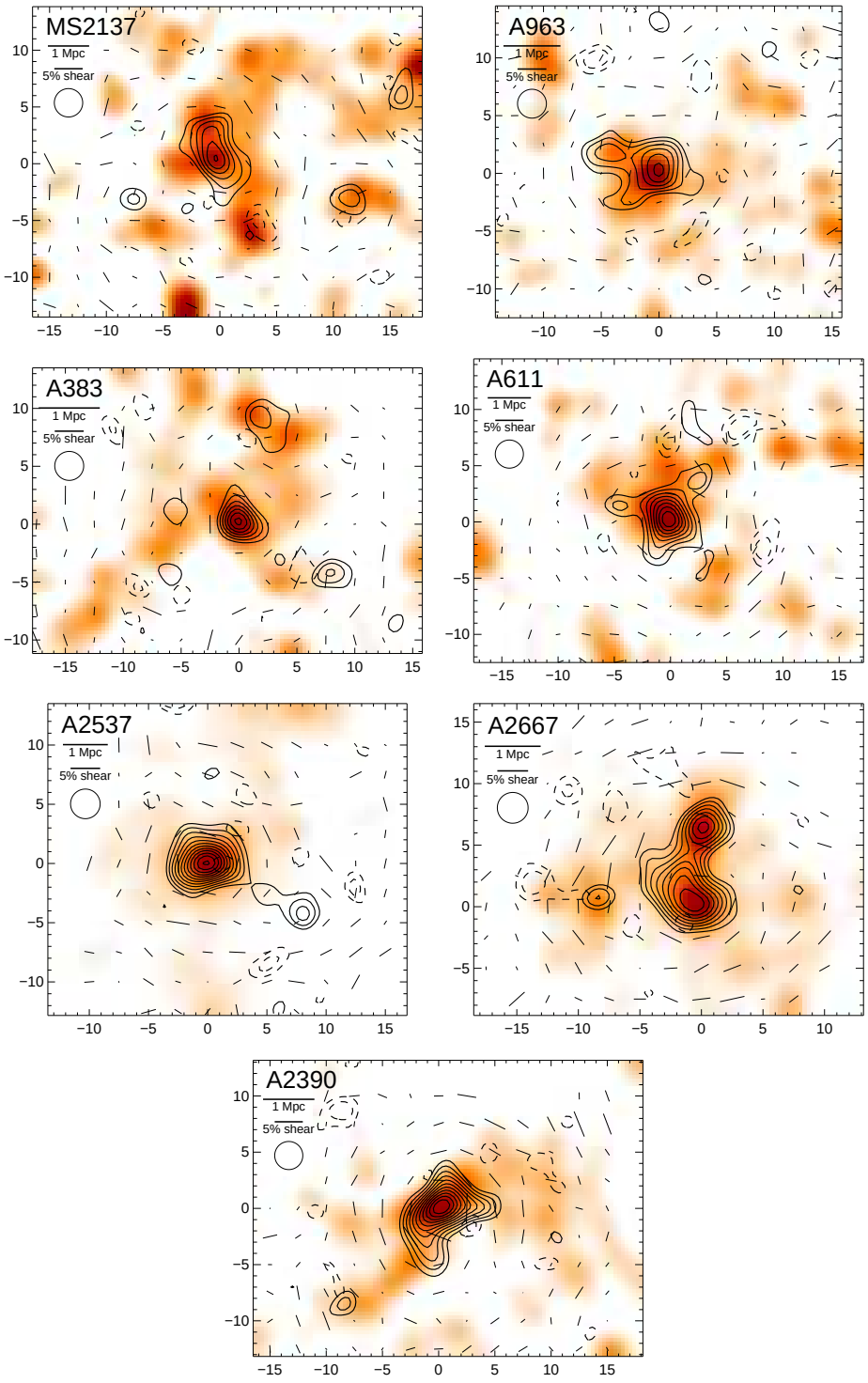

Figure 3.10: Surface density κ contours, derived from our weak-lensing analysis, are overlaid on the smoothed I-band light from galaxies near the cluster redshift, identified as described in Section 3.3.8. Contours begin at 3σ and increase by 1σ. Dashed contours show the absolute value of the κ map derived instead from the B-mode signal, which should be null and is used to assess the noise and systematics. The smoothed shear field is also overlaid. All quantities are smoothed by a Gaussian with FWHM $= 150''$ as indicated by the circle in the upper left. Axes indicate the distance from the BCG in arcmin, with north up and east left.

are strongly lensed, which is the case for five of the seven clusters in our sample, even stronger constraints can be derived. Every cluster in our sample has been imaged by *HST*, which provides the resolution crucial for precisely locating conjugate images, and every one except A2537 has been the subject of an earlier lensing study. We refer to and build upon these earlier models, as described below. In Sections 3.3.1–3.3.7, we consider each cluster individually, and in Section 3.3.8 we describe the construction of catalogs of cluster galaxies relevant as perturbers in our strong lens models.

The positions of the multiple images are illustrated in Figure 3.11 and listed in Table 3.3. We have retained the nomenclature of various authors; however, in all cases the final number or letter distinguishes multiple images of the same source. In several cases, we have added new spectroscopic redshifts based on the observations detailed in Section 3.5.1. These spectra are shown in Figure 3.12.

3.3.1 MS2137

This famous cluster presents tangential and radial arcs at $z = 1.501$ and 1.502, respectively (Sand et al. 2002). We incorporate two additional images to the model of Sand et al. (2008): a fourth counter-image 3d to system 3, and the mirror image (2c) of the radial arc. The latter was not included in our previous analyses due to the difficulty of securing a clear identification in the light from the BCG, but the counter-image is clear in recent, deeper imaging from the CLASH survey (Postman et al. 2012b).

3.3.2 A963

A set of merging images forms the "northern arc" at $z = 0.771$ (Ellis et al. 1991). Since conjugate points could not be clearly identified, we incorporate this arc as constraint on the position of the critical line, following Richard et al. (2010, R10), which is assumed to pass through the arc.

3.3.3 A383

The model follows Newman et al. (2011), which built upon Sand et al. (2004, 2008) and Smith et al. (2005). We add the pair of $z = 6.027$ images (system 5) later identified spectroscopically by Richard et al. (2011), along with minor shifts to other image positions made based on deeper imaging from CLASH. The radial and tangential arc system at $z = 1.01$ (systems 1 and 2, Smith et al. 2001; Sand et al. 2004) and a complex system with a redshift $z = 2.55$ (system 3, Newman et al. (2011)) strongly constrain the mass model. Subsequent near-infrared observations confirmed the latter redshift via Hα and [O III] emission lines and provided a more precise value $z = 2.58$ (Belli et al., in preparation). We have not included system 6 as a constraint due to its peculiar and unexpected symmetry (see discussion by Morandi & Limousin 2012), but do report a spectroscopic redshift $z = 1.826$.

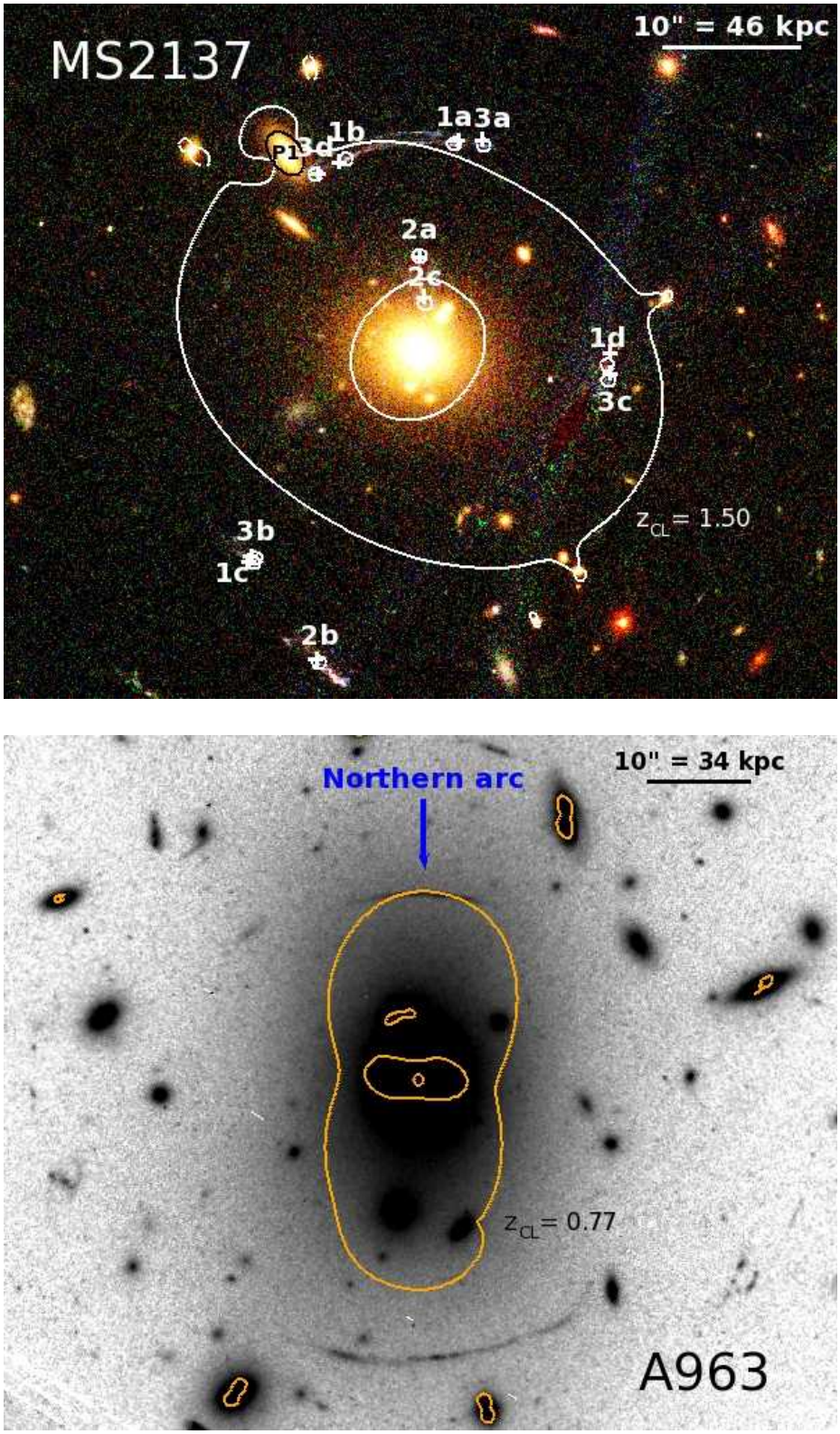
MS2137
10" = 46 kpc
1a3a
1b
P1
3d
2a
2c
1d
3c
3b
1c
2b
z_{CL} = 1.50
10" = 34 kpc
Northern arc
z_{CL} = 0.77
A963

Figure 3.11

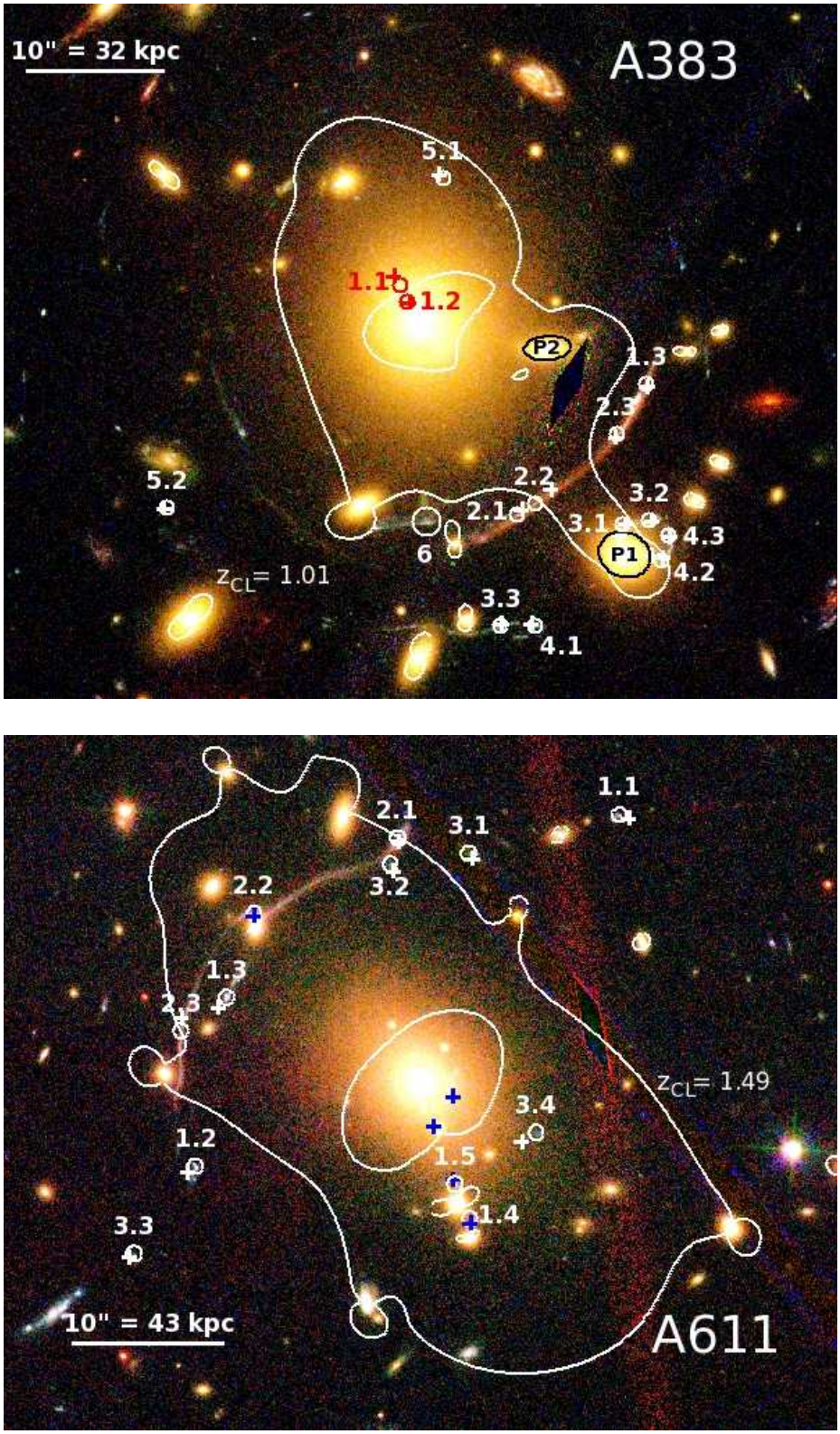
10" = 32 kpc
A383
5.1
1.1
1.2
P2
1.3
2.3
5.2
2.2
3.2
2.1
3.1
4.3
6
P1
4.2
z_{CL}= 1.01
3.3
4.1
2.1
3.1
1.1
3.2
2.2
1.3
2.3
z_{CL}= 1.49
3.4
1.2
1.5
1.4
3.3
10" = 43 kpc
A611

Figure 3.11

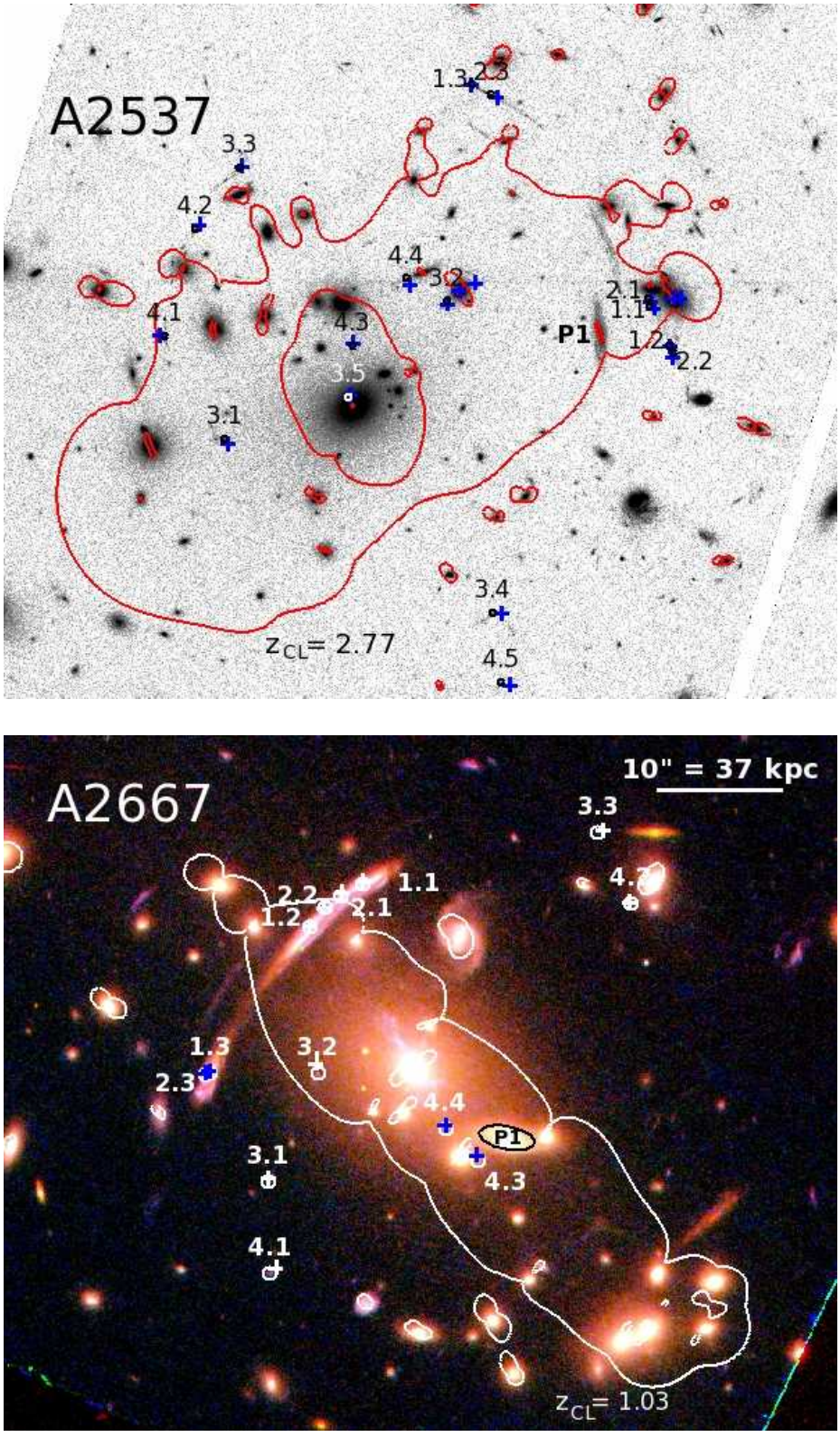
A2537
1.3
2.3
3.3
4.2
4.4
3.2
2.1
1.1
4.1
4.3
P1
1.2
2.2
3.5
3.1
3.4
z_{CL}= 2.77
4.5
A2667
10" = 37 kpc
3.3
4.2
2.2
1.1
1.2
2.1
1.3
3.2
2.3
4.4
P1
3.1
4.3
4.1
z_{CL}= 1.03

Figure 3.11

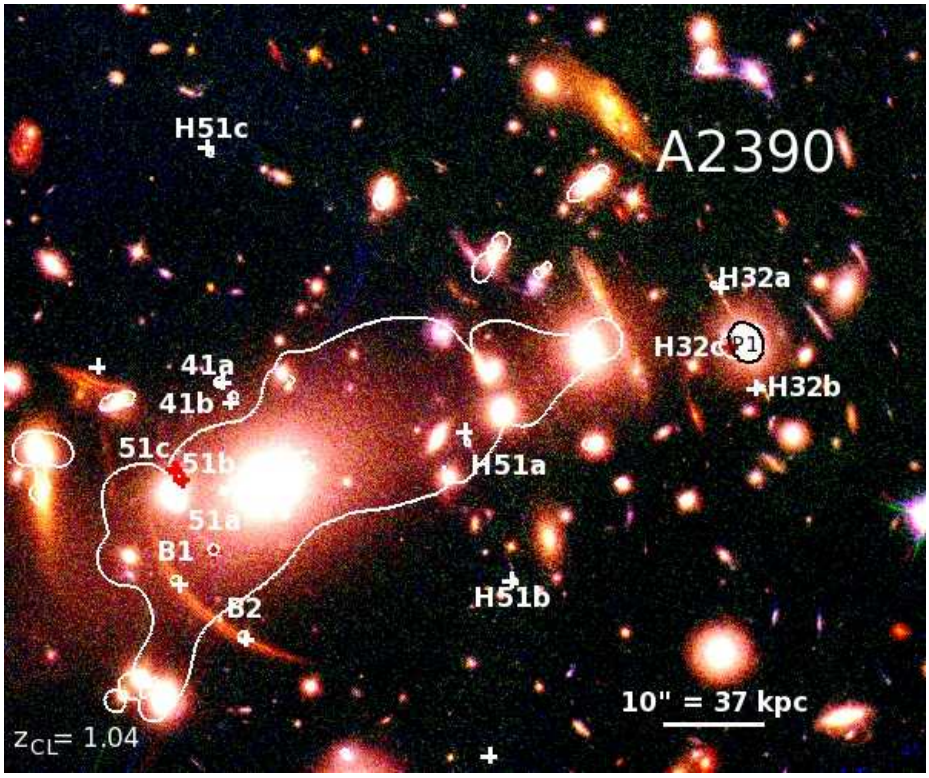

Figure 3.11: *HST* images of the central cluster cores, with multiply imaged sources identified (circles). Where possible we show color composite images, using data from the sources in Table 3.4 or from the CLASH survey (A611, MS2137, A383). Reconstructed image positions based on the models described in Chapter 4 are indicated by crosses (colors vary for clarity); critical lines are also overlaid at the redshifts $z_{\rm CL}$ indicated in each panel. Individually-optimized perturbing galaxies are denoted P1, P2, etc.

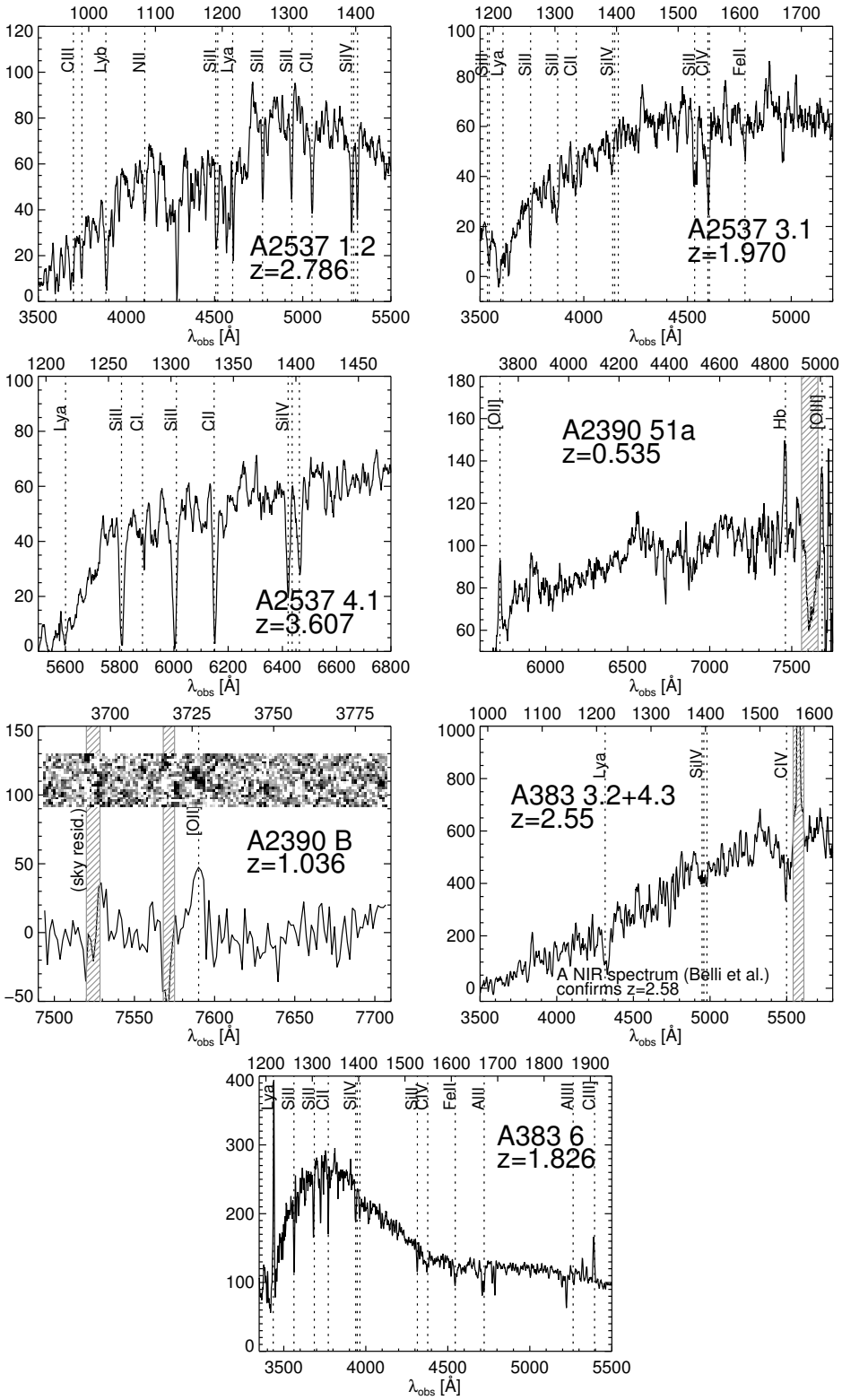

Figure 3.12: Spectra of multiply imaged sources obtained in new observations described in Section 3.5.1. The axis at the top of each plot indicates the rest-frame wavelength. Selected lines are identified, and areas of residual sky emission or absorption are hatched. The spectra are not flux calibrated, and the flux units are arbitrary. Multiple features are identified in each spectrum, resulting in a unique redshift determination with the exception of A2390 B. The identification of the single weak emission line in the latter case as [O II] is supported by photometric redshift estimates of this red arc.

3.3.4 A611

We adopt the model of Newman et al. (2009), comprising a five-image system with an originally-reported redshift of $z = 2.06$ (system 1), a giant tangential arc at $z = 0.908$ (system 2), and a four-image system with no spectroscopic redshift (system 3). These redshifts were published in R10. A subsequent near-infrared spectrum of system 1 revealed an unambiguous redshift of $z = 1.49$ via Hα, Hβ, and [O III] emission (Belli et al., in preparation). This shows that the redshift $z = 2.06$ in R10 resulted from a misidentification of the single rest-UV emission line C III] λ1909 as C IV λ1549. We return to the impact of this on mass models in Section 4.3.4. Additionally, the counter-image of the faint Lyα emitter identified in R10, whose position was suggested by the original lens model, is a less likely identification in models based on the new redshift. Thus, we do not include this system as a constraint. We located probable central counterimages of systems 1 and 3 well within the BCG light (see Newman et al. 2009, Figure 6) based on predictions of the lens models. Although we have conservatively not imposed their positions as constraints, we verified that including the central image of system 1 (the more reliable identification) would not significantly influence our results.

3.3.5 A2537

This cluster displays many spectacular arcs that have so far not been modeled in the literature. We identify four systems with new spectroscopic redshifts of $z = 1.970, 2.786$, and 3.607 (Figures 3.11 and 3.12). Several conjugate images were initially identified on the basis of similar morphology to construct a preliminary lens model, which was iteratively refined to locate the positions of the other images. Image systems 1 and 2 are located within a three-fold "naked cusp" arc at $z = 2.786$. Systems 3 and 4 form five-fold images at $z = 1.970$ and $z = 3.607$, respectively, both containing central images within the radial critical line. We discuss the inclusion of galaxy P1 as a perturber in our lens model in Section 4.1.

3.3.6 A2667

Our model is based on that of Covone et al. (2006, C06). It consists of an extremely bright giant tangential arc at $z = 1.034$ (Sand et al. 2005) and two systems with no spectroscopic redshifts named B and D in C06 (3 and 4, respectively, in our nomenclature). Based on interim lens modeling, we identified two additional counter-images 4.3 and 4.4 shown in Figure 3.11. The giant arc is incorporated via two features (systems 1 and 2) located as flux maxima and minima.

3.3.7 A2390

The lens model is based on those presented in Jullo (2008) and R10. It contains two arcs at $z = 4.05$, the H3 and H5 systems of Pelló et al. (1999). (For reasons discussed in Section 4.2, we do

Table 3.3. Positions of multiple images

Cluster	Image	Δx	Δy	$z_{\rm spec}$	Source	Cluster	Image	Δx	Δy	$z_{\rm spec}$	Source
A611	1.1	13.0	17.5	1.49	B12	A2667	1.1	−4.0	14.8	1.0334	S05
...	1.2	−14.7	−5.5	...	...	...	1.2	−8.3	11.3	...	...
...	1.3	−12.7	5.6	...	...	...	1.3	−16.2	−0.4	...	...
...	1.4	3.2	−8.9	...	...	...	2.1	−5.8	13.8	...	...
...	1.5	2.2	−6.6	...	...	...	2.2	−7.0	12.9	1.0334	...
...	2.1	−1.5	16.0	0.908	R10	...	2.3	−16.6	−0.5	...	...
...	2.2	−10.9	11.0	...	...	...	3.1	−11.6	−9.0	—	...
...	2.3	−15.7	3.4	...	...	...	3.2	−7.6	−0.4	...	...
...	3.1	3.2	15.0	—	...	...	3.3	14.8	18.8	...	...
...	3.2	−2.0	14.3	...	...	...	4.1	−11.4	−16.4	—	...
...	3.3	−18.7	−11.2	...	...	...	4.2	17.4	13.2	...	...
...	3.4	7.6	−3.3	...	...	...	4.3	5.3	−7.4	...	...
A383	1.1	−1.5	2.5	1.01	S04	...	4.4	2.6	−4.8	...	...
...	1.2	−0.9	1.3	...	...	A2537	1.1	35.6	11.9	2.786	This work
...	1.3	16.2	−4.7	...	...	...	1.2	38.0	7.2	...	...
...	2.1	6.9	−14.0	1.01	S01	...	1.3	14.3	38.6	...	...
...	2.2	8.2	−13.2	...	...	...	2.1	35.4	12.8	2.786	This work
...	2.3	14.1	−8.2	...	...	...	2.2	38.4	6.4	...	...
...	3.1	14.6	−14.7	2.58	N11, B12	...	2.3	16.6	37.3	...	...
...	3.2	16.5	−14.4	...	...	...	3.1	−15.4	−3.9	1.970	This work
...	3.3	5.8	−22.0	...	...	...	3.2	11.3	12.6	...	...
...	4.1	8.2	−22.0	2.58	N11, B12	...	3.3	−13.6	28.5	...	...
...	4.2	17.4	−17.3	...	...	...	3.4	16.7	−24.8	...	...
...	4.3	17.9	−15.5	...	...	...	3.5	−0.6	1.0	...	...
...	5.1	1.6	10.2	6.027	R11	...	4.1	−22.6	8.4	3.607	This work
...	5.2	−18.3	−13.5	...	...	...	4.2	−19.0	21.3	...	...
...	6†	0.3	−14.6	1.826	This work	...	4.3	0.0	7.3	...	...
MS2137	1a	2.6	14.9	1.501	S02	...	4.4	6.4	15.3	...	...
...	1b	−5.2	13.7	...	...	...	4.5	17.7	−33.1	...	...
...	1c	−11.9	−15.3	...	...	A2390	41a	−4.8	10.0	—	...
...	1d	13.6	−1.1	...	...	...	41b	−3.4	8.5	...	...
...	2a	0.1	6.8	1.502	S02	...	51a	−5.3	−6.8	0.535	This work
...	2b	−7.2	−22.5	...	...	...	51b	−8.7	0.3	...	...
...	2c	0.5	3.3	...	...	...	51c	−9.3	1.3	...	...
...	3a	4.7	14.7	1.501	S02	...	B1	−9.1	−9.9	1.036	This work
...	3b	−11.7	−15.0	...	...	...	B2	−2.3	−15.5	...	...
...	3c	13.7	−2.2	...	...	...	H32a	44.8	19.7	4.05	P99
...	3d	−7.4	12.7	...	...	...	H32b	49.5	9.4	...	...
A963	NA††	−0.55	12.18	0.771	E91	...	H32c	46.4	13.5	...	...
						...	H51a	20.0	4.0	4.05	P99
						...	H51b	24.8	-9.9	...	...
						...	H51c	-5.7	32.9	...	...

Note. — Positions are given relative to the BCG in arcseconds, with $\Delta x > 0$ and $\Delta y > 0$ representing offsets to the west and the north, respectively. "—" indicates that no spectroscopic redshift is available. † Not used as a constraint; see Section 3.3.3. †† Location of break point used to constrain critical line position. Sources: E91: Ellis et al. (1991), P99: Pelló et al. (1999), R10: Richard et al. (2010), R11: Richard et al. (2011), S01: Smith et al. (2001), S02: Sand et al. (2002), S04: Sand et al. (2004), S05: Sand et al. (2005), N11: Newman et al. (2011), B12: Belli et al, in preparation.

not include all the detectable conjugate points within these arcs as constraints.) The 41a/b system was previously identified on the basis of clear mirror symmetry but has no spectroscopic redshift. We secured a new spectroscopic redshift $z = 0.535$ for the 51a/b system near the cluster center, as well as a redshift $z = 1.036$ for the giant red arc (system B) to the southeast of the BCG based on very weak [O II] emission (Figure 3.12). Two conjugate points in the red arc were identified as flux minima in an *HST*/WFC3-IR F125W image (proposal ID 11678). The lens model predicts a counter-image to the northeast of the BCG, which we locate but do not include as a constraint due to uncertainty concerning its precise position (it appears to be superposed on a singly imaged portion of the galaxy).

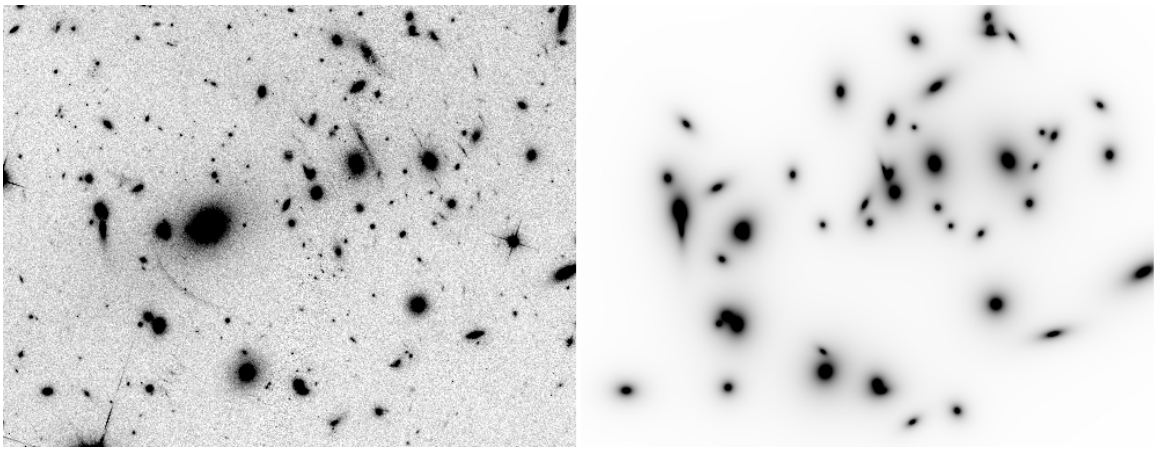

Figure 3.13: Left: *HST* image of the core of A2390, observed with ACS in the F850LP filter. **Right:** Surface density map of cluster galaxies selected as described in the text. In addition to the cluster-scale DM halo and the stellar mass in the BCG, these comprise the mass components used in the strong lens models. Both images are displayed with a linear scaling.

3.3.8 Cluster galaxy identification

Strong lens models must also account for mass in cluster galaxies, which perturb the positions of critical lines locally. We initially identified likely cluster galaxies as those with photometric redshifts near that of the cluster ($|\Delta z| < 0.15$). In A2537 and A2667, for which only two colors are available, we instead identified the locus of the cluster in the color-color plane. Absolute magnitudes in the r band were estimated and compared to $M_{r,*} = -21.38$ (Rudnick et al. 2009), appropriate to cluster galaxies at the redshifts of our sample. Only galaxies brighter than $0.1L_{r,*}$ were considered, unless they fell close to a multiple image. Early-type galaxies with $L \simeq 0.1L_*$ have $\sigma \approx 90$ km s^{-1} using the scaling relations we introduce in Section 4.1, which corresponds to deflection angle of $\simeq 0\farcs15$ in the singular isothermal sphere approximation, well within the uncertainty of $\sigma_{\rm pos} = 0\farcs5$ that we assign to the image positions. The radial extent of the sample was limited to extend safely beyond the strong lensing zone. This catalog was manually refined in some cases to include a few additional galaxies likely to be at or near the cluster redshift, but narrowly missing the criteria described above, or galaxies in close proximity to a multiple image. Although initially based on our multi-color ground-based catalogs, the parameters of the galaxies (center, ellipticity, P.A., flux) were refined using the *HST* imaging. The final catalogs contain $\simeq$ 10–60 galaxies, varying with the richness of the cluster and the extent of the strong lensing zone. Figure 3.13 illustrates the cluster galaxy selection in A2390, one of the richest clusters in the sample.

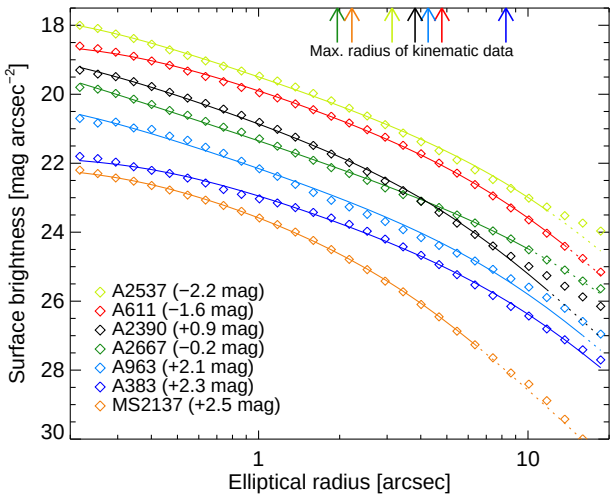

Figure 3.14: Surface brightness profiles of BCGs, measured in *HST* imaging through the filters indicated in Table 3.4. Data are shown as diamonds, with formal errors usually smaller than the symbol size. These are vertically offset as shown in the caption for clarity. dPIE fits are drawn as solid lines throughout the radial interval most relevant for dynamical modeling and dotted outside. The critical interval is estimated approximately as where the surface brightness exceeds 10% of that at the outer limit of the kinematic data (indicated by top arrows).

3.4 BCG photometry

In order to model the distribution of stellar mass in the BCG and to interpret our kinematic observations, the luminosity profile of the galaxy must be known. Furthermore, we wish to relate the stellar mass-to-light ratios derived in our models to estimates from SPS. In this section, we present fits to the surface brightness profiles and broadband colors of the BCGs.

3.4.1 Surface brightness profiles

Interpreting stellar dynamics in the BCG requires a model for the distributions of luminous tracers and mass. The dPIE parameterization[3] is particularly appropriate, since it is analytically convenient, widely used in lensing studies, and provides good fits to observed galaxies. It is characterized by two scale radii $r_{\rm core}$ and $r_{\rm cut}$, and the three-dimensional (3D) density is defined by

$$\rho_{\rm dPIE}(r) = \frac{\rho_0}{(1+r^2/r_{\rm core}^2)(1+r^2/r_{\rm cut}^2)}. \tag{3.10}$$

The analytic properties of the profile and the introduction of ellipticity are discussed by Elíasdóttir et al. (2007). The spherical radius enclosing half of the light is $r_h \approx r_{\rm cut}$, while the projected effective radius is $R_e \approx \frac{3}{4} r_{\rm cut}$ in the limit $r_{\rm core}/r_{\rm cut} \ll 1$. We fit dPIE profiles to the BCGs in our sample using *HST* imaging obtained in reduced form from the Hubble Legacy Archive, selecting observations

[3]Also referred to as a PIEMD, or pseudo-isothermal elliptical mass distribution.

Table 3.4. *HST* surface photometry of BCGs

Cluster	Instrument/Filter	dPIE fit parameters					$L_{\rm V}$	Proposal
		$r_{\rm cut}$ (kpc)	$r_{\rm core}$ (kpc)	b/a	P.A.	Mag.	($10^{11} L_{\odot}$)	ID
MS2137	ACS/F625W	18.7 ± 2.6	1.4	0.89	75	17.31	3.20	12102
A963	WFPC2/F702W	35.6 ± 4.6	0.47	0.81	6.4	15.41	4.61	8249
A383	ACS/F606W	38.2 ± 3.0	1.2	0.89	8.7	15.81	4.06	12065
A611	ACS/F606W	46.2 ± 3.4	1.2	0.73	42.3	16.81	5.47	9270
A2537	ACS/F606W	52.7 ± 6.5	0.75	0.74	-58.5	16.90	5.86	9270
A2667	WFPC2/F606W	68.8 ± 10.6	0.26	0.69	40.4	16.33	3.89	8882
A2390	ACS/F850LP	24.4 ± 2.9	0.44	0.73	-50.6	15.79	2.92	10504

Note. — Uncertainties in $r_{\rm cut}$ include random and systematic errors assessed by varying the background. Errors in $r_{\rm core}$, b/a and P.A. (measured in degrees east of north) are negligible for our analysis. Circularized radii are reported. The rest-frame $L_{\rm V}$ is corrected for Galactic extinction; the observed magnitude is not. The uncertainty in the observed magnitude and in $L_{\rm V}$ assuming a dPIE model is $\simeq 0.1$ mag.

Table 3.5. Stellar population synthesis fits to BCGs

Cluster	$\Upsilon_{*\rm V}^{\rm SPS}$	$N_{\rm filt}$	Photometry source
MS2137	2.05	10	*HST* ACS & WFC3 (CLASH)
A963	2.31	4	SDSS DR8
A383	2.26	7	*HST* ACS & WFC3 (CLASH)
A611	2.24	5	*Subaru* & *HST* WFC3-IR
A2537	2.32	4	SDSS DR8
A2667	2.04	5	*HST* WFPC2, ACS, NICMOS (proposal IDs 8882 & 10504)
A2390	1.80	5	SDSS DR8

Note. — Stellar mass-to-light ratios $\Upsilon_{*\rm V}^{\rm SPS}$ are derived from SPS fits assuming a Chabrier IMF. $N_{\rm filt}$ denotes the number of filters used in the fit. The luminosities $L_{\rm V}$ are given in Table 3.4 and include any internal dust extinction.

around 6000 Å, which is close in wavelength to the absorption features used to derive kinematics (Section 3.5). In A2390 we opted to use a F850LP observation instead, due to a prominent central dust feature, although this had little effect ($\sim 8\%$) on the derived radius. The filters and instruments used are listed in Table 3.4.

The background level in the *HST* images was adjusted based on blank sky regions far from the BCG. A noise map was constructed based on the background and shot noise from the BCG. Light from other galaxies in the field was carefully excluded using large elliptical masks generated from `SExtractor` parameters and then manually tuned. The geometric parameters of ellipticity, position angle (P.A.), and center were first determined by fitting an $R^{1/4}$ profile to the 2D data using `Galfit` (Peng et al. 2002). We then extracted elliptical isophotes and fit the 1D surface brightness profile in the inner $20''$ to a dPIE model using a custom code, accounting for the *HST* PSF. MS2137 and A383 present gradients in P.A., and the BCG geometry contributes to the modeling of their radial arcs. In these clusters, we thus fixed the P.A. to that measured near these arcs.

Figure 3.14 demonstrates that this procedure produces goods fits to the data, particularly within the radial range most critical for the dynamical modeling (solid lines). In the inner $10''$, rms residuals are typically 5%. At larger radii, some BCGs have a cD-type upturn in their surface brightness profile that is not well fit with a single component model (e.g., Gonzalez et al. 2005). This causes errors in the total luminosity and radii, but these are correlated such that the surface luminosity density within $\simeq 10''$ is well fixed. This is all that is necessary for our dynamical and lens models, given that the kinematic data are confined to $R < 5''$ in all but one case (A383), and the mass budget is always DM-dominated beyond a few arcseconds.

Varying the background level produced $5\% - 10\%$ systematic variations in $r_{\rm cut}$. In five clusters we additionally fit a redder band (F850LP, F125W, or F160W) in Advanced Camera for Surveys (ACS) or WFC3 imaging to investigate trends with color. In three cases the derived radii agree to $< 7\%$, within the systematic errors, while in the remaining pair (A611 and A383) the radii are $\simeq 20\%$ smaller in the redder band. Even in these cases, the color gradients are minimal (< 0.1 mag) within $R \lesssim 7''$, so the differences mainly reflect gradients beyond $\sim R_e$. While the redder data likely better trace the stellar mass, the dynamics are DM-dominated at these large radii. We therefore considered it more important to accurately model the tracers and adopted the measurements at $\simeq 6000$ Å. This choice is justified further in Section 5.5.

3.4.2 Stellar population synthesis

Since a principal goal of this project is the measure the stellar and dark matter distributions in the cluster cores, it is useful to place the stellar mass measures we derive from lensing and dynamics in context by comparing them to estimates from SPS models. Therefore, we additionally fitted SPS models to the broadband colors of the BCGs. Since the BCG is often saturated in our Subaru

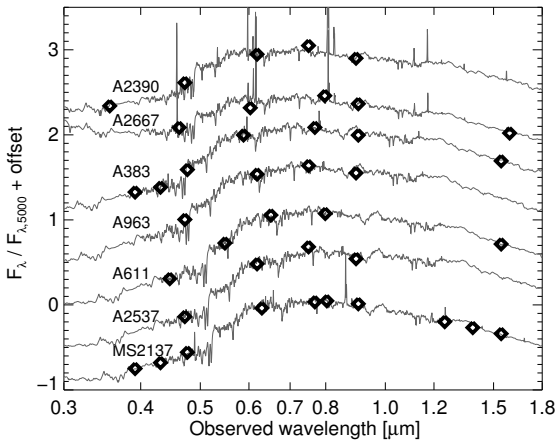

Figure 3.15: Photometric observations of the BCGs (black diamonds) are overlaid on SPS fits (grey) derived with the `kcorrect` code and used to estimate the stellar mass-to-light ratio Υ_{*V}^{SPS}.

imaging, we also rely on photometry from the SDSS or *HST* imaging. The SDSS colors are based on model magnitudes, while colors in *HST* imaging are measured in apertures with radii $\simeq 2\farcs5$ that avoid other galaxies, local dust features, and arcs. (This aperture corresponds to roughly the radial extent over which the stellar mass dominates.) The `kcorrect` code (Blanton & Roweis 2007) was used to fit SPS models from which a k-correction to the rest-frame V-band luminosity L_V was computed (Table 3.5). The luminosity was scaled to match total flux of the dPIE model and corrected for Galactic extinction. We assigned errors of 10% to all photometric measurements in the fitting process – much larger than the random errors – to account for systematic errors in the photometry and models.

These SPS models fits also provide an estimate of the stellar mass-to-light ratio $\Upsilon_{*V}^{SPS} = M_*/L_V$ appropriate for a Chabrier (2003) initial mass function (IMF). Following standard practice, the stellar masses refer to the current mass in stars and do not include any gas lost during stellar evolution (e.g., Treu et al. 2010; Cappellari et al. 2012a). The photometric data and derived Υ_{*V}^{SPS} ratios are listed in Table 3.5. Figure 3.15 shows the photometric data and the fits from `kcorrect`. Overall the Υ_{*V}^{SPS} estimates are quite uniform, with an rms scatter of only 9%. Reassuringly, the BCGs with the lowest estimates (A2667, A2390, MS2137) are those that show the strongest emission lines (Section 3.5) and the most prominent cooling cores. The far-infrared emission detected by *Herschel* in A2390 and A2667 also indicates that these systems host some ongoing star formation (Rawle et al. 2012).

By perturbing the photometric measurements by their errors, we estimate the typical random uncertainty in Υ_{*V}^{SPS} is about 0.07 dex. Systematic uncertainties were estimated by comparing measurements derived from a variety of codes. First, we used `FAST` (Kriek et al. 2009b) to construct grids of both Bruzual & Charlot (2003, BC03) and Charlot & Bruzual (2007, CB07) models with

exponentially declining star formation histories. The range of parameters was restricted appropriately for massive ellipticals: ages t with $9.5 < \log t/\mathrm{yr} < 10$, star-formation timescales τ with $8 < \log \tau/\mathrm{yr} < 9.5$, dust attenuation with $0 < A_V < 0.5$ mag, and solar metallicity. Mean stellar masses were estimated by marginalizing over the likelihood surface. (Simply taking the best-fitting model elevated $\log M_*$ by $\simeq 0.05$ dex on average.) Second, for A963 and A611 we are able to compare to the MPA/JHU catalog of SDSS galaxies (DR7; Kauffmann et al. 2003a). Finally, in addition to the above comparisons involving our BCG sample, we also used `kcorrect` to fit massive ellipticals at $0.15 < z < 0.35$ with four-band photometry observed in the SLACS survey. The resulting stellar masses were compared to those of Auger et al. (2009), which were based on carefully constructed priors. In all of the above comparisons, we find systematic mean offsets of < 0.06 dex compared to the masses derived using `kcorrect`. This level of uncertainty is typical given the current state of SPS. We conclude that our stellar mass scale is close to that of other authors who use similar data.

3.5 BCG kinematics

We now turn to the smallest spatial scales and present unique spectroscopic observations of the BCGs in our sample, along with the radially resolved stellar kinematics derived from them. These data are unique for galaxies located at the cosmological distances of lensing clusters, and they are the essential ingredient that allows us to probe the innermost decade in radius. As we demonstrate below, the data are of sufficient quality to measure stellar velocity dispersions to typical radial limits of $\approx 10-20$ kpc, while the long-slit width and seeing limit the resolution on small scales to ≈ 3 kpc. The stellar kinematic data thus probe the mass distribution from the smallest scales, where stars dominate the mass, out to radii where DM is dynamically significant. In combination with lensing, they provide a long lever arm with which to study the inner mass distribution.

3.5.1 Observations and reduction

We undertook spectroscopy of the BCGs using the Keck I and II and Magellan Clay telescopes, as recorded in Table 3.6. Total exposure times ranged from roughly two to seven hours. Five clusters were observed using the Low-Resolution Imaging Spectrometer (LRIS) on Keck I (Oke et al. 1995) using the 600 mm^{-1} grism blazed at 4000 Å in the blue arm and the 600 mm^{-1} grating blazed at 7500 Å in the red arm. A2537 and A2390 were observed through slitmasks in order to simultaneously secure redshifts of multiply imaged sources and of cluster members. The A383, A611, and A963 BCGs were observed using a long slit. In A383, we additionally observed a slitmask designed to cover gravitational arcs. MS2137 was observed using the Echelle Spectrograph and Imager (ESI; Sheinis et al. 2002) on the Keck II telescope, as presented by Sand et al. (2002). Finally, A2667 was observed using LDSS-3 at the Magellan Observatory. In all but one case, the slit (Table 3.6)

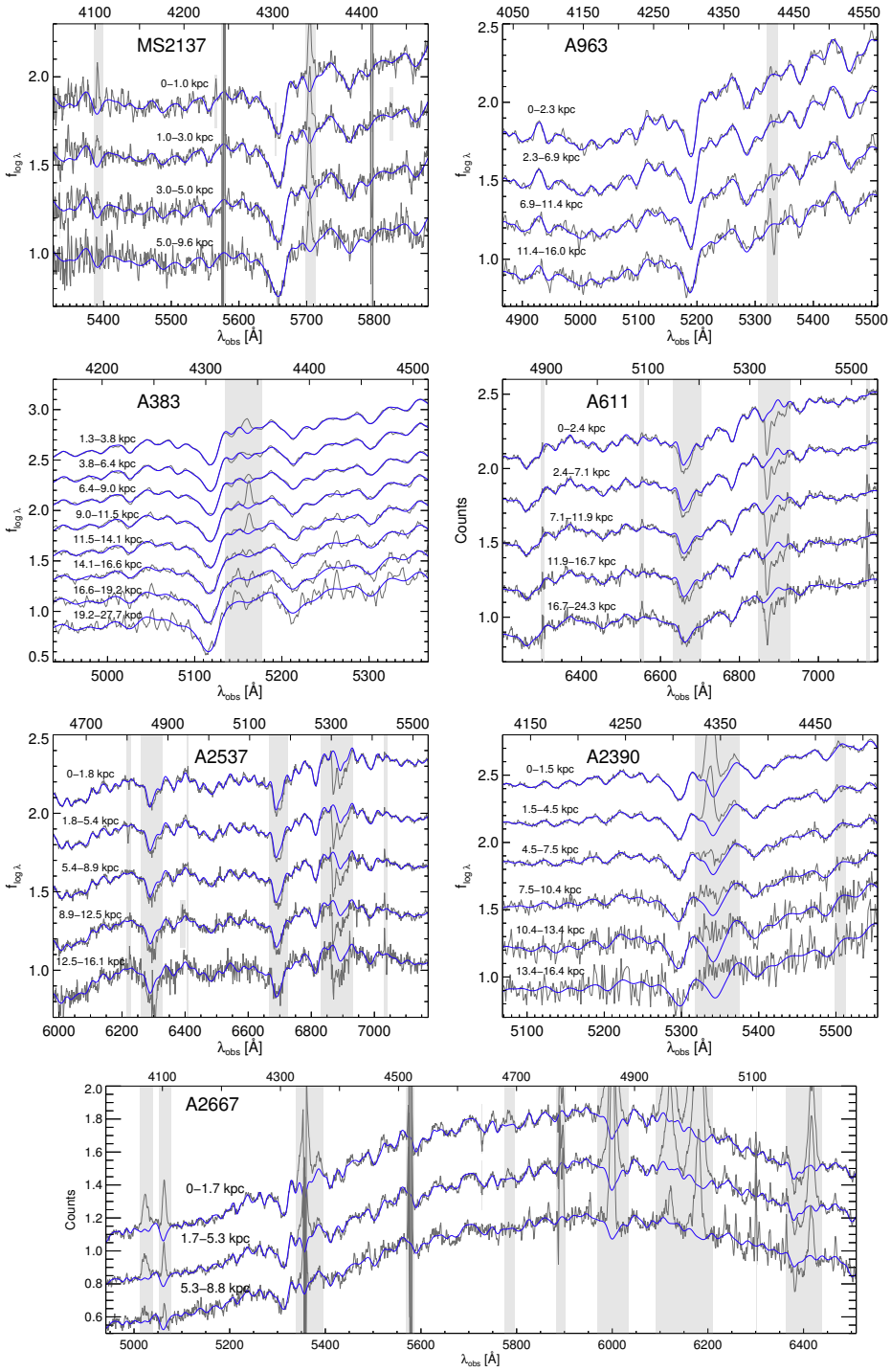

Figure 3.16: Spatially resolved spectra of BCGs with fits used to measure kinematics. Gray lines show the data, and the fitted models are shown in blue. Each spatial bin is normalized to a median flux density of unity. The bins are then offset vertically for clarity. The top axis indicates the rest-frame wavelength. Gray bands denote masked pixels as described in the text. In A2390, A963, and A383 the Mg b/Fe spectral region was also observed and fitted, but only the G-band region is shown here. Symmetric spatial bins on either side of the BCG center are co-added for display purposes where possible, although fits were performed separately. (This was not done in A2390 due to its low-level rotation.) Spectra have been lightly smoothed with a 2 Å boxcar.

Table 3.6. Spectroscopic observations

Cluster	Instrument	Date	Exposure (ks)	P.A. (deg)	Seeing (″)	Slit width (″)	Mode
MS2137	ESI	2001 Jul. 28	6.7	0	0.8	1.25	Cross-dispersed
A963	LRIS	2012 Apr. 18	7.8	−15.5	2.5	1.5	Long-slit
A383	LRIS	2009 Oct. 12-14	23.7	2	0.7	1.5	Long- & multi-slit
A611	LRIS	2008 Mar. 1	7.8	45	1.4	1.5	Long-slit
A2537	LRIS	2009 Oct. 12-14	14.4	125	0.8	1.5	Multi-slit
A2667	LDSS-3	2007 Jul. 15, 17	19.8	27.4	0.9	1.0	Long-slit
A2390	LRIS	2009 Oct. 12-14	14.4	−45	0.8	1.5	Multi-slit

was aligned close to the major axis of the BCG, with some minor deviations tolerated to include gravitational arcs. For MS2137 the slit was instead aligned along the radial arc near the minor axis, although its isophotes are nearly circular.

The long-slit spectra were reduced with `IRAF` using standard techniques for bias subtraction, flat fielding, wavelength calibration, trace rectification, and sky subtraction. For this work we have re-reduced the order of the ESI spectrum containing the G band in MS2137 using similar methods. Multi-slit data were reduced using the software developed by Kelson (2003). The wavelength-dependent instrumental resolution was measured via unblended sky lines or arc lamps and fitted with a low-order polynomial. The typical resolutions of the blue and red LRIS spectra are $\sigma = 159$ and 115 km s^{-1}, respectively, while the ESI and LDSS-3 observations have resolutions of $\sigma = 32$ and 84 km s^{-1}. These are much smaller than the velocity dispersions encountered in BCGs, so the uncertainties of a few km s^{-1} in resolution have a negligible $\simeq 1\%$ effect on the derived dispersions.

The center of the BCG was shifted to the center of a pixel during the reduction processes so that spatially-binned spectra could be extracted symmetrically on either side of the center. Our analysis focuses on two spectral regions with strong absorption features appropriate for kinematic study: the G band at λ4308 and the Mg I b region containing Fe λ5270, Fe λ5335 and other weaker lines. For the LRIS observations, the spatial bins were determined by adding CCD rows until a minimum signal-to-noise ratio (S/N) of 20 Å^{-1} was reached in the Mg b/Fe spectral region of the LRIS-R spectrum, suitable for reliable kinematic measurements. A minimum number of rows comparable to the seeing element was also required. In some cases, the outermost bin constructed by this scheme was conservatively excluded due to contamination of the key absorption features by sky residuals. Bins likely contaminated by flux from interloping galaxies were also excluded; this includes the innermost bin in A383.

When possible (A963, A2390, A383) identical spatial bins were extracted in the spectral region around the G band in the LRIS-B spectrum, which was facilitated by the equal pixel scale of the detectors. Although the formal S/N is lower at the G band, we found these spectra could nonetheless be reliably followed due to the cleaner sky. For A2537 and A611, the LRIS-B spectra

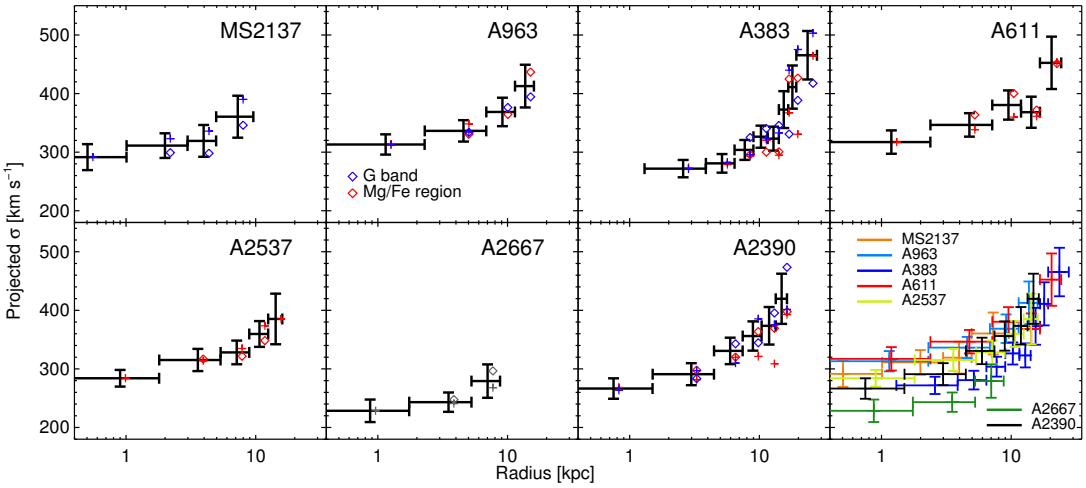

Figure 3.17: Resolved stellar velocity dispersion profiles, with cross and diamond symbols denoting independent measurements on either side of the BCG center and colors denoting measurements in the spectral regions indicated in the caption. Radii are measured along the slit (i.e., are not circularized). Points with error bars show the weighted mean measurements, with errors including a systematic estimate as described in the text. The final panel combines these measurements for the full sample.

were not used owing to the coincidence of the G band with the O I λ5577 sky line and the dichroic transition, respectively. For the ESI spectrum of MS2137, we considered only the order containing the G band, since the Mg b/Fe region was strongly affected by atmospheric absorption. For the LDSS-3 spectrum of A2667, we extracted the rest-frame 4000–5280 Å interval, which was covered continuously. Figure 3.16 shows the extracted spectra.

3.5.2 Kinematic measurement technique

In each spatial bin, the velocity and velocity dispersion were measured by direct fitting of Gaussian-broadened, redshifted stellar spectra using the `pPXF` software (Cappellari & Emsellem 2004), accounting for the instrumental resolution. An additive continuum polynomial was included in the fit, with the order determined identifying that beyond which the fit quality in the highest-S/N bin did not improve significantly. The derived velocity dispersions were insensitive to reasonable choices of the continuum order to a precision of $\simeq 1\% - 3\%$. For the spectra that were not flux calibrated (A2667 and A611), a first- or second-order multiplicative polynomial was allowed to modulate the spectral shape. For flux-calibrated spectra this yielded no improvement in the fit, and the additional freedom was therefore excluded. Emission lines, regions of prominent sky subtraction residuals or absorption, and remaining defects were masked. Random uncertainties were assessed by shuffling the residuals in five-pixel chunks, which maintains their correlation properties, adding these to the best-fitting model, and re-fitting the resulting spectra many times. This generally produced 1σ error estimates only slightly larger than those derived from the χ^2 surface.

The stellar templates used to fit the BCG spectra were constructed from the MILES library (Sánchez-Blázquez et al. 2006). By default we allowed `pPXF` to build an optimal template from a linear combination of 203 MILES stars with spectral types G5–K5 and luminosity classes III and IV, appropriate for old stellar populations. The template was determined using the spatially integrated spectrum and was then used to fit each spatial bin. Mg I b, which is enhanced in massive galaxies, was masked since it generally produced biased results, consistent with other studies (Barth et al. 2002). The resulting templates produce excellent fits to the BCG spectra, as shown in Figure 3.16.

We experimented with including a wider range of stellar templates, including all non-peculiar stars of spectral types A–K in the MILES library and a subset that excludes those with low metallicity. For the A2390 and A2667 BCGs, some A- and F-type stars were preferred, consistent with the likely star formation activity discussed in Section 3.4.2. Our inclusion of these earlier spectral types impacts the derived dispersions in these systems by $\lesssim 5\%$. We also constructed templates based on the Indo-US coudé library (Valdes et al. 2004). Finally, we experimented with templates optimized to each bin, rather than constructing a single template based on the integrated light; this led to no noticeable systematic changes. Details of the template construction led to systematic changes in the derived velocity dispersions at the $3\% - 5\%$ level. Based on our estimates of uncertainties related to the template and the continuum polynomial order, we assign a systematic uncertainty of 5% to all velocity dispersions, consistent with previous studies.

3.5.3 Velocity dispersion profiles

We detected no significant rotation in all but one BCG. In A2390, the measured rotation of 44 ± 13 km s^{-1} is negligible compared to the central velocity dispersion, with $(v/\sigma)^2 = 0.026$. In the remainder of our analysis, we thus focus only the velocity dispersions. When multiple measurements of the dispersion in the same radial bin were available, either from fits on either side of the BCG center or in different spectral regions, they were combined with a weighted mean to produce a more precise estimate. This is justified given that the agreement between independent measurements is very good overall: of the 87 pairs of overlapping measurements, 79% agree within 1σ using the random error estimates only. In a few bins the spread among estimates appeared greater than could likely be explained by random errors only, and in these cases the error bars were inflated based on the spread in estimates. In all cases, 5% was added in quadrature to the final uncertainty to account for the systematic effects described in Section 3.5.2.

The derived velocity dispersion profiles for each cluster are shown in Figure 3.17, including the weighted mean estimate and the individual measurements described above. The data are listed in Table 3.7. In all seven clusters, the velocity dispersion rises with radius. This contrasts strikingly with massive field ellipticals, which show velocity dispersion profiles that are flat or slowly declining (e.g., Carollo et al. 1995; Gerhard et al. 2001; Padmanabhan et al. 2004). Our data imply a strongly

Table 3.7. Velocity dispersion profiles

Cluster	Radial bin (arcsec)	σ (km s^{-1})	Cluster	Radial bin (arcsec)	σ (km s^{-1})
MS2137	$0 - 0.22$	292 ± 22	A2537	$0 - 0.41$	284 ± 14
...	$0.22 - 0.65$	311 ± 21	...	$0.41 - 1.22$	315 ± 19
...	$0.65 - 1.08$	319 ± 27	...	$1.22 - 2.03$	328 ± 20
...	$1.08 - 2.09$	360 ± 36	...	$2.03 - 2.84$	360 ± 22
A963	$0 - 0.68$	313 ± 17	...	$2.84 - 3.65$	385 ± 43
...	$0.68 - 2.03$	336 ± 18	A2667	$0 - 0.47$	228 ± 19
...	$2.03 - 3.38$	369 ± 24	...	$0.47 - 1.42$	243 ± 16
...	$3.38 - 4.73$	413 ± 36	...	$1.42 - 2.36$	279 ± 28
A383	$0.41 - 1.22$	272 ± 15	A2390	$0 - 0.41$	266 ± 17
...	$1.22 - 2.03$	281 ± 16	...	$0.41 - 1.22$	291 ± 19
...	$2.03 - 2.84$	304 ± 17	...	$1.22 - 2.03$	331 ± 23
...	$2.84 - 3.65$	326 ± 19	...	$2.03 - 2.84$	356 ± 25
...	$3.65 - 4.46$	323 ± 20	...	$2.84 - 3.65$	374 ± 32
...	$4.46 - 5.27$	373 ± 31	...	$3.65 - 4.46$	420 ± 43
...	$5.27 - 6.08$	411 ± 37			
...	$6.08 - 8.78$	465 ± 41			
A611	$0 - 0.55$	317 ± 20			
...	$0.55 - 1.65$	347 ± 20			
...	$1.65 - 2.75$	380 ± 25			
...	$2.75 - 3.85$	368 ± 27			
...	$3.85 - 5.61$	452 ± 45			

Note. — Line-of-sight velocity dispersions are derived from averaging observations on either side of the BCG center and, in most cases, in multiple wavelength intervals, as described in Section 3.5.1. Radii are measured along the slit, which is oriented near the major axis with the exception of MS2137; they can be circularized using the axis ratios in Table 3.4. Error bars include a 5% systematic component added in quadrature.

rising total mass-to-light ratio, which, as we show in Section 5.7, can be naturally explained by the cluster-scale halo. An alternative explanation for the rising dispersions is that the stellar orbits rapidly become more tangential at large radii. This can be tested using the detailed shape of stellar absorption lines in nearby systems, which would reveal "peakier" profiles at large radii if circular orbits dominate. Observations of local cD galaxies instead favor nearly isotropic or mildly radial orbits (Carter et al. 1999; Kronawitter et al. 2000; Saglia et al. 2000; Hau et al. 2004), which indicates that the rising dispersions are not an artifact of the orbital distribution but reflect the genuine dynamical influence of the cluster potential.

3.5.4 Comparison to previous work

In the current analysis we have reanalyzed the spectra of A611 and MS2137 presented in Newman et al. (2009) and Sand et al. (2002), respectively, and obtained a new, deeper spectrum of A963 compared to Sand et al. (2004). The A383 spectrum and kinematic measurements are identical to Newman et al. (2011), with the exception of a small adjustment ($< 1\sigma$) to the outermost bin only. However, the velocity dispersion measurements in A611, MS2137, and A963 have changed systematically and significantly compared to the previously published values. While the earlier works (Sand et al. 2002, 2004, 2008; Newman et al. (2009)) indicated a flat or even declining (in the case of MS2137) dispersion profile in these clusters, we now find a rising trend in common with the rest of the sample.

Given that multiple codes and techniques were used to reduce the present data, yielding very similar dispersion profiles (Figure 3.17, final panel), the differences in these measurements appear unrelated to the data reduction itself. More likely they arise from improvements to the velocity dispersion measurement procedure. In particular, we now (and in Newman et al. 2011) rely on large libraries of high-quality stellar spectra to construct templates, whereas earlier works were restricted to a relatively small number of stars observed with ESI. Furthermore, we now construct composite templates from linear combinations of these spectra, rather than taking a single star. This provides much higher-quality fits (Figure 3.16) with virtually no residual "template mismatch." We have also tested the dispersion measurements in MS2137 using an independent code developed by M. Auger and find identical results (A. Sonnenfeld, private communication). The earlier suboptimal templates used in earlier works probably led to biases at higher σ or lower S/N. Given the high quality of the data (the rising σ can be seen by eye in many panels of Figure 3.16), the improved methodology, and the resulting uniformity of the dispersion profiles, we have confidence in the present results.

Chapter 4

Modeling the Cluster Mass Distribution

Having introduced the observational data that form the basis of our analysis, we now describe the models and methods that we use to infer the cluster mass distribution. Our mass model consists of three components: the DM halo, the stars in the BCG, and the mass in other cluster galaxies. Each is described by one or more analytic models, which are introduced in Section 4.1. The parameters of these models are constrained simultaneously using our full data set, and the inference is conducted within a Bayesian framework. Section 4.2 describes the calculation of the likelihood of the data, given a mass model proposed by a Markov Chain Monte Carlo (MCMC) sampler that is used to explore the large parameter space. Finally, in Section 4.3, we show how the combination of lensing and X-ray data can be used to constrain the line-of-sight (l.o.s.) geometry of the cluster, thus addressing the role of projection effects in our analysis.

4.1 Mass model ingredients

Two flexible functional forms are adopted to describe the dark halo. In addition to length and density scaling parameters, each includes a third parameter that allows for variation in the shape of the density profile. In particular, they allow for deviations in the inner regions from the CDM density profiles produced in numerical simulations. As we described in Chapter 2, this is the region where the effects of baryons or non-standard DM should be the most pronounced. The generalized NFW profile (gNFW, Zhao 1996), given by

$$\rho_{\rm DM}(r) = \frac{\rho_s}{(r/r_s)^{\beta}(1+r/r_s)^{3-\beta}}, \tag{4.1}$$

reduces to the NFW profile when $\beta = 1$, but the asymptotic inner slope $d\log\rho_{\rm DM}/d\log r = -\beta$ as $r \to 0$ can be varied. When we fix $\beta = 1$ to fit NFW models, we refer to the virial mass M_{200} as that within a sphere of radius r_{200} that has a mean density equal to 200 times the critical density

$\rho_{\rm crit}$ of the universe at the cluster redshift. The concentration is then $c_{200} = r_{200}/r_s$.

In order to verify that our results do not strongly depend on the functional form of the density profile, we have introduced a second parameterization that we refer to as a "cored NFW" (cNFW) model:

$$\rho_{\rm DM}(r) = \frac{b\rho_s}{(1+br/r_s)(1+r/r_s)^2}. \tag{4.2}$$

This is simply an NFW profile with a core introduced, i.e., with asympotically constant density as $r \to 0$. The scale of the core is controlled by the parameter b. A characteristic core radius can be defined as $r_{\rm core} = r_s/b$; at this radius, the density falls to half that of an NFW profile with equal r_s and ρ_s. As $r_{\rm core} \to 0$ ($b \to \infty$) the profile approaches the NFW form. We follow the `Lenstool` convention and use the parameter $\sigma_0^2 = \frac{8}{3}G\rho_s r_s^2$ in place of ρ_s. This is simply a defined scaling and should not be taken as the actual velocity dispersion.

We also considered using Einasto models, which have been shown to provide more accurate representations of halos in numerical simulations (e.g., Merritt et al. 2006; Navarro et al. 2010; Gao et al. 2012b). However, this form is not optimal for observational studies of the inner halo, because the behavior at large and small radii are strongly coupled: to explore flat inner profiles, one has to accept steep declines in the outer regions. By contrast, the large-radius behavior of the gNFW and cNFW density profiles are invariant. Further, Einasto profiles with the range of shape parameters seen in simulations can be approximated by gNFW profiles within $\simeq 10\%$ over the relevant range of radii.

The stellar mass in the BCG is modeled with a dPIE profile, introduced in Section 3.4.1.[1] The center, P.A., ellipticity, and scale lengths $r_{\rm core}$ and $r_{\rm cut}$ are fixed based on the fits to *HST* imaging described in that section. The only free parameter is then the stellar mass-to-light ratio $\Upsilon_{*\rm V} = M_*/L_{\rm V}$, which we assume to be spatially invariant within the BCG. (This assumption is discussed further in Section 5.5.) We parameterize $\Upsilon_{*\rm V}$ relative to the values $\Upsilon_{*\rm V}^{\rm SPS}$ derived from our SPS fits, based on a Chabrier IMF (Section 3.4.2):

$$\log \alpha_{\rm SPS} = \log \Upsilon_{*\rm V}/\Upsilon_{*\rm V}^{\rm SPS} \tag{4.3}$$

(Treu et al. 2010). We place a very broad uniform prior on $\log \alpha_{\rm SPS}$, corresponding to a mass that is 1.5× lighter than $\Upsilon_{*\rm V}^{\rm SPS}$ to a mass 2× heavier than the $\Upsilon_{*\rm V}^{\rm SPS}$ inferred using a Salpeter IMF, where we take $\log M_{*,\rm Salp}/M_{*,\rm Chab} = 0.25$. The total allowed range in $\Upsilon_{*\rm V}$ is thus a factor of 5.3.

The final ingredient in the mass model is the dark and luminous mass in non-BCG cluster galaxies, which are significant perturbations in the strong-lensing analysis. The identification of these galaxies was described in Section 3.3.8. Their mass is modeled using dPIE profiles. The

[1] Note that we make no distinction between the halo of the BCG and that of the cluster, which would be observationally impossible and is not well defined theoretically.

center, ellipticity, and P.A. are fixed to that of the light, and for most of the cluster galaxies, the structural parameters are tied to scaling relations specific to each cluster (e.g., Limousin et al. 2007; Newman et al. 2009; Richard et al. 2010):

$$\begin{aligned} r_{\rm cut} &= r_{\rm cut,*}(L_r/L_{r,*})^{1/2}, \\ r_{\rm core} &= r_{\rm core,*}(L_r/L_{r,*})^{1/2}, \\ \sigma &= \sigma_*(L_r/L_{r,*})^{1/4}. \end{aligned} \tag{4.4}$$

Following previous work (e.g., Newman et al. 2009; Richard et al. 2010), we place a Gaussian prior on σ_* of 158 ± 27 km s^{-1} based on the observed scaling relations in the SDSS (Bernardi et al. 2003a). Based on the galaxy-galaxy lensing study of Natarajan et al. (2009), we allow $r_{\rm cut,*}$ to vary from 15 to 60 kpc. As those authors note, this is much larger than the optical radius of the galaxies, and our dPIE models therefore include galaxy-scale dark halos. Our analysis is insensitive to $r_{\rm core,*}$, which is thus fixed to 0.15 kpc.

These scaling relations are sufficient for the majority of cluster galaxies. In some cases, however, the position of a multiple image can be strongly influenced by a nearby galaxy. In these situations, the galaxy is freed from the scaling relations and modeled individually. These galaxies are indicated in Figure 3.11. It is sufficient to free either σ or $r_{\rm cut}$, since their effects are degenerate, and in practice we usually fix σ based on the Bernardi et al. (2003a) results and vary $r_{\rm cut}$. We note one peculiar case, that of galaxy P1 in A2537 (Section 3.3.5). We found that individually optimizing this perturber improved the modeling of the arc system composed of images families 1 and 2, although P1 is clearly deflected and located behind the cluster ($z_{\rm phot} = 0.59 \pm 0.04$ in SDSS DR8). This suggests a possible interesting two-plane effect, which is beyond the scope of this paper to fully model. Nevertheless, we find that the inferred mass parameters are consistent with an $\simeq L_*$ galaxy, which agrees reasonably with the (demagnified) luminosity.

The ICM gas is not modeled as a distinct mass component in our analysis and is therefore implicitly incorporated into the halo. Based on the $\simeq 3$ kpc spatial resolution of our spectra, we also do not consider a supermassive black hole. Observations of local BCGs indicate this becomes dynamically significant only at smaller scales $\lesssim 1$ kpc (e.g., Kelson et al. 2002).

4.1.1 Additional mass components

In A2667 the weak lensing map (Figure 3.10) shows a clear second clump located $\simeq 1.4$ Mpc north of the BCG, which is likely in the foreground (Section 3.2.4). Due to the large separation, this mass is unimportant for our strong lensing and dynamical analysis, but it must be considered for weak lensing. We therefore added a second dark halo to the model near the position indicated in the 2D mass map, as listed in Table 4.1. Since the internal structure is not well constrained by the shear

Table 4.1. Prior distributions used in cluster mass models

Parameter	Units	Prior
Cluster-scale dark matter halo		
ϵ (pseudoellipticity)	...	$U(\ldots)^\dagger$
P.A.	deg	$U(\ldots)^\dagger$
r_s	kpc	$L(50, 1000)$
σ_0	km s^{-1}	$L(500, 3500)$
β (gNFW models)	...	$U(0.01, 1.5)$
b (cored NFW models)	...	$L(1, 1000)$
Stellar mass in BCG		
$\log \alpha_{\rm SPS}$	...	$U(-0.176, 0.551)$
Cluster galaxy scaling relations		
σ_*	km s^{-1}	$G(158 \pm 27)$
$r_{\rm cut,*}$	kpc	$U(15, 60)$
Individually-optimized galaxies each add an additional parameter as discussed in the text.		
Weak-lensing shear calibration		
$m_{\rm WL}$	...	$G_{2\sigma}(0.89 \pm 0.05)$
Additional parameters for individual clusters		
A611		
Redshift of source 3	...	$U(1, 2)$
A2667: second NFW clump at $R \simeq 1.4$ Mpc		
Δx	arcsec	$G(7 \pm 45)$
Δy	arcsec	$G(370 \pm 45)$
ϵ	...	$U(0, 0.3)$
P.A.	deg	$U(0, 180)$
M_{200}	$M_\odot$	$L(10^{13}, 10^{15})$
ln c_{200}	...	$G(\ln(4) \pm 0.4)$
Redshift of source 3	...	$U(1, 4.5)$
Redshift of source 4	...	$U(1, 4.5)$
A2390		
Δx	arcsec	$G(0 \pm 1.5)$
Δy	arcsec	$G(0 \pm 1.5)$
A383 (see Section 4.3.3)		
$q_{\rm DM}$	...	$U(1, 2.5)$
q_*	...	see Section 4.3.3
$m_{\rm X}$	...	$G_{2\sigma}(0.9 \pm 0.1)$

Note. — $U(x, y)$ denotes a uniform prior over the interval bounded by x and y. $L(x, y)$ denotes a prior that is uniform in the logarithm. $G(\mu \pm \sigma)$ denotes a Gaussian prior with mean μ and dispersion σ, while $G_{2\sigma}$ denotes a Gaussian prior truncated at 2σ. Positions Δx and Δy are given relative to the BCG; positive values indicate west and north, respectively. Position angles are measured east of north. † The intervals were determined based on initial lensing fits; see the text for the special case of A963.

data, an NFW profile is assumed with a broad log-normal prior on c_{200}. The mean of this prior was taken to be 4, appropriate to the virial mass of $\log M_{200}/\,\mathrm{M}_\odot = 14.7$ inferred from the full modeling discussed below, although adopting an even broader prior did not significantly affect the results.

We experimented with adding a second mass clump to the west of the BCG in A2390, based on the extension of galaxies and X-ray emission on $\simeq 100$ kpc scales discussed in Section 3.1, but found that this did not improve the quality of the fit to the lensing data and substantially lowered the Bayesian evidence. We therefore consider a single dark clump to be sufficient. In A2537 the curvature of the arcs suggests a possible additional mass clump to the north of the BCG, which is given further credence by the multimodal dynamical structure described in Section 3.1. We experimented with adding a second clump and found that it did improve the Bayesian evidence when only strong-lensing constraints are fit, but not with the full data set. The inferred mass was small ($\simeq 1 \times 10^{13}\,\mathrm{M}_\odot$), and correspondingly the most relevant parameters for our study (halo mass and concentration, inner slope, $\Upsilon_{*\mathrm{V}}$) change little. Therefore, we retain a single dark clump when fitting this cluster also.

4.2 Inferring mass models from data

Our analysis is based on the `Lenstool` ray-tracing code (Kneib et al. 1993; Jullo et al. 2007), which has been widely used for studying strong lenses. For this project we have added components to `Lenstool` that incorporate weak lensing and stellar kinematic constraints into the likelihood calculation. The inference method is fully Bayesian. The prior distributions we adopted are listed in Table 4.1. For the key parameters (i.e., those describing the DM halo and $\Upsilon_{*\mathrm{V}}$) we chose uninformative priors that are broad and flat. An MCMC method is used to explore the large parameter space (Jullo et al. 2007). We checked for convergence of the MCMC chains by inspecting their traces, running means, and auto-correlation functions, as well as by comparing the results from individual chains and from independent MCMC runs.

For each model proposed by the MCMC sampler, a likelihood is computed based on the full data set. Since we assume the errors in our measurements are independent and Gaussian, this is equivalent to summing χ^2 terms based on the strong lensing, weak lensing, and stellar velocity dispersion constraints:

$$\chi^2 = \chi^2_{\mathrm{SL}} + \chi^2_{\mathrm{WL}} + \chi^2_{\mathrm{VD}}. \tag{4.5}$$

The strong lensing analysis is conducted in the image plane, with

$$\chi^2_{\mathrm{SL}} = \sum_i \frac{(x_i - x_i^{\mathrm{obs}})^2 + (y_i - y_i^{\mathrm{obs}})^2}{\sigma^2_{\mathrm{pos}}}, \tag{4.6}$$

where (x_i, y_i) and $(x_i^{\mathrm{obs}}, y_i^{\mathrm{obs}})$ are the predicted and observed image-plane positions, respectively,

of a single image, and the sum runs over all multiple images. For a given mass model, `Lenstool` iteratively refines the source positions using the image transport method of Schneider et al. (1999) to minimize $\chi^2_{\rm SL}$ (see Jullo et al. 2007); this is the slowest part of the likelihood calculation.

In two clusters somewhat different techniques were used. In A383, $\chi^2_{\rm SL}$ was instead calculated using a quicker technique that avoids solving the lens equation. In this method, $\chi^2_{\rm SL}$ is evaluated by computing the source plane positions of the various images of a given source and evaluating their scatter; the positional uncertainty in the source plane is demagnified from the image plane uncertainty using the local magnification matrix (Jullo et al. 2007). The source plane method was done only when we included kinematic data, due to the slower two-integral dynamics computed only for this cluster (Section 4.3.3). We verified that this has a minimal effect on the results. Second, in A963 the merging images that form the tangential arc could not be clearly separated (Section 3.3.2). We therefore identified a symmetry point and required that the critical line pass through it, with a positional uncertainty of $0\farcs2$. We also imposed Gaussian priors of $\epsilon = 0.21 \pm 0.02$ (the pseudoellipticity introduced below) and P.A. $= (86 \pm 3)^\circ$, based on the shape of the isophotes at the radius of the tangential arc, since the break point provided to `Lenstool` cannot constrain them.

The uncertainty in the image positions $\sigma_{\rm pos}$ is a key quantity when combining strong lensing with other data sets. Although compact images can in principle be located in *HST* imaging with an astrometric precision of $\lesssim 0\farcs05$, cluster lens models are generally not able to reproduce image positions to better than $\sigma \simeq 0\farcs2$–$0\farcs3$, with a scatter of up to $\sim 3''$ in the best-studied clusters (e.g., Limousin et al. 2007). This is likely partly due to perturbations by unmodeled substructures, either in the cluster or along the l.o.s. (Jullo et al. 2010). An additional factor is that simply parameterized models are not perfect representations of real or simulated clusters. This is particularly important when combining diverse data: since strong-lensing constraints are exquisitely precise, assigning a very small positional uncertainty can fully constrain the model. Given that strong lensing, weak lensing, and stellar kinematics contribute comparably to the logarithmic radial extent of our study, it is important not to overly concentrate the weight of the data in one radial interval.

We find that $\sigma_{\rm pos} = 0\farcs5$ strikes an appropriate balance and adopt this for our analysis (except see Section 4.2.1 on A2390, for which we take $\sigma_{\rm pos} = 1\farcs0$). For the same reason, we have generally not imposed the detailed substructure of arcs as constraints on the model. One tool to evaluate $\sigma_{\rm pos}$ empirically is the Bayesian evidence ratio. We compared the evidence obtained using $\sigma_{\rm pos} = 0\farcs3$ and $1\farcs0$ relative to our default $\sigma_{\rm pos} = 0\farcs5$ in fits to the full set of lensing and kinematic data.[2] In all clusters $\sigma_{\rm pos} = 1\farcs0$ is disfavored, with a decisive total evidence ratio $\Sigma(\ln E_{1\farcs0}/E_{\rm default}) = -50.6$. The clusters are divided over whether $\sigma_{\rm pos} = 0\farcs3$ is favored over our default $0\farcs5$. In total we find

[2]In A963, for which the data consist of a critical line position, we instead varied the error in its position to $0\farcs1$ and $0\farcs5$ from our default $0\farcs2$. A2390 was excluded in this comparison due to the special treatment described in Section 4.2.1.

$\Sigma(\ln E_{0\farcs3}/E_{\rm default}) = 7.0$, which indicates that the smaller uncertainty is somewhat preferred. We found, however, that the key parameter inferences do not shift significantly (see Section 5.5), while the error estimates shrink slightly when $\sigma_{\rm pos} = 0\farcs3$ as expected. Thus, we have retained our more conservative $\sigma_{\rm pos} = 0\farcs5$, but note that other reasonable estimates for the positional uncertainty yield very similar results.

Weak lensing constraints are incorporated by the term

$$\chi^2_{\rm WL} = \sum_i \frac{(g_{1,i} m_{\rm WL} - g^{\rm obs}_{1,i})^2 + (g_{2,i} m_{\rm WL} - g^{\rm obs}_{2,i})^2}{\sigma_g^2}, \tag{4.7}$$

where $(g^{\rm obs}_{1,i}, g^{\rm obs}_{2,i})$ is the observed reduced shear polar $g = \gamma/(1-\kappa)$ for galaxy i, $(g_{1,i}, g_{2,i})$ is the model reduced shear at the angular position and photometric redshift of galaxy i, and the factor $m_{\rm WL}$ incorporates our shear calibration. Based on the results in Section 3.2.2, we assign a Gaussian prior of 0.89 ± 0.05 to $m_{\rm WL}$. The uncertainty σ_g is dominated by the intrinsic ellipticities of galaxies ("shape noise") and is estimated using the standard deviation in shear measurements far from the cluster centers to be $\sigma_g = 0.32$.

Only the halo is considered in the weak-lensing modeling, since the mass is DM-dominated on $\gtrsim$ 100 kpc scales. The ellipticity of the halo in the plane of the sky is incorporated using the "pseudo-elliptical" formalism of Golse & Kneib (2002), in which the ellipticity is introduced in the lens potential. Using their notation, we derive

$$\gamma_{1,\epsilon} = -|\gamma| \cos(2\phi_\epsilon) - \epsilon\kappa, \tag{4.8}$$

$$\gamma_{2,\epsilon} = -|\gamma| \sin(2\phi_\epsilon) \sqrt{1-\epsilon^2}, \tag{4.9}$$

$$\kappa_\epsilon = \kappa + \epsilon |\gamma| \cos(2\phi_\epsilon), \tag{4.10}$$

where $\gamma_{1,\epsilon}, \gamma_{2,\epsilon}$, and κ_ϵ are the shear components and convergence for the elliptical model, and $|\gamma|$ and κ are the corresponding values for a circular lens. (See also Dúmet-Montoya et al. 2012.) As described by Golse & Kneib (2002), the pseudoellipticity ϵ is approximately the ellipticity of the potential and *not* that of the surface mass density, which is about twice as large. The pseudoelliptical formalism is also used for the strong lensing modeling. It is a reasonable approximation for the moderate ellipticities $\epsilon \lesssim 0.3$ encountered in our sample (Sand et al. 2008).

Finally, we compute the l.o.s. velocity dispersions $\sigma_{\rm los}$ using the spherical Jeans equation. We assume the BCGs are completely pressure-supported, consistent with the lack of observed rotation (Section 3.5.1):

$$\Sigma_* \sigma^2_{\rm los}(R) = 2G \int_R^\infty \frac{\nu_*(r) M(r) \mathcal{F}(r)}{r^{2-2\beta_{\rm aniso}}} \, {\rm d}r. \tag{4.11}$$

By default we consider isotropic orbits with $\beta_{\rm aniso} = 0$ and $\mathcal{F}(r) = \sqrt{r^2 - R^2}$ (Cappellari 2008).

More general expressions for $\mathcal{F}(r)$ can be found in Cappellari (2008), including ones for constant $\beta_{\rm aniso} \neq 0$, which we use. Here ν_* and Σ_* are the density and surface density profiles of the stellar tracers, as measured in Section 3.4.1, and $M(r)$ is the total mass (stars and DM) enclosed within a radius r. (In A383, axisymmetric two-integral dynamical models are used due to the significant l.o.s. elongation of this cluster. These are described in Section 4.3.3.)

The observational effects of seeing and the slit width are included following Sand et al. (2004). Briefly, the effect of seeing is accounted for following Equation 4.8 of Binney & Merrifield (1998)[3]:

$$\Sigma_*^{\rm blur}(R) = \int_0^\infty dR' \Sigma_*(R') R' I_0 \left(\frac{RR'}{\sigma_{\rm PSF}^2} \right) \exp \left(-\frac{1}{2} \frac{R^2 + R'^2}{\sigma_{\rm PSF}^2} \right), \tag{4.12}$$

where $\sigma_{\rm PSF}$ is the dispersion of the PSF and I_0 is the modified Bessel function of order zero. In order to match the rectangular aperture used in the observations, determined by the width w of the spectrograph slit and the radial interval $x_0 < x < x_1$ along the slit within which the spectrum was extracted, we then integrate the seeing-convolved surface luminosity over a rectangle:

$$\Sigma_*^{\rm extr} = \int_{x_0}^{x_1} dx \int_{-w/2}^{w/2} dy \Sigma_*^{\rm blur}(x, y). \tag{4.13}$$

The calculations in Equations 4.12 and 4.13 are then repeated with Σ_* replaced by $\Sigma_* \sigma_{\rm los}^2$, the luminosity weighted second moment of the l.o.s. velocity distribution. In practice, for efficiency, we compute $\sigma_{\rm los}$ on a grid and use a spline interpolation when evaluating the integrand. Finally, the quotient

$$\sigma^{\rm model} = \sqrt{(\Sigma_* \sigma_{\rm los}^2)^{\rm extr} / \Sigma_*^{\rm extr}} \tag{4.14}$$

results in a measure of the l.o.s. velocity dispersion that can be compared directly to the observations, including the effects of seeing and spatial binning. These constraints are incorporated as

$$\chi^2_{\rm VD} = \sum_i \frac{(\sigma_i^{\rm model} - \sigma_i^{\rm obs})^2}{\Delta_i^2}, \tag{4.15}$$

where $\sigma_i^{\rm model}$ and $\sigma_i^{\rm obs}$ are the model and observed l.o.s. dispersions in bin i, respectively, and Δ_i is the measurement uncertainty.

As discussed by Sand et al. (2004, 2008), a spherical treatment is a good approximation to the dynamics of the galaxies in our sample, which have a mean axis ratio $\langle b/a \rangle = 0.8$. Furthermore, detailed local studies find that massive, non-rotating ellipticals are intrinsically close to spherical and have low anisotropy (e.g., Gerhard et al. 2001; Cappellari et al. 2007). We discuss the effects of introducing mild orbital anisotropy into our dynamical models in Section 5.5.

[3]This equation corrects a typo in Binney & Merrifield (1998).

4.2.1 Alignment between the halo center and the BCG

In order to locate the center of the DM halo, we fit the lensing data with gNFW-based models in which the center of the halo was allowed to vary from that of the BCG, taking a Gaussian prior with $\sigma = 3''$ along each axis. Since we are concerned only with an astrometric measurement, we adopted a lower $\sigma_{\rm pos} = 0\farcs3$ for these fits only. The inferred offsets between the centers of the halos and BCGs are given in Table 3.1. They are typically $\simeq$ 1–4 kpc with a 1σ uncertainty of $\simeq$ 1–3 kpc, roughly consistent with the typical offset between the BCG and X-ray centroid. Given that the offsets are small and often not significant, we have fixed the center of the halo to that of the BCG in the following analysis. This allows for a consistent lensing and dynamical analysis. We note also that the P.A. of the DM halo is close to the BCG light in all cases, never differing by more than 14° in projection. (Given that BCGs often exhibit $\simeq 15°$ gradients in P.A., such small differences are not completely well defined.)

The one exception to the above is A2390. While its lensing and kinematic data can be well fit when the halo center is fixed to the BCG, the resulting models demand an unusually high $\Upsilon_{*\rm V}$ ($\log \alpha_{\rm IMF} > 0.42$ at 95% confidence). Given the possible complexities in the mass distribution in A2390 described in Section 3.1, we considered it prudent to increase the freedom in this model and allow the center of the halo to vary slightly from the BCG. We took a Gaussian prior having $\sigma = 1\farcs5$, based on the lensing analysis described above. The positional uncertainty $\sigma_{\rm pos}$ was also relaxed to $1\farcs0$. (Nonetheless, the best-fitting models still reproduce the image positions with a fidelity of $0\farcs5$.)

4.3 Estimating and modeling line-of-sight ellipticity

4.3.1 The role of line-of-sight geometry in coupling lensing and dynamics

Strong lensing constrains the *projected* ellipticity of the mass distribution (parameterized by the pseudoellipticity ϵ) very precisely, but it provides no information about the geometry of the cluster mass distribution along the l.o.s. Stellar dynamics, on the other hand, respond to the 3D gravitational potential. Therefore, if the goal is to couple lensing and stellar dynamics to determine the density profile, the l.o.s. geometry can have an important impact. For example, if the mass is very elongated along the l.o.s. (a "cigar" pointed at the observer), then qualitatively we expect that some of the mass that contributes to the lensing will be outside the orbits of the stars in the BCG, and therefore have no effect on their dynamics.

We can investigate the effect of l.o.s. ellipticity using a simple model in which the DM density is stratified on ellipsoids with coordinates

$$r_{\epsilon,\rm DM}(x,y,z) = \sqrt{(1-\epsilon_\Sigma)x^2 + (1+\epsilon_\Sigma)y^2 + (z/q_{\rm DM})^2}. \tag{4.16}$$

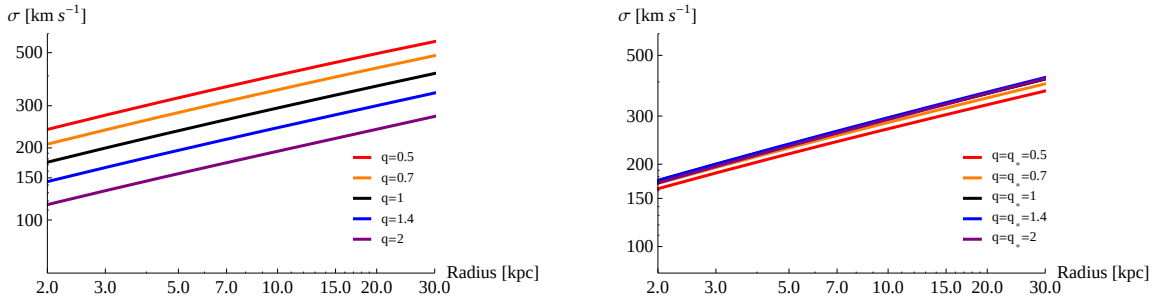

Figure 4.1: Left: Projected velocity dispersion $\sigma_{\rm los}$ for a fiducial mass distribution consisting of an NFW halo with $c = 4$ and $M_{200} = 8 \times 10^{14}\,{\rm M}_\odot$, along with massless stellar tracers distributed as a Jaffe (1983) profile with a projected half-light radius $R_e = 30$ kpc. The different curves show how $\sigma_{\rm los}$ changes significantly as the l.o.s. ellipticity q of the massive halo varies, while the geometry of the stellar tracers remains spherical ($q_* = 1$). **Right:** Same as the left panel, but the l.o.s. ellipticity of the tracers is fixed to that the of the massive halo ($q = q_*$). The observed $\sigma_{\rm los}$ remains nearly constant.

Here the z axis is taken to be the l.o.s.; therefore, ϵ_Σ and q parametrize the ellipticity in the plane of the sky and along the l.o.s., respectively. In the following discussion we take $\epsilon_\Sigma = 0$ to isolate the effect of the l.o.s. geometry. Therefore, the geometry of the mass distribution is axisymmetric, and the symmetry axis is the l.o.s. Note that $q_{\rm DM} > 1$ and < 1 correspond to prolate and oblate geometries, respectively. We define the DM density as

$$\rho_{\rm DM}(R, z) = \frac{1}{q_{\rm DM}} \rho^{\rm sph}_{\rm DM}(r_{\epsilon,{\rm DM}}(R, z)), \tag{4.17}$$

where $\rho^{\rm sph}_{\rm DM}(r)$ is a model for the radial density variation (e.g., Equation 4.1 for the gNFW profile). The prefactor $1/q_{\rm DM}$ ensures that the surface density is preserved as $q_{\rm DM}$ varies. Similarly, we can define a stellar density profile stratified on ellipsoids with coordinates given by Equation 4.16; however, since the l.o.s. geometry of the DM and stars in general may be distinct, we introduce q_* to refer to the l.o.s. ellipticity of the BCG stars.

In order to compute stellar kinematics, we consider solutions of the axisymmetric Jeans equation for which the distribution function can be written as $f(E, L_z)$ (the two-integral solutions). The equations below follow Gavazzi (2005) (see also Qian et al. 1995 and Chandrasekhar 1969). Since the observed velocity moments are entirely in the z-direction, the only relevant Jeans equation is

$$\frac{1}{\nu_*} \partial_z (\nu_* \overline{v_z^2}) = \partial_z \Phi, \tag{4.18}$$

where $\Phi(R, z)$ is the gravitational potential and ν_* is the luminosity density of the stellar tracers.

The force can be expressed as

$$\partial_z \Phi = -2\pi G q z \int_0^\infty \frac{du}{\Delta(u)(q^2+u)} \rho(U), \tag{4.19}$$

where $\Delta(u) = (1+u)\sqrt{q^2+u}$ and $U^2 = \frac{R^2}{1+u} + \frac{z^2}{q^2+u}$. In this subsection, we will assume for simplicity that the stellar tracers are massless, so that $\rho = \rho_{\rm DM}(R,z)$ and $q = q_{\rm DM}$. However, this is easily generalized to the more realistic case of massive tracers by computing the force $\partial_z \Phi$ for the stars and DM separately and summing the results. (This is done in the actual model of A383.) Finally, the observable luminosity-weighted l.o.s. velocity dispersion $\sigma_{\rm los}$ is computed as

$$\sigma^2_{\rm los}(R) = \frac{\int_{-\infty}^{\infty} dz \nu_*(R,z)\overline{v_z^2}}{\int_{-\infty}^{\infty} dz \nu_*(R,z)}. \tag{4.20}$$

We can now consider how the $\sigma_{\rm los}$ changes as we vary $q_{\rm DM}$ and q_*. Crucially, since the surface density is kept constant, *no lensing observables change* in this process. The left panel Figure 4.1 considers the variation in $\sigma_{\rm los}$ as $q_{\rm DM}$ ranges from $0.5 < q_{\rm DM} < 2$ and $q_* = 1$ (i.e., the stellar tracers are kept spherical). For concreteness, this figure adopts an NFW halo with parameters typical of massive clusters (see caption). Clearly, large effects on the observed $\sigma_{\rm los}$ are possible. Qualitatively, we expect that as the DM distribution is compressed along the l.o.s. ($q_{\rm DM} \ll 1$), more mass is moved within the fixed stellar orbits. The stellar velocities then increase, as the plot indeed indicates.

The right panel of Figure 4.1 illustrates the effect of varying the l.o.s. ellipticity of the mass and stellar tracers in step ($q_* = q_{\rm DM}$). In this case, there is very little effect on $\sigma_{\rm los}$ – less than a few percent. Qualitatively, as the mass and tracers are elongated along the l.o.s. ($q > 1$), two effects occur: the density decreases, which tends to lower σ, and the velocity anisotropy increases, which boosts $\sigma_{\rm los}$ (i.e., we are viewing stars along the major axis, where they move fastest). These effects nearly cancel. From this we conclude that when coupling lensing and dynamics, the most important l.o.s. effect is not the absolute ellipticity, but the relative ellipticities of the mass and stellar tracers.[4] Since the light of the BCG is almost always obseved to be extended in the same direction as the lensing-inferred mass in projection, we expect that $q_* = q_{\rm DM}$ may be a more realistic scenario. However, the stars may be more spherical than the DM distribution (e.g., $1 < q_* < q_{\rm DM}$), which would produce effects intermediate between the two extremes illustrated in Figure 4.1.

Table 4.2. NFW parameters derived from X-ray and lensing analyses

Cluster	X-ray			Lensing (Strong + weak)			
	r_s (kpc)	c_{200}	Source	r_s (kpc)	c_{200}	$\log M_{200}/\,\mathrm{M}_\odot$	r_{200} (kpc)
MS2137	180^{+20}_{-20}	$8.19^{+0.54}_{-0.56}$	S07	119^{+49}_{-32}	$11.03^{+2.81}_{-2.39}$	$14.56^{+0.13}_{-0.11}$	1318^{+140}_{-107}
A963	390^{+120}_{-80}	$4.73^{+0.84}_{-0.77}$	S07	197^{+48}_{-52}	$7.21^{+1.59}_{-0.94}$	$14.61^{+0.11}_{-0.15}$	1430^{+127}_{-151}
A383	470^{+130}_{-100}	$3.8^{0.7}_{-0.5}$	A08	260^{+59}_{-45}	$6.51^{+0.92}_{-0.81}$	$14.82^{+0.09}_{-0.08}$	1691^{+128}_{-102}
A383 (prolate)	...	...	...	372^{+63}_{-51}	$4.49^{+0.50}_{-0.48}$	14.80 ± 0.08	1665^{+107}_{-95}
A611	320^{+200}_{-100}	$5.39^{+1.60}_{-1.51}$	S07	317^{+57}_{-47}	$5.56^{+0.65}_{-0.60}$	14.92 ± 0.07	1760^{+97}_{-89}
A2537	370^{+310}_{-150}	$4.86^{+2.06}_{-1.62}$	S07	442^{+46}_{-44}	$4.63^{+0.35}_{-0.30}$	15.12 ± 0.04	2050^{+65}_{-69}
A2667	700^{+479}_{-207}	$3.02^{+0.74}_{-0.85}$	A03	725^{+118}_{-109}	$2.99^{+0.32}_{-0.27}$	15.16 ± 0.08	2164^{+137}_{-129}
A2390	757^{+1593}_{-393}	$3.20^{+1.59}_{-1.57}$	A03	763^{+119}_{-107}	$3.24^{+0.35}_{-0.31}$	$15.34^{+0.06}_{-0.07}$	2470^{+112}_{-123}

Note. — All X-ray fits are to the total gravitating mass and have been standardized to the same cosmology. Sources: S07 = Schmidt & Allen (2007), A08 = Allen et al. (2008), A03 = Allen et al. (2003). The A383 (prolate) row shows a fit to lensing and X-ray data using triaxial isodensity surfaces (Equation 4.16); we report sphericalized NFW parameters in this case.

4.3.2 Constraining the line-of-sight ellipticity through lensing and X-ray observations

These delicacies in coupling lensing and stellar kinematics arise because the two data sets span nearly disjoint radial intervals. By comparing 3D and projected mass probes with significant overlap in radius, we can turn around the discussion in Section 4.3.2 and use the observations to *constrain* the l.o.s. geometry by requiring that they trace the same underlying mass distribution. Lensing and X-ray data are eminently suitable for such a comparison.

Whereas lensing directly probes the gravitational potential projected along the l.o.s., the ICM follows the 3D potential. Mock observations of simulated clusters show that to a remarkable degree, X-ray observations are able to recover *spherically-averaged* mass profiles with a scatter of only $\simeq 5\% - 10\%$ arising from the viewing angle (Nagai et al. 2007; Lau et al. 2009; Meneghetti et al. 2010b; Rasia et al. 2012). This is true even when a spherical geometry is (incorrectly) imposed in the analysis. The same simulations show that X-ray masses are biased slightly low due to non-thermal pressure support, arising primarily from bulk gas motions. This bias is generally estimated to be only $\simeq 10\%$, although this depends on the detailed physics included in the simulations and may be somewhat higher (see Rasia et al. 2012). When much larger discrepancies between X-ray- and lensing-derived masses are encountered in relaxed clusters, they most likely arise from elongation or compression of the mass distribution along the l.o.s. Therefore, by comparing projected (lensing- or Sunyaev-Zel'dovich-based) and nearly spherical (X-ray) mass measures, the l.o.s. shape can be inferred (e.g., Piffaretti et al. 2003; Gavazzi 2005; de Filippis et al. 2005; Sereno et al. 2006; Morandi

[4]Gavazzi (2005) neglected the factor $1/q_{\rm DM}$ in Equation 4.17. Therefore, although they find large variations in the kinematic mass estimates as $q_* = q_{\rm DM}$ varies, this is largely because the total mass is actually varying with q.

et al. 2010, 2011; Newman et al. 2011; Morandi & Limousin 2012) assuming that the ICM is near equilibrium.

In order to compare our lensing results to X-ray analyses, we have compiled the results of several studies listed in Table 4.2. X-ray studies typically adopt a parametric form for either the density or temperature profiles, and these studies adopted an NFW profile to represent the total density. For a clean comparison, it is thus appropriate to restrict to NFW models for the dark halo when fitting the lensing data in this section. Further, since X-ray studies generally do not separately model the BCG, we include only the dark halo in the lensing mass measurements below; this has a minor effect outside the innermost bin. Figure 4.2 shows the ratio $M_{\rm lens}/M_{\rm X}$ of the spherically-enclosed mass $M_{\rm lens}$ derived from lensing by assuming a spherical deprojection, to the mass $M_{\rm X}$ based on X-ray analyses. The inner error bars in Figure 4.2 reflect the statistical uncertainty, which for the lensing mass is derived from the Markov chains. Estimating the uncertainty in the X-ray-based mass at a given radius cannot be done precisely with published NFW parameters, since the covariance is usually not given. We therefore estimated this using the full A383 mass profile provided by S. Allen (private communication), including properly propagated errors, rescaling the errors based on the X-ray flux and exposure time as appropriate for Poisson-dominated formal errors. This is sufficiently accurate for our purposes given that systematic uncertainties are comparable. The larger error bars in Figure 4.2 include an additional 10% systematic contribution added in quadrature that reflects uncertainties in the *Chandra* temperature calibration (Reese et al. 2010).

In general the agreement between the X-ray- and lensing-based masses assuming a spherical deprojection is very close, as Figure 4.2 and Table 4.2 demonstrate. A383 is clearly discrepant, with $M_{\rm lens} \gg M_{\rm X}$; as discussed in Section 4.3.3, this can be explained by a prolate halo that is elongated along the l.o.s. For the remaining six clusters, however, the mean trend

$$M_{\rm lens}/M_{\rm X} = (1.07 \pm 0.01) - (0.16 \pm 0.04) \log r/100 \text{ kpc} \tag{4.21}$$

(dashed in Figure 4.2; errors are random only) is consistent with unity within the systematic uncertainty of ≈ 0.1. None of these 6 clusters show systematic deviations larger than $|M_{\rm lens}/M_{\rm X} - 1| \gtrsim 0.2$ over scales of 50–600 kpc. At $r \sim 100$ kpc, where strong lensing fixes the mass, the spherically-deprojected mass $M_{\rm lens}$ scales roughly $\propto q^{0.6}$ for an NFW profile with the range of r_s encountered in our sample. (Here we follow the notation of Equation 4.16.) Therefore, the similarity of the X-ray and lensing measures implies that $|q - 1| \lesssim 0.3$ in these systems, with the mean l.o.s. ellipticity being smaller ($\langle q - 1 \rangle \approx 0.1 - 0.2$). The asphericity will be yet smaller if some of the elevation of $M_{\rm lens}/M_{\rm X}$ is not due to geometry but to non-thermal pressure in the ICM, which is expected.

Strong-lensing-selected clusters as an ensemble are sometimes thought to be biased toward clusters elongated along the l.o.s., since this orientation boosts the lensing cross-section. Given that

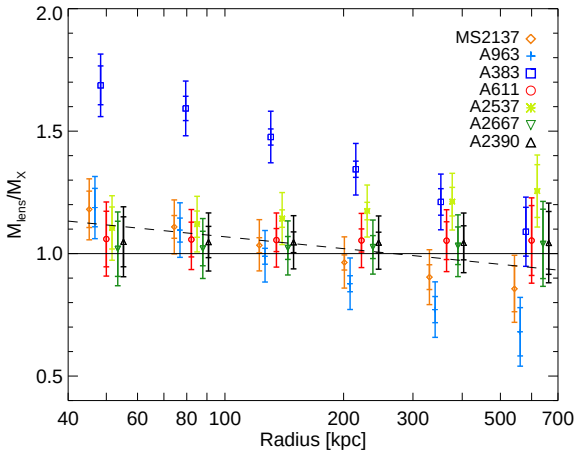

Figure 4.2: Spherically-enclosed masses $M_{\rm lens}$ derived from strong- and weak-lensing analyses, assuming a spherical deprojection, are compared to those derived from published X-ray studies, $M_{\rm X}$. The random and total (including a 10% systematic estimate) errors are reflected in the inner and outer error bars, respectively. Note that measurements at various radii are not independent, as they are derived from two-parameter NFW models. The dashed line indicates the mean trend excluding A383 (Equation 4.21).

l.o.s. elongation and non-thermal pressure support would both act to elevate $M_{\rm lens}/M_{\rm X}$, our results show that the clusters in our sample must be both close to hydrostatic equilibrium and not strongly elongated along the l.o.s. (excepting A383). We note that our sample consists of fairly massive clusters, and that an orientation bias may be stronger at lower masses. Since any compression or elongation along the l.o.s. is constrained to be both small and consistent with null within the systematic uncertainties, $q = 1$ is fixed for the remainder of our analysis in all clusters except A383, which is discussed individually below. In other words, the mean radius of an isodensity surface projected in the sky plane is taken as equal to that projected along the l.o.s. The effect on our results of varying q within the allowed limits is discussed in Section 5.5. The good agreement between lensing and X-ray masses further supports our contention that we have selected relaxed clusters (Section 3.1).

4.3.3 The case of A383: modeling line-of-sight ellipticity

Figure 4.2 indicates that A383 is significantly elongated along the l.o.s. This is unique in our sample and necessitates a special treatment for A383 in several ways, which we review in this section. First, in order to constrain $q_{\rm DM}$, we explicitly incorporate X-ray observations into the likelihood (Equation 4.5) via an additional term

$$\chi^2_{\rm X} = \sum_i \frac{(M^{{\rm X},i} - M^{{\rm model},i}/m_{\rm X})^2}{\sigma^2_{{\rm X},i}}, \tag{4.22}$$

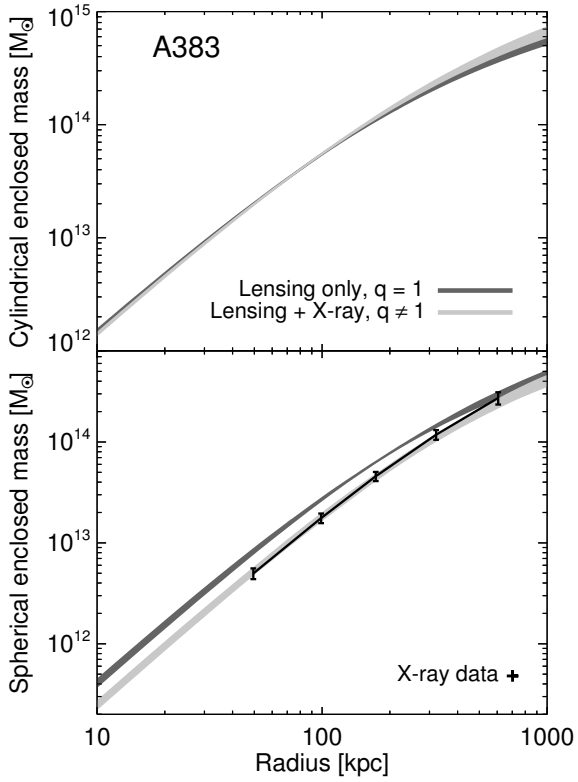

Figure 4.3: A383 DM mass profiles measured in cylinders (i.e., in projection; top panel) and in spheres (bottom). Dark curves show measurements derived from strong and weak lensing data only, assuming a spherical deprojection $q_{\rm DM} = 1$ and an NFW halo, while light curves show fits to the lensing and X-ray constraints jointly with a free $q_{\rm DM}$. X-ray constraints are indicated with error bars. Fitting the lensing and X-ray data simultaneously requires $q_{\rm DM} > 1$. The thickness of the curves indicates the 68% confidence interval.

where $M^{{\rm X},i}$ is the spherically-enclosed mass estimated from X-ray observations within a radius r_i, $\sigma_{{\rm X},i}$ is the uncertainty in this measurement, $M^{{\rm model},i}$ is the spherically-enclosed mass in the proposed model within r_i, and $m_{\rm X}$ is a calibration factor. We introduce $m_{\rm X}$ as a new parameter in the model with a Gaussian prior of 0.9 ± 0.1. The mean of 0.9 accounts for an expected $\simeq -10\%$ bias in X-ray–derived masses due to non-thermal pressure support (e.g., Nagai et al. 2007; Lau et al. 2009), while the scatter of 0.1 reflects both an estimate of the cluster-to-cluster scatter in the non-thermal fraction, as well as the uncertainty in the *Chandra* temperature calibration (Reese et al. 2010). The data are taken from the X-ray study of Allen et al. (2008). From their total mass profile of A383, we selected five points spaced uniformly in $\log r$ between 50 and 600 kpc to match the number of independent temperature measurements. (The results are not sensitive to the inner limit.) Finally, we added 10% in quadrature to the uncertainty in each data point to allow for systematic errors with a radial dependence (e.g., gradients in the non-thermal pressure).

Figure 4.3 compares the DM mass profiles obtained from the lensing data only, fixing $q_{\rm DM} = 1$,

with those obtained from a joint lensing and X-ray fit in which $q_{\rm DM}$ is allowed to vary. The top panel shows the surface density profile. As expected, the projected mass is invariant with $q_{\rm DM}$, and the lensing data are matched equally well in the two fits. The bottom panel, however, shows that simultaneously matching the X-ray data requires $q_{\rm DM} = 1.88 \pm 0.23$, i.e., a DM halo elongated along the l.o.s. by nearly a factor of two.

This demonstrates that the combination of lensing and X-ray data (i.e., projected and spherical mass measures) can constrain the l.o.s. shape of the DM halo on $\gtrsim 50$ kpc scales, modulo uncertainties in the degree of non-thermal pressure support; in the case of A383, the latter are much smaller than the observed effect that we ascribe to simple geometry. In order to incorporate these constraints into our dynamical modeling, we use the axisymmetric two-integral kinematic models described in Section 4.3.1, which is the second key difference in our treatment of A383. These generalize the spherical dynamical models that are adequate for the remainder of the sample (Section 4.3.2). Since A383 is nearly circular in projection, any major asphericity must be nearly along the l.o.s. Therefore, an axisymmetric model with the symmetry axis aligned with the l.o.s. should be a good approximation to the true mass distribution. Indeed, our observations imply DM axis ratios of $x : y : z \simeq 1 : 1.1 : 1.9$.

In addition to q, computing stellar dynamics requires an estimate of q_*, which is not constrained by X-ray and lensing data. It is unlikely that $q_* = q_{\rm DM}$; rather, we can expect that $1 < q_* < q_{\rm DM}$ for several reasons. Simulated DM halos are much more flattened ($\langle c/a \rangle \simeq 0.5$; Jing & Suto 2002) than stars in elliptical galaxies ($\langle c/a \rangle \simeq 0.7$; Tremblay & Merritt 1995). Consistent with this observation, no BCG in our sample has a projected axis ratio flatter than 0.7, whereas the A383 DM halo has $1/q_{\rm DM} \simeq 0.54$. On the other hand, $q_* \lesssim 1$ is also unlikely, given that, in our sample, the BCG light is always elongated along the direction of the halo in projection.

Therefore, a more informative approach is to place a prior on q_* based on statistical studies of the intrinsic axis ratios of elliptical galaxies. We use a fit to the distribution inferred by Tremblay & Merritt (1995) based on a prolate population, which peaks at $q_* \simeq 1.3$. Figure 4.4 illustrates the effect of the l.o.s. ellipticities $q_{\rm DM}$ and q_* on a key parameter of interest, the inner DM slope β in the gNFW models. The left panel shows how the mean inferred β varies in joint fits to the strong and weak lensing, stellar kinematic, and X-ray data, while the right panel shows the joint posterior probability density. (Since q_* is nearly unconstrained by the data, the marginalized distribution for q_* is nearly identical to the Tremblay & Merritt (1995) prior.)

As anticipated in Section 4.3.1, the primary dependence of β is on the ratio $q_*/q_{\rm DM}$ (constant along dotted lines in the left panel). However, the effect is relatively small within the range allowed by the data, with $|\Delta\beta| \simeq 0.1$. Note that if we forced $q_* = q_{\rm DM} \simeq 1.9$, the inferred β would become yet shallower, while if we instead insisted that $q_* = 1$, the DM slope would steepen to $\beta \simeq 0.7$ – still shallower than a canonical NFW cusp with $\beta = 1$. While we have implicitly assumed an axis ratio for

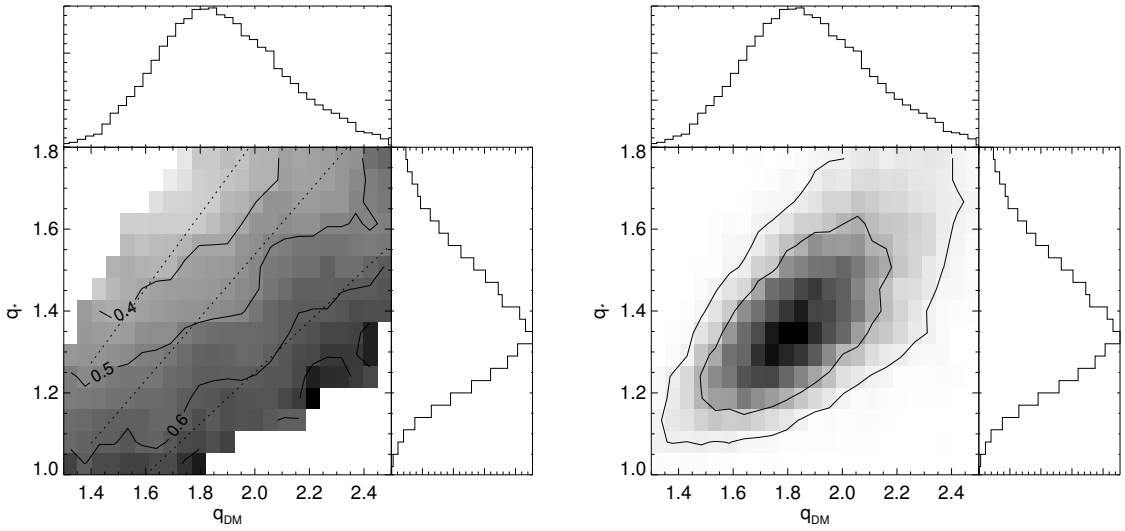

Figure 4.4: Left: The variation of the mean inferred DM inner slope β, marginalized over all other parameters, with the l.o.s. ellipticities of the dark and stellar mass distributions $q_{\rm DM}$ and q_*, as inferred in joint fits to strong and weak lensing, stellar kinematic, and X-ray data in A383. Colors and solid contours indicate $\langle\beta\rangle$, while dotted lines show regions of constant $q_*/q_{\rm DM}$. Histograms show the marginalized posterior probability densities of $q_{\rm DM}$ and q_*. **Right:** Joint posterior probability density for $q_{\rm DM}$ and q_*, with the 68% and 95% confidence regions indicated as solid lines. Histograms are the same as the left panel.

the DM isodensity surfaces that does not vary with radius, we expect that the DM distribution could be more spherical on the scales of the BCG than is measured at $r \gtrsim 50$ kpc through the combination of lensing and X-ray data, since isotropic dissipation processes in the baryon-dominated regime yield rounder mass distributions (e.g., Abadi et al. 2010). In that case, a rounder DM distribution at any value of q_* would require a smaller β to fit the data. In summary, $\beta < 1$ appears to be robust against the precise geometry of A383. In the following chapter we describe our results on the DM profiles of the entire sample.

4.3.4 Comparison to previous results

Morandi & Limousin (2012) also combined strong lensing and X-ray observations to measure the 3D geometry of the DM halo in A383. Although they used a more sophisticated model of the intracluster medium, the long-to-short axis ratio they infer ($c/a = 0.55 \pm 0.06$) agrees closely with our result ($1/q_{\rm DM} = 0.54 \pm 0.07$). Furthermore, they quantify the angle between the major axis and the l.o.s. to be 21 ± 10 deg, consistent with our assumption that the major axis is close to the l.o.s.

Gavazzi (2005) studied the mass distribution in MS2137 using strong and weak lensing and reported substantial differences between lensing- and X-ray-based mass models. They inferred that a significant elongation along the l.o.s. was a likely explanation, and suggested that this could be a

major source of bias in the work by Sand et al. (2004, 2008). In contrast, we do not find evidence for a strong l.o.s. elongation in this cluster. Our lensing results instead agree closely with a recent analysis by Donnarumma et al. (2009), and they are also consistent with X-ray measurements by Schmidt & Allen (2007). This is incompatible with the highly prolate shape ($q \approx 2$) suggested by Gavazzi (2005). The discrepancy likely arises from a numerical error in their results (R. Gavazzi, private communication).

Sand et al. (2002, 2004, 2008) discussed the possible effects of halo triaxiality on their measurements of the inner DM density slope. They concluded that it was a significant source of systematic uncertainty, although unlikely to completely account for the shallow slopes they inferred. To first order, the geometry of the mass distribution is significant because we compare projected (lensing) and 3D (stellar kinematic) data sets, which are coupled by the l.o.s. ellipticity. We have now quantified the l.o.s. geometry of the DM halos in our sample. In six of the seven clusters, we find no evidence for strong elongation or compression of the cluster along the l.o.s., based on a comparison between X-ray- and lensing-derived mass measures. In the exceptional case of A383, we are able to measure the l.o.s. elongation and account for this geometry in our modeling.

Chapter 5

Dark and Stellar Mass Profiles: Results and Interpretation

Having introduced the sources of data in our analysis and the mathematical framework for inferring mass models, we now present the results of this study and their physical interpretation. Section 5.1 assesses the quality of fit achieved by the models introduced in Chapter 4. We then turn to the mass distribution on small scales. Section 5.2 quantifies the slope of the *total* density profile over radii $r/r_{200} = 0.003$–0.03. In Section 5.3 we introduce a method to constrain the BCG stellar mass using information derived from the entire cluster sample. We then use this information to reduce the degeneracy between stellar and dark material in the cluster core and isolate the small-scale dark matter density profile in Section 5.4. Section 5.5 discusses the remaining sources of systematic uncertainty in our analysis, and Section 5.6 compares our results to earlier work. Finally, in Section 5.7 we compare our results to recent numerical simulations and present a physical interpretation. Section 5.8 summarizes our main findings.

5.1 Mass models and fit quality

The top panel of Figure 5.1 shows the total density profiles $\rho_{\rm tot}(r)$ that are inferred using gNFW (solid) and cNFW (dotted) models for the halo in each of the seven clusters in our sample, based on joint fits to the strong lensing, weak lensing, and stellar kinematic data outlined in Chapter 4.[1] The colored bars at the bottom of the panels illustrate the radial extent of each data set, which taken together provide coverage over most of the three decades in radius plotted. Correspondingly, the mass models are tightly constrained over the entire range. Furthermore, the density profiles derived using gNFW and cNFW models (Section 4.1) are virtually identical. This demonstrates that within the range well constrained by the data, the derived density profiles do not strongly depend on the particular parameterization of the halo.

[1] As discussed in Section 4.3.3, X-ray data are also incorporated in our A383 models to measure and account for its significant l.o.s. ellipticity, which is unique in our sample.

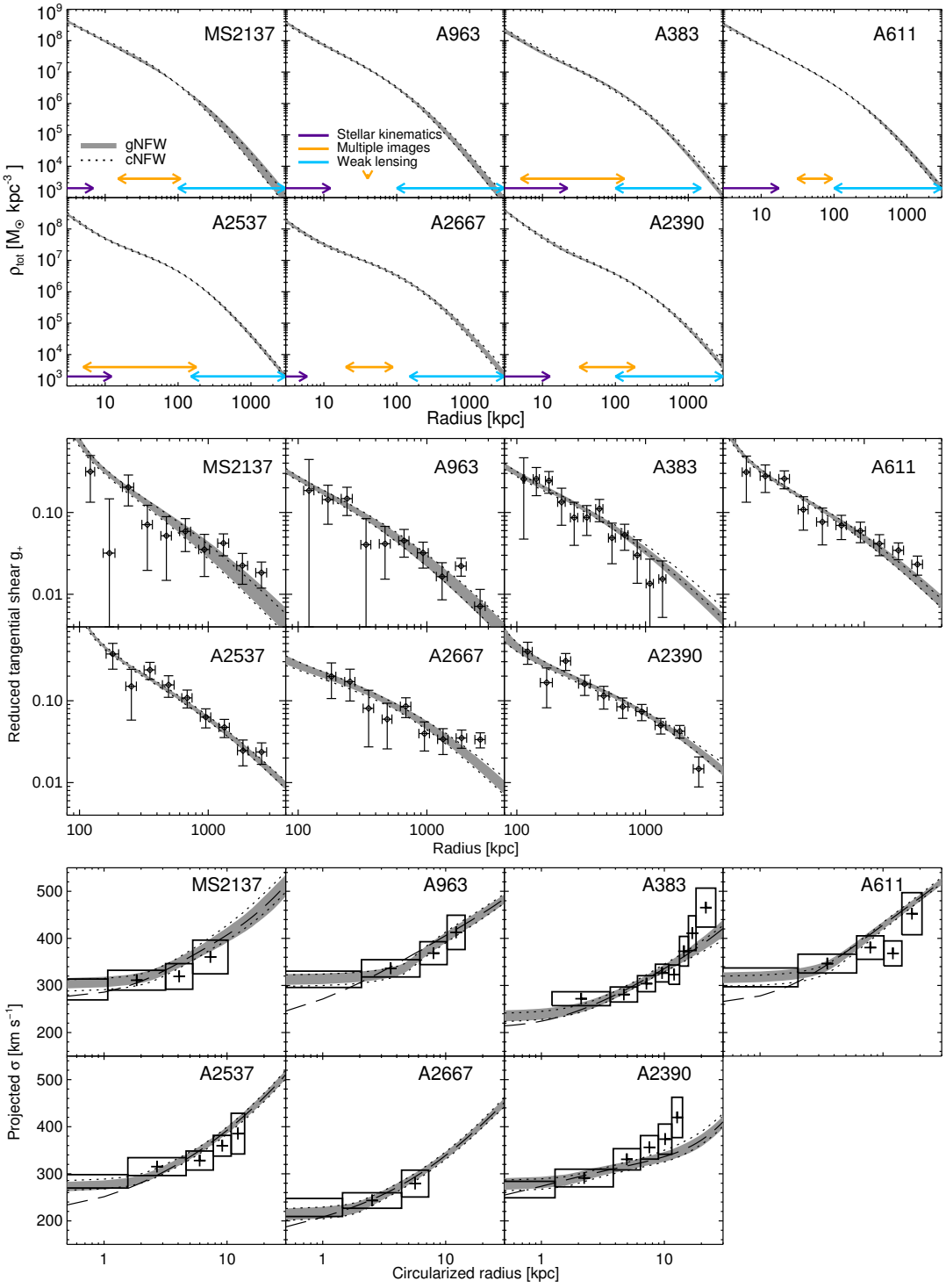

Figure 5.1: Total density (top), tangential reduced shear (middle), and velocity dispersion (bottom panel) profiles for fits to lensing and stellar kinematic data. In all panels the shaded region and dotted lines indicate the 68% confidence intervals for the gNFW and cNFW models, respectively. **Top:** The radial intervals spanned by each data set are indicated. **Middle:** The shear averaged in circular annuli is shown for display purposes, although elliptical models are used throughout the quantitative analysis. For A2667, the shear from the second clump is subtracted as described in the text. **Bottom:** Model dispersions (shaded and dotted) include the effects of seeing and the slit width; the dashed line shows the mean gNFW model excluding these effects. The extraction radii of the data have been circularized.

Given the simple parameterization of the mass distribution, it is important to verify that good fits are achieved to the wide range of data. The middle and bottom panels of Figure 5.1 demonstrate that, in all cases, a statistically acceptable fit to the weak lensing and stellar kinematic data is obtained. The quality of the strong-lensing fits is shown in Figure 3.11, in which the positions of the multiple images in the best-fitting model are indicated as crosses. The image positions are typically matched within $0\farcs5$, which is fairly typical of other studies using similar models (e.g., Richard et al. 2010). In some cases, the best models predict images that were not included as constraints because they could not be unambiguously identified (Section 3.3), particularly when buried in cluster galaxy light, but no predicted counterimages lack a plausible identification when one should be observable.

In A2667, the modeled shear arising from the second mass clump located at $R \simeq 1.4$ Mpc has been subtracted from the data points in Figure 5.1. Nevertheless, the measured shear exceeds the model at $R \gtrsim 2$ Mpc, which may indicate a more complex mass distribution near the virial radius. The fit quality at smaller radii and the close agreement with X-ray measurements reassure us that the mass is well modeled within $\simeq 2$ Mpc.

Table 5.1 quantifies the quality of fit for the various sources of data in each cluster. For the weak-lensing data, the noise is easily characterized, since it is dominated by random shape errors; thus, these data are fit with $\chi^2_{\rm WL}/N_{\rm WL} \simeq 1$. For the strong lensing and velocity dispersion data, the mean reduced $\langle \chi^2/N \rangle \simeq 0.6$. This indicates that the error bars may be conservatively overestimated by $\simeq 30\%$. However, the similarity of $\langle \chi^2/N \rangle$ indicates that the relative weighting of the kinematic and strong lensing data is appropriate. These data essentially set the density slope on small scales that we derive below. However, the weak lensing data are essential when comparing to simulations, since they constrain the scale and virial radii and thus characterize the radial span over which the inner slope is measured in terms of these key theoretical scales.

Considering the entire sample, we find no notable difference in the quality of the fit between the gNFW and cNFW models: $\Sigma(\chi^2_{\rm gNFW} - \chi^2_{\rm cNFW}) = 3.0$, while the total Bayesian evidence ratio $\Sigma(\ln E_{\rm gNFW}/E_{\rm cNFW}) = -3.5 \pm 3.1$. These indicate a slight preference for the cNFW models, but it is not very significant, as expected based on the similarity of the derived density profiles discussed above. In Section 5.3 we impose a more informative prior on Υ_*, using results derived from the whole sample, and find that the evidence ratio is close to unity. We conclude that the data do not clearly prefer one of our flexible DM halo models over the other. For this reason, we focus on the gNFW models in the following, unless otherwise stated.

5.2 The total inner density slope

The top panel of Figure 5.2 shows that the density profiles of these clusters are similar in their inner regions. At very small radii $\lesssim 0.003 r_{200} \approx 5$ kpc, the density profiles often steepen. As we describe

Table 5.1. Fit quality to strong lensing, weak lensing, and stellar kinematic data

	gNFW models				cNFW models				
Cluster	$\sigma_{\rm img}$	$\chi^2_{\rm SL}/N_{\rm SL}$	$\chi^2_{\rm WL}/N_{\rm WL}$	$\chi^2_{\rm VD}/N_{\rm VD}$	$\sigma_{\rm img}$	$\chi^2_{\rm SL}/N_{\rm SL}$	$\chi^2_{\rm WL}/N_{\rm WL}$	$\chi^2_{\rm VD}/N_{\rm VD}$	$\ln E_{\rm gNFW}/E_{\rm cNFW}$
MS2137	$0\farcs44$	8.6/16	13136.8/12670	1.6/4	$0\farcs43$	8.1/16	13137.2/12670	1.4/4	−2.2
A963	0	0/2	32092.5/31132	0.3/4	0	0/2	32092.5/31132	0.2/4	0.1
A383	$0\farcs46$	2.5/18	7070.4/6936	7.4/8	$0\farcs41$	2.0/18	7070.9/6936	7.4/8	0.7
A611	$0\farcs60$	17.1/18	14140.9/14252	8.9/5	$0\farcs58$	16.4/18	14141.5/14252	9.0/5	−2.1
A2537	$0\farcs65$	27.4/24	12812.3/12912	3.2/5	$0\farcs66$	28.0/24	12813.3/12912	2.4/5	0.2
A2667	$0\farcs29$	4.4/18	18734.3/18526	0.2/3	$0\farcs27$	3.7/18	18732.2/18526	0.2/3	−2.3
A2390	$0\farcs53$	3.7/16	16319.5/16186	3.9/6	$0\farcs60$	4.6/16	16319.9/16186	2.0/6	1.0

Note. — χ^2 for the best-fitting gNFW and cNFW models are shown, with degrees of freedom defined as follows: for weak lensing, $N_{\rm WL}$ is twice the number of background galaxies, corresponding to the two shear components; for velocity dispersion data, $N_{\rm VD}$ is the number of extracted spatial bins; for strong lensing $N_{\rm SL} = 2(N_{\rm img} - N_{\rm src})$, where $N_{\rm img}$ is the number of images and $N_{\rm src}$ is the number of distinct sources. Note that $\chi^2_{\rm SL}$, $N_{\rm SL}$, and $\sigma_{\rm pos} = 0\farcs5$ (the uncertainty in the image positions) are presented on a *per coordinate* basis, whereas following common practice, the rms error in the model image-plane positions $\sigma_{\rm img}$ refers to the total. Thus, $\chi^2_{\rm SL}/N_{\rm SL} \simeq 1$ when $\sigma_{\rm img} \simeq \sqrt{2}\sigma_{\rm pos}$. In A963 the single strong lensing constraint (Section 4.2) can be fitted exactly. In A383 X-ray data are also fit (Section 4.3.3), with $\chi^2_{\rm X}/N_{\rm X} = 5.8/5$ and $\chi^2_{\rm X}/N_{\rm X} = 4.1/5$ for the gNFW and cNFW models. The final column gives the natural logarithm of the Bayesian evidence ratio; the typical sampling error in this quantity, estimated from repeated MCMC runs, is 1.0.

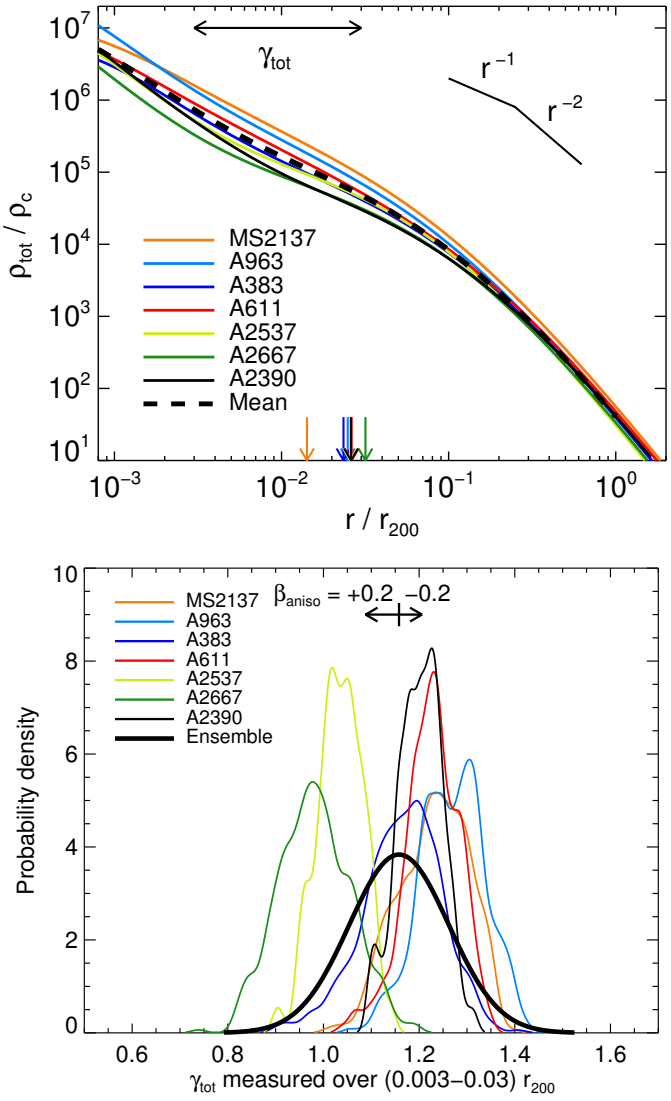

Figure 5.2: Top: Spherically averaged profiles of the *total* density, normalized by the virial radius r_{200} (Table 4.2) and the critical density $\rho_c(z_{\rm clus})$. Uncertainties are shown in Figure 5.1. The range over which the inner slope $\gamma_{\rm tot}$ is defined is shown at the top of the panel. Arrows at the bottom indicate the 3D half-light radii r_h of the BCGs. **Bottom:** Marginalized probability densities for the inner slope $\gamma_{\rm tot}$ of the *total* mass distribution, measured over $r/r_{200} = 0.003$–0.03. The thick curve shows the inferred parent Gaussian distribution, as described in the text. The top of the panel indicates the effects of introducing mild orbital anisotropy (Section 5.5).

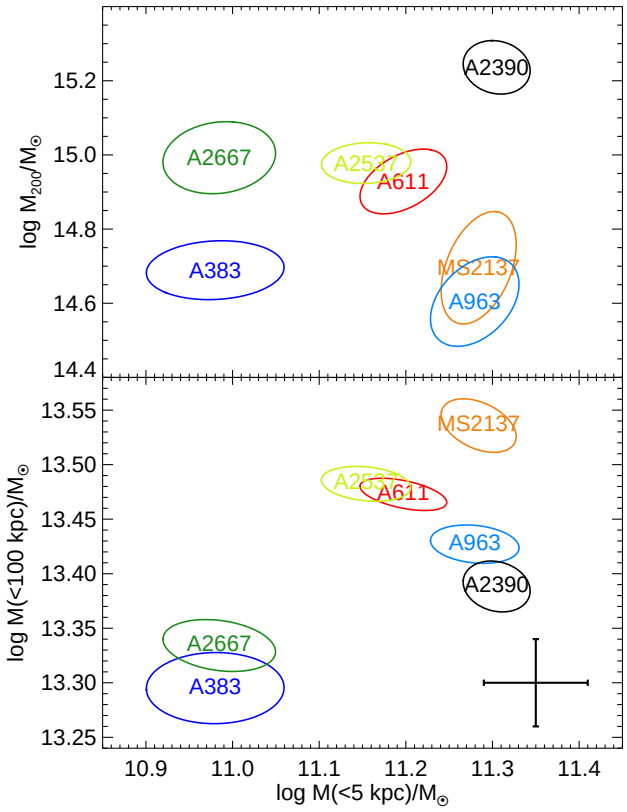

Figure 5.3: Comparison of mass contained within the central 5 kpc, comprising mostly stars, to that within the virial radius (top, showing no correlation) and within 100 kpc (bottom, showing a positive correlation), which are both dominated by DM. Error ellipses (1σ) indicate the formal model uncertainty. Error bars in the bottom panel estimate the systematic uncertainties due to orbital anisotropy (see Section 5.5) and projection effects (Section 4.3.2).

in Section 5.4.1, this is where the density becomes strongly dominated by stars. However, outside this innermost region the slopes of the total density profiles are quite comparable. To quantify this similarity, we introduce a measure of the *total* inner slope $\gamma_{\rm tot} = -d\log\rho_{\rm tot}/d\log r$. Since the BCG and the DM halo are modeled as distinct components, $\gamma_{\rm tot}$ is not a directly inferred parameter. We define it by fitting a line in the $\log r - \log\rho_{\rm tot}$ plane over the interval $r/r_{200} = 0.003$–0.03, illustrated at the top of the panel, with errors derived by repeating this for many models in the Markov chains.[2] For the median r_{200} in our sample (Table 4.2), the corresponding interval is 5–53 kpc, or typically ≈ 0.2–$2R_e$ in terms of the effective radius R_e of the BCG. The endpoints of this range are well constrained by stellar kinematics and strong lensing, and therefore $\gamma_{\rm tot}$ is observationally robust.

The bottom panel of Figure 5.2 shows the probability distributions of $\gamma_{\rm tot}$, which is tightly constrained for each cluster, with a typical formal 1σ uncertainty of 0.07. In order to characterize the mean inner slope and its scatter, we assume that the distribution of $\gamma_{\rm tot}$ in the parent population of massive, relaxed galaxy clusters is Gaussian. Following the formalism described by Bolton et al. (2012), we can the infer the mean $\langle\gamma_{\rm tot}\rangle$ and dispersion σ_γ of this parent distribution. Briefly, we compute the posterior probability density as

$$\begin{aligned} P(\langle\gamma_{\rm tot}\rangle, \sigma_\gamma | D) &= P(D|\langle\gamma_{\rm tot}\rangle, \sigma_\gamma) P(\langle\gamma_{\rm tot}\rangle, \sigma_\gamma) \\ &= \prod_i \int d\gamma'_{\rm tot} \frac{1}{\sqrt{2\pi}\sigma_\gamma} \exp\left[-\frac{1}{2}\left(\frac{\langle\gamma_{\rm tot}\rangle - \gamma'_{\rm tot}}{\sigma_\gamma}\right)^2\right] P_i(\gamma'_{\rm tot}), \end{aligned} \tag{5.1}$$

where $P_i(\gamma'_{\rm tot})$ refers to the posterior probability densities for $\gamma_{\rm tot}$ in cluster i (Figure 5.2) and the product runs over the seven clusters. We take a broad, uniform prior on $\langle\gamma_{\rm tot}\rangle$ and σ_γ. Obtaining marginalized probability densities for $\langle\gamma_{\rm tot}\rangle$ and σ_γ in this manner, we infer a mean $\langle\gamma_{\rm tot}\rangle = 1.16 \pm 0.05^{+0.05}_{-0.07}$ (errors are random and systematic, respectively, with the latter described below) and an intrinsic cluster-to-cluster scatter of $\sigma_\gamma = 0.10^{+0.06}_{-0.04}$. Interestingly, in Sections 5.4.1 and 5.7.2 we compare this slope to numerical simulations and show that the measured *total* density slope is very close to that seen in high-resolution *CDM-only* simulations, with fairly small scatter. This is one of our main findings, and we return to its physical interpretation in Section 5.7.

A conservative approach is to view the intrinsic scatter in the inner slope σ_γ as an upper limit: $\sigma_\gamma < 0.13$ (68% CL). This is because systematic errors may contribute additional scatter in the measurements (Section 5.5) beyond that reflected in the formal errors, which would imply that the true physical scatter is smaller. We note that these results are not very sensitive to the precise radial interval over which the slope is measured; taking $r/r_{200} = 0.005$–0.03 or 0.003–0.05, for example, only shifts $\langle\gamma_{\rm tot}\rangle$ within its 1σ uncertainty.

Figure 5.3 illustrates the uniformity of the inner mass distribution via a different metric, demonstrating a connection between the mass on very small scales of 5 kpc and the mass of the cluster

[2]Grid points are logarithmically spaced and equally weighted.

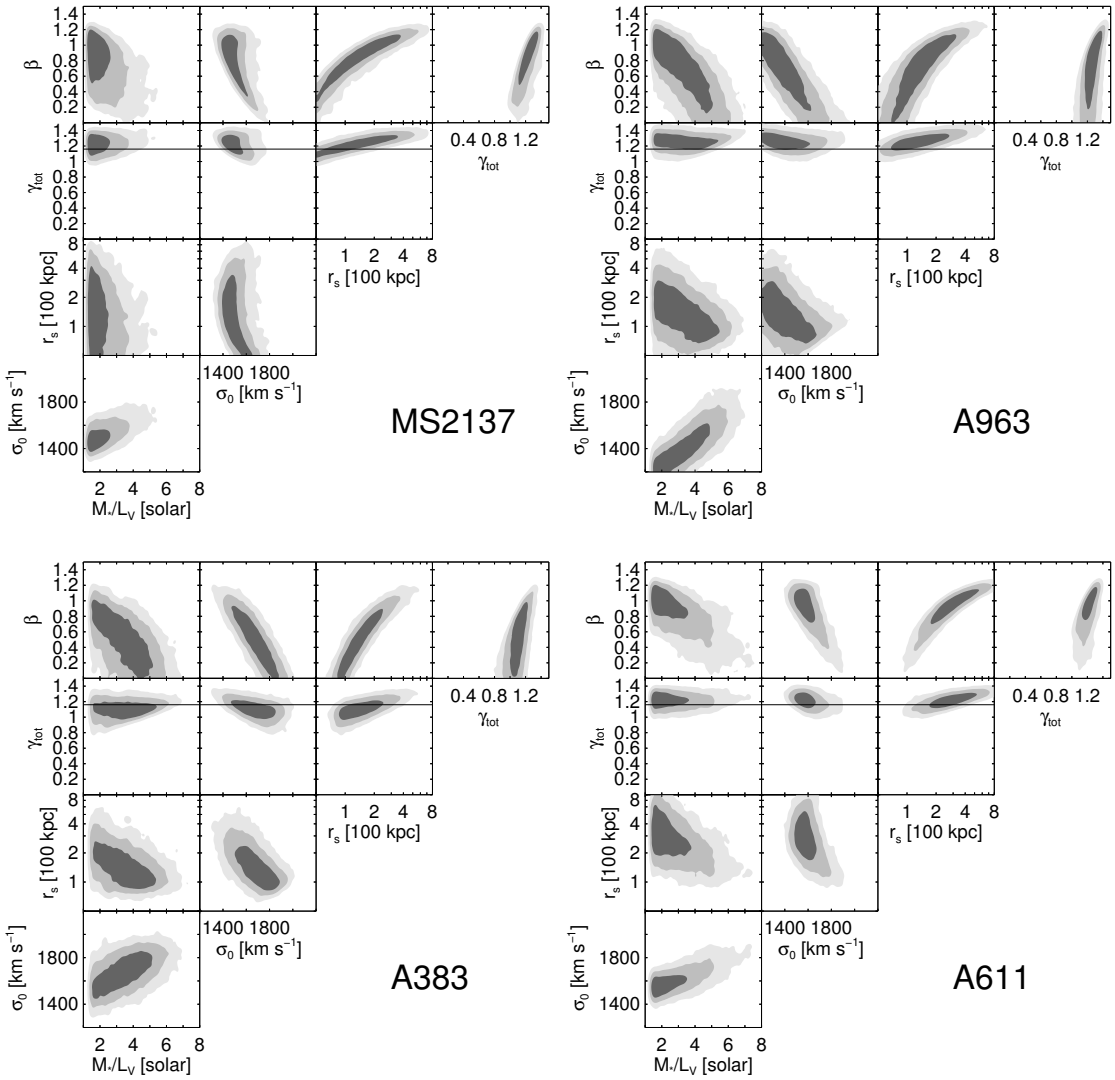

Figure 5.4: Degeneracies among key parameters describing the radial density profiles for gNFW-based fits. Contours indicate the 68%, 95%, and 99.5% confidence regions. Note that $\gamma_{\rm tot}$ is derived from the other parameters and is not independent. The horizontal line indicates the mean $\gamma_{\rm tot}$ among the whole sample. (Continued)

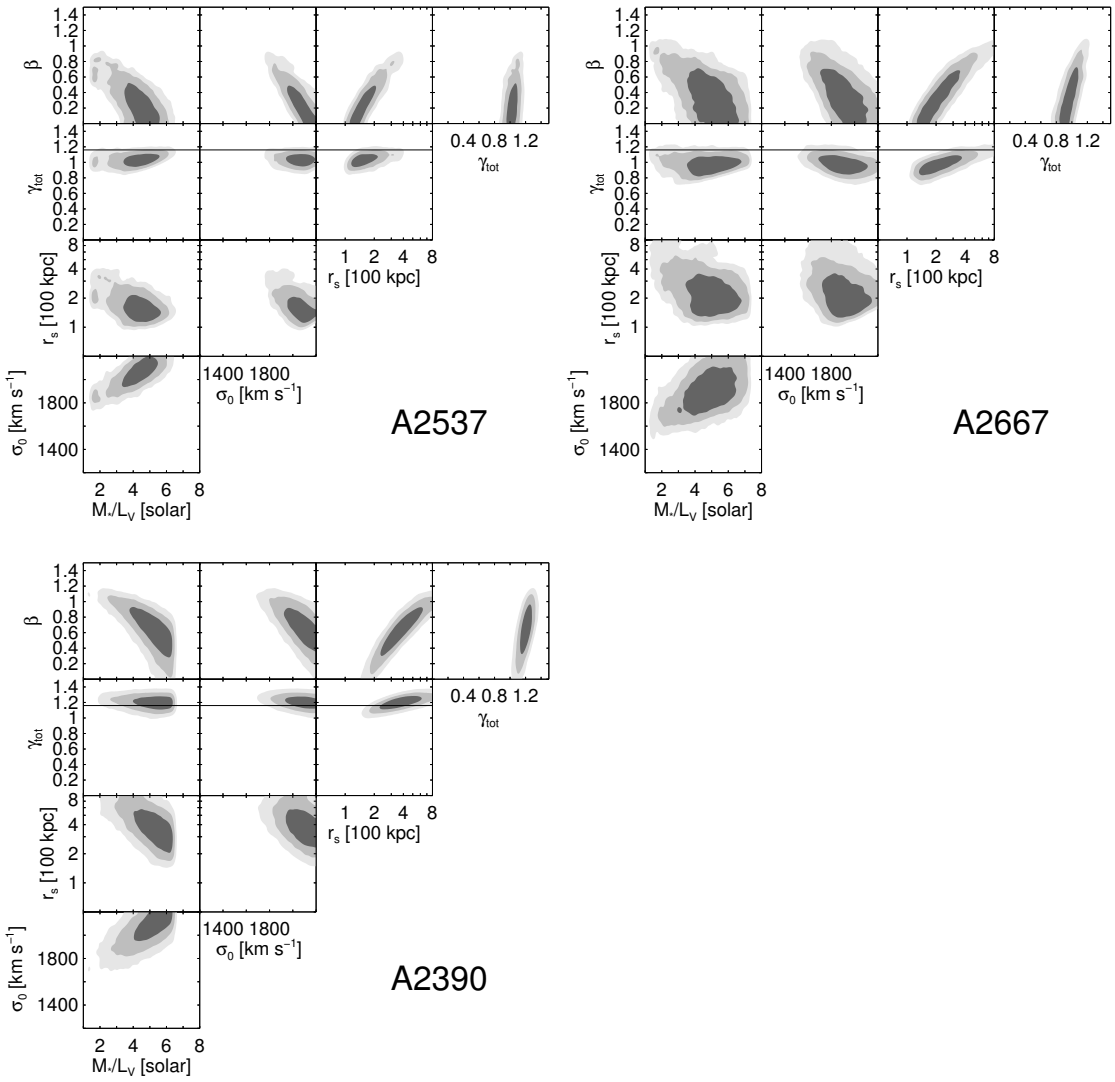

Figure 5.4: Continued

core within 100 kpc. In Section 5.4.1 we show that stars typically compose 75% of the mass within 5 kpc, whereas the mass on 100 kpc scales is almost entirely DM. Despite this and the small range in these masses within our sample – each roughly a factor of two – we detect a probable correlation (Pearson correlation coefficient $r = 0.70$, two-sided $P = 0.08$). The top panel of the figure shows that, in contrast, there is no correlation when the virial mass of the cluster is considered instead. As we discuss further in Section 5.7, this can be understood if the innermost regions of the present BCG and cluster halo were in place at early times and changed little in mass subsequently, with accretion mostly adding mass to the outer regions to grow the BCG and the cluster halo.

The key degeneracies among the parameters relevant to the radial density profile (β, r_s, σ_0 for the DM halo and M_*/L_V for the BCG) are illustrated in Figure 5.4. The best-constrained parameter is $\gamma_{\rm tot}$, which is easily understood based on two physical reasons: first, $\gamma_{\rm tot}$ refers to a slope measured over a fixed radial interval, unlike the inner gNFW slope β which is approached only asymptotically; second, measuring the total density profile requires no separation of the dark and luminous components. Clearly, measurements of the inner DM slope β could be improved using additional information on M_*/L_V beyond that which can be inferred on a cluster-by-cluster basis. This is the subject of the following section.

5.3 Separating luminous and dark mass: The role of the stellar mass-to-light ratio

In individual clusters there is a degeneracy between the stellar mass-to-light ratio $\Upsilon_{*\rm V} = M_*/L_{\rm V}$ and the inner DM slope, which is illustrated in Figure 5.5. This degeneracy is expected, since stellar mass in the BCG can be traded against DM. However, the model degeneracy is not complete, and each cluster does carry information on both Υ_* and β or b. Two aspects of the models and data form the essential reason for this. First, the most important physical assumptions are that stellar mass follows light and that the DM halo is adequately described by a gNFW- or cNFW-like profile. The precise parametric form is not as critical as the assumption that the DM density turns over smoothly at small radii – either to a power-law cusp in the gNFW case, or to a constant density in the cNFW models – without a sharp upturn on small scales. This is reasonable: by design these profiles describe pure CDM halos in the appropriate limits, and although the effects of adding baryons are uncertain, adiabatic contraction prescriptions (Gnedin et al. 2004, 2011) predict DM profiles that are well fit by gNFW models over the relevant range of radii when applied to halos and BCGs representative of our sample. Second, even under these model assumptions, it is impossible to constrain the dark and stellar mass profiles separately without a high density of observational mass probes than span the stellar- to DM-dominated regimes. Owing to the multiplicity of observations we have presented (extended stellar kinematic profiles, strongly-lensed galaxies usually at multiple

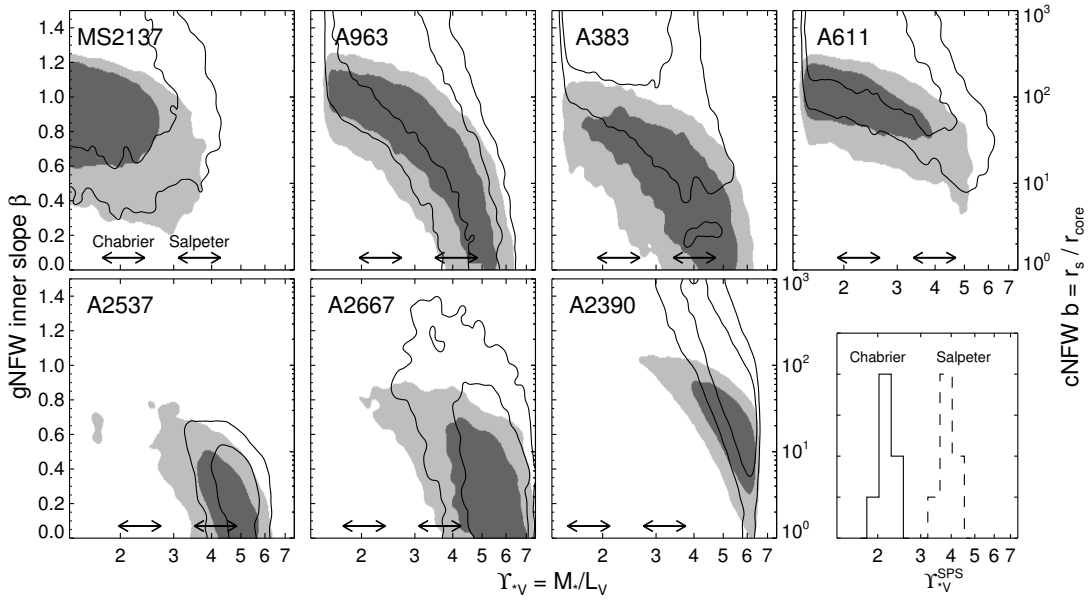

Figure 5.5: Degeneracy between $\Upsilon_{*\mathrm{V}}$ and the DM inner density profile when the halo is parameterized with a gNFW (left axis, filled contours) or cNFW (right axis, lines) model. The 68% and 95% confidence regions are shown. Arrows at the bottom of each panel show estimates $\Upsilon_{*\mathrm{V}}^{\mathrm{SPS}}$ derived from SPS fits to the broadband colors of the BCGs, spanning the 68% confidence interval, when adopting Chabrier and Salpeter IMFs; the distribution of these is shown in the bottom right panel. The permitted range in $\Upsilon_{*\mathrm{V}}$ is set proportionally to $\Upsilon_{*\mathrm{V}}^{\mathrm{SPS}}$ and therefore varies slightly from cluster to cluster (see Section 4.1).

redshifts, weak lensing), we are able to consider quite general families of DM halos in each cluster.

It is already evident in Figure 5.5 that most of the clusters in our sample prefer a DM inner slope that is shallower than an NFW profile (i.e., $\beta < 1$), consistent with our previous findings (Sand et al. 2002, 2004, 2008; Newman et al. 2009, 2011). However, it is also clear that the precision of the constraints on the inner slope could be increased if additional information regarding Υ_* is available. Indeed, most clusters are consistent with a wide range of Υ_* when viewed in isolation, due to the uncertainty arising from the degeneracy described above. Furthermore, the figure suggests a possible variation from cluster to cluster in the DM inner slope, but this conclusion may be contingent upon substantial variations in Υ_* as well. We do not have strong a priori expectations about the possible variation from cluster to cluster in the DM inner slope, particularly recalling the uncertain role of baryons in theoretical predictions. There are, however, several strong reasons to believe that the true physical variation in Υ_* within our sample is small.

First, Figure 5.5 shows estimates of the stellar mass-to-light ratio $\Upsilon_{*\mathrm{V}}^{\mathrm{SPS}}$ derived by fitting SPS models to the broadband colors of the BCGs (Section 5.2). Currently, SPS models cannot predict absolute masses more accurately than to a factor of $\simeq 2$, primarily due to the unknown stellar initial mass function (IMF), which we discuss further in Section 5.6.1. On the other hand, *relative* stellar masses are more robust, especially within a homogeneous galaxy population. As the bottom right

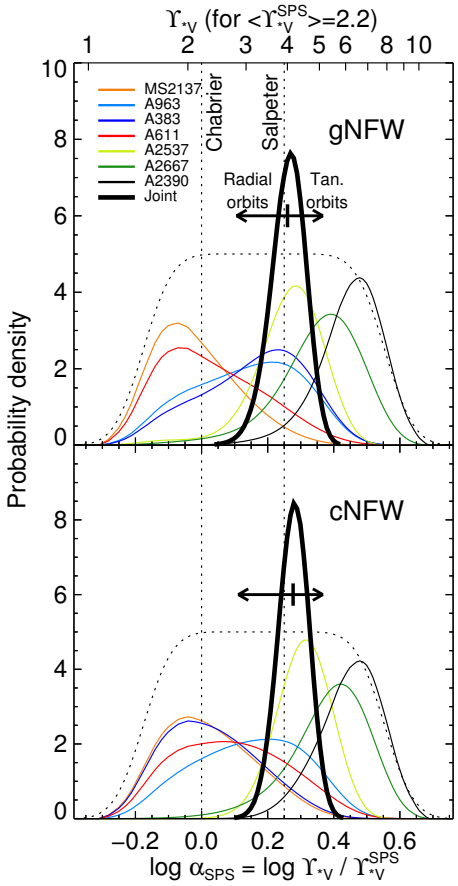

Figure 5.6: Probability densities for $\log \alpha_{\rm SPS}$, which parameterizes the stellar mass-to-light ratio $\Upsilon_{*\rm V}$ relative to SPS models (Equation 5.2), are shown for each cluster (thin lines) and jointly for the entire sample (thick). The dotted curve shows the effective prior, composed of the flat prior on $\log \Upsilon_{*\rm V}$ convolved with a Gaussian uncertainty on $\Upsilon_{*\rm V}^{\rm SPS}$ of $\sigma_{\rm SPS} = 0.07$ dex. Arrows indicate the effect of adopting mildly anisotropic orbits with $\beta_{\rm aniso} = \pm 0.2$.

panel of Figure 5.5 demonstrates, the range in $\Upsilon_{*\mathrm{V}}^{\mathrm{SPS}}$ within our sample at a fixed IMF is small. Assuming a Chabrier (2003) IMF, the median $\langle\Upsilon_{*\mathrm{V}}^{\mathrm{SPS}}\rangle = 2.2$; the full range is only 1.80–2.32, and the rms scatter is 9%.[3]

Second, the rms dispersion in the absolute luminosities L_{V} of the BCGs in our sample is only 0.1 dex. This small variation is consistent with previous studies of BCGs as "standard candles" with uniform luminosities and colors (e.g., Sandage 1972; Postman & Lauer 1995; Collins & Mann 1998; Bernardi et al. 2007). Finally, the environments of the BCGs are the same: by construction they are all central galaxies in massive clusters, and their central velocity dispersions are comparable. It would be very surprising if this uniformity in luminosity and $\Upsilon_{*\mathrm{V}}^{\mathrm{SPS}}$, which are thought to derive from a similar assembly history, were the result of a conspiracy that masks larger variations in stellar mass. Instead, based on these physical similarities, it is very likely that the BCGs in our sample have similar stellar masses and $\Upsilon_{*\mathrm{V}}$. As we discuss in Section 5.6.1, this is further supported by recent, independent studies.

With the well motivated assumption that the BCGs in our sample have a similar $\Upsilon_{*\mathrm{V}}$, we can use the full sample of seven clusters to *jointly* constrain its value, thereby improving the precision and robustness of our measurements of the DM profile. Before embarking on this, we consider how to handle the small variations in $\Upsilon_{*\mathrm{V}}$ that we do anticipate, despite the overall similarity. The sample spans a redshift range $z = 0.19 - 0.31$, so some mild passive evolution is expected. Additionally, the BCGs with the lowest $\Upsilon_{*\mathrm{V}}^{\mathrm{SPS}}$ estimates show optical emission lines and far-infrared photometry indicative of ongoing star formation (although it involves a small fraction of the stellar mass; see Section 3.4.2). These BCGs reside in the cool core clusters, consistent with earlier studies (Bildfell et al. 2008; Loubser et al. 2009; Sanderson et al. 2009).

Therefore, a more precise technique is to define Υ_* for each cluster *relative to the SPS measurement*:

$$\log \alpha_{\mathrm{SPS}} = \log \Upsilon_{*\mathrm{V}} / \Upsilon_{*\mathrm{V}}^{\mathrm{SPS}}. \tag{5.2}$$

We can then use the full cluster sample to constrain $\langle \log \alpha_{\mathrm{SPS}} \rangle$, which parameterizes a common, systematic offset from photometrically-derived stellar mass-to-light ratios. As described in Section 5.6.1, the most probable source for large systematic offsets is an IMF that differs from that assumed in the SPS models: in this case, that of Chabrier. However, our analysis does *not* depend on the physical origin of the offset, only that is it common among our BCGs. Since the variation in $\Upsilon_{*\mathrm{V}}^{\mathrm{SPS}}$ is small compared to the range of $\Upsilon_{*\mathrm{V}}$ explored in our fits (25% versus a factor of 5.3), this approach is not radically different from assuming a common $\Upsilon_{*\mathrm{V}}$. However, it improves on that assumption by making use of SPS models to adjust for small differences in $\Upsilon_{*\mathrm{V}}$ arising from age and

[3]Throughout, L_{V} and $\Upsilon_{*\mathrm{V}}$ refer to the observed luminosity, including any internal reddening from dust within the BCG. If we removed the reddening to obtain the intrinsic L_{V} and $\Upsilon_{*\mathrm{V}}$ of the stellar populations, their scatter would increase. (Reddening is indicated only in cool core clusters hosting some current star formation.) However, the SPS *stellar mass* estimates, which are significant for our analysis, are much more robust.

dust, while making no assumption on the validity of their absolute mass scale.

Figure 5.6 shows the probability distribution for $\log \alpha_{\rm SPS}$ derived in each cluster. The uncertainty in $\log \alpha_{\rm SPS}$ arises from two sources: that in the $\Upsilon_{*\rm V}$ derived from dynamics and lensing, and the uncertainty in $\Upsilon_{*\rm V}^{\rm SPS}$ arising from random photometric errors. In Section 3.4.2 we estimated the latter as $\sigma_{\rm SPS} = 0.07$ dex. Thus, the probability distributions for $\log \alpha_{\rm SPS}$ are derived by broadening those for $\log \Upsilon_{*\rm V}$ by a Gaussian distribution with a dispersion of $\sigma_{\rm SPS}$.

We have argued that there are strong a priori reasons to expect that $\alpha_{\rm SPS}$ is uniform across our sample of BCGs. Using the probability distributions in Figure 5.6, we can ask whether the lensing and kinematic data are indeed consistent with this assumption. One way to quantify this is to suppose that the true distribution of $\log \alpha_{\rm SPS}$ is Gaussian and infer its intrinsic dispersion $\sigma_{\log \alpha}$, as in Section 5.2. The preference for non-zero intrinsic scatter can then be assessed by

$$\Delta P = \sqrt{2 \ln[P(\sigma_{\log \alpha} = \sigma_{\rm peak})/P(\sigma_{\log \alpha} = 0)]}, \tag{5.3}$$

where $\sigma_{\rm peak}$ is the location of the maximum of $P(\sigma_{\log \alpha})$. For a Gaussian distribution, ΔP is the number of standard deviations from the mean. We find $\Delta P = 0.85$, i.e., a $< 1\sigma$ preference for intrinsic scatter. Thus, the lensing and kinematic data are consistent with (although they alone cannot prove) our assumption that there is little intrinsic variation in $\alpha_{\rm SPS}$ within our sample.

With the physically motivated assumption that $\alpha_{\rm SPS}$ is the same for each BCG, we can constrain its common value simply by multiplying the seven independent probability distributions. The results are shown by the thick curves in Figure 5.6. Very similar values of $\log \alpha_{\rm SPS} = 0.28 \pm 0.05$ and 0.26 ± 0.05 are derived using the gNFW and cNFW models, respectively, demonstrating that these results do not strongly depend on the exact halo model. Given the closeness of these results, in the following analysis we adopt $\log \alpha_{\rm SPS} = 0.27 \pm 0.05$. Despite marginalizing over fairly general parameterizations of the DM profile, we are able to obtain informative results due to the high density of observational constraints and the sample size.

Taking the median $\langle \Upsilon_{*\rm V}^{\rm SPS} \rangle = 2.2$, we find that $\log \alpha_{\rm SPS} = 0.27$ corresponds to $\Upsilon_{*\rm V} = 4.1$. In Section 5.5 we describe sources of systematic uncertainty leading to a final estimate $\log \alpha_{\rm SPS} = 0.27 \pm 0.05^{+0.10}_{-0.16}$. In Section 5.6.1, we discuss the physical implications of this result and compare to the recent literature on the stellar mass-to-light ratio and IMF in early-type galaxies.

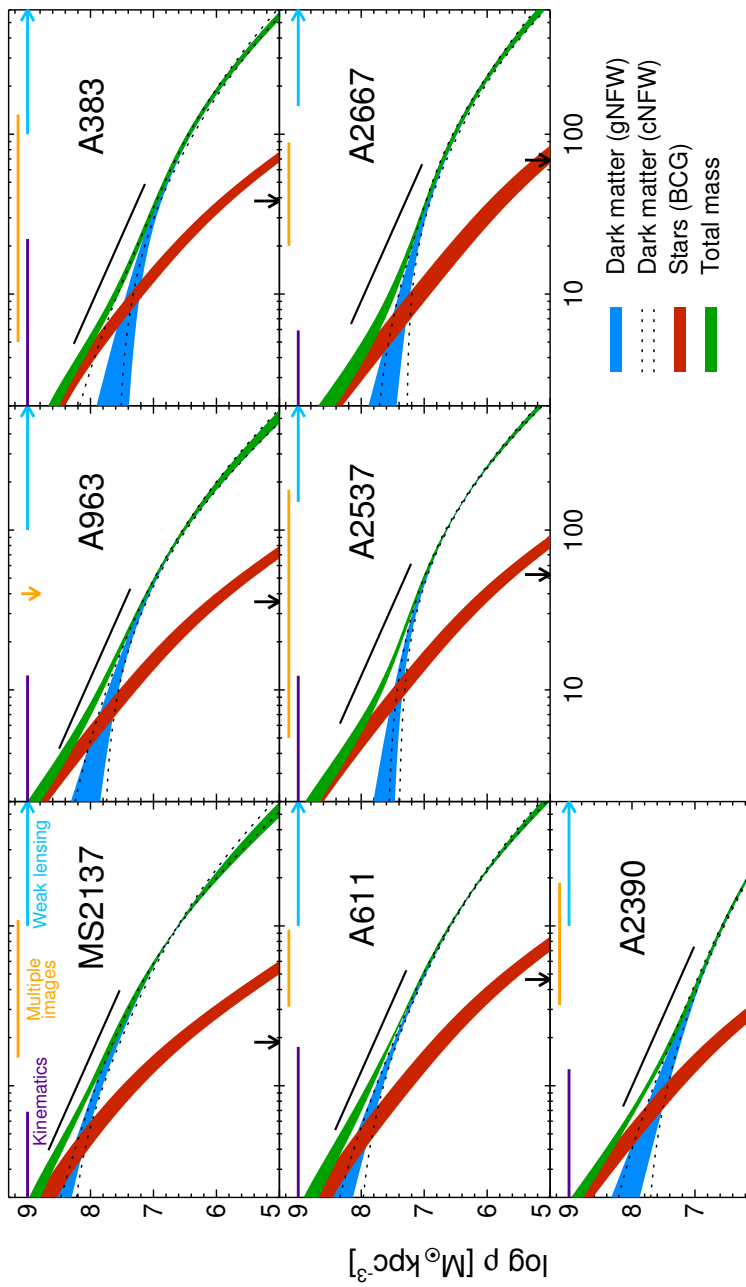

Figure 5.7: Radial density profiles for the DM halo, stars in the BCG, and their total in each cluster, adopting the joint constraint on $\log \alpha_{\rm IMF}$ from Figure 5.6. The spatial extent of each data set is indicated at the top of each panel. The black line segment spans $r/r_{200} = 0.003$–0.03 and has the slope $\rho \propto r^{-1.13}$ that is the average of clusters in the Phoenix DM-only simulations (Gao et al. 2012b) over the same interval. The width of the bands indicates the uncertainty, including both 1σ random uncertainties for isotropic models and a systematic component estimated by taking $\beta_{\rm aniso} = \pm 0.2$ (Section 5.5.1). Arrows at the bottom of each panel indicate the 3D half-light radius r_h of the BCG.

5.4 The inner dark matter density profile

We now turn to the inner DM density profiles. Earlier work (Sand et al. 2002, 2004, 2008; Newman et al. 2009, 2011) studied the inner DM density slope β by marginalizing over the uncertainty in Υ_* separately in each cluster. With the benefit of a larger sample with improved data, we have now combined constraints from seven clusters to arrive at a joint measurement of the stellar mass scale $\alpha_{\rm SPS}$ (Section 5.3). Incorporating this information, we can now conduct our analysis in a more physically consistent way that recognizes the homogeneity of the BCGs, as well as further reducing the remaining degeneracies between dark and stellar mass.

Technically, we implement the joint constraint on $\log \alpha_{\rm SPS}$ via importance sampling (e.g., Lewis & Bridle 2002), reweighting the Markov chain samples to effectively convert our flat prior on $\log \alpha_{\rm SPS}$ to a Gaussian with mean $\langle \log \alpha_{\rm SPS} \rangle = 0.27$ and dispersion $\sigma = (\sigma_\alpha^2 + \sigma_{\rm SPS}^2)^{1/2} = 0.09$. Here $\sigma_\alpha = 0.05$ dex is the uncertainty in $\langle \log \alpha_{\rm SPS} \rangle$, and $\sigma_{\rm SPS} = 0.07$ dex is the random error in $\Upsilon_{*\rm V}^{\rm SPS}$ for each BCG. The latter accounts for the fact that $\alpha_{\rm SPS}$ refers to a systematic offset from SPS-based mass estimates, but random errors due to photometric noise remain in each cluster.[4]

5.4.1 Dark and stellar mass profiles

Figure 5.7 shows the resulting spherically averaged density profiles for the DM halo, BCG stars, and their sum. The results based on gNFW and cNFW models are again quite similar, showing that the choice of parameterization does not strongly affect the derived density profiles. We do not detect an overall preference for one model over the other: the ratio of the total Bayesian evidence is consistent with unity.[5]

In order to place our results in context, we compare the density profiles to those from the Phoenix project (Gao et al. 2012b), which is the highest-resolution suite of *CDM-only* simulations of clusters to date. The typical convergence radius of 2.9 h^{-1} kpc achieved in these simulations is well matched to our observations, as is the mass range $M_{200} = 0.6{-}2.4{\times}10^{15}\ h^{-1}\,{\rm M}_\odot$. In the following comparisons we omit Phoenix-G and H, which are the latest clusters to assemble and remain in a unrelaxed state to $z = 0$, inconsistent with the properties of the observed sample. This leaves seven simulated clusters. We measure the mean density slope over the interval $r/r_{200} = 0.003$–0.03, following the same procedures used for the data (Section 5.2). The black line segment in each panel spans this radial range and has the mean slope $d\log\rho/d\log r = -1.13 \pm 0.02$ found in the simulations.

As anticipated in Section 5.2, the stars and DM sum to produce a slope very close to CDM-only simulations over this interval. (In Section 5.7 we return to the Gao et al. (2012b) simulations and

[4]This estimate of $\sigma_{\rm SPS}$ may be conservative, given that the dispersion in $\Upsilon_{*\rm V}^{\rm SPS}$ measurements among the BCGs is smaller, and $\chi^2/{\rm dof} \leq 1$ in the SPS model fits. Thus, in practice we are likely allowing for some mild intrinsic variation in $\alpha_{\rm SPS}$.

[5]In Section 5.1 we found that the evidence ratio mildly favored the cNFW models when taking a uniform prior on $\log \alpha_{\rm SPS}$. When the joint constraint derived in this paper is taken as a prior, the evidence ratio is consistent with unity ($\ln E_{\rm gNFW}/E_{\rm cNFW} = -0.8 \pm 3.2$).

Table 5.2. Parameters describing the inner DM profile

Cluster	β (gNFW)	$\log r_{\rm core}/{\rm kpc}$ (cNFW)
MS2137	$0.65^{+0.23}_{-0.30}$	$0.45^{+0.38}_{-0.48}$
A963	$0.50^{+0.27}_{-0.30}$	$0.87^{+0.61}_{-0.71}$
A383	$0.37^{+0.25}_{-0.23}$	$0.37^{+0.72}_{-0.64}$
A611	$0.79^{+0.14}_{-0.19}$	$0.47^{+0.39}_{-0.50}$
A2537	$0.23^{+0.18}_{-0.16}$	$1.67^{+0.24}_{-0.23}$
A2667	$0.42^{+0.23}_{-0.25}$	$1.29^{+0.49}_{-0.49}$
A2390	$0.82^{+0.13}_{-0.18}$	$0.30^{+0.53}_{-0.34}$
	Ensemble mean	
All clusters	0.50 ± 0.13	1.14 ± 0.13
$\beta_{\rm aniso} = +0.2$	$0.38^{+0.09}_{-0.07}$	$1.11^{+0.14}_{-0.10}$
$\beta_{\rm aniso} = -0.2$	$0.64^{+0.05}_{-0.09}$	$0.96^{+0.24}_{-0.11}$
Separate $\alpha_{\rm SPS}$	0.62 ± 0.14	$1.09^{+0.12}_{-0.21}$

Note. — Median parameters are shown, obtained after weighting samples to incorporate our joint constraint on $\alpha_{\rm SPS}$, as described in the text. Error bars encompass the $16-84$th percentiles and account for *random errors only*; see Section 5.5 for an estimation of systematic uncertainties and the total error budget. Results are shown for individual clusters (top) and for the ensemble mean (bottom), including for several alternative assumptions described in Section 5.5.

compare to our measurements in greater detail.) We can now see that both stars and DM contribute significantly to the mass in this regime: stars dominate the density in the inner radius, while virtually all the mass is DM at the outer radius. This suggests a coordination between the inner DM profile and the distribution of stars: the NFW-like density slope is not a property of the DM halo or the BCG alone, but of their sum. At yet smaller radii $r \lesssim 5-10$ kpc where stars are dominant – well within the mean effective radius $\langle R_e \rangle = 30$ kpc – the total density profile generally steepens.

As expected if the total density is NFW-like, the DM profiles become shallower only on scales where the BCG contributes significantly, roughly within R_e. As we describe in Section 5.6, our results thus do not conflict with other studies that claim the DM alone follows an NFW profile but are confined to $r \gtrsim R_e$. The stellar mass density in our models reaches that of the DM at a median radius of $\langle r \rangle = 7$ kpc. In terms of enclosed mass, equality occurs at $\langle r \rangle = 12$ kpc. Within 5 kpc the median DM fraction is $\langle f_{\rm DM} \rangle = 25\%$, similar to massive field ellipticals (e.g., Auger et al. 2010a), but within their 3D half-light radii r_h the BCGs are far more DM-dominated: $\langle f_{\rm DM} \rangle = 80\%$.

5.4.2 Inner DM density slopes and core radii

Figure 5.8 shows the probability distributions for β (gNFW) and $r_{\rm core}$ (cNFW) obtained by marginalizing over the other parameters, again weighting the samples to incorporate our joint constraint on

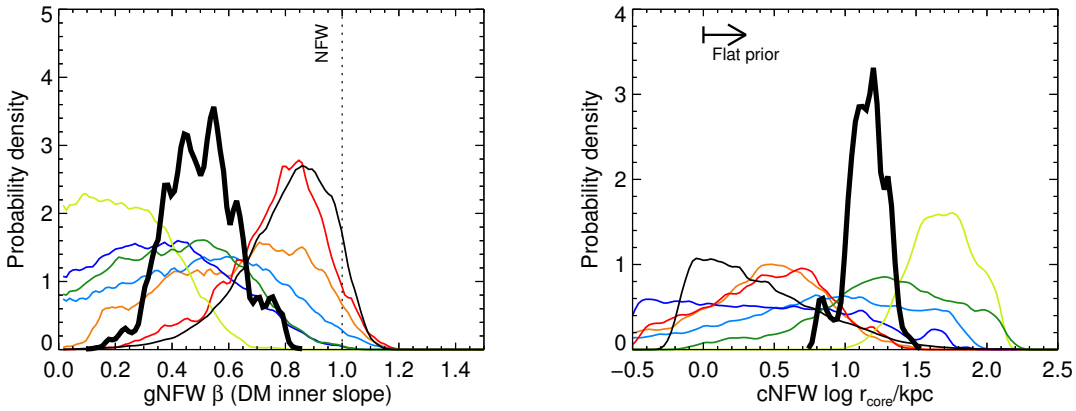

Figure 5.8: Marginalized posterior probability densities for the gNFW inner slope β (left) and the cNFW core radius (right). Thick black lines show joint constraints on the mean. Colors follow Figure 5.6. Each curve is normalized to integrate to unity. Our adopted priors (Section 4.1) are flat in $\log r_s$ and b and therefore not in $\log r_{\rm core} = \log r_s/b$ over the whole plotted range. The arrow in the right panel indicates the region over which the effective prior on $\log r_{\rm core}$ is flat.

$\alpha_{\rm SPS}$. Results for the individual clusters are listed in Table 5.2. Every cluster prefers $\beta < 1$, i.e., an inner slope shallower than an NFW model. Thick black lines show constraints on the mean: $\langle\beta\rangle = 0.50 \pm 0.13$ and $\langle \log r_{\rm core}/{\rm kpc}\rangle = 1.14 \pm 0.13$; the method for deriving these is outlined in the Appendix (Section 5.9). We note that while the typical $r_{\rm core} \approx 14$ kpc is small, the cNFW profile turns over rather slowly at small radii. Thus, while $r_{\rm core}$ is the radius where the density falls to half of the corresponding NFW profile, significant deviations extend to $r \simeq (3-4)r_{\rm core}$.

We can also ask whether there is evidence for intrinsic variation in the inner DM profiles. This can be quantified by assuming that the parent distributions of β and $\log r_{\rm core}$ are Gaussian, and using the method described in Section 5.2 to infer its dispersion. We find some evidence for intrinsic scatter with $\sigma_\beta = 0.22^{+0.15}_{-0.11}$ and $\sigma_{\log r_{\rm core}} = 0.57^{+0.33}_{-0.21}$. Its statistical significance can be assessed with the ΔP statistic (Equation 5.3): we derive $\Delta P = 1.5$ and 2.6 for β and $\log r_{\rm core}$, respectively. This indicates a $\simeq 2\sigma$ preference for the presence of intrinsic scatter in the inner DM profile shape. While we have focused on relaxed clusters, we expect this variation would increase if a broader sample of clusters that includes recent mergers was considered.

A possible physical origin of this scatter is illustrated in Figure 5.9. Gray points in the top panel show the total density slope $\gamma_{\rm tot}$. As described in Section 5.2, these show mild scatter around the mean slope measured in CDM-only simulations (dashed line, Gao et al. 2012b) over the same radial interval ($r/r_{200} = 0.003$–0.03). Here we see signs of a correlation with the size of the BCG, with more extended BCGs corresponding to shallower total slopes. The effect on the DM slope (colored points) appears stronger: larger BCGs are hosted by clusters with shallower DM slopes β, or equivalently larger core radii $r_{\rm core}$ (bottom panel). Such a correlation is necessary for the dark and stellar mass to combine to a similar total density profile. The significance can be assessed using the Spearman

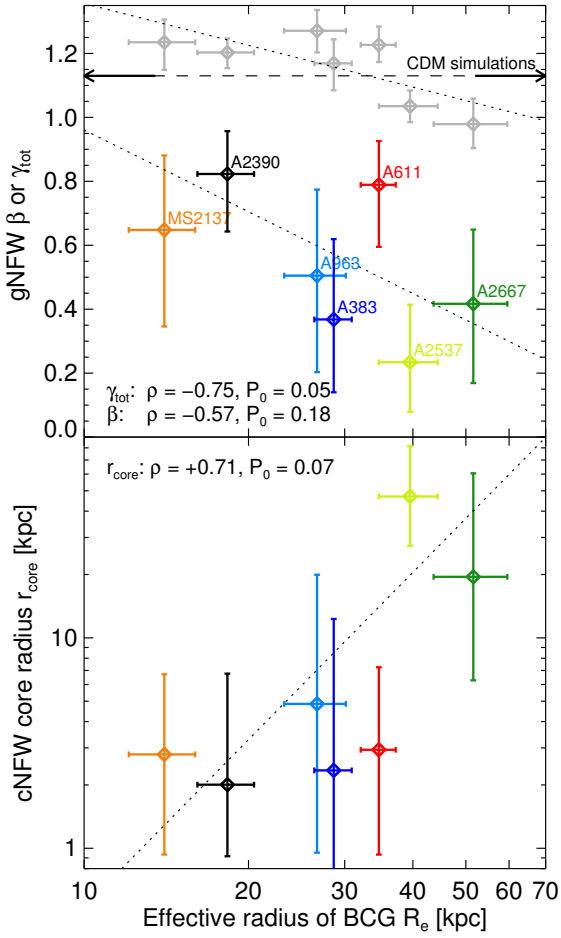

Figure 5.9: Correlation between the size of the BCG and the inner DM profile. **Top:** Gray points show the total density slope $\gamma_{\rm tot}$; this is measured over $r/r_{200} = 0.003$–0.03 and is not an asymptotic slope. The dashed horizontal line shows the mean slope measured in CDM-only cluster simulations (Gao et al. 2012b) over the same interval. Colored points denote the asymptotic DM density slope β measured in the gNFW models. Dotted lines show least-squares linear fits. The Spearman rank correlation coefficient ρ and the corresponding two-sided P_0-value are listed. **Bottom:** The core radii $r_{\rm core}$ of the cNFW models are shown, again indicating a correlation with R_e.

rank correlation test. We find a probabilities $P_0 = 0.18$ and 0.07 of obtaining an equally strong correlation between R_e and β or $r_{\rm core}$, respectively, in the null hypothesis of uncorrelated data (see caption to Figure 5.9).

Figure 5.9 suggests that the DM profile in the cluster core is connected to the build-up of stars in the BCG. We return to this point in Section 5.7 and discuss physical scenarios that may explain this. Although the correlations with R_e are most convincing, they are not unique: we find correlations between β or $r_{\rm core}$ and the stellar mass or luminosity with nearly equal statistical significance. There is no sign of a correlation with the virial mass M_{200} ($\rho = 0.11$ and 0.04 for the gNFW and cNFW models; see caption to Figure 5.9).[6]

We emphasize that it is preferable to compare directly to the physical density profiles (Figure 5.7) when possible, rather than only marginalized distributions for β. These results do not imply, for example, that a CDM density profile should be modified simply by maintaining the same r_s and changing $\beta = 1$ to $\beta = 0.5$. Rather, r_s also shifts in our fits such that significant changes in $\rho_{\rm DM}$ are kept within $r \lesssim 30$ kpc. This degeneracy is simply a result of the gNFW parameterization.

5.5 Systematic uncertainties

Before turning to the physical interpretation of these results, we first review and quantify the remaining sources of systematic uncertainty in our analysis.

5.5.1 Dynamical modeling

Our dynamical models are based on isotropic stellar orbits. Prior studies (e.g., Carter et al. 1999; Gerhard et al. 2001; Cappellari et al. 2007, and see references in Section 3.5.3) have shown this to be a good approximation for luminous, non-rotating ellipticals in their central regions. (Our kinematic data are confined to $R \lesssim R_e/2$.) Nonetheless, individual galaxies can exhibit mild anisotropy with $|\beta_{\rm aniso}| = |1 - \sigma_\theta^2/\sigma_r^2| \approx 0.2$, and the population as a whole also may be slightly radially biased. We reran our analysis using a constant $\beta_{\rm aniso} = +0.2$ (radial bias) or -0.2 (tangential bias) in the dynamical calculations, where $\beta_{\rm aniso} = 1 - \sigma_\theta^2/\sigma_r^2$ characterizes deviations from an isotropic velocity dispersion tensor (e.g., Binney & Tremaine 1987).

The mean shifts in $\gamma_{\rm tot}$ were -0.07 and 0.05, respectively. This could be a common bias among the whole sample. Variable anisotropy could also introduce spurious scatter in the measured $\gamma_{\rm tot}$ at the same level; in that case, the true physical scatter would be less. In terms of the separation between stellar and dark mass, arrows in Figure 5.6 show that individual clusters may shift by $\Delta \log \Upsilon_* = -0.16$ ($\beta_{\rm aniso} = +0.2$) or $\Delta \log \Upsilon_* = +0.10$ ($\beta_{\rm aniso} = -0.2$). Again, this bias may be

[6] Interestingly, the reverse seems to hold for $\gamma_{\rm tot}$: there is no sign of a correlation with the stellar mass or luminosity, but a possible correlation with M_{200} ($\rho = -0.68$, $P_0 = 0.09$). The latter may simply be because the radial range over which $\gamma_{\rm tot}$ is measured is proportional to r_{200}.

correlated among the BCGs in our sample. We note that the effects of anisotropy are larger here than for studies of field elliptical lenses (e.g., Auger et al. 2010a), since the latter do not resolve kinematics well within R_e where the impact of anisotropy on the l.o.s. velocity dispersion is largest.

Uncertainties in the orbital distribution have a milder effect on the parameters describing inner DM profile. If we adopt the same prior in $\langle \log \alpha_{\rm SPS} \rangle$, taking $\beta_{\rm aniso} = \pm 0.2$ leads to systematic shifts of $\Delta\langle\beta\rangle = \pm 0.13$ and $\Delta\langle \log r_{\rm core} \rangle \approx -0.18$ (Table 5.2). If we instead shift the prior on $\langle \log \alpha_{\rm SPS} \rangle$ to match the results obtained with the corresponding $\beta_{\rm aniso}$, we find $\Delta\langle\beta\rangle = +0.11, -0.02$ and $\Delta\langle \log r_{\rm core} \rangle = -0.21, +0.08$. Based on these results, we estimate systematic uncertainties of $\Delta\langle\beta\rangle = \pm 0.13$ and $\Delta\langle \log r_{\rm core} \rangle = -0.2, +0.1$ due to the orbital anisotropy.

Since we measure kinematics well within the effective radii of the BCGs, taking $|\beta_{\rm aniso}| = 0.2$ corresponds to changes in $\sigma_{\rm los}$ by $\simeq 5\% - 10\%$ for the same mass distribution. This is larger than the systematic errors of $\lesssim 5\%$ in the measurements themselves (Section 3.5.2), and therefore the resulting errors are less than from those from anisotropy. Furthermore, most of the systematic measurement errors are probably not correlated across all BCGs. Errors arising from the spherical dynamical treatment are expected to be similarly small (e.g., Kronawitter et al. 2000; Jiang & Kochanek 2007) for nearly-round systems like our sample.

5.5.2 Residual line-of-sight ellipticity

As introduced in Section 4.3.1, spherical mass estimates derived from lensing will be biased if the cluster is elongated or compressed along the l.o.s. In Section 4.3.2, we found a mean tendency for the lensing mass to exceed that derived from X-ray measurements by 7% at 100 kpc. Although this is consistent with zero within the uncertainties in the X-ray calibration, a 7% bias in the spherically averaged mass profile would shift $\langle \gamma_{\rm tot} \rangle$ by only -0.03. Cluster-to-cluster variation with $|q-1| \lesssim 0.3$ (Section 4.3.2) could introduce scatter of $\sigma_\gamma \lesssim 0.08$; accounting for this would again lower the inferred intrinsic scatter in $\gamma_{\rm tot}$. In terms of the inner DM profile, we estimate based on our study of A383 that a mean l.o.s. ellipticity of this magnitude would cause systematic shifts of $\Delta\langle\beta\rangle \approx 0.06$ and $\Delta\langle \log r_{\rm core} \rangle \approx -0.1$.

5.5.3 Simulations of off-center BCGs

We can also explore the impact on our dynamical analysis if the BCG is not precisely at rest in the center of the halo. As discussed in Section 3.1, the X-ray centroid and the lensing center are generally quite close to the optical center of the BCG. However, small offsets of a few kpc are not excluded. In order to assess how the stellar dynamics could be affected by small-scale oscillations around the center of the cluster potential, we performed some simple numerical simulations using

the parallel N-body code FVFPS (Londrillo et al. 2003; Nipoti et al. 2003).[7] The BCG is modeled as a single-component equilibrium isotropic γ model (Dehnen 1993) with $\gamma = 1.5$, scale radius $a = 23.5$ kpc (i.e., 3D half-mass radius $r_{\rm half} \simeq 40$ kpc), and total mass $M_* = 1.5 \times 10^{12} M_\odot$, representative of the BCGs in the observed sample. The galaxy was realized with $N \simeq 2 \times 10^5$ particles following the same procedure as Nipoti et al. (2003, 2009b), using a softening parameter $\varepsilon = 0.03a$. At the beginning of each simulation the galaxy is placed at a distance $r_{\rm offset}$ from the center of a fixed gravitational potential representing the cluster DM halo, either at rest or in a circular orbit. We explored two halo models: a steep halo ($\gamma = 1$, $a = 352$ kpc) that approximates an NFW profile with $\rho_s = 1.52 \times 10^6\,{\rm M}_\odot\ {\rm kpc}^{-3}$ and $r_s = a$ (see Equation 4.1) within the scale radius, and a shallow halo ($\gamma = 0.5$, $a = 226$ kpc) that approximates a gNFW profile with $\beta = 0.5$, $\rho_s = 5.37 \times 10^6\,{\rm M}_\odot\ {\rm kpc}^{-3}$, and $r_s = a$. The two models were chosen to nearly match at $r > 100$ kpc but differ in their inner slope.

In the halo with the steeper NFW-like cusp, we found that small displacements – even up to 40 kpc – are highly unstable. Even when initially set on a circular orbit, the BCG quickly falls to the halo center within 350 Myr. During this time the isophotes are clearly disturbed, which is inconsistent with the galaxies in our sample. In the halo with a shallower density cusp, on the other hand, we found that stable oscillations with an amplitude of $\simeq 5$ kpc are possible. During these oscillations, the central velocity dispersion varies from that attained by the same system with a stationary BCG (at the cluster center) by only a few percent. We conclude that small offsets between the BCG and cluster center do not pose a significant problem for our Jeans analysis. Furthermore, if the small offsets are genuine, they appear to imply a DM cusp with $\beta \lesssim 1$.

5.5.4 Other sources of uncertainty

Our analysis assumes that the stellar mass in the BCGs follows the light measured at $\simeq 6000$ Å, i.e., that $\Upsilon_{*\rm V}$ does not vary with radius. Color gradients indeed appear to be small in the majority of the sample (Section 3.4.1), but two BCGs (A611 and A383) show a stronger gradient. We take A383 as an example. Assuming that the near-infrared light measured in the F160W filter is a better proxy of the stellar mass, we applied a radial gradient to the model stellar mass profile based on the ratio of the F160W and F606W fluxes. For the same tracers, the velocity dispersions should change by $\lesssim 4\%$, less than the systematic uncertainty in the measurements. This is because the $M_*/L_{\rm F606W}$ gradient becomes significant only at large radii where DM is dominant. We also tested the impact of the BCG size $r_{\rm cut}$ by perturbing it by its 10% uncertainty in A2537 and repeating our analysis, accounting for the correlated change in $L_{\rm V}$. This led to no significant shifts in $\Upsilon_{*\rm V}$, β, or b (see also the discussion in Sand et al. 2004).

To assess the impact of the strong-lensing positional uncertainty $\sigma_{\rm pos}$ on our findings, we reran

[7] The simulations described here were kindly performed by C. Nipoti.

Table 5.3. Final inferences on the mean of key mass profile parameters

Parameter	Inferred mean
$\gamma_{\rm tot}$	$1.16 \pm 0.05^{+0.05}_{-0.07}$
$\log \alpha_{\rm SPS}$	$0.27 \pm 0.05^{+0.10}_{-0.16}$
β (gNFW models)	$0.50 \pm 0.13^{+0.14}_{-0.13}$
$\log r_{\rm core}$ (cNFW models)	$1.14 \pm 0.13^{+0.14}_{-0.22}$

Note. — The first and second error bars indicate the random and total systematic uncertainties (Section 5.5), respectively, on the mean over the full sample of seven clusters.

our analysis with $\sigma_{\rm pos} = 0\farcs3$ (see Section 4.2). This had very little effect on $\gamma_{\rm tot}$, typically shifting the inferred values in individual clusters by $\lesssim 0.02$, with no net bias on $\langle\gamma_{\rm tot}\rangle$. The effect on the DM slope is mildly larger: we find a mean shift of $\Delta\beta = -0.1$ when taking $\sigma_{\rm pos} = 0\farcs3$ rather than our fiducial $\sigma_{\rm pos} = 0\farcs5$, while $\Delta\beta = +0.1$ when $\sigma_{\rm pos} = 1\farcs0$ (although this choice is strongly disfavored by the Bayesian evidence; see Section 4.2). There is no significant dependence of $\log \alpha_{\rm SPS}$ on $\sigma_{\rm pos}$. We conclude that our results are robust to reasonable changes in the weighting of the lensing data.

We note that the clusters with the lowest inferred $\alpha_{\rm SPS}$ in Figure 5.6 (MS2137 and A611) are those with the highest halo concentration parameters (Section 4.3.2). These clusters have NFW-like *total* density profiles down to unusually small radii, with very weak steeping on small scales. In view of the similarity of $\alpha_{\rm SPS}$ among the other five clusters and the agreement with independent results discussed in Section 5.6.1, a likely explanation is that some of the stellar mass is effectively counted in the halo when Υ_* is allowed to vary freely from cluster to cluster. Nevertheless, omitting MS2137 and A611 would shift $\langle\log \alpha_{\rm SPS}\rangle$ by only +0.02. In this respect our results are encouragingly robust. While we have argued that our method of deriving a common value of $\alpha_{\rm SPS}$ is superior, we note that marginalizing over $\Upsilon_{*\rm V}$ separately in each cluster would shift the mean $\langle\beta\rangle$ by $< 1\sigma$ (see "Separate $\alpha_{\rm SPS}$" Table 5.2).

We recall evidence presented in Section 3.1 that A2537 is a possible l.o.s. merger. Such an alignment could produce a spuriously shallow DM profile in a lensing analysis, and A2537 indeed has the shallowest slope in our sample. However, Figure 5.9 provides another explanation: A2537 has the second-largest BCG in the sample. Thus, it does not appear that our results for A2537 are exceptional. Nevertheless, recognizing its unique nature in our sample, we note that excluding A2537 yields $\langle\beta\rangle = 0.69^{+0.10}_{-0.14}$ and $\log r_{\rm core} = 0.59^{+0.26}_{-0.37}$, which does not change our main conclusions.

5.5.5 Total error budget

Considering the uncertainties discussed above, the largest source of global systematic bias in $\gamma_{\rm tot}$ is likely the orbital distribution. Thus, we take the uncertainty $\Delta\gamma_{\rm tot} = +0.05, -0.07$ arising from orbital anisotropy as the systematic error in the mean $\langle\gamma_{\rm tot}\rangle$. Turning to the total impact of residual l.o.s. ellipticity and orbital anisotropy on the separation between dark and stellar mass, we sum their effects in quadrature to arrive at total systematic error estimates of $\Delta\langle\beta\rangle = +0.14, -0.13$, $\Delta\langle\log r_{\rm core}\rangle = +0.14, -0.22$, and $\Delta\langle\log\alpha_{\rm SPS}\rangle = +0.10, -0.16$. Table 5.3 summarizes our final inferences on the mean of the key parameters, including random and systematic components. While these estimates apply to uncertainties that may be correlated across the sample, variations in orbital anisotropy or l.o.s. ellipticity could cause naturally larger shifts on a cluster-by-cluster basis. Such effects could decrease the intrinsic scatter in $\gamma_{\rm tot}$, β, and $r_{\rm core}$ that we infer, although they would have to be correlated with the size or mass of the BCG (Figure 5.9).

5.6 Comparison to previous results

5.6.1 Stellar mass-to-light ratio

These results on the inner DM profile are informed by the common stellar mass normalization that we infer, so it is important to compare this result to other measurements to assess its reliability (see also Cappellari et al. 2012c for a recent review). As shown in Section 5.3, we find $\log\alpha_{\rm SPS} = 0.27 \pm 0.05$ for isotropic orbits, with a corresponding $\Upsilon_{*\rm V} = 4.1 \pm 0.5$ and $\Upsilon_{*\rm B} = 5.3 \pm 0.6$ at the median $\Upsilon^{\rm SPS}_{*\rm V}$ and $\Upsilon^{\rm SPS}_{*\rm B}$. When comparing mass-to-light ratios at different redshifts, it is essential to account for luminosity evolution. Where necessary, we evolve samples as $d\log\Upsilon_{*\rm V}/dz = -0.64$ (Treu et al. 2001). We note that the $\simeq 0.05$ dex systematic uncertainty in $\Upsilon^{\rm SPS}_{*\rm V}$ (Section 3.4.2) is relevant only for the interpretation of $\Upsilon_{*\rm V}$ in terms of stellar populations, but it does *not* affect the stellar mass and so has no effect on the derived mass profiles.

Discussion of Υ_* is often tied to the IMF. This is because the unknown IMF is the dominant source of uncertainty in the absolute mass scale for SPS models, especially for old galaxies (e.g., Bell & de Jong 2001; Bundy et al. 2005; Cappellari et al. 2006; Auger et al. 2009; Grillo et al. 2009; Stott et al. 2010). If interpreted as a difference in IMF, our measured $\alpha_{\rm SPS}$ indicates a normalization consistent with that of the Salpeter (1955) IMF,[8] which has $\log M_{*,\rm Salp}/M_{*,\rm Chab} = 0.25$ when extended over $0.1 - 100\,{\rm M}_\odot$.

Several other studies have used lensing and stellar dynamics to probe massive field and group ellipticals. Auger et al. (2010b) study the SLACS samples of early-type lenses using strong and weak lensing and stellar kinematics (see also Gavazzi et al. 2007; Treu et al. 2010). Assuming an NFW

[8] While Salpeter (1955) did not measure the mass function down to $0.1\,{\rm M}_\odot$, this is the common meaning of a "Salpeter" IMF in extragalactic studies.

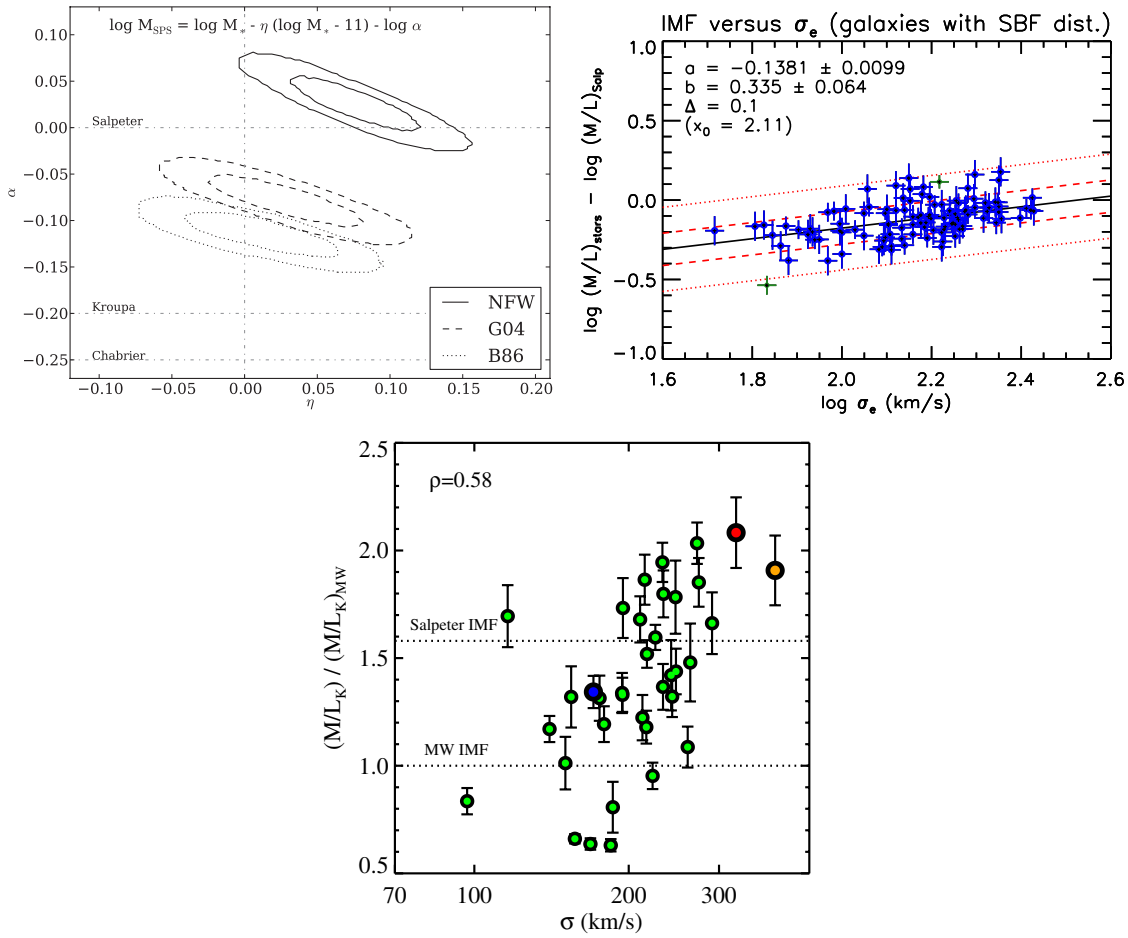

Figure 5.10: Recent results on the stellar IMF in early-type galaxies. **Top left:** Constraints on the IMF in massive elliptical galaxies in the SLACS survey based on lensing and dynamics, reproduced from Auger et al. (2010b). Their α corresponds to $\log \alpha_{\rm SPS} - 0.25$ in our notation, since their fidicual IMF is Salpeter. $\eta > 0$ corresponds a trend of "heavier" IMFs in more massive ellipticals. While the results depend on the adopted DM halo (NFW, G04, B86), none of the tested models favors a Milky Way-like IMF. **Top right:** Results on the *stellar* mass-to-light ratio based on integral field kinematics in the ATLAS$^{\rm 3D}$ survey, reproduced from Cappellari et al. (2012c). The ordinate again corresponds to $\log \alpha_{\rm SPS} - 0.25$ in our notation. Thus, early-type galaxies with the highest dispersion have a Salpeter-like Υ_*. **Bottom:** Inferred trends in the IMF (parameterized by Υ_* relative to that inferred with a Milky Way IMF) with velocity dispersion, as inferred from spectral synthesis models; reproduced from Conroy & van Dokkum (2012). In contrast to the above dynamical studies, these constraints derive from surface gravity-sensitive stellar absorption lines and so are completely independent. All studies shown here indicate an increasingly "heavy" IMF for high-dispersion early-types.

halo, they infer $\log \alpha_{\rm SPS} = 0.28 \pm 0.03$ at $M_* = 10^{11}\,{\rm M}_\odot$. Assuming an adiabatically-contracted halo lowers this value by 0.11–0.14, i.e., still heavier than a Chabrier IMF. They infer an intrinsic scatter of < 0.09 dex in $\log \alpha_{\rm SPS}$ within their sample of $\sigma \gtrsim 200$ km s^{-1} lenses (Treu et al. 2010). Lagattuta et al. (2010) study ellipticals at slightly higher redshift using strong and weak lensing. Evolving their Υ_* from $\langle z \rangle \approx 0.6$ to our $\langle z \rangle = 0.25$ yields $\Upsilon_{*{\rm V}} = 4.7 \pm 0.7$, consistent with our results. Both of these works assume an NFW halo and a mass–concentration relation that follows theoretical expectations (i.e., a one-parameter halo). Our models include much more general halos, and the BCGs are much more DM-dominated. Thus, the uncertainty in Υ_* on an object-by-object basis is larger; nonetheless, the ensemble averages agree well. Sonnenfeld et al. (2012) studied a rare early-type lens that presents two Einstein rings, which allowed them also to relax assumptions on the DM profile. They find $\alpha_{\rm SPS} = 0.30 \pm 0.09$ in our notation (see also Spiniello et al. 2011). Zitrin & Broadhurst (2009) took advantage of the unusually flat surface density profile in the lensing cluster MACS J1149.5+2223 ($z = 0.544$), which offers a clean subtraction of the dark halo to isolate the mass of the BCG. They estimate $\Upsilon_{*{\rm B}} \approx 4.5 \pm 1$ ($\approx 7 \pm 2$ if evolved to our $\langle z \rangle = 0.25$).

Other studies have used integral field spectroscopy to construct detailed dynamical models of local ellipticals. Cappellari et al. (2012a,c,b) discuss the ATLAS$^{\rm 3D}$ sample of early-type galaxies. At the highest velocity dispersions present, they infer $\log \alpha_{\rm SPS} = 0.25$ (Cappellari et al. 2012c, Figure 9, converted to our definition of $\alpha_{\rm SPS}$). Interestingly, there appears to be little or no intrinsic scatter in $\alpha_{\rm SPS}$ at $\sigma_e \gtrsim 250$ km s^{-1}, nearly at the lower limit of our BCGs, although only a handful of such objects are present in their sample. Along with the tightness of the $M/L - \sigma_e$ relation at high σ_e (Cappellari et al. 2012b), this supports our claim that $\alpha_{\rm SPS}$ should be nearly constant within our sample of BCGs. McConnell et al. (2011) studied the BCG of A2162 using long-slit kinematics and integral field spectroscopy with adaptive optics, finding $\Upsilon_{*{\rm R}} = 4.6^{+0.3}_{-0.7}$ in their "maximum halo" solution. For comparison, our result evolved to $z = 0$ is $\Upsilon_{*{\rm R}} = 4.1 \pm 0.5$.

Finally, the IMF in early-type galaxies has recently been studied using detailed spectral synthesis models that take advantage of surface gravity-sensitive stellar absorption lines. In very high-quality spectra, these constrain the abundance of low-mass dwarfs that contribute much to the stellar mass but very little to the integrated light. Although the degree of scatter remains unclear, these studies suggest that a Salpeter-like IMF – or possibly even heavier – is typical in high-dispersion ellipticals (van Dokkum & Conroy 2010, 2012; Conroy & van Dokkum 2012; Smith et al. 2012). Importantly, this work is completely independent of the gravity-based studies described above and makes no assumptions regarding the form of the DM profile. Furthermore, this spectral technique has the potential to constrain the *shape* of the IMF, whereas lensing and dynamical studies constrain only the integrated mass-to-light ratio.

In summary, our measurements are consistent with a variety of other recent works indicating a heavy (Salpeter-like) Υ_* in massive early-type galaxies. Encouragingly, studies based on completely

independent techniques are beginning to converge on the same results. Figure 5.10 reviews the key results from several of the recent studies described above.

5.6.2 The total inner density slope

When comparing results on the inner density profiles of clusters, it is essential to understand the *radial range* that is being fit and whether the *total* density profile or that of the *DM only* is being considered. This distinction is most important at radii $\lesssim 30$ kpc where the BCG contributes noticeably to the total mass. We showed that the *total* density profiles in our sample are consistent with CDM-only simulations down to $r \simeq 5-10$ kpc. Whereas the metric $\gamma_{\rm tot}$ that we introduced is measured over a specific radial interval, other authors have fit gNFW profiles to the *total* density profile and quote the asymptotic inner slope, which we denote as $\beta_{\rm tot}$ (versus $\beta_{\rm DM}$ to emphasize the inner slope of the DM alone). Recall that $\beta = 1$ for an NFW profile.

Most observational studies have focused on the total density profile. Umetsu et al. (2011) stacked density profiles for four clusters with high-quality lensing data and found that $\beta_{\rm tot} = 0.89^{+0.27}_{-0.39}$, with the inner 40 kpc/$h$ excluded from their fit. Morandi et al. (2011) measured $\beta_{\rm tot} = 0.90 \pm 0.05$ in A1689, excluding the inner 30 kpc, and Coe et al. (2010) also found that the total mass distribution is NFW-like. Using imaging from the CLASH survey (Postman et al. 2012b), Umetsu et al. (2012) and Zitrin et al. (2011b) derived $\beta_{\rm tot} = 0.96^{+0.31}_{-0.49}$ (their "method 7") and $\beta_{\rm tot} = 1.08 \pm 0.07$ in MACS J1206.2-0847 and A383, respectively. These lensing results are consistent with our claims that the *total* density profile is NFW-like at $r \gtrsim 5-10$ kpc.

Morandi & Limousin (2012) use lensing and X-ray data to derive a total slope $\beta_{\rm tot} = 1.02 \pm 0.06$ in A383 and contrast this with our earlier finding that $\beta_{\rm DM} = 0.59^{+0.30}_{-0.35}$ in the same cluster (Newman et al. 2011).[9] These results are not inconsistent. Figure 5.7 shows that the DM profile we infer in A383 becomes shallower than an NFW model only at $r \lesssim 30$ kpc. These scales are excluded by Morandi & Limousin in their fits precisely because of the uncertainty in the BCG stellar mass that we have addressed using stellar kinematics. At $r \gtrsim 30$ kpc the total density profile in our models – nearly equal to that of the DM – is NFW-like.

5.6.3 The dark matter inner density slope

Among the main scientific goals of studying the inner regions of clusters is testing the predictions of the collisionless CDM paradigm, and understanding the formation of the central galaxy and its impact on the DM halo. Thus, although precise and robust measurements of the total density profile are very valuable, for these goals it is clearly important to understand how much of this mass is DM and how much is baryonic. Over the past decade, we have been developing tools to perform this

[9]The present measurement of β in A383 (Table 5.2) is slightly shallower, but consistent with, Newman et al. (2011) due to our new joint constraint on $\alpha_{\rm SPS}$.

separation (Sand et al. 2002, 2004, 2008; Newman et al. 2009, 2011). The history of this progress was described in Chapter 2.

Sand et al. (2004) measured a mean $\langle\beta_{\rm tot}\rangle = 0.52 \pm 0.05$ in a sample of six clusters. We have improved on this earlier work in many ways: through the use of elliptical lens models, the addition of weak lensing data, the incorporation of multiple strongly-lensed sources (usually located at different redshifts), the comparison with X-ray results to quantify l.o.s. effects, the deeper spectroscopic observations of the BCGs that have yielded more precise and radially-extended kinematic profiles, and through joint constraints on the stellar mass scale $\alpha_{\rm SPS}$. This work has essentially confirmed the initial findings, with the present value $\langle\beta_{\rm DM}\rangle = 0.50 \pm 0.10^{+0.14}_{-0.13}$ consistent with Sand et al. (2004). (The smaller error bars quoted in the latter work are due to the more restrictive model assumptions, particularly a fixed scale radius r_s.)

Four of the clusters in the present sample have been previously studied in our earlier papers. In general our results for MS2137 and A963 are consistent with Sand et al. (2004, 2008) within their uncertainties, although the present measurements supercede earlier ones due to the improvements described above. Our analysis of A383 is consistent with Newman et al. (2011). The results presented here for A611, on the other hand, are significantly different from Newman et al. (2009): we find $\beta = 0.79^{+0.14}_{-0.19}$, rather than $\beta < 0.3$ (68% confidence). This is attributable to two changes in the data: a revised spectroscopic redshift for a multiply imaged galaxy, and improved stellar kinematic measurements (see Sections 3.3 and 3.5.4).

As we have shown, it is difficult to separate the BCG and DM profiles with lensing alone due to the low density (or lack) of constraints near the center. Only in clusters with exceptional lensing configurations is this feasible. An interesting such case is A1703, which presents an unusual quad image close to the BCG. Limousin et al. (2008) and Richard et al. (2009) performed a two-component fit – a gNFW halo and BCG stars following light, as in this work – and derive $\beta_{\rm DM} = 0.92^{+0.05}_{-0.04}$. (See Oguri et al. 2009 for a consistent result with a much larger error bar.) This may not be inconsistent with our findings, since two clusters in our sample prefer a similar slope (A611 and A2390, see Figure 5.8), and there may be scatter from cluster to cluster.[10] Zitrin et al. (2010) found that the *total* density profile in A1703 is well fit by an NFW model.

X-ray studies of two nearby clusters (A2589 and A2029) have also shown that the total density follows an NFW profile down to $\approx 0.002 - 0.01 r_{\rm vir}$ (Lewis et al. 2003; Zappacosta et al. 2006). The latter authors noted that for any reasonable Υ_*, this implies a shallower DM profile in the central regions where the stellar mass is significant. Their finding agrees well with our work, which has quantified the split between stars and DM. Schmidt & Allen (2007) studied a large sample of distant

[10]Limousin et al. (2008) imposed a tight prior on the BCG stellar mass derived from SPS fits, but did not consider uncertainty from the IMF. Their SPS estimates are quite high: $\Upsilon^{\rm SPS}_{*\rm B} \approx 11$, whereas we find $\Upsilon^{\rm SPS}_{*\rm B} = 3.0$ from fitting the SDSS photometry to this BCG, also using a Chabrier IMF. Adjusting the latter to our preferred $\alpha_{\rm SPS} = 0.27$ yields $\Upsilon_{*\rm B} = 5.7$, which agrees with the estimate $\Upsilon_{*\rm B} \approx 6$ by Zitrin et al. (2010) in this cluster.

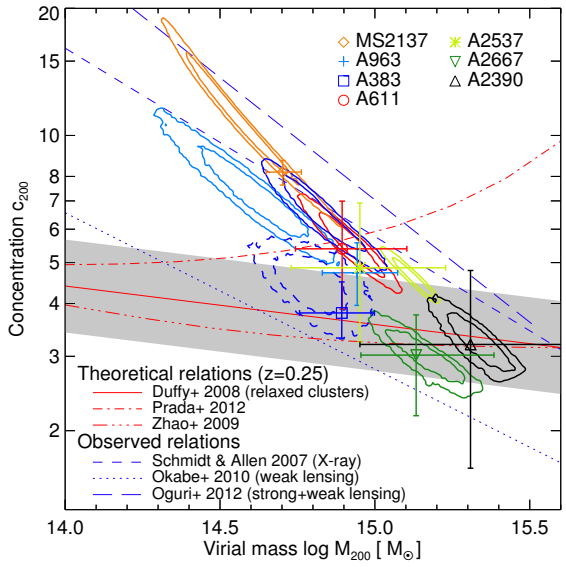

Figure 5.11: Mass–concentration relation based on strong+weak lensing (contours; 68% and 95% confidence) and X-ray (points with marginalized 1σ error bars) analyses for the full sample. Empirical (Schmidt & Allen 2007; Okabe et al. 2010; Oguri et al. 2012) and theoretical relations (Prada et al. 2012; Zhao et al. 2009; Duffy et al. 2008, with shading indicating the 1σ scatter) are shown for comparison, standardized to the same overdensity. Dashed contours for A383 show the effect of adopting a prolate halo, which brings the lensing and X-ray measures into agreement (Section 4.3.3).

X-ray clusters. By assuming a typical BCG stellar mass, they estimated $\langle \beta_{\rm DM} \rangle = 0.88 \pm 0.29$ (95% CL). Often the inner $\simeq 40$ kpc must be excluded from their analysis, making a direct comparison difficult.

5.7 Discussion and interpretation

We now consider the physical implications of our results and compare our measured density profiles to recent simulations. After discussing the mass–concentration relation, we turn to evidence for a uniform total inner density slope and compare to both DM-only simulations and those that include baryons. We conclude with a discussion of the processes that may be responsible for establishing the observed density profiles – both of dark matter and total mass – that we observe.

5.7.1 The mass–concentration relation

Figure 5.11 shows the mass–concentration relation for our sample, which was derived from NFW fits to the gravitational lensing data in Section 4.3.2. Halo concentrations are generally expected to vary inversely with mass, due to lower background densities at the later epochs in which more massive halos assemble (e.g., Bullock et al. 2001; Wechsler et al. 2002). The more massive clusters

($M_{200} \gtrsim 10^{15}\,\mathrm{M}_{\odot}$) in our sample have concentrations in line with the predictions of most numerical simulations, although we note that current simulations do not have the necessary volume to provide good statistics in this regime. The exception is Prada et al. (2012), who surprisingly have reported an *increasing* concentration at higher masses.[11] However, as we move toward lower mass the concentrations become significantly higher than CDM simulations. MS2137, in particular, has a quite high concentration inferred from both lensing and X-ray measurements, which has long been recognized (Gavazzi et al. 2003). The effect is to produce a significantly steeper slope in the mass–concentration relation compared to CDM simulations. Interestingly, the steep slope defined by our sample agrees well with measurements by Schmidt & Allen (2007, X-ray), Okabe et al. (2010, weak lensing), and Oguri et al. (2012, strong and weak lensing).

Lensing-based concentrations could potentially be biased high for two reasons. First, projection effects can cause an upward bias if the major axis of the cluster is near the l.o.s. This is unlikely to be a major effect in our sample given the overall good agreement between the lensing- and X-ray-based measures (Section 4.3.2). Second, more concentrated clusters – particularly among the lower-mass systems – are more likely to reach the critical surface density for forming multiple images, which is a necessary condition for entering our sample. Simulations of this potential bias suggest that the population of cluster lenses may have $\simeq 10\% - 35\%$ higher concentrations on average (Hennawi et al. 2007; Fedeli et al. 2007; Meneghetti et al. 2010b), but that highest concentrations seen in MS2137 and other clusters (e.g., Broadhurst et al. 2008; Zitrin et al. 2011a) are still not explained. Baryon cooling is also generally expected to increase cluster concentrations by only $\lesssim 20\%$ (e.g., Duffy et al. 2010; Mead et al. 2010). Larger samples of lenses (e.g., Postman et al. 2012b) and close comparisons with X-ray observations (e.g., Morandi et al. 2010) should allow the significance of these trends to be verified or otherwise in the near future.

5.7.2 The uniformity of the total inner mass distribution and comparison to numerical simulations

While the mass–concentration relation has a significant intrinsic scatter of $\sigma_{c_{200}} \simeq 25\%$ (Neto et al. 2007, and higher when measured only in projection), the shape of the density profile is expected to be more uniform (e.g., Gao et al. 2012b). Thus, if the goal is a precise measure of the shape of the mass profile, i.e., its logarithmic slope, sample size is secondary to the density and radial extent of observational constraints. The combination of data sets we have presented provides precise constraints over the full range of radial scales, and thus forms an excellent basis for detailed study of the density profile, particularly in the inner regions.

The slope of the total density profile at small radii is very similar within our sample (Section 5.2).

[11] Figure 5.11 represents an extrapolation to higher masses than are contained in the simulations on which their model is calibrated.

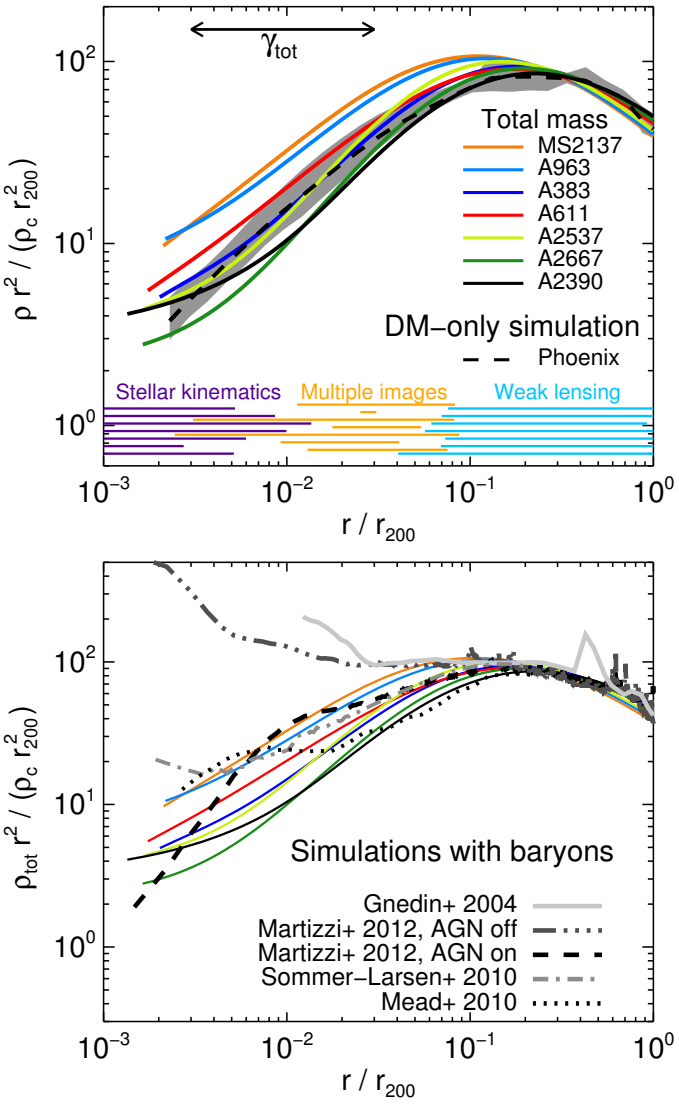

Figure 5.12: Top: Total scaled density profiles for the full sample (colored lines) are compared to simulated clusters – containing only DM – from the Phoenix project (Gao et al. 2012b). The dashed line shows the mean of the seven simulated Phoenix clusters, while the gray band outlines the envelope they define. Observed profiles are plotted down to 3 kpc. The radial range spanned by each data set is indicated at the bottom, and the interval over which $\gamma_{\rm tot}$ is defined is shown at the top of the panel. Note that the density has been multiplied by r^2 to reduce the dynamic range; thus, an isothermal slope $\rho \propto r^{-2}$ is horizontal. **Bottom:** The observed total density profiles (thin lines, as in left panel) are compared to several hydrodynamical simulations that include baryons, cooling, and feedback. The Gnedin et al. (2004) results are taken from their Figure 2, the Sommer-Larsen & Limousin (2010) curves refer to their Coma "Rz2" simulation, and the Mead et al. (2010) results are for their C4 simulation with cooling, star formation, and AGN feedback.

In Figure 5.12 we compare the measured density profiles, scaled by the virial radius r_{200}, to recent numerical simulations. In the top panel these are overlaid on spherically averaged density profiles from the Phoenix project (Gao et al. 2012b), introduced in Section 5.4.1. The range of density profiles spanned by the seven simulated clusters is illustrated by the gray band. Remarkably, the observed *total* density profiles closely parallel the Phoenix clusters that contain *only DM*, despite the fact that the stellar mass in the BCG contributes noticeably within $\simeq 30$ kpc ($\simeq 0.02 r_{200}$, comparable to R_e). Since our parametric models for the DM halo have the same large-radius behavior as the NFW profile, similar behavior at $r/r_{200} \gtrsim 0.3$ is guaranteed. At smaller radii, however, the agreement is not trivial, since it results from a combination of the concentration and inner slope (r_s and β or b) of the halo and the contribution of stellar mass ($\Upsilon_{*\mathrm{V}}$). The high concentrations of MS2137 and A963 cause them to appear shifted leftward of the Phoenix clusters in this plot, but even in these cases the *slope* of the density profile is similar. The bottom of the panel indicates the radial intervals over when the models are constrained by the various data sets.[12]

The similarity of the observations to DM-only simulations suggests that the net effect of adding baryons to the cluster core should mainly be to displace DM such that the total density does not change much at radii $\gtrsim$ 5–10 kpc. In the bottom panel of Figure 5.12 we compare our results to several hydrodynamical simulations that include baryons, cooling, and star formation (Gnedin et al. 2004, G04; Sommer-Larsen & Limousin 2010, SL10; Martizzi et al. 2012b, M12). In general many such simulations suffer from a well known "overcooling" problem (see discussions and solutions in, e.g., G04, McCarthy et al. 2010; Puchwein et al. 2010; Teyssier et al. 2011), in which the inability to suppress late cooling leads to the formation of far too much stellar mass at the cluster center. The build-up of baryons then leads to a significant contraction of the halo, increasing the central DM density. Thus in the G04 and M12 "AGN off" simulations, the central densities are much too high; even the density of DM alone (not plotted) exceeds the measured *total*. SL10 estimated the effects of overcooling through an ad hoc simulation in which late-forming stars were slowly removed following $z = 2$ (their "Rz2" runs). This ameliorates the problem but still leaves a steeper total density slope than observed, with $\gamma_{\mathrm{tot}} = 1.5$.

M12 performed a very high-resolution simulation that included feedback from an AGN. Interestingly, the AGN is effective not only at quenching late star formation but also at removing DM from the center. The latter is accomplished through several mechanisms that M12 discuss, including rapid fluctuations in the potential due to expulsion of gas during AGN outbursts.[13] The process is rather too effective, as it results in a 10 kpc stellar core that is much bigger than the largest observed example (Postman et al. 2012a). Still, this work points to a possibly important role for the

[12] Minor "wiggles" appearing $r/r_{200} \approx 10^{-2}$ should not be overinterpreted given that we lack constraints there and the mass model parameterization is simple.

[13] This is similar to the mechanism suspected of producing cores in dwarf galaxies, fueled in that case by supernovae (Pontzen & Governato 2012).

supermassive black hole in shaping the small-scale DM distribution. Mead et al. (2010) also found that the inclusion of AGN feedback results in more realistic total density profiles in their simulations. Although overcooling is significantly alleviated, the total density slope remains somewhat steeper ($\gamma_{\rm tot} = 1.7$) than we observe. We note that, except for SL10, the simulated clusters discussed here are less massive ($M_{200} \simeq 1$–$4 \times 10^{14}\,{\rm M}_{\odot}$) than the observed sample. High-resolution simulations of more massive clusters are needed to make a more detailed comparison.

Currently, the observed total density profiles appear more similar to those in CDM-only simulations than to results from hydrodynamical simulations, although the inclusion of AGN feedback in high-resolution simulations is producing much improved results. The similarity of the total density slope is quantified further in the top panel of Figure 5.13, which compares the $\gamma_{\rm tot}$ measurements of individual clusters, along with their inferred parent distribution (dashed; see Section 5.2), to the inner slopes of the Phoenix clusters defined in the same manner. The mean slope $\gamma_{\rm tot} = 1.13 \pm 0.02$ in the CDM-only Phoenix simulations agrees well with measured total density slope: $\langle\gamma_{\rm tot}\rangle = 1.16 \pm 0.05$ (random) $^{+0.05}_{-0.07}$ (systematic). The intrinsic scatter in $\gamma_{\rm tot}$ is possibly larger in the observations, but this cannot be asserted with much certainty due to the systematic limitations discussed in Section 5.5. We stress again that these are DM-only simulations and that their relevance to the total mass in real clusters over this range of radii is surprising.

The uniformity of the total inner mass distribution is futher supported by the striking homogeneity in the shapes of the velocity dispersion profiles. The bottom panel of Figure 5.13 plots these profiles normalized to the observed dispersion at $R = 3$ kpc. With this single scaling, the velocity dispersion profiles for all seven clusters are mutually consistent within their uncertainties. In this figure, we also compare to the BCG of the nearby cluster A2199 ($z = 0.03$; Kelson et al. 2002). Where the data overlap they are consistent with our sample, except at $\lesssim 1$ kpc where the black hole is probably dynamically significant (note that we cannot resolve these scales due to the slit width and seeing).[14] Although rising σ profiles in cD galaxies have been observed since Dressler (1979), there has been some uncertainty (e.g., Fisher et al. 1995; Dubinski 1998; Carter et al. 1999; Hau et al. 2004) about the frequency of this phenomenon, which is the expected response of stars to the central cluster potential. Our observations suggests that it is ubiquitous in BCGs that are well aligned with the centers of relaxed clusters.

5.7.3 The role of baryons in shaping the small-scale dark matter profile

In ΛCDM-based models the formation of BCGs is expected to occur relatively late and be dominated by dry (dissipationless) merging (e.g., de Lucia & Blaizot 2007). Since NFW profiles are simply the product of collisionless collapse and merging, one interpretation of our findings is that the processes

[14]The Kelson et al. (2002) data are higher than our models at radii $\gtrsim 25$ kpc, beyond the outer limits of our velocity dispersion measures but within the range of $\simeq 30 - 100$ kpc where strong lensing constrains the mass. This could indicate that the dynamical structure becomes less homogeneous near R_e.

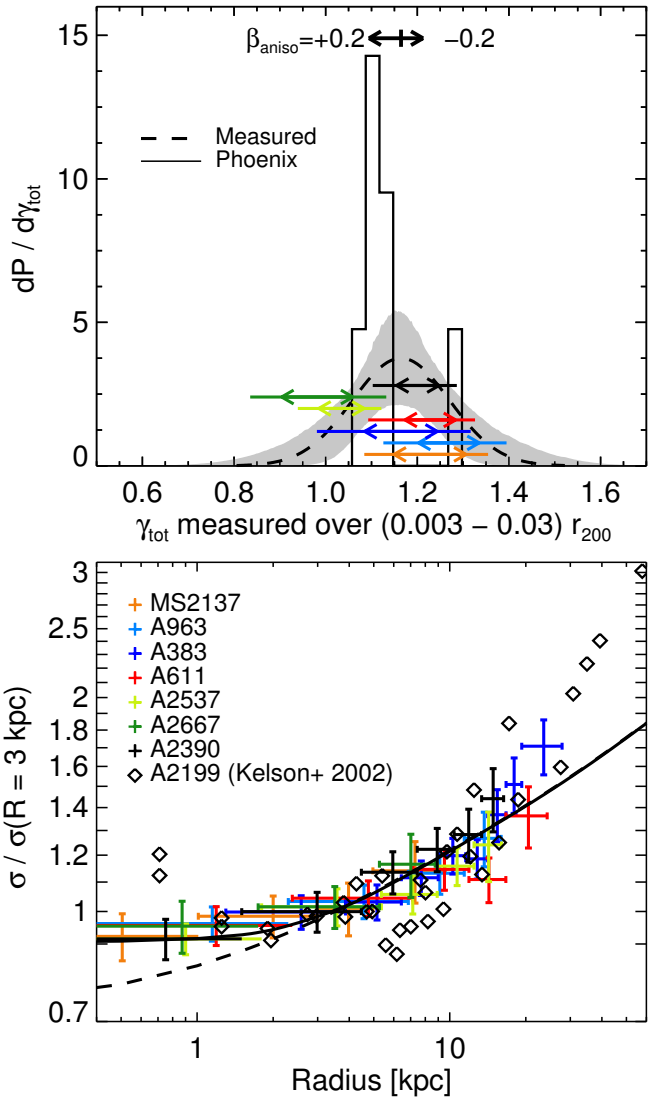

Figure 5.13: Top: The total inner density slope $\gamma_{\rm tot}$ is shown for each cluster (colored lines, following the legend in Figure 5.12) and compared to the slopes derived for the Phoenix clusters (DM-only simulations, black histogram). For the individual observed clusters, inner arrows and the full length of each line indicate the 68% and 95% confidence intervals, respectively. The inferred Gaussian parent population (Section 5.2) is shown by the dashed curve, with the gray band showing the 68% confidence region. The effects of mild orbital anisotropy on the observational results are illustrated at the top of the panel. **Bottom:** Velocity dispersion data, as in Figure 3.17, normalized for each cluster by $\sigma_{\rm los}$ at $R = 3$ kpc by interpolating the measurements. Diamonds indicate measurements in NGC 6166, the BCG of A2199 ($z = 0.03$), from Kelson et al. (2002). The solid line shown the mean of the mass models for the full sample, normalized in the same way, while the dashed line shows the same if observational effects (slit width and seeing) are excluded.

that set the inner density profile in clusters are primarily gravitational. Understanding how the total density profile remains similar to that expected of CDM alone is not trivial. Loeb & Peebles (2003) and Gao et al. (2004) hypothesized that repeated merging might drive the total collisionless (stars and DM) density toward an NFW-like profile, noting that this could solve two puzzles: the lack of very high-dispersion galaxies with $\sigma_e \gtrsim 400$ km s^{-1}, and our own earlier observations that the DM density profile is shallower than the NFW form in cluster cores (Sand et al. 2002, 2004). As a starting point, based on both analytic arguments and CDM simulations, they showed that the mass in the central regions of present-day massive clusters changes very little at $z \lesssim 6$, but the identity of these particles changes considerably. The particles arriving in mergers displace those already present, maintaining the central density.

In reality we expect the progenitors of the BCG and the infalling galaxies to have been compressed due to baryon loading (e.g., Blumenthal et al. 1986, and see references in Section 1). Indeed, the total density profiles we derive do appear to steepen slightly in the inner $\simeq$ 5–10 kpc. This is the regime in which the stellar density exceeds that of DM. Although it is difficult to pinpoint this scale precisely, it is certainly well within the present effective radius (median $\langle R_e \rangle = 34$ kpc), where stars begin to contribute non-negligibly to the total density. Furthermore, this scale bears a striking similarity to sizes of the most massive galaxies at high redshift, which many observations now indicate are quite compact (e.g., Trujillo et al. 2006; van Dokkum et al. 2008; Williams et al. 2010; Newman et al. 2012). For example, a simple extrapolation of the observed stellar mass–size relation at $z \approx 2.5$ (Newman et al. 2012) would yield a size of $R_e \sim$ 2–6 kpc for likely progenitors.[15] Indirect support for this comes from our observation (Figure 5.3) that the mass contained in the inner 5 kpc – mostly stars, but only a small fraction of the stars in the present BCG – is correlated with the mass of the cluster core within 100 kpc, which is also expected to be in place by $z \approx 3$ and change relatively little subsequently (G04, Figure 1). Interestingly, color gradients in BCGs (when present) occur mostly at $R \gtrsim 10$ kpc, while the innermost regions are more homogeneous in both color and luminosity (Postman & Lauer 1995; Bildfell et al. 2008).

This suggests a picture in which stars in the innermost $\simeq$ 5–10 kpc are formed early within the BCG progenitor, where dissipation establishes a steep stellar density profile, while subsequent dry merging of infalling satellites mostly adds stars to the outer regions of the BCG in a manner that nearly maintains the total density. This requires that the stars and DM arriving in mergers displace a roughly equal amount of existing DM. Simulations indeed indicate that stars arriving in minor (low mass ratio) mergers, which dominate the accretion history of very massive galaxies, are primarily added to the outskirts of the BCG (e.g., Naab et al. 2009; Laporte et al. 2012). However, the precise effect of these mergers on the DM already in place is not clear. Using dissipationless N-body

[15] We caution that low-z BCGs do not lie on a simple extrapolation of the trend defined by lower-mass ellipticals (e.g., von der Linden et al. 2007), but the situation for the very most massive galaxies at high-z is uncertain due to the small volumes surveyed.

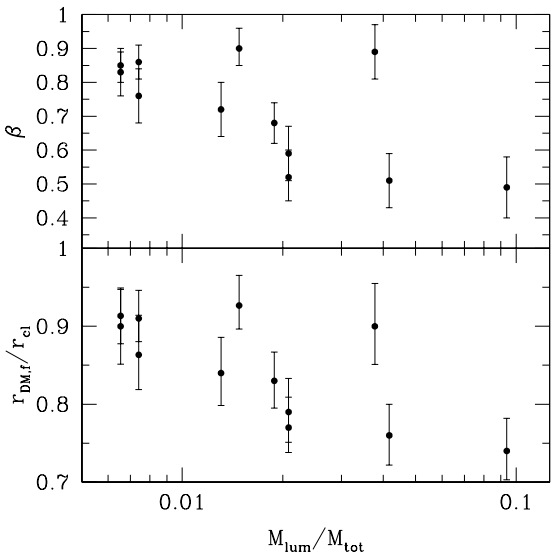

Figure 5.14: Left: Final inner DM density slope β (top) and break radius $r_{\rm DM,f}$ (relative to the initial break radius; bottom) compared to the fraction of the total cluster mass in stars, as seen in a suite of purely dissipationless simulations following the mergers of several BCG progenitors over $z = 0 - 0.6$. Note the negative correlation between the DM slope and the final stellar mass of the BCG, which is qualitatively similar to our Figure 5.9. The figure is reproduced from Nipoti et al. (2004).

simulations, several authors have shown that dynamical friction of the infalling satellites on the halo can "heat" the cusp and reduce the central DM density (e.g., El-Zant et al. 2001; Nipoti et al. 2004; Jardel & Sellwood 2009, and see references in Chapter 2), and that this can more than overcome the deeper central potential that results from the central build-up of baryons. Figure 5.14 shows how the DM profile varies with the mass of the BCG in the simulations of Nipoti et al. (2004). These simulations follow the mergers of several massive $z = 0.6$ galaxies at the bottom of a cluster-scale DM halo, which coalesce to form a BCG by $z = 0$. As the properties of the progenitors are varied, Nipoti et al. (2004) find that flatter DM cusps are produced by $z = 0$ in simulations with more massive merger remnants (BCGs). This correlation between the inner DM halo and the assembled stellar mass is qualitatively in agreement with our observations in Figure 5.9; this correlation is expected if the net effect of adding stars is to scatter DM particles to larger orbits. Del Popolo (2012) discusses a similar correlation arising in their analytic models for the same physical reason.

Nonetheless, this process is sensitive to the nature of the satellites (e.g., Ma & Boylan-Kolchin 2004; Jardel & Sellwood 2009), and a fully realistic treatment has been lacking in cluster simulations to date. Satellites will bring in their own DM, counteracting this central depletion. A shortcoming of the Nipoti et al. (2004) simulations is that the progenitor galaxies are purely stellar, whereas we know that galaxies in cluster cores retain individual DM subhalos (e.g., Natarajan et al. 2009). Furthermore, tightly-bound galaxies are more effective at dynamical friction heating, since they are

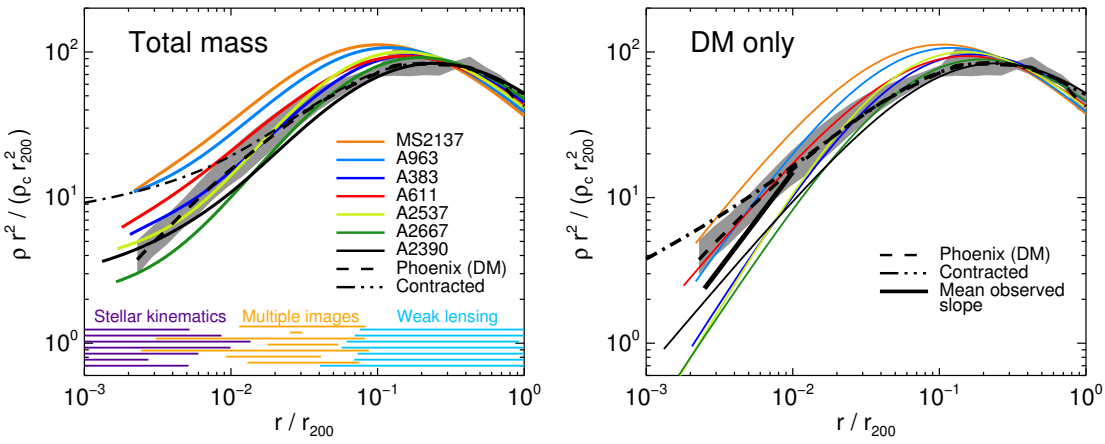

Figure 5.15: Left: *Total* density profiles, including baryons and DM, for our sample are overlaid on CDM-only simulations of massive clusters, as in top panel of Figure 5.12. The dot-dashed line shows the result of an AC model, in which we applied the prescription of Gnedin et al. (2011) to an NFW halo with concentration $c_{200} = 4.5$ and a BCG described by a Jaffe (1983) profile with scale length $r_J/r_{200} = 0.02$ and mass fraction $M_*/M_{200} = 0.002$, which are representative of our sample. Model parameters of $A_0 = 1.5, w_0 = 0.85$ were used. **Right:** As in the left panel, but showing DM only. (The Phoenix simulations thus do not change.) Note that CDM halos match the observed total density slopes better than those of DM alone. The inclusion of halo contraction (dot-dashed line) only exacerbates the difference with the mean observed DM slope (thick black segment).

more resistant to stripping and so survive longer. Laporte et al. (2012) point out that the compact stellar configuration observed in high-z massive galaxies is significant in this context. They find that as stars in the progenitors are made more compact, the dark matter profile of the $z = 0$ merger product is shallower. Interestingly, when a stellar mass–size relation in line with $z \gtrsim 2$ observations is imposed in their simulations, the central DM cusp is flattened to $\beta \simeq 0.3$–0.7, comparable to our observations. The interpretation of their results is uncertain, since they rely on reinterpretations (i.e., the identification of collisionless particles as DM versus stars) of a single dissipationless simulation; therefore, the dark matter profile of the $z = 2$ progenitors is forced to be the fixed total mass less the target stellar distribution, rather a cosmologically-motivated halo. Martizzi et al. (2012b) show that infalling central black holes in the BCG progenitors can also have a significant effect on the DM profile through three-body effects in the late merger. In summary, it is plausible that purely dynamical processes could flatten the DM density profile and produce the correlation with the stellar distribution that we observe. However, improved high-resolution cluster-scale simulations (even dissipationless ones) with a more realistic and consistent treatment of the satellites are needed to verify this.

In this scheme there is little room for additional contraction or steepening of the mass profile, and the relevant physics is primarily dissipationless. In contrast, a major focus in the theoretical literature has been the "adiabatic contraction" (AC) formalism (Blumenthal et al. 1986) and its modified versions (e.g., Gnedin et al. 2004, 2011), which predict the *steepening* of the inner DM

profile resulting from the slow cooling and central condensation of baryons. In contrast to the scheme described above, in which the orbital energy lost by infalling stellar clumps is transferred to the halo, the energy lost by baryons is radiated and lost from the system; thus, the AC model emphasizes the role of *dissipation* in forming the BCG (e.g., Lackner & Ostriker 2010). This model takes no account of mergers at all.

Figure 5.15 compares our measurements to the mean density profiles from the CDM-only Phoenix simulations, and to the result of applying the modified AC model of Gnedin et al. (2011) based on a CDM halo and BCG with parameters typical of our sample (dot-dashed line; see details in caption). This shows clearly that the DM-only simulations are a much better match to the total density slope (left panel) than to that of the DM alone (right). As expected, the DM profile steepens when including AC, which only worsens the disagreement with our observations. It has been argued that this increase in central DM density from AC will boost the gamma-ray flux from DM annihilation in clusters (Ando & Nagai 2012).[16] However, our results suggest that AC is not the main process that sets the density profile and that the net effect on the halo is actually the opposite of its predictions. (As we describe below, this does not necessarily imply that the same theory cannot make valid predictions at the galaxy scale, where the star formation efficiency and assembly history are very different.) The relevance of AC in describing the results of earlier cosmological simulations with gas probably reflects the known overcooling problem that cause the effects of dissipation to be overstated. The inclusion of AGN appears to solve most of this problem and may additionally lower the central DM density (Section 5.7.2).

Given that several baryonic mechanisms may play a role in altering the small-scale DM distribution (contraction from gas cooling, dynamical friction from infalling clumps, potential fluctuations due to AGN-driven gas outflows), continually improving simulations will be essential to better understand their relative importance, and our observations will provide a basis for detailed comparison. Martizzi et al. (2012a) recently coupled a full cosmological cluster simulation with idealized simulations in order to isolate the most important physics for setting the inner DM profile. They found that dynamical friction from satellites initially flattens the DM cusp. Contraction from gas cooling becomes important at later times. At still later epochs, when the black hole is sufficiently massive, its effect on the central DM through fluctuations in the gas density is the dominant one.

The results we present for BCGs are quite different from observations of massive field ellipticals, which uniformly show a total density slope within their effective radii that is nearly isothermal ($\rho_{\rm tot} \propto r^{-2}$; Treu et al. 2006; Koopmans et al. 2009; Auger et al. 2009). The massive halos we consider are much less efficient at converting their baryons into stars (e.g., Guo et al. 2010; Leauthaud et al. 2012). As a consequence, BCGs are much more DM-dominated, so it is not surprising that dissipation would play a lesser role in their formation. The greater importance of minor mergers in

[16] In any case, the highly uncertain contribution from subhalos may dominate this signal (e.g., Gao et al. 2012a).

their assembly may also be important (Naab et al. 2009). Thus, our results do not directly conflict with studies claiming that AC effects may be significant in lower-mass ellipticals (e.g., Dutton et al. 2011; Sonnenfeld et al. 2012). They do show if the currently discussed prescriptions for halo contraction are valid, they have a limited range of applicability that likely varies with star-formation efficiency and assembly history. Although the isothermal and NFW limits have often been discussed as special configurations in the literature, we should be able to see intermediate density slopes in galaxy groups. Indeed, this may have already be observed by Spiniello et al. (2011) and Sonnenfeld et al. (2012).

5.7.4 Possible signatures of dark matter microphysics

In addition to the effect of baryons on the halo, various DM particle scenarios have also been proposed to reduce tension between CDM and observations on small scales, including the "missing satellites" problem and evidence for central DM cores or shallow cusps (for a recent review, see Primack 2009). These include warm sterile neutrinos at the $\sim$ keV scale (e.g., Abazajian et al. 2001; Boyarsky et al. 2009; Macciò et al. 2012; Menci et al. 2012), "fuzzy" CDM composed from an ultralight scalar particle (Hu et al. 2000; Woo & Chiueh 2009), DM produced from early decays (Kaplinghat 2005), and DM that itself decays with a long timescale (Peter et al. 2010), among many other possibilities. The goal is to preserve the large-scale successes of CDM, while allowing for modifications at higher densities where the detailed properties of the DM particle might manifest. A scenario for which halo density profiles has been worked out in detail is a self-interacting DM particle (Spergel & Steinhardt 2000; Yoshida et al. 2000; Davé et al. 2001). Rocha et al. (2012) and Peter et al. (2012) showed that a cross-section $\sigma/m \sim 0.1$ cm^2 g^{-1} can produce ≈ 20 kpc cores in clusters without violating any current constraints, e.g., from the asphericity of cluster cores or the Bullet Cluster (Randall et al. 2008). Only the dense central regions of the halo are affected, where scattering can occur within a Hubble time.

These ≈ 20 kpc core sizes are intriguingly similar to our observations. On the other hand, they are also very similar to the scale of the baryons, i.e., the size of the BCG. It is unclear why the total density profile should then match the shape expected of collisionless CDM. In these scenarios, the core size arises from the microphysics of the DM particle and presumably should not "know" about the size of the central galaxy (Figure 5.9), for example. Thus, observations of clusters alone cannot provide unambiguous support for alternative DM theories. Global comparisons across a wide range of mass scales (for instance, a cross-section that also produces correct core sizes and densities in dwarf galaxies) remain an essential test for attempts to explain low central halo densities in terms of the DM particle.

5.8 Summary

We presented observations of a sample of seven massive, relaxed galaxy clusters at $\langle z \rangle = 0.25$. The data comprise 25 multiply imaged sources (21 with spectroscopic redshifts, of which 7 are original to this work) that present 80 images, weak lensing constraints from multi-color imaging, and spatially resolved stellar kinematics within the BCGs. Taken together, these data from the *HST*, Subaru, and Keck telescopes extend from $\simeq 0.002 r_{200}$ to beyond the virial radius, providing detailed constraints on the global mass distribution.

1. We find that the clusters in our sample are not strongly elongated along the l.o.s. (except A383) and that their intracluster media are close to equilibrium, based on the agreement between mass profiles derived from independent lensing and X-ray observations (Section 4.3.2).

2. Physically motivated and simply parameterized models provide good fits to the full range of data. The inner logarithmic slope of the total density profile measured over $r/r_{200} = 0.003$–0.03 (on average, 5–55 kpc) is remarkably uniform, with

$$\langle \gamma_{\rm tot} \rangle = 1.16 \pm 0.05 \text{ (random) } {}^{+0.05}_{-0.07} \text{ (systematic)}$$

   and an intrinsic scatter $\sigma_\gamma = 0.10^{+0.06}_{-0.04}$ ($\sigma_\gamma < 0.13$ at 68% confidence). The mean is consistent with the slope 1.13 ± 0.02 measured in the same manner in *CDM-only* cluster simulations (Gao et al. 2012b).

3. Supporting the uniformity of the inner mass distribution, the extended stellar velocity dispersion profiles show a clear rise with radius and display a very homogeneous shape after a single scaling.

4. By comparing the stellar mass of the BCGs derived from lensing and dynamics with estimates from SPS models, we find a mean offset of $\langle \log \alpha_{\rm SPS} \rangle = 0.27 \pm 0.05^{+0.10}_{-0.16}$ relative to a Chabrier (2003) IMF. This normalization is consistent with a Salpeter IMF, or one that is equivalently "heavy," in line with several recent studies based on lensing, dynamics, and detailed spectral synthesis models. These rapid developments in our understanding of stellar populations promise significant advances in disentangling the distributions of dark and baryonic mass across a range of systems.

5. Incorporating these joint constraints on the BCG stellar mass from the entire sample, we reduce the remaining degeneracy between dark and stellar mass on small scales and derive a mean inner DM density slope of $\langle \beta \rangle = 0.50 \pm 0.13^{+0.14}_{-0.13}$, shallower than a canonical NFW profile with $\beta = 1$. The data are equally consistent with a mean core radius of $\langle \log r_{\rm core}/{\rm kpc} \rangle = 1.14 \pm 0.13^{+0.14}_{-0.22}$.

6. We find a likely correlation between the inner DM profile and the properties (size, luminosity) of the BCG, suggesting a connection between DM in the cluster core and the assembly of stars in the central galaxy.

7. The shape of the *total* density profile is in surprisingly good agreement with high-resolution simulations containing only CDM, despite a significant contribution of stellar mass within the BCG over the scales we measure. Hydrodynamical simulations including baryons, cooling, and feedback currently provide poorer descriptions, although the inclusion of AGN in recent high-resolution simulations has resulted in a major improvement.

8. Our findings support a picture in which an early dissipative phase associated with star formation in the BCG progenitor establishes a steeper total density profile in the inner ≈ 5–10 kpc – comparable to the size of very massive, red galaxies at $z > 2$ – while subsequent accretion of stars (still within the present effective radius) mostly replaces DM so that the total density is nearly maintained. Improved simulations are needed to clarify the physical origin of the small-scale dark and stellar density profiles, and the observations presented here will provide strong constraints.

Acknowledgments

It is a pleasure to thank Jason Rhodes, Joel Berge, Jean-Paul Kneib, Graham Smith, Richard Massey, Annika Peter, Marceau Limousin, and Simon White for their assistance, comments, and stimulating discussion. We thank Liang Gao, Davide Martizzi, and Jesper Sommer-Larsen for providing tabulated results from their simulations. We are grateful to Steve Allen for kindly providing X-ray measurements of the A611 gas and A383 mass profiles. Some of the data presented were obtained at the W.M. Keck Observatory. The Observatory was made possible by the generous financial support of the W.M. Keck Foundation. The authors recognize and acknowledge the cultural role and reverence that the summit of Mauna Kea has always had within the indigenous Hawaiian community. We are most fortunate to have the opportunity to conduct observations from this mountain.

5.9 Appendix

In Section 5.4.2, we described how posterior probability distributions $P(\beta)$ and $P(\log r_{\rm core})$ are derived for each cluster by weighting the samples in the Markov chains. The weights

$$w = \frac{1}{\sqrt{2\pi}\sigma} \exp\left[-\frac{1}{2}\left(\frac{\log\alpha_{\rm SPS} - \langle\log\alpha_{\rm SPS}\rangle}{\sigma}\right)^2\right] \tag{5.4}$$

effectively convert a flat prior on $\log \alpha_{\rm SPS}$ (Section 4.1) to a Gaussian with mean $\langle \log \alpha_{\rm SPS} \rangle = 0.27$ and a dispersion $\sigma = (\sigma_\alpha^2 + \sigma_{\rm SPS}^2)^{1/2}$. This dispersion accounts for two sources of error: the uncertainty $\sigma_\alpha = 0.05$ dex in the global systematic offset $\langle \log \alpha_{\rm SPS} \rangle$ from SPS estimates $\Upsilon_{*\rm V}^{\rm SPS}$, and the random photometric uncertainty $\sigma_{\rm SPS} = 0.07$ dex in $\Upsilon_{*\rm V}^{\rm SPS}$ for each cluster. The first uncertainty is correlated across the entire sample, while the second is not.

Therefore, to obtain constrains on the mean $\langle \beta \rangle$ and $\langle \log r_{\rm core} \rangle$, the probability distributions derived for each cluster in this manner cannot simply be multiplied, since they are not independent. Instead, we calculate the posterior probability of $\langle \beta \rangle$ as

$$P(\langle \beta \rangle) \propto \int P(\langle \beta \rangle | \log \alpha_{\rm SPS}) P(\log \alpha_{\rm SPS})\, d\alpha_{\rm SPS}. \tag{5.5}$$

Here $P(\langle \beta \rangle | \log \alpha_{\rm SPS})$ is the posterior distribution of $\langle \beta \rangle$ at a fixed value of $\log \alpha_{\rm SPS}$. It is obtained by multiplying the probability densities $P(\beta | \log \alpha_{\rm SPS})$ for the seven clusters in our sample, which are each computed with Gaussian weights centered at the fixed value of $\log \alpha_{\rm SPS}$ and a dispersion $\sigma_{\rm SPS}$ (i.e., $\sigma = \sigma_{\rm SPS}$ in Equation 5.4; we now account for only the random photometric errors in $\Upsilon_{*\rm V}^{\rm SPS}$ since $\log \alpha_{\rm SPS}$ is fixed). $P(\log \alpha_{\rm SPS})$, which represents our constraint on the common stellar mass scale, is simply a Gaussian with mean $\langle \log \alpha_{\rm SPS} \rangle = 0.27$ and dispersion $\sigma_\alpha = 0.05$ dex, as derived in Section 5.3 for isotropic orbits.

We estimate the intrinsic scatter in β (Section 5.4.2) using the posterior probability densities $P(\beta | \log \alpha_{\rm SPS} = 0.27)$ for each cluster. That is, we evaluate the cluster-to-cluster scatter in β at a fixed value of $\log \alpha_{\rm SPS}$. All of the above comments apply equally to our study of the cNFW models, simply replacing β by $\log r_{\rm core}$.

Chapter 6

Part II: The Growth and Merger History of Quiescent Galaxies since $z = 2$

Galaxies in the local universe exhibit striking bimodalities and correlations in their physical properties (reviewed by Roberts & Haynes 1994) that provide clues to their origins. In the color–magnitude diagram, galaxies separate into a "blue cloud," comprised of star-forming galaxies, and a "red sequence," whose members contain old stars and are nearly devoid of current activity. A correlation with morphology and dynamical structure has long been recognized (Holmberg 1958): red galaxies tend to be spheroidal systems, supported primarily by pressure, whereas blue galaxies tend to be rotating disks. Color and morphology also correlate with spectral type and indicators of star formation history. There is a fairly sharp transition in stellar mass, with galaxies exceeding $M_* \approx 3 \times 10^{10}\,\mathrm{M}_\odot$ predominately being red spheroids (Kauffmann et al. 2003b). At least half of the stars in the present universe are found in spheroidal galaxies (Bell et al. 2003). The fraction of galaxies that are red or spheroidal is higher in denser environments (Dressler 1980), and the most massive galaxies found in the centers of clusters are exclusively ellipticals. While exceptions can be found to all of these correlations (Renzini 2006), understanding the origin of these observed regularities is vital to uncovering the story of galaxy formation.

Part II of this thesis is concerned with the evolution of red galaxies.[1] Historically, two scenarios were widely debated for the formation of red galaxies. The "monolithic collapse" picture involves direct gravitational collapse of primordial gas (Eggen et al. 1962; Larson 1975). Violent relaxation allows particles to exchange energy on a short timescale and accounts for the disordered stellar motions characterizing ellipticals. Star formation occurs early and rapidly and is followed by simple passive fading of the stars to the present. In this picture, the formation of stars and the assembly of the galaxy occur simultaneously.

[1] When necessary, we use "quiescent" to emphasize a genuinely low star-formation rate, as opposed to galaxies reddened only by virtue of dust. "Spheroids" and "spheroidal galaxies" includes elliptical and lenticular (S0) galaxies.

While monolithic collapse can explain some key features of the elliptical population, such as the observation that stars in massive ellipticals formed early and rapidly, it lacks cosmologically-motivated initial conditions. Modern theories of galaxy formation follow the collapse of early density perturbations imaged in the CMB. As described in Chapter 2, structure formation in CDM cosmologies proceeds in a "bottom-up" fashion, with larger halos built up from smaller ones. The epoch of *star formation* may be very different from that of *mass assembly*, which is more gradual. Galaxy mergers are fundamental to the hierarchical model, and disk–disk mergers are typically invoked to explain the formation of spheroids (Toomre 1977; Barnes & Hernquist 1992). As hierarchical models have accommodated progressively earlier formation of massive galaxies forced by observations, the distinction between the two theories has been blurred. Modern theories effectively include some aspects of both (see discussion in Mo, van den Bosch, & White 2010).

In this chapter, we first review the main clues to the formation of ellipticals, both those provided by the "fossil record" of local galaxies and by observations to lookback times of ~ 8 Gyr ($z \sim 1$). We then review the role of mergers in interpreting these observations and current open questions. After briefly describing the discovery and characterization of high-redshift quiescent galaxies at $z = 1$–2.5 over the past decade, we turn to evidence for substantial structural evolution in the quiescent galaxy population since $z \approx 2.5$, which is the main subject of Chapters 7 and 8. We summarize evidence for growth in size (half-light radius) by a factor of $\simeq 4\times$ over this interval and place this remarkable evolution in the context of earlier work. Finally, we describe the associated uncertainties in both the observations and the proposed physical drivers of this growth, and outline the specific routes toward addressing these in Part II.

6.1 Fossil evidence from nearby spheroidals

Local elliptical galaxies delineate a number of tight correlations between their physical parameters that supply clues to their formation. The trend between color and absolute magnitude of ellipticals and its potential use in understanding their stellar populations were recognized by Baum (1959) and Visvanathan & Sandage (1977). Using precise and uniform CCD photometry of ellipticals in the Virgo and Coma clusters, Bower, Lucey, & Ellis (1992) made an important advance in demonstrating the uniformity and small scatter ($\sigma_{U-V} < 0.04$ mag) of the color–magnitude relations. To achieve such a small scatter, they showed that the stars in cluster ellipticals must have formed at $z \gtrsim 2$ unless their formation was improbably synchronized. Likewise, they found that subsequent bursts of star formation cannot contribute more than $\sim 10\%$ of the present light.

The slope of the color–magnitude relation is ascribed to systematic variations in metallicity with luminosity, with more massive systems being more metal-rich. Spectral absorption diagnostics can in principle constrain the age, metallicity, and chemical abundance patterns separately, although

the models and data necessary to perform this reliably have arrived only fairly recently (see review by Renzini 2006). Bender et al. (1993) demonstrated the tightness of the Mg b–σ correlation, which relates the equivalent width of the Mg triplet to the stellar velocity dispersion. This restricts variations in age or metallicity at a given σ to $< 15\%$ if the other is held fixed. In a landmark paper, Thomas et al. (2005) showed that age, metallicity, and [α/Fe] are all positively correlated with σ. Since the production of Fe-peak elements lags that of α elements, owing to their respective production in Type Ia and core-collapse supernovae, [α/Fe] functions as a "clock" for the timescale of star formation activity. Thomas et al. (2005) inferred that most massive ellipticals form their stars *earlier* and *more rapidly*.

In addition to the above relations involving their stellar populations, spheroidal galaxies obey tight correlations among their structural parameters. In particular, they occupy a narrow plane in the space spanned by σ, the effective radius R_e, and the luminosity L (or equivalently, the effective surface brightness $I_e = L/\pi R_e^2$) known as the *fundamental plane* (FP, Djorgovski & Davis 1987; Dressler et al. 1987). Among its projections are the classical L–σ (Faber & Jackson 1976) and R_e–I_e (Kormendy 1977) scaling relations. The form and scatter in the FP and its projections are important constraints on assembly history. Importantly, the FP "tilts" slightly away from the form $L \propto \sigma^2 R_e$ expected from a naive application of the virial theorem, under the assumptions that ellipticals are a self-similar "homologous" family with a uniform M/L. This could indicate either a lack of homology or a variation in M/L. Evidence from the latter comes from the lack of tilt seen in the "mass plane," in which the mass measured from lensing or detailed dynamical models is used in place of L (Bolton et al. 2008; Cappellari et al. 2012b). This variation is highly tuned: as the luminosity increases by a factor of ~ 100 and M/L increases by a factor of ~ 3, the scatter in M/L remains $\lesssim 10\%$ through the FP (Bender et al. 1992; Renzini 2006).

The form of the fundamental plane and the scaling relations described above are generally shown to vary weakly with environment (Eisenstein et al. 2003; Bernardi et al. 2003b; Hogg et al. 2004; Nair et al. 2010). Although differences can be detected with the statistical power of modern surveys, it is clear that mass is a much more important determinant of an elliptical's properties at $z = 0$ than local density. The velocity dispersion σ, which serves as a proxy for the depth of the central potential, is likely even more fundamental, as it correlates most directly with properties of the stellar population (e.g., Graves et al. 2009; van der Wel et al. 2009).

6.2 Lookback studies to $z \sim 1$

The precise local scaling relations are stringent boundary conditions that any theory for the formation of ellipticals must meet, but they do not specify the formation history of ellipticals uniquely. For example, a simple "monolithic collapse" picture followed by passive stellar evolution could plausibly

account for many of the observations described above. To make further progress it is essential to observe the progenitors of today's ellipticals at significant lookback times. Furthermore, since *ab initio* simulations currently cannot produce fully realistic galaxies, it is common to tune semi-analytic models to match $z = 0$ data. Observations at earlier epochs then provide the test.

One approach is to identify likely progenitors of present spheroids at higher redshifts, typically selected by morphology,[2] in order to measure the rate of evolution in color and M/L. The resolution of *HST* imaging is essential to perform this morphological identification. Ellis et al. (1997) identified spheroidals in a $z = 0.5$ cluster and measured their color–magnitude relation, which they found to be indistinguishable in slope and scatter from that in Coma and Virgo within the observational uncertainties. The color evolution they detected was consistent with simple stellar aging. Extending the analysis of Bower, Lucey, & Ellis (1992), they inferred a star formation epoch $z \gtrsim 3$. The lack of evolution in the slope also provided direct evidence that its origin is due to metallicity and not age variation (Kodama & Arimoto 1997).

Assuming that luminosity fading dominates the evolution of the FP, its parallel shifting over time traces evolution in M/L (e.g., Treu et al. 2001). For a given cosmology and IMF this constrains the stellar age, and the constraint becomes increasingly powerful with data at earlier epochs. For a decade beginning in the mid 1990s, a string of studies pushed the FP to higher redshifts. The FP evolution was tracked in $z < 1$ clusters by, e.g., van Dokkum & Franx (1996), Kelson et al. (1997), van Dokkum et al. (1998), and Jørgensen et al. (2006); in a few cluster galaxies at $z \simeq 1.25$ by van Dokkum & Stanford (2003) and Holden et al. (2005); and in the field by Treu et al. (2002), van Dokkum & Ellis (2003), Gebhardt et al. (2003), and van der Wel et al. (2005), mostly based on spectroscopy at the Keck telescopes. These studies revealed slow luminosity evolution to $z \sim 1$ consistent with an early formation epoch $z \gtrsim 2$–3. A breakthrough came with Keck/DEIMOS spectroscopy of a large, well defined sample of field spheroidal galaxies at $z \approx 0.2 - 1$ with associated *HST* imaging (Treu et al. 2005). This analysis clearly showed that the rate of luminosity evolution and the scatter in M/L varies systematically with mass, which was taken as evidence that essentially all stars in the most massive spheroids formed early at $z \gtrsim 2$, whereas those in lower-mass systems continued forming later. This interpretation was corroborated by the higher frequency of optical emission lines and blue cores seen in the lower-mass spheroids.

This *downsizing* trend, in which the sites of active star formation move to lower mass galaxies over time, mirrors that seen in global studies of the galaxy population (e.g., Cowie et al. 1996; Bundy et al. 2006). The older stellar ages of more massive galaxies is sometimes called "anti-hierarchical" and has often been seen as paradoxical in light of the "bottom up" assembly that characterizes hierarchical growth. Modern semi-analytic models account for the downsizing by invoking feedback

[2]van Dokkum & Franx (1996) stressed the "progenitor bias" that will arise if the progenitors of the present spheroid population are not exclusively spheroids.

from an active nucleus to regulate cooling – thus depriving the galaxy of material for star formation – in sufficiently massive halos (e.g., Croton et al. 2006; Bower et al. 2006). A more fundamental tenet of the cosmological model is the hierarchical *assembly of mass*, in which the most massive galaxies are expected to *assemble* the latest via mergers (e.g., de Lucia & Blaizot 2007). To reconcile this with the observed lack of recent activity in these systems, "dry" mergers involving other red galaxies are commonly invoked. Dry mergers are observed through tidal features and close galaxy pairs (e.g., van Dokkum et al. 1999; Bell et al. 2006; Tal et al. 2009), so hierarchical assembly is clearly occurring in many systems. One way to assess its importance in driving spheroid evolution is to search for signatures of mergers and estimate their frequency and the associated rate of mass assembly. This approach is taken in Chapter 8.

Another way is to quantify the evolving stellar mass function of galaxies of different colors and morphological types using complete statistical samples, which allows one to track the movements of galaxy populations over time. This approach requires accurate stellar mass estimates for large samples of galaxies, which demands optical and near-infrared photometry and as many spectroscopic redshifts as possible, as well as a wide area to probe the rarest massive galaxies and overcome cosmic variance. Brinchmann & Ellis (2000) pioneered the now standard technique of spectral energy distribution (SED) fitting to estimate stellar masses and applied this to morphologically-selected subsamples at $z = 0$–1. They showed that the number of spheroids has slightly increased since $z = 1$, accompanied by a decline in irregular galaxies – suggesting that the latter are transforming into spheroids. Bundy et al. (2005) reported "morphological downsizing," in which the transition mass between the disk- and spheroid-dominated populations increases with redshift. The COMBO-17 (Bell et al. 2004) and DEEP2 (Bundy et al. 2006; Faber et al. 2007) surveys showed that the mass density of red sequence galaxies has approximately doubled since $z = 1$. These results require a substantial transformation from blue to red (and disk to spheroidal) galaxies over this relatively recent interval. However, this is again a strongly mass-dependent trend that is dominated by $\sim L_*$ galaxies. Among more massive systems there appears to be little evidence for significant number density evolution to $z = 1$.

6.3 The role of mergers in spheroid formation and growth

Mergers clearly play an important role in both the formation of spheroids and their subsequent growth in mass, especially in the most massive systems (e.g., Bundy et al. 2009). The main observational questions concern their quantitative impact as a function of mass and redshift. Below we briefly describe several avenues for constraining the role of mergers in forming present-day ellipticals:

1. *The rate of arrival of new spheroids*

   Traditionally a major merger (i.e., a mass ratio near unity) of disks is invoked to account for

spheroid formation in hierarchical models. However, the rate at which new spheroids appear at $z < 1$ outstrips estimates of the major merger rate derived either empirically or in CDM simulations (Bundy et al. 2007, 2009). This suggests additional secular modes of spheroid formation may be necessary, such as disk instability-fed bulge growth in disks. These are now incorporated in modern semi-analytic models (e.g., Bower et al. 2006) and are widely studied at high redshift (e.g., Dekel et al. 2009).

2. *The assembly epoch of the most massive galaxies*

   Early assembly of the most massive galaxies poses a more severe challenge to hierarchical growth than the downsizing of star formation (e.g., Cimatti et al. 2006). Even the stellar mass of brightest cluster galaxies appear to change little since $z = 1$ (Stott et al. 2010), whereas growth by a factor of ~ 3 is expected (de Lucia & Blaizot 2007). However, the robustness of this claimed "assembly downsizing" trend is strongly debated (e.g., Faber et al. 2007). Measurements of the mass function at the very steep high-mass end are limited by sampleThe variance (i.e., large-scale structure viewed in small fields), demanding photometric precision, uncertainties in stellar mass estimates (Marchesini et al. 2009), and the poorly-understood contribution of faint "intracluster light" composed of stripped stars (e.g., Burke et al. 2012).

3. *The tightness of the scaling relations*

   Simulations show that merger remnants are kept within the FP, but generally do not move parallel to all of its projections (Boylan-Kolchin et al. 2005, 2006; Robertson et al. 2006). This implies that successive generations of mergers will increase the scatter in, for example, the mass–radius relation. The observed scatter can therefore constrain the merger history. Nipoti et al. (2009a,b) find that less than half of the present mass can have been assembled in dry mergers following the initial dissipational formation. Many of the scaling relations, such as Mg b–σ and color–magnitude, are heavily weighted toward the luminous central regions of ellipticals. If the merger history is dominated by low-mass accretion that mainly deposits stars on the outskirts of the galaxy – as suggested by simulations and observations (Section 6.5) – then mergers may have a weak effect on these relations. This could help explain their low scatter and apparent lack of environmental dependence; spectroscopy extending well beyond the effective radius would then provide a valuable archaeological record (Greene et al. 2012).

6.4 Red galaxies at $z > 1.5$

The location and characterization of intrinsically red galaxies at $z \gtrsim 1.5$ lagged behind that of high-redshift blue galaxies, which can be efficiently selected based on their optical colors (e.g., Steidel et al. 1996, 2004). For quiescent galaxies, the main spectral feature is the Balmer/4000 Å break,

which is redshifted into the near-infrared (NIR). The difficulties associated with working in the NIR, particularly the bright sky, noisier detectors, and (until recently) the lack of multiplexing spectrographs, present a major challenge to the study of these objects.

The existence of galaxies with very red optical–NIR colors was realized with early generations of NIR imagers. Cowie et al. (1990) identified several galaxies with $(I-K)_{\rm Vega} > 5$ in a $1'$ field and suggested them to be "normal" galaxies at $z \sim 2$. Throughout the 1990s a number of authors investigated similar objects identified using criteria that were similar in spirit, being based on a single very red optical–NIR color, but which differed in the details of the filter selection and color threshold. This gave rise to a zoo of terminology and acronyms: extremely red objects (EROs), very red objects (VROs), faint red outlier galaxies (FROGs), and so on. Developments in this period were reviewed by McCarthy (2004).

A red optical–NIR color alone does not give much information about the source, which could be reddened by either dust or age. Nor does it localize the redshift, except that it must be $z \gtrsim 1$, due to the wide wavelength interval spanned. Franx et al. (2003) introduced a selection $(J-K_s)_{\rm Vega} > 2.3$, based purely on NIR photometry, in an attempt to locate the Balmer break of high-redshift evolved galaxies (the "distant red galaxy," or DRG selection). The narrower wavelength range isolates the redshift to $z \gtrsim 2$. The breakthrough in their paper was its use of deep, large-format NIR imaging on an 8 m-class telescope (ISAAC at the VLT). Daddi et al. (2004) introduced a two-color selection in the BzK plane to select galaxies at $z = 1.4$–2.5 and classify them as star-forming or passive.

Several authors studied the overlap between galaxies selected by the DRG, BzK, and various optical selection criteria (e.g., Reddy et al. 2005; van Dokkum et al. 2006). In general, no one simple color selection suffices to build an unbiased sample, as each often selects only parts of the distribution of color and star-formation rate at a given mass. This is particularly important when the goal is to construct a sample that is complete above some limiting stellar mass. Today photometric redshift estimates, based on fitting many bands of broad- or medium-band photometry to a set of spectral templates, are more commonly used. In principle, this allows a more complete selection of galaxies above a given mass or flux, independent of color, although the reliability of this procedure necessarily rests on the quality of the templates and must be validated against spectroscopic data.

Daddi et al. (2000, 2003) showed that the reddest galaxies are the most spatially clustered. This implies that at least a significant subset reside in more massive dark matter halos than the typical optically-selected source at $z \simeq 2$. Spectroscopic indicators of evolved stellar populations and suppressed star formation are clearly the most direct observational probes. The Gemini Deep Deep Survey (GDDS, McCarthy et al. 2004; Glazebrook et al. 2004) and the K20 survey (Cimatti et al. 2004) conducted optical spectroscopy of a K magnitude-limited samples at $z \lesssim 2$. Although traditional optical spectral signatures such as Balmer absorption, recombination lines, and the 4000 Å break are shifted into the NIR at $z \gtrsim 1.4$, the rest-frame ultraviolet does present several photospheric absorp-

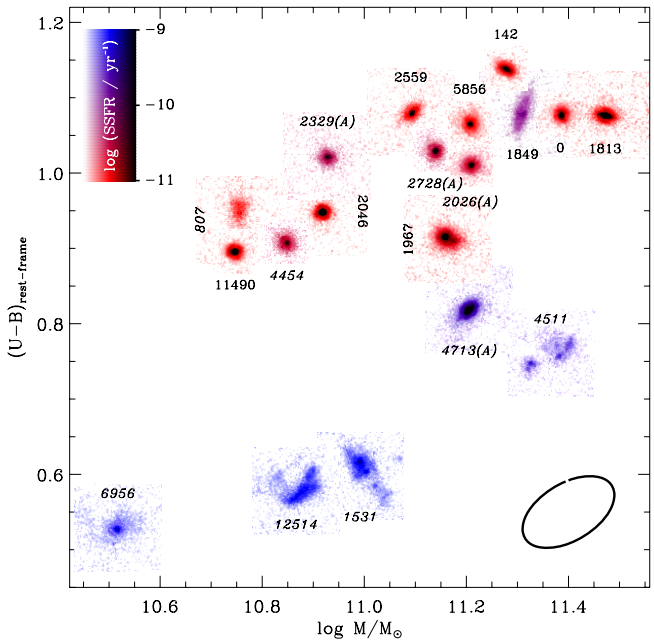

Figure 6.1: Color–mass diagram for a K-magnitude limited sample spectroscopically confirmed at $z = 2$–2.7. Note the presence of a red sequence and a correlation between rest-frame color and morphology, as described in the text. Reproduced from Kriek et al. (2009a).

tion lines (e.g., Mg II 2800) and small continuum breaks indicative of stars older than ~ 0.5 Gyr. Most of the brightest red galaxies were found to be red due to old stellar populations with ages of $\sim$ 1–2 Gyr, corresponding to formation redshifts $z \approx 2.5$–4, not due to dust. These K-bright red galaxies have high inferred stellar masses $\gtrsim 10^{11}\,M_\odot$, and by $z \approx 2$, they exist in roughly equal numbers as similarly massive star-forming galaxies. The high abundance of massive galaxies at this early epoch challenged formation models at the time.

Kriek et al. (2006, 2008b,a, 2009a) made a key advance by using NIR spectroscopy from 1–2.4 μm to access the rest-frame *optical continuum* spectra of 36 K-bright galaxies at $z_{\rm phot} = 2 - 2.7$, approaching the formation epoch inferred in earlier studies. They detected Balmer/4000 Å breaks and no Hα emission in half of the sample, demonstrating that these are already truly quiescent systems. A fairly tight color–magnitude relation is in place by $z \simeq 2.3$ (though broader than the local one, as expected; Whitaker et al. 2010), and a bimodality in galaxy colors appears present to at least $z \simeq 2$ as well (Brammer et al. 2009). Kriek et al. found that simple passive evolution of red sequence members cannot explain the slow rate of color evolution observed over $z = 0$–2.3, and it cannot accommodate the strong number density evolution that is observed either. A mixture of passive aging, dry mergers, minor star formation episodes ("frosting"), and transformations from the blue cloud to red sequence are likely at play.

By coupling their sample with *HST* rest-optical imaging, Kriek et al. (2009a) found that the

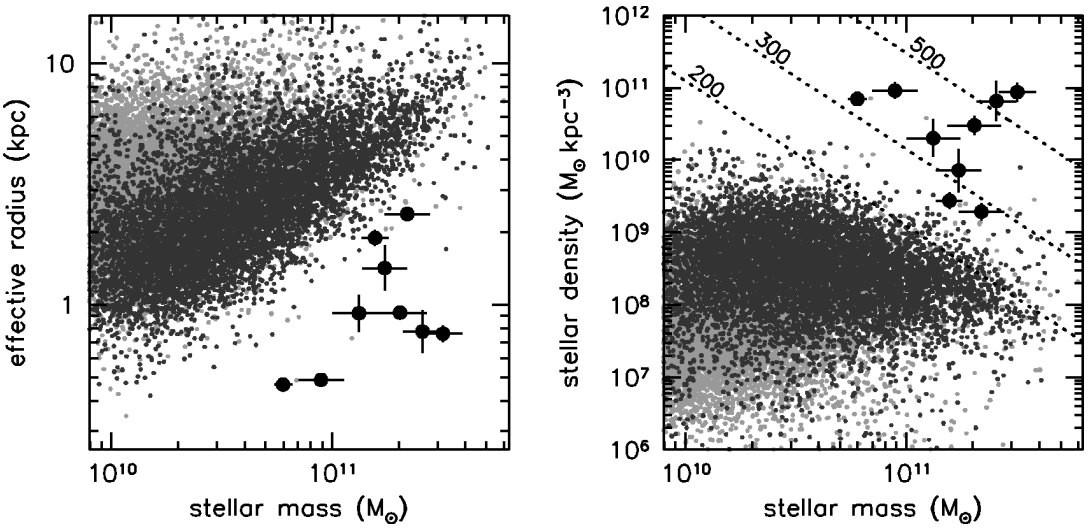

Figure 6.2: Relations between stellar mass and effective radius (left) and mean stellar density within the effective radius (right) for nearby galaxies in the SDSS (small points; red sequence galaxies are dark grey) and for $z \simeq 2.3$ red galaxies identified spectroscopically as quiescent (large points). Lines in the right panel indicate the expected stellar velocity dispersion in km s^{-1}. The high-redshift quiescent galaxies are much smaller than nearby galaxies of equal mass; there is virtually no overlap despite the large volume probed in the SDSS sample. Reproduced from van Dokkum et al. (2008).

correlation between color and morphology familiar in the local universe is broadly in place at $z \simeq 2.2$: red sequence galaxies predominantly have concentrated, symmetric light profiles, whereas blue galaxies usually have either a disky or irregular, clumpy appearance in the rest-optical (Figure 6.1). However, there are clues that the light distributions of the red galaxies are less concentrated and more flattened than local ellipticals, suggesting that many harbor disks (e.g., van der Wel et al. 2011; Weinzirl et al. 2011).

6.5 Size evolution of quiescent galaxies

Perhaps the most remarkable observation about $z \simeq 2$ quiescent galaxies is that they are extremely compact in physical size. Daddi et al. (2005) was one of the first studies to recognize this by examining spectroscopically-identified passive objects at $z > 1.4$ in the Hubble Ultra-Deep Field. They noted that five of the seven objects in their sample had very small effective radii $R_e < 1$ kpc: far from the Kormendy relation of local ellipticals, even accounting for luminosity fading. an Dokkum-VAN DOKKUM et al. (2008) undertook deep *HST*/NICMOS and Keck adaptive optics imaging of the massive $z \simeq 2.3$ sample whose quiescence had been confirmed by Kriek et al. (2006, 2008b) based on NIR spectroscopy. They measured remarkably small radii given the typical high mass of $M_* = 2 \times 10^{11}\,\mathrm{M}_\odot$, with a median effective radius of only 0.9 kpc (Figure 6.2). Furthermore, they found essentially no overlap with the size distribution of nearby galaxies: such compact galaxies

appear to be absent or very rare in the local universe (Trujillo et al. 2009; Taylor et al. 2010). This implies that the nearly all of the massive, quiescent galaxies seen at high redshift must evolve structurally, and it is direct evidence against a simple monolithic collapse followed by passive evolution.

Many studies soon explored larger samples and charted the rate of size growth of quiescent galaxies over $z = 0-3$ (e.g., Trujillo et al. 2007; Buitrago et al. 2008, and see references in Chapter 8). These generally showed persistent size growth extending over the entire redshift range. (The state of the field as of 2010 is summarized in Chapter 7, when the growth rate at $z \approx 1$–2 remained somewhat confused, while Chapter 8 reviews progress in the interim and presents a state-of-the-art measurement.) A strong relation between size or surface density and quiescence persists to at least $z \simeq 2$, with the quiescent sources being the most compact at each redshift (Williams et al. 2010).

An important insight into the nature of size evolution came from examining the detailed luminosity profiles of high-z compact galaxies, as opposed to only their effective radii. This revealed that the growth is not self-similar: the mass density within a fixed physical aperture (say 1 kpc) evolves far less than that within the effective radius. Most of the evolution in the light profiles occurs at larger radii (Bezanson et al. 2009; Hopkins et al. 2010a; van Dokkum et al. 2010). This suggests an"inside out" growth mode in which the core of present ellipticals is in place at early times, while the extended stellar envelope is built up gradually through a process that does not involve (much) new star formation. This could occur if the core forms in an early, dissipative fashion (e.g., Robertson et al. 2006), while the envelope is assembled gradually through dry mergers.

Mergers thus provide a natural route toward explaining the substantial observed size growth, which would provide evidence for hierarchical growth. For the most massive galaxies, most mergers must be dry to avoid excessive secondary episodes of star formation, which are tightly constrained by observations. Additionally, "major" mergers involving nearly equal-mass galaxies cannot provide most of the material. They are observed to be rare (e.g., Bundy et al. 2009, and see references in Chapter 8), so one might expect a significant number of compact galaxies remaining at $z = 0$, which is not observed. A less stochastic process seems necessary to explain the lack of late compact remnants and the smooth size growth over time. Furthermore, major mergers grow galaxies in size roughly in proportion to mass. Generating a factor of $\simeq 5$ in size growth for most massive $z \simeq 2$ galaxies would require them to grow in mass by an equal factor, which would produce too many massive galaxies by $z = 0$ (Bezanson et al. 2009). Adding any dissipation to the merger process is generally thought to worsen the problem, since this would lead to more compact remnants.

"Minor" dry mergers involving lower-mass satellites may address both of these problems. They must be more frequent than major mergers, owing to the higher abundance of low-mass galaxies. Furthermore, both dissipationless merger simulations and simple virial arguments show that stripped, lower-density material is mostly accreted to large radius. This leads to a more efficient growth mechanism – an expansion in size by a factor of five may require a growth in mass by a factor

of only two to three – and is consistent with the "inside-out" growth suggested by observations (e.g., Naab et al. 2009).

While mergers certainly occur and must contribute to size growth at some level, other physical processes could simultaneously be at play (Hopkins et al. 2010a). If gas is driven from a compact galaxy by stellar winds or an active nucleus, for example, this will lead to a growth in radius as the galaxy equilibrates (Fan et al. 2008). The main difficulty with this proposal accounting for the entire phenomenon is whether the expansion can persist over a long interval of several Gyr, as is needed to explain growth in systems that are already quiescent; this seems not to be the case (Ragone-Figueroa & Granato 2011). Nevertheless, expansion through mass loss could contribute to some part of the observed size growth.

Several authors have raised concerns about the validity of the high-z observations and suggested that the rate of size growth may be exaggerated. One potential source of error is the stellar masses, which are inferred using stellar population synthesis models that face a number of systematic uncertainties; these may become particularly acute at high redshifts when the oldest galaxies have ages of $\simeq$ 1–2 Gyr, when the uncertain contribution of TP-AGB stars is maximal (e.g., Maraston 2005). While it is very unlikely that mass errors alone can erase the entire observed signal, it may reduce the needed growth rate (Muzzin et al. 2009b). The best way to verify the masses is using robust *dynamical* estimates derived from absorption line spectroscopy. As described in Chapter 7, acquiring a significant sample of spectra with the necessary signal-to-noise is very difficult at $z > 1$, and progress has been possible only recently (e.g., Newman et al. 2010; Toft et al. 2012; Bezanson et al. 2012; van de Sande et al. 2012).

Another worry is that the effective radii at high-z could be underestimated (e.g., Mancini et al. 2010). This might occur if the imaging is too shallow to detect a faint extended envelope (e.g., Mancini et al. 2010), or if the galaxies are much more compact in light than in mass (e.g., Hopkins et al. 2010a). The latter is a particular concern when sizes are measured in the rest-ultraviolet, which may be more compact than the underlying mass distribution if the galaxy hosts nuclear star-formation, for example. Gross size errors are no longer a significant concern. Deep, *HST*-resolution imaging in the NIR (i.e., rest optical at $z \sim 2$) using WFC3 can now trace the luminosity profiles of passive objects to many effective radii, even at $z = 2$, for large samples (Chapter 8). Furthermore, with multi-color *HST* data, one can estimate the radial profile of stellar mass, rather than luminosity in a particular band. Using this approach, Szomoru et al. (2012) found early quiescent galaxies are slightly *more* compact in mass than in light. Since the mean ratio between the mass- and light-weighted sizes is redshift-independent, this does not affect the rate of evolution.

6.6 Goals of Part II of this thesis

The first goal of Part II is to verify the stellar masses of high-redshift spheroidal galaxies via dynamical estimates from absorption line spectroscopy. While velocity dispersions have been obtained for large samples at $z \lesssim 1.1$ (e.g., Treu et al. 2005), obtaining adequate signal-to-noise has been very difficult at higher redshifts, because most of the flux and the main absorption lines are redshifted beyond ~ 8500 Å. With the installation of deep-depletion CCDs in the LRIS spectrograph at Keck, which exhibit negligible fringing in the far red and have enhanced sensitivity to $\simeq 1$ μm, it is possible to probe the kinematics of field spheroids at $z \simeq 1.1$–1.5 in reasonable numbers for the first time. Chapter 7 presents measurements for a sample of 17 spheroids. The goal is to use the measured velocity dispersions to compare the dynamical and photometric stellar mass estimates, and to evaluate the rate of size growth at fixed dynamical mass. If earlier red galaxies are indeed more compact, we expect to find elevated velocity dispersions at a given mass or radius. Future NIR observations with MOSFIRE will allow this program to be extended to yet higher redshifts $z > 1.5$.

While mergers – particularly low-mass ratio "minor" mergers – are widely suspected to drive size growth of quiescent galaxies, it is not certain that the merger rate is high enough to generate for the full rate of growth observed. Simulations are in some disagreement on this point (Hopkins et al. 2010a; Oser et al. 2011), and semi-analytic estimates have also indicated that the cosmologically expected merger rate may be insufficient (Nipoti et al. 2012). In Chapter 8 we take an empirical approach by searching for low-mass companions to massive, quiescent galaxies at $z = 0$–2. Whereas many earlier studies have used this pair counting technique at lower redshifts or higher mass ratios ("major" mergers), imaging with the depth and resolution necessary to identify low-mass satellites at high redshift has only recently become feasible. The goal of Chapter 8 is to estimate the merger and mass accretion rates using *HST* WFC3/IR imaging from the CANDELS survey. By coupling this with timescales and size growth prescriptions derived in published merger simulations, we estimate the size growth resulting from mergers of observed close pairs. Using the same sample, we make a state-of-the-art measure of the evolution of the mass–size relation, based on a large, homogeneous sample with deep, rest-frame NIR imaging. We then compare this to the observed size growth rate, measured in the same sample, to ask if mergers alone fully account for this growth.

Chapter 7

Keck Spectroscopy of $z > 1$ Field Spheroidals: Dynamical Constraints on the Growth Rate of Red "Nuggets"

7.1 Introduction

The observation that many red galaxies with large stellar masses at $z \simeq 2$ are three to five times more compact than equivalent ellipticals in the local Universe (e.g., Daddi et al. 2005; Trujillo et al. 2007; van Dokkum et al. 2008; Buitrago et al. 2008; Damjanov et al. 2009) has been a source of much puzzlement. How can an early galaxy grow primarily in physical size without accreting significant stellar mass as required if these objects are the precursors of the most massive ellipticals observed today? Furthermore, studies of the fundamental plane and other stellar population indicators do not permit substantial recent star formation since $z \sim 2$ in massive galaxies, thus precluding growth by accretion of young stars or via gas-rich ("wet") mergers (e.g., Treu et al. 2005, hereafter T05). Some have questioned the reliability of the observations, suggesting an underestimate of physical sizes or an overestimate of stellar masses (Hopkins et al. 2010a; however, see Cassata et al. 2010 for a contrasting view). Others have proposed size expansion driven by self-similar dissipationless "dry" mergers, or mass accretion from minor mergers (Khochfar & Silk 2006; Naab et al. 2009; Hopkins et al. 2010a, and references therein).

To verify the compact nature of distant sources and to track their evolution in size and mass, it is preferable to use dynamical masses M_{dyn} from absorption line spectra, which do not suffer from uncertainties associated with the assumed initial mass function and stellar mass estimates derived from broad-band photometry (e.g., Muzzin et al. 2009a). M_{dyn} measurements are available for relatively large samples out to $z \sim 1$ (T05; van der Wel et al. 2008, hereafter vdW08), suggesting a small but detectable difference in average size at fixed mass when compared to the local universe.

But beyond $z \simeq 1$, there is little high-quality dynamical data for field spheroidals. an DokkumVAN DOKKUM et al. (2009) undertook a heroic observation of a single $z > 2$ source with a stellar mass $\simeq 2 \times 10^{11} M_{\odot}$ and an effective radius $r_e = 0.8$ kpc typical of compact galaxies at $z \simeq 2.3$. The spectrum has a claimed stellar velocity dispersion of $\sigma = 510^{+165}_{-95}$ km s^{-1}, suggesting a remarkably dense system. Van Dokkum et al. postulate the initial dissipative collapse at $z \simeq 3$ of a high mass "core" but are unable to account for its subsequent evolution onto the $z \simeq 1$ scaling relations. The quantitative effect of minor mergers on the physical size of a galaxy involves many variables, and it is unclear whether such dramatic size evolution is possible while maintaining the tightness of the fundamental plane and its projections (Nipoti et al. 2009b).

Interpretation of the observed trends at fixed M_{dyn} is further complicated by the so-called "progenitor bias" (van der Wel et al. 2009): if galaxies grow by dry mergers, the main progenitor of a present-day massive galaxy did not have the same mass at $z \sim 2$. Similarly, if galaxies become recognizable as spheroidals only above a certain threshold in stellar velocity dispersion σ_{ET} that depends on redshift, it is clear that the addition of a new – and less dense – population could mimic a false evolutionary trend. This bias can be reduced by considering galaxy sizes at fixed σ. Foremost, σ changes very little under a variety of growth mechanisms (e.g., Hopkins et al. 2010a) and it is therefore a better "label" than M_{dyn} to track the assembly history. Second, σ is closely correlated with stellar age (van der Wel et al. 2009) and therefore offers the most direct way to track the evolving population.

Given there is no clear consensus in understanding the continuity between the galaxy population at $z < 1$ and that at $z > 2$, we have embarked on a campaign to measure σ and M_{dyn} for a large sample of field spheroidals at $1 < z < 1.7$. This has recently become practical using multi-object optical spectrographs equipped with deep depletion red-sensitive CCDs. Our goal is to extend the earlier work at $z < 1$ (T05, vdW08) to within $\simeq$1 Gyr of the sample of ultracompact galaxies at $z \simeq 2.3$. In this first analysis, we present new results spanning the redshift range $1.05 < z < 1.60$.

We adopt a ΛCDM cosmology with $(\Omega_m, \Omega_v, h) = (0.3, 0.7, 0.7)$; all magnitudes are in the AB system. A Chabrier IMF is assumed where necessary.

7.2 Sample and observations

Our targets were selected from archival *HST*/ACS data in the EGS (GO 10134, PI: Davis), SSA22 (GO 9760, PI: Abraham & GO 10403, PI: Chapman), and GOODS-N (PI: Giavalisco) fields. For the EGS, we used the Bundy et al. (2006) catalog which matches CFHT (*BRI*, Coil et al. 2004; *ugriz*, CFHTLS) and Palomar (JK_s) photometry. Photometric redshifts are supplemented by spectroscopic redshifts from the DEEP2 survey. For SSA22, we used a photometric redshift catalog based on Subaru ($BVRIz$) and UH 2.2m (JHK_s) imaging kindly provided by P. Capak et al. (2004). In

GOODS-N, we used the Bundy et al. (2009) catalog which matches ACS and Subaru K_s photometry. Galactic extinction corrections were based on the dust maps of Schlegel et al. (1998). The parent sample for spectroscopic study in EGS and SSA22 was defined by $I - K_s > 2$, $I < 23.5$, and $z > 1$; in GOODS-N, the photometric criteria were F850LP $- K_s > 1.5$ and F850LP < 23.5. All galaxies satisfying these criteria were visually inspected in the ACS images by one of us (RSE) and those with E/S0 or early-disk morphology retained.

Keck I LRIS observations were made for 14 EGS and SSA22 targets on 2009 June 26–28 in median seeing of $0\farcs9$. The 600 mm^{-1} grating blazed at 1 μm was used, providing a velocity resolution of $\sigma_{\rm inst} = 58$ km s^{-1} at 9000 Å. The total integration times were 40.8 ks and 32.4 ks in the EGS and SSA22 fields, respectively. On 2010 April 5–6 LRIS observations were made of seven GOODS-N targets with 34.8 ks of integration in $0\farcs8$ seeing. One additional GOODS-N spectrum was secured with Keck II DEIMOS observations on 2010 April 11–12 using the 831 mm^{-1} grating. The LRIS data were reduced using the code developed by Kelson (2003). Spectra were extracted using optimal weighting based on Gaussian fits to the spatial profile. Telluric absorption correction and relative flux calibration were provided by a DA star observed at matching airmass at the end of each night.

7.3 Velocity dispersions and photometry

We measured stellar velocity dispersions, σ, by fitting broadened stellar templates using the `PPXF` code of Cappellari & Emsellem (2004). The instrumental resolution was measured using unblended sky lines; their variation with wavelength was well fit by a low-order polynomial. The template collection comprised 348 stars of type F0–G9 from the Indo-US coudé library (Valdes et al. 2004) with a range of metallicities and luminosities (classes III–V). We verified that including A star templates does not affect our measurements. For each galaxy, `PPXF` constructed an optimal template as a linear combination of these stellar spectra, although our results do not significantly differ if the best-fitting single template is used. To avoid systematic errors, we masked pixels contaminated by strong OH emission. Based on tests with the continuum filtering, sky masking threshold, and stellar template choices, we assigned a systematic uncertainty to each velocity dispersion, typically $5 - 10\%$. We were able to secure a reliable dispersion for 17 of the 22 galaxies (see Figs. 7.1 and 7.2). Measured velocity dispersions $\sigma_{\rm raw}$ were corrected to dispersions σ measured in an effective circular aperture of radius $R_e/8$, as described in Treu et al. (1999); the mean correction factor is $\sigma/\sigma_{\rm raw} = 1.13$.

Surface photometry was measured in the *HST* images using `GALFIT` (Peng et al. 2002) with a PSF determined from a nearby isolated star. F814W imaging was used in EGS and SSA22, while F850LP data were adopted in GOODS-N. For consistency with the local SDSS sample, we fit de Vaucouleurs profiles and determine circularized radii. We also fit Sérsic profiles but found that the

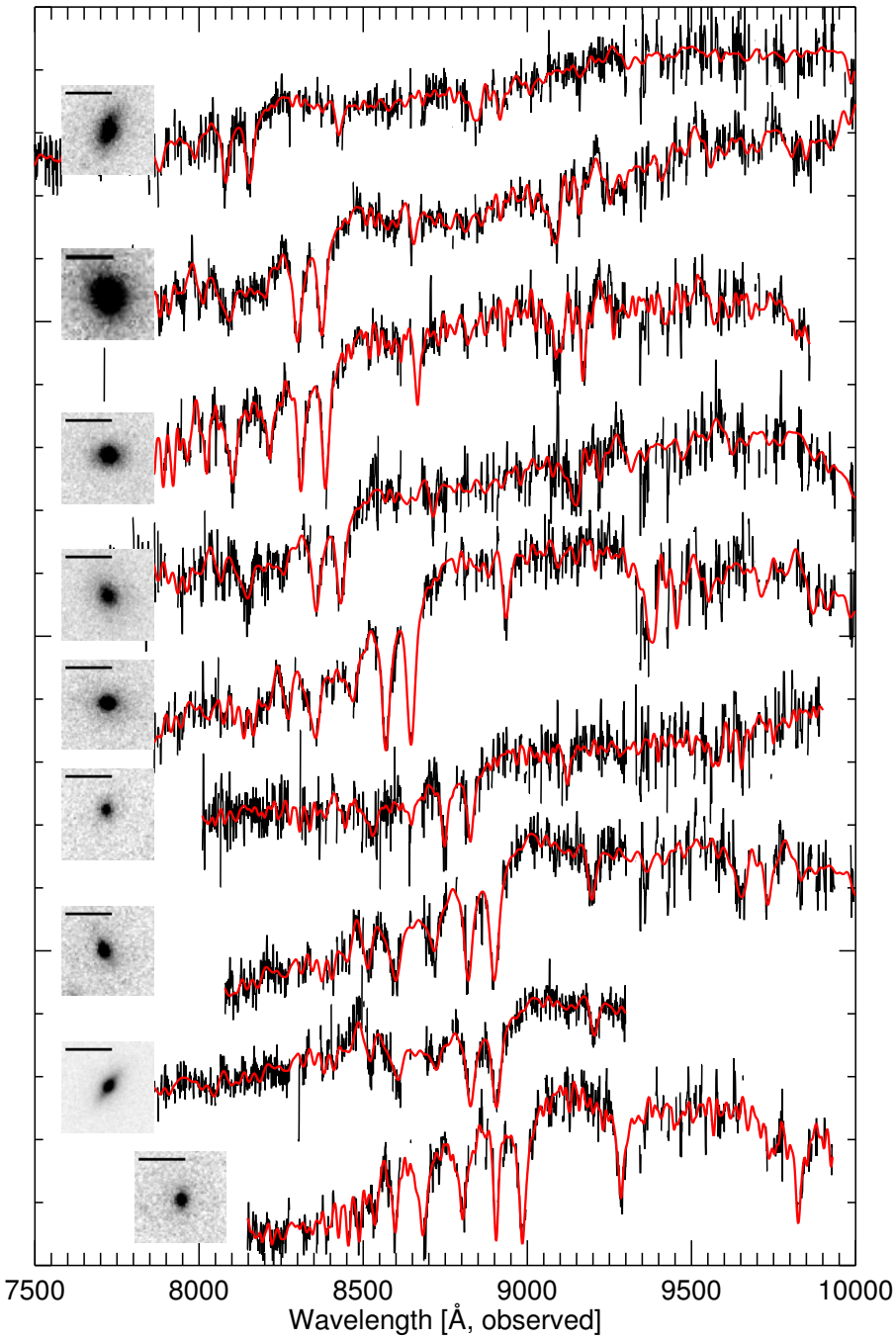

Figure 7.1: Keck spectra of our 17 targets ordered by redshift (continued in Fig. 7.2). Each is smoothed with a 3 pixel (2.4 Å) running median with sky lines omitted (black) and compared to fits to broadened stellar templates (red). *HST* images are inset with a 1" ruler. The order of objects matches that in Table 1.

mean Sérsic index n is consistent with 4 (i.e., a de Vaucouleurs profile). We estimate uncertainties of $\sim 10\%$ in R_e based on testing the background level, simulating the recovery of synthetic de Vaucouleur profiles placed in blank sky patches, and comparing with the independent measurements

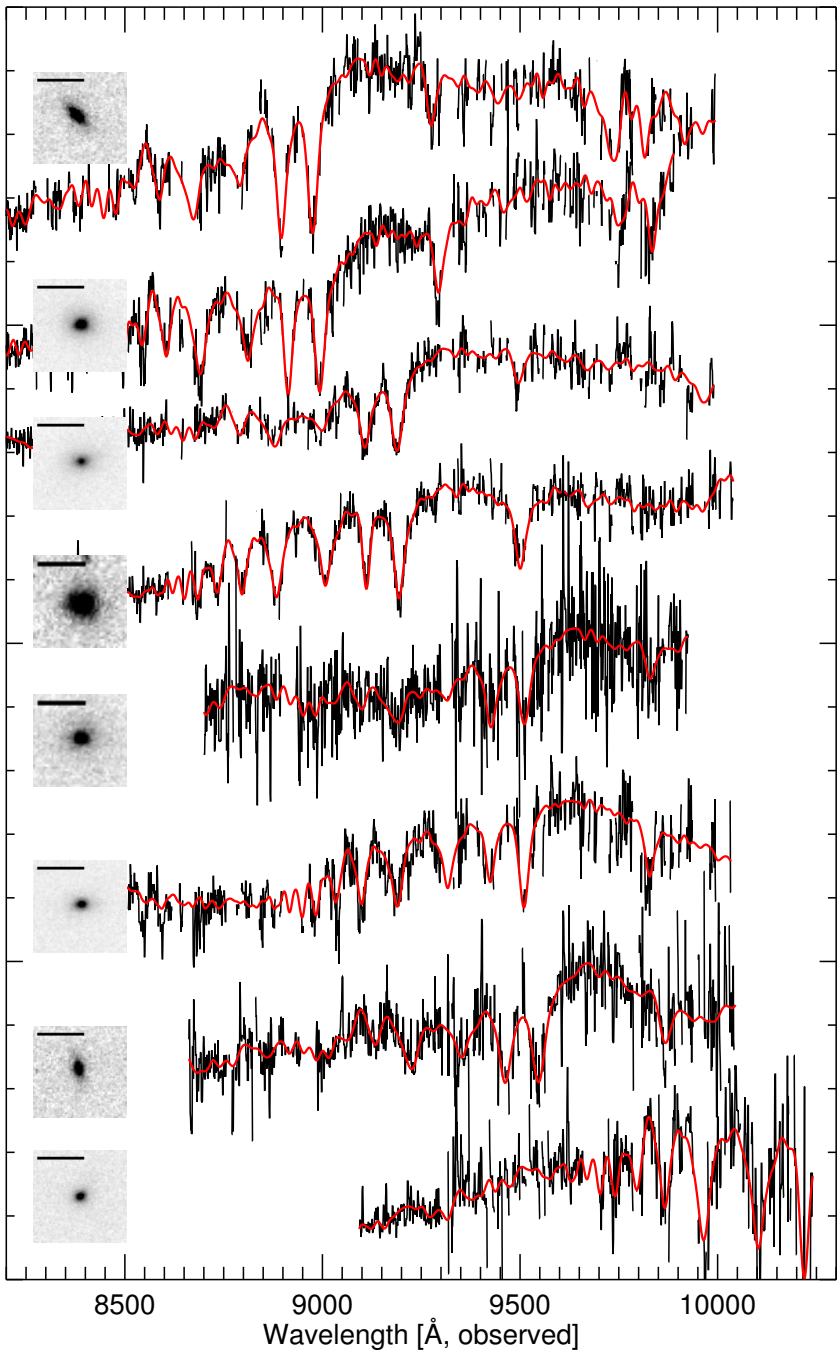

Figure 7.2: Continuation of Figure 7.1.

of vdW08 for the T05 subsample.

We convert the observed ACS magnitude to the rest B magnitude by matching the observed $I-K_s$ color to a grid of Bruzual & Charlot (2003) single-burst models of varying age and metallicity. The uncertainty in this k-correction is $\sim 4\%$. Based on the optical and NIR photometry discussed in Section 2, stellar masses were estimated by fitting Bruzual & Charlot (2003) population synthesis

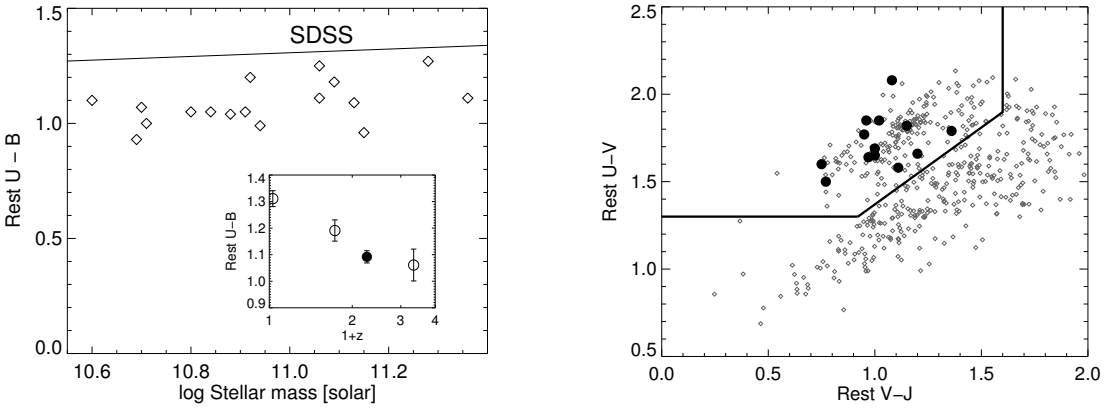

Figure 7.3: Left: Stellar mass–color relation delineated by our sample, as compared to that seen in the local universe in the SDSS and to measurements in several studies at higher redshift (inset). The inset shows the mean color and its uncertainty at a stellar mass of $\log M_* = 11.05$. (This corresponds to $2 \times 10^{11}\,\mathrm{M}_\odot$ for Salpeter-based masses.) Open points are taken from Kriek et al. (2009b), and the filled point with $U - B = 1.09 \pm 0.02$ refers to the present sample.[2] **Right:** Color–color plane used for separating quiescent and star-forming galaxies. Light grey points show a field sample with $\log M_* > 10$ and $z = 1$–1.5 from the catalogs presented in Chapter 8. Lines delineate the red sequence region from Williams et al. (2010). Thick black points show those galaxies in our sample with available IRAC photometry, which is necessary to reach the rest-frame J band. All these galaxies fall within the quiescent selection box.

models using the `FAST` code (Kriek et al. 2009b). The model grid is described in more detail in Chapter 8 (although the adopted models and IMF differ). Stellar masses were scaled based on the total flux in the de Vaucoulers fits. An exponentially-decaying star formation history and a Chabrier (2003) IMF were assumed. Table 1 summarizes the dynamical and photometric properties for our sample of 17 $z > 1$ galaxies.

7.4 Rest-frame colors[1]

In order to characterize our sample and place it in the context of other studies, we computed the rest-frame colors using the `InterRest` code (Taylor et al. 2009). In the left panel of Figure 7.3 we show the stellar mass–color relation delineated by our sample, which is compared to that seen in the local universe and in several bins of higher redshift. The slope of the red sequence and its color offset are consistent with earlier measures of its evolution; this confirms that we have selected spheroidal galaxies on the red sequence. In the right panel, we place those galaxies in our sample with available IRAC photometry in the UVJ color–color plane, which is often used to separate quiescent and star-forming galaxies (e.g., Brammer et al. 2009; Williams et al. 2010). All of the galaxies in our sample fall in the quiescent region.

[1]This section was added for the thesis and was not present in Newman et al. (2010).

Table 7.1. Photometric and Spectroscopic Data

	R.A.	Dec.	Morph.	z	R_e	$\sigma_{\rm raw}$	σ	M_B	$I-K_s$	$z-K_s$	K_s	$\log M_{\rm dyn}/M_\odot$	$\log M_*/M_\odot$
E1	214.9853	52.9513	S0?	1.054	6.44	209 ± 30	228 ± 32	-22.32	2.14	1.70	19.79	11.59 ± 0.13	11.06 ± 0.08
S1	334.3529	0.2734	E	1.110	4.74	221 ± 17	242 ± 18	-22.72	2.63	1.81	19.58	11.51 ± 0.07	11.28 ± 0.22
E2	214.9702	52.9911	E/S0	1.113	4.02	136 ± 14	151 ± 15	-22.18	2.15	1.69	20.16	11.03 ± 0.09	10.89 ± 0.11
E3	215.0061	52.9755	Sab	1.124	6.11	245 ± 26	266 ± 28	-22.20	2.40	2.01	20.04	11.70 ± 0.09	11.14 ± 0.13
E4	214.9847	52.9614	E/S0	1.179	2.65	231 ± 18	258 ± 19	-22.21	2.23	1.76	20.02	11.31 ± 0.07	10.95 ± 0.07
E5	214.9815	52.9501	E	1.225	1.43	123 ± 22	139 ± 25	-21.20	2.45	1.93	21.16	10.51 ± 0.16	10.60 ± 0.14
E6	215.0351	52.9830	S0	1.243	2.38	269 ± 26	302 ± 29	-22.20	2.57	2.06	19.79	11.40 ± 0.08	11.08 ± 0.11
GN1*	189.2681	62.2264	Sab	1.243††	1.29	253 ± 23	290 ± 26	-22.19	2.79	2.07	20.26	11.12 ± 0.08	11.04 ± 0.11
E7†	215.1319	53.0163	E/S0	1.262	1.57	92 ± 19	103 ± 21	-21.83	2.58	2.02	20.43	10.29 ± 0.18	10.68 ± 0.17
E8	215.1371	53.0173	Sab	1.262	1.38	246 ± 30	280 ± 34	-21.90	2.38	1.90	20.76	11.10 ± 0.11	10.80 ± 0.13
GN2	189.0634	62.1623	E/S0	1.266	1.58	211 ± 32	239 ± 36	-22.24	2.54	1.74	20.55	11.02 ± 0.13	11.02 ± 0.14
GN3	188.9345	62.2068	E/S0	1.315	3.44	259 ± 26	288 ± 28	-22.32	2.77	2.07	20.45	11.52 ± 0.09	11.39 ± 0.07
S2†	334.3502	0.3032	Sab	1.315	2.47	153 ± 26	171 ± 29	-22.37	2.29	1.51	20.80	10.93 ± 0.15	10.69 ± 0.16
S3	334.4233	0.2256	E/S0	1.394	2.50	241 ± 64	271 ± 71	-22.01	3.20	2.44	20.74	11.33 ± 0.23	11.14 ± 0.23
GN4†	189.1132	62.1325	E	1.395	0.77	179 ± 43	206 ± 49	-21.93	2.24	1.71	21.24	10.58 ± 0.21	10.72 ± 0.10
E9	215.1219	52.9576	S0/a	1.406	1.19	294 ± 70	337 ± 79	-22.02	2.39	2.19	20.82	11.20 ± 0.21	10.86 ± 0.22
GN5†	188.9625	62.2286	E	1.598	0.68	240 ± 36	274 ± 41	-22.51	2.71	2.25	20.69	10.77 ± 0.13	10.91 ± 0.09

Note. — † denotes systems with strong Balmer absorption. * denotes the DEIMOS observation. †† corrects a typographical error in Newman et al. (2010). R.A. and Dec. are in the J2000 equinox. R_e is in kpc. The velocity dispersions $\sigma_{\rm raw}$ (in km s^{-1}) is as measured in the spectrum, while σ refers to dispersions standardized to a circular aperture of radius $R_e/8$. Uncertainties include the systematic component added in quadrature. M_B is the rest-frame B band absolute magnitude. $I-K_s$ and $z-K_s$ photometry has been interpolated to a uniform system of Bessell I and SDSS z. Dynamical mass uncertainties reflect the total uncertainty (statistical and systematic) in σ. Stellar masses assume a Chabrier IMF. The order of galaxies (by redshift) matches Figs. 7.1 and 7.2.

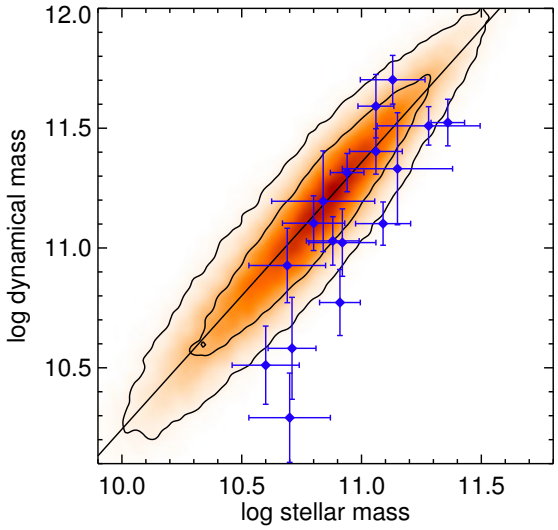

Figure 7.4: Comparison between the stellar and dynamical masses of SDSS red sequence galaxies, selected as described in the text (red shaded region, with contours enclosing 68% and 95% of the galaxies), and our sample of 17 spheroids at $z > 1$ (blue points with error bars).

7.5 Stellar versus dynamical masses[3]

In order to compare the stellar and dynamical masses derived for our sample, we constructed a set of red sequence galaxies from the SDSS DR7 (Abazajian et al. 2009). Galaxies in the spectroscopic SDSS sample with $0.05 < z < 0.15$, $\sigma > 70$ km $^{-1}$, and a spectrum with signal-to-noise ratio of at least 10 in the r band were first identified. We then isolated red sequence galaxies using the cut in the color–magnitude diagram proposed by Yan et al. (2006, Equation 1). Velocity dispersions were converted to a standard measurement aperture of $R_e/8$, following Jorgensen et al. (1995). Dynamical masses were estimated as

$$M_{\rm dyn} = \frac{5\sigma^2 R_e}{G}, \tag{7.1}$$

where we take the radius R_e from the de Vaucoulers fits in the SDSS database, interpolated to the rest-frame B band. We take stellar masses from the MPA-JHU DR7 database (Kauffmann et al. 2003a)[4] and subtract 0.05 dex to convert from their assumed Kroupa IMF to our choice of Chabrier.

Figure 7.4 compares the stellar and dynamical mass estimates for these SDSS galaxies and our $z > 1$ sample. The line $\log M_{\rm dyn} = 11.36 + 1.114(\log M_* - 11)$ is a simple linear fit to the SDSS data. For the entire high-z sample, we find a mean vertical offset of $\langle \Delta M_{\rm dyn} \rangle = -0.19 \pm 0.06$ from this linear fit. In terms of stellar mass, this is equivalent to a horizontal offset of $\langle \Delta M_* \rangle = -0.17 \pm 0.05$. This offset may be mass dependent: if we restrict to sources with $M_* > 10^{11}\,{\rm M}_\odot$, we find no strong evidence for any offset from local galaxies ($\langle \Delta M_{\rm dyn} \rangle = -0.09 \pm 0.07$). The mean stellar-to-dynamical

[3]This section significantly expands on that presented in Newman et al. (2010).
[4]`http://www.mpa-garching.mpg.de/SDSS/DR7/`

mass ratio within the high-z sample is $\langle \log M_*/M_{\rm dyn} \rangle = -0.17 \pm 0.06$.

We conclude that the stellar masses in our sample are close to those expected from their measured dynamical masses and the relationship seen in the local universe. There may be a genuine but modest offset from the local relation. In that case, the size growth at a fixed stellar mass will therefore differ from that measured at a fixed dynamical mass. However, offsets of this magnitude are much too small to fully explain the compactness of the $z \simeq 2$ galaxies discussed in Section 7.1. There are several possible explanations for an offset in the stellar–dynamical mass relation. First, systematic differences between stellar masses derived using different photometry, models, and codes are commonly at the $\simeq 0.05$–0.1 dex level for old galaxies (see Section 3.4.2). While this is less than the mean offset $\langle \Delta M_* \rangle = -0.17 \pm 0.05$, these systematic differences may contribute significantly to it. Second, evolution in the distributions of stellar and dark mass over time would cause the virial coefficient (the pre-factor 5 in Equation 7.1) to evolve. The mean Sérsic indices of the SDSS and $z > 1$ galaxies are consistent, but subtle variations are still possible. Thirdly, all spectroscopic samples are biased to high surface brightness objects. This selection effect may become important at low masses and large radii. Since large radii correlate with high $M_{\rm dyn}/M_*$ in the SDSS (Padmanabhan et al. 2004), we may be biased against such galaxies at low masses. Finally, if the offset is genuine, it could point to an increase in the dark matter fraction within the effective radius over time. This is indeed expected in some cosmological merger simulations (e.g., Hilz et al. 2012).

7.6 Size evolution

Size evolution has commonly been studied by comparing spheroids of the same mass at different epochs. Although an unlikely evolutionary path for individual galaxies, it is the most observationally direct approach, particularly at $z > 1.5$ where dynamical measures are scarce. We first conduct this comparison in Section 7.6.1. We then examine size evolution at fixed velocity dispersion in Section 7.6.2.

7.6.1 Size evolution at fixed mass

Using the same sample of SDSS red sequence galaxies, we derive a mean dynamical mass–radius relation of $R_e = 2.88\ (M_{\rm dyn}/10^{11}\,{\rm M}_\odot)^{0.55}$ kpc.[5] Figure 7.5 shows the size evolution inferred by comparing the present sample and the T05 E/S0 galaxies to this SDSS relation. The T05 and present samples are well matched in morphology and rest optical colors and so comprise an excellent dataset for studying evolution over a wide redshift interval. A simple power law fit $(1+z)^{-0.75\pm0.10}$ to the $M_{\rm dyn} > 10^{11}\,{\rm M}_\odot$ sample is indicated by the solid line. This corresponds to a 40% decrease in

[5]The relation is consistent with that of vdW08, taking into account the different apertures to which we normalize velocity dispersions.

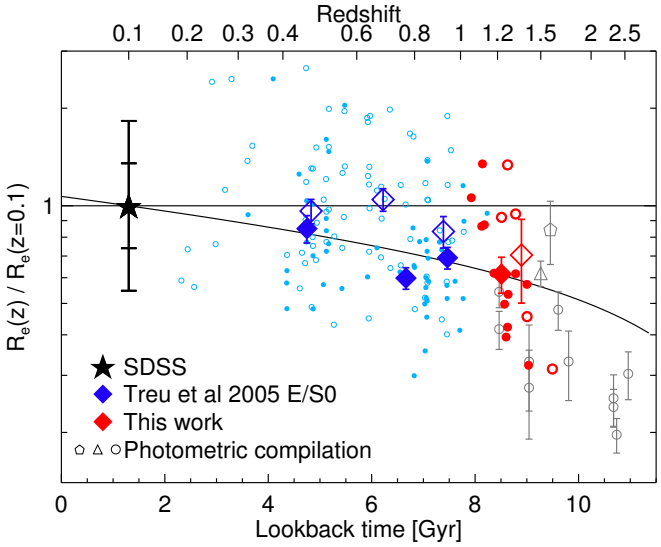

Figure 7.5: Size evolution of spheroids at fixed mass. Solid diamonds show the mean size and its uncertainty for massive ($\log M_{\rm dyn}/\,{\rm M}_\odot > 11$) spheroids relative to red sequence galaxies in SDSS of the same dynamical mass (computed in log space). Open diamonds refer to intermediate-mass ($10 < \log M_{\rm dyn}/\,{\rm M}_\odot < 11$) systems. The solid line shows a $(1+z)^{-0.75\pm0.10}$ fit to the more massive sample. Individual galaxies in the spectroscopic samples are shown by colored circles. Light gray points with error bars are based on photometric stellar masses and show mean sizes relative to SDSS galaxies of the same stellar mass, based on the Shen et al. (2003) relation, for several samples: Saracco et al. (2011, triangle), Mancini et al. (2010, pentagon), and the vdW08 (circles) compilation.

size by $z = 1$, and marginally slower evolution than that inferred by vdW08 for $M_{\rm dyn} > 3 \times 10^{10}\,{\rm M}_{\odot}$ spheroidals ($(1+z)^{-0.98\pm0.11}$; corresponding to a 50% decrease at $z = 1$). However, the difference is partly explained by the correction applied by vdW08 to their measured sizes based on simulations. In contrast, we do not apply any corrections to our measured sizes given the lack of consensus on this matter in the literature (see also Hopkins et al. 2009; Mancini et al. 2010) and the results of our own simulations.

Our $\langle z \rangle = 1.3$ sample probes an epoch within 2 Gyr of the $z \sim 2.3$ samples whose compact sizes have motivated the present work. Figure 3 illustrates that, given the size dispersion in the dynamical sample at a given redshift and the difficulties of comparing our dynamical sample with one whose masses are likely less precise, the sharp drop in size seen over this short time interval may not be that significant. If confirmed, however, the implied size evolution is quite large compared to the expected accretion from mergers over the same period, which we estimate to be 40% of a typical $10^{11}\,{\rm M}_{\odot}$ galaxy at $z = 1.3$.[6] Thus, if minor mergers are responsible, these results imply a very high efficiency of $d\log R_e/d\log M \simeq 2.6$ for growing spheroids, just consistent with the upper end of estimates determined from merger simulations (e.g., Hopkins et al. 2010a).

Also striking is the different trend seen in less massive $10 < \log M_{\rm dyn}/\,{\rm M}_{\odot} < 11$ galaxies (open diamonds in Figure 7.5). Although the high-z samples are small and include some compact examples, we find no evidence for mean size evolution over $0 < z < 1.6$, i.e. $\propto (1+z)^{0.02\pm0.15}$. This is consistent with a picture in which more massive galaxies formed earlier and from wetter mergers with more dissipation, creating more compact remnant spheroids (e.g., Khochfar & Silk 2006; Trujillo et al. 2006), and at variance with the model proposed by van der Wel et al. (2009) in which lower-mass galaxies display the strongest evolution. However, we caution that the lower mass samples may be affected by selection effects, since the brighter – and therefore possibly larger – objects may be preferentially selected given our flux limits. This is not a concern for the $>10^{11}$ ${\rm M}_{\odot}$ sample, where we are complete for any reasonable mass-to-light ratio. A characterization of the bias requires a self-consistent model with Monte Carlo simulations, which is beyond the scope of this chapter and is left for future work when larger samples will be available.

7.6.2 Size evolution at fixed velocity dispersion

Comparisons at fixed mass may be affected by "progenitor bias." A preferred approach, when dynamical data are available, is to examine galaxies of the same *velocity dispersion*. This offers the two advantages discussed in Section 1 and is illustrated in Figure 7.6. A cut in ${\rm M}_{\rm dyn}$ includes only the largest galaxies at a fixed σ. Therefore, if galaxies below some threshold $\sigma_{\rm ET}$ are missing from the high-redshift samples, this could mimic an evolutionary trend in mass-selected samples. According to the preferred prescription of van der Wel et al. (2009), $\sigma_{\rm ET} = 233$ km s^{-1} at $z = 1.3$.

[6] Estimated using the merger rate calculator presented in Hopkins et al. (2010b).

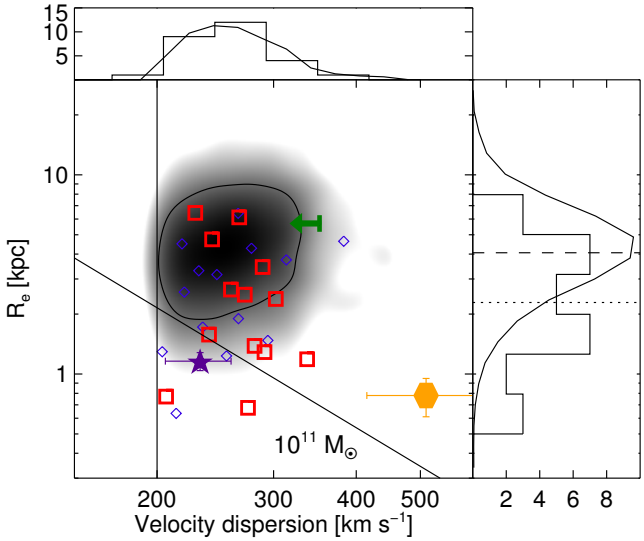

Figure 7.6: Distribution of effective radii at matched velocity dispersion for spheroids with $\sigma >$ 200 km s^{-1} in the present sample (red), the T05 $z > 0.9$ sample (blue), and SDSS (smoothed grayscale with 1σ contour). The histogram (this data) and solid line (SDSS) in the top panel agree by construction. The right panel compares the distribution of R_e for the matched samples. Dashed and dotted lines indicate the means in log space. For comparison, the $z \sim 1.7$ stacked sample of Cappellari et al. (2009) is shown (star), along with the single galaxies of van Dokkum et al. (2009, hexagon, $z = 2.186$) and Onodera et al. (2010, green upper limit, $z = 1.823$). The diagonal line represents M_{dyn}=10^{11} $M_\odot$.

Therefore we should expect to see some effect for our sample, even though the presence of lower σ objects in our sample already suggests that the progenitor bias is not as strong.

Figure 7.6 shows this comparison in terms of the $\sigma - R_e$ plane. To avoid luminosity selection biases, we consider only galaxies with $\sigma > 200$ km s^{-1}, where we are 90% complete, based on the SDSS distribution of luminosity at fixed σ and a conservative estimate of luminosity evolution, consistent with passive evolution of an old stellar population formed at $z_f = 3$. The SDSS galaxies (grayscale) are weighted so as to match the σ distribution of the $0.9 < z < 1.6$ sample (top panel). The right panel of Figure 7.6 then compares the size distributions of the local and $0.9 < z < 1.6$ samples at matching σ. By fitting for size evolution at fixed σ we find that sizes evolve as $(1+z)^{-0.88\pm0.19}$. The good agreement with the size evolution inferred at fixed mass rules out strong progenitor bias. A full evolutionary model with selection effects is needed to include objects with lower σ and quantify progenitor bias and size evolution more accurately. This is left for future work with larger samples.

7.7 Conclusions

Our Keck spectra have shown the utility of securing individual spectroscopic and photometric measures for a representative sample of $z > 1$ massive spheroidals. By probing to $z \simeq 1.6$, we are sampling velocity dispersions, sizes and dynamical masses within 1.2 Gyr of the puzzling population of compact red galaxies at $z \simeq 2.3$. We confirm the overall reliability of the stellar mass estimates at this epoch, although we find possible evidence for an offset from the local stellar mass–dynamical mass relation at the low-mass end.

Importantly, the size evolution we infer over $0 < z < 1.6$ at fixed dynamical mass is modest: $\simeq \times 2$ for the most massive ($\log M_{\rm dyn}/M_{\odot} > 11$) examples but possibly smaller for lower mass systems. If the compact red galaxies at $z \simeq 2$–2.3 are their precursors, they must have grown dramatically in size over a very short time interval.

Acknowledgments

We thank Peter Capak for kindly providing photometric catalogs for the SSA22 field and Arjen van der Wel for helpful comments regarding size measurements. We thank Dan Stark for conducting the DEIMOS observation. We are grateful to the staff of the Keck Observatory and Connie Rockosi, in particular, for ensuring our early access to the upgraded LRIS-R was successful.

Chapter 8

Can Minor Merging Account for the Size Growth of Quiescent Galaxies? New Results from the CANDELS Survey

8.1 Introduction

The compact nature of massive quiescent galaxies at redshifts $z \simeq 2$ was a surprising discovery when it was announced some years ago (e.g., Daddi et al. 2005; Trujillo et al. 2006; Buitrago et al. 2008; van Dokkum et al. 2008). Many red galaxies with stellar masses $M_* \simeq 10^{11}\,\mathrm{M}_\odot$ have effective radii $R_e \simeq 1$ kpc, three to five times smaller than comparably massive early-type galaxies in the local Universe. This suggests that they grew significantly in size, but much less in stellar mass. Initially there was some suspicion that the stellar masses of the $z \simeq 2$ sources were overestimated, but deep spectroscopic data (Cappellari et al. 2009; Newman et al. 2010; van de Sande et al. 2011) have verified dynamically the high masses of selected $1 < z < 2$ sources and, in conjunction with the abundance of dynamical masses for lower redshift sources (Treu et al. 2005; van der Wel et al. 2005), provided a valuable, independent confirmation of the size evolution.

Only two physical explanations have been put forward to explain this remarkable growth in size while avoiding the over-production of present-day high-mass galaxies. Adiabatic expansion through significant mass loss can lead to size growth (Fan et al. 2008, 2010). A galaxy that loses mass as a result of winds driven by an active nucleus or supernovae, for example, will adjust its size in response to the shallower central potential. However, the "puffing up" arising from baryonic mass loss occurs only when the system is highly active and young in terms of its stellar population (Ragone-Figueroa & Granato 2011, see also Bezanson et al. 2009), so it is difficult to see how this mechanism can account for the gradual and persistent growth in size observed for compact sources that are mostly quiescent in nature.

In a hierarchical picture of galaxy formation, mergers are expected to lead to growth in size and stellar mass. Whereas major mergers, involving nearly equal-mass components, will lead to comparable growth in both size and mass, minor mergers involving lower-mass companions can produce more efficient size growth (Bezanson et al. 2009; Naab et al. 2009; Hopkins et al. 2010a). This mechanism requires a high rate of occurrence of minor mergers, a significant fraction of which must involve gas-poor companions. Although the major merger rate is observationally constrained reasonably well over $0 < z < 1$ (e.g., Kartaltepe et al. 2007; Lin et al. 2008; Bundy et al. 2009; de Ravel et al. 2009; Lotz et al. 2011) and via a few measurements up to $z \simeq 3$ (e.g., Bluck et al. 2009; Man et al. 2011), the rate at which minor merging occurs requires exquisitely deep photometric data. For this hypothesis, the key question is whether observations confirm that minor merging occurs at the required rate.

The infrared Wide Field Camera 3 (WFC3/IR) on board the Hubble Space Telescope (*HST*) enables us to address the question of whether minor merging is sufficiently frequent to account for the size growth of compact sources since $z \simeq 2$. The CANDELS survey (GO 12444/5, PIs: Ferguson & Faber) provides an excellent resource for addressing this question since in the first two fields to be observed – the UKIRT Ultra Deep Survey and southern GOODS fields – the associated ground- and space-based and photometry spanning $0.4 - 8\mu$m is sufficiently deep not only to identify possible companions ten times less massive than their hosts, but also to reliably determine their photometric redshifts so that a physical association can be evaluated.

Our goal in this paper is thus two-fold. First, exploiting the unique combination of depth and angular resolution in the CANDELS near-infrared data, we aim to measure the size growth of massive galaxies. We will show that the most compact sources virtually always have quiescent stellar populations. We then estimate the minor merger fraction by searching for low-mass companions around these quiescent sources within a fixed search annulus of $10 < R < 30\ h^{-1}$ kpc. A physical association can be made through their photometric redshifts. We will then interpret the minor merger fraction as a possible cause for the growth rate of compact massive galaxies.

A plan of the paper follows. In Section 2, we introduce the CANDELS WFC3/IR images and the associated photometric data. We describe the selection of 935 galaxies with stellar masses $> 10^{10.7}\,M_{\odot}$ in the photometric redshift range $0.4 < z < 2.5$. Section 3 analyzes the size growth for this sample and compares our results to earlier work. Section 4 introduces our search for faint companions around 404 quiescent galaxies spanning the redshift range $0.4 < z < 2$ in which we can confidently detect companions with 10% of the stellar mass of their hosts. We discuss the robustness of our search, make corrections for spurious unassociated pairs, and assess the stellar mass content and colors of these companions. Finally, in Section 5 we interpret our minor merger rate in the context of size growth. After discussing the size growth of the quiescent population, we turn to a test that asks whether the merger rate is consistent with the increasing rarity of compact examples

at later times. Finally, we summarize our conclusions and the remaining uncertainties in Section 6.

Throughout the paper, we adopt a concordance cosmology with $(\Omega_m, \Omega_v, h) = (0.3, 0.7, 0.7)$ and use the AB magnitude system (Oke & Gunn 1983).

8.2 Data and Catalogs

We have compiled an extensive database of optical and infrared observations from space and the ground in the UKIRT Deep Survey (UDS, Lawrence et al. 2007) and GOODS-South (Giavalisco et al. 2004) fields, offering the wide spectral coverage from 0.4–8μm necessary to secure quality photometric redshifts, stellar masses, and stellar population parameters for mass-complete samples of galaxies to $z \simeq 2.5$. Although our supplementary photometry covers a much wider area, we restrict our attention to the CANDELS WFC3/IR footprints, since our program requires the depth and angular resolution in the rest-frame optical afforded by *HST*.

8.2.1 Imaging data

The UDS and GOODS-S fields have been observed with *HST*/WFC3 in the J (F125W) and H (F160W) filters (Grogin et al. 2011; Koekemoer et al. 2011). In the UDS, the v0.5 mosaics of the two epochs of WFC3/IR imaging were coadded. For the ACS F606W and F814W imaging in the UDS, we used only the second epoch of observation, since the first epoch contained some reduction artifacts at the time of this work. The *HST* imaging was supplemented by deep Subaru $BVRiz$ imaging from the Subaru/XMM-Newton Deep Survey (SXDS, Furusawa et al. 2008), using the mosaics prepared by Cirasuolo et al. (2010), and by K-band imaging from the UKIDSS UDS Data Release 6. Deep *Spitzer* IRAC data from the SpUDS survey (PI: Dunlop) allows us to access the rest-frame near-infrared to $z \simeq 3$. We cross-referenced our catalogs to the SpUDS MIPS catalog using a positional tolerance of 1".

In GOODS-S, we use the first three epochs of WFC3/IR imaging in the CANDELS Deep area and the first epoch of the Wide region. To this we add the GOODS $BViz$ ACS imaging, as well as ground-based data in U, R and K from VIMOS (Nonino et al. 2009) and ISAAC (Retzlaff et al. 2010) at the Very Large Telescope (VLT). The two epochs of ultradeep IRAC imaging from the *Spitzer* GOODS Legacy Science Program (PI: Dickinson) were coadded to produce a single mosaic. We again cross-referenced our catalog to the MIPS catalog.

8.2.2 Catalogs

For the main photometric catalog, we chose the WFC3 H band as the detection image, thereby taking advantage of the high-resolution *HST* imaging while maintaining a selection that is as complete in

stellar mass as possible. The H mosaic, distributed on a 60 mas pixel scale, was rebinned to a 120 mas scale, and all other imaging was registered to this grid. Object detection and photometric precision are insignificantly affected by this slightly coarser sampling, but the computational efficiency is greatly increased. For measurement of structural parameters, where the highest possible resolution is critical, we created catalogs for each *HST* mosaic at the original scale (60 mas for WFC3/IR and 30 mas for ACS) and matched these to the main catalog.

Each image (ground, *HST*, and IRAC) was first registered to the H-band mosaic using smooth transformations as determined by the IRAF task `geomap`. The images were then drizzled onto the uniform grid, precisely conserving flux, using `geotran`. A composite point-spread function (PSF) was constructed in each image by stacking suitably normalized cutouts of bright, unresolved sources. Matching PSFs is critical for accurate colors across images of widely varying resolution, yet one wishes to avoid unnecessary degradation of the high-resolution data as far as possible. We struck the following compromise: the ACS and WFC3 J images, each of higher resolution than the detection H image, were convolved to match the H-band PSF. Colors were then measured in fixed apertures of $1\farcs5$ diameter by running `SExtractor` (Bertin & Arnouts 1996) in dual image mode. For the lower-resolution imaging from ground-based instruments and IRAC, we measured the X band flux f_X in a wider aperture (see below) appropriate to the PSF in a given band X. We then convolved the H image to match the X PSF and measured the H flux $f_{H,\mathrm{wide}}$ in the wide aperture. Finally, f_X was scaled by the ratio $f_{H,1\farcs5}/f_{H,\mathrm{wide}}$, in order to refer all fluxes to a common aperture. In this way, the *HST* resolution is degraded as minimally as necessary for each band.

To determine a convolution kernel that matches two PSFs, we took the analytic Moffat kernel that best matched the curves of growth, weighting toward the radii relevant for our aperture photometry. This method typically matched curves of growth to $\simeq$ 1%–2%. Colors between *HST* filters were measured in fixed apertures of $1\farcs5$ diameter. For broader PSFs, the aperture diameter was set proportionally to the size of the PSF: four times the half-light radius, but restricted to lie within the range $1\farcs5$–$3''$. The upper limit was chosen to avoid excessive confusion in the IRAC data. Aperture colors were scaled to total fluxes using the `SExtractor` AUTO aperture in the H-band image. Photometric uncertainties were determined using apertures placed at random in blank sections of the images. Systematic uncertainties of 4% (10% in the IRAC bands) were added in quadrature to account for zeropoint errors, aperture mismatch, and color-dependent flat-field errors in IRAC. Small Galactic extinction corrections were made based on the dust maps of Schlegel et al. (1998).

8.2.3 Photometric redshifts and other derived parameters

Using this photometry spanning 0.4–8μm, photometric redshifts were estimated using the `EAZY` code (Brammer et al. 2008). We permitted linear combinations of all templates in its default set and adopted the prior based on K-band flux. Spectroscopic redshift surveys have been conducted with

the VLT in GOODS-S by Vanzella et al. (2008), Popesso et al. (2009), and Balestra et al. (2010), while Wuyts et al. (2008) have compiled redshifts from a number of additional sources. In the UDS[1] we draw from Simpson et al. (in preparation), Akiyama et al. (in preparation), and Smail et al. (2008). Only spectra with high quality flags were included. These spectroscopic data provide an opportunity to test the accuracy of our photometry by forcing `EAZY` to fit templates at the known redshifts and averaging the residuals in each filter (e.g., Capak et al. 2007). The resulting systematic offsets were small (typically $\lesssim 0.03$ mag), confirming the high quality of the photometric calibration and PSF matching. The one exception was the VIMOS R-band image, to which we added a -0.10 mag correction. In Section 8.4.1 we assess the accuracy of our photometric redshifts by comparing to this spectroscopic database.

Stellar population parameters, including stellar masses, were measured by fitting the latest Charlot & Bruzual (2007, private communication) models to the broad-band photometry using the `FAST` code (Kriek et al. 2009b). A large grid of models with exponentially-declining star-formation histories was created, with redshifts between 0.01 and 7 in steps of $0.01(1+z)$, ages between $t = 10^7$ and $10^{10.1}$ years (always less than the age of the Universe) in 32 logarithmic steps, star-formation timescales τ between $\tau = 10^7$ and 10^{10} years in 31 logarithmic steps, and dust content varying between $A_V = 0$ and 3 in 31 steps. Solar metallicity, the Calzetti et al. (2000) extinction law, and a Salpeter initial mass function (IMF) were adopted. We chose the Salpeter IMF because it may be more appropriate for massive galaxies (Treu et al. 2010; van Dokkum & Conroy 2010; Auger et al. 2010b; Newman et al. 2011; Spiniello et al. 2011), but our analysis is insensitive to this choice since we require only relative stellar masses. Rather than adopting the stellar population parameters of the single best-fitting model, we obtain the mean of each parameter by marginalizing over the likelihood function. Finally, rest-frame colors were computed using the `InterRest` code (Taylor et al. 2009).

[1] `http://www.nottingham.ac.uk/astronomy/UDS/data/dr3.html`

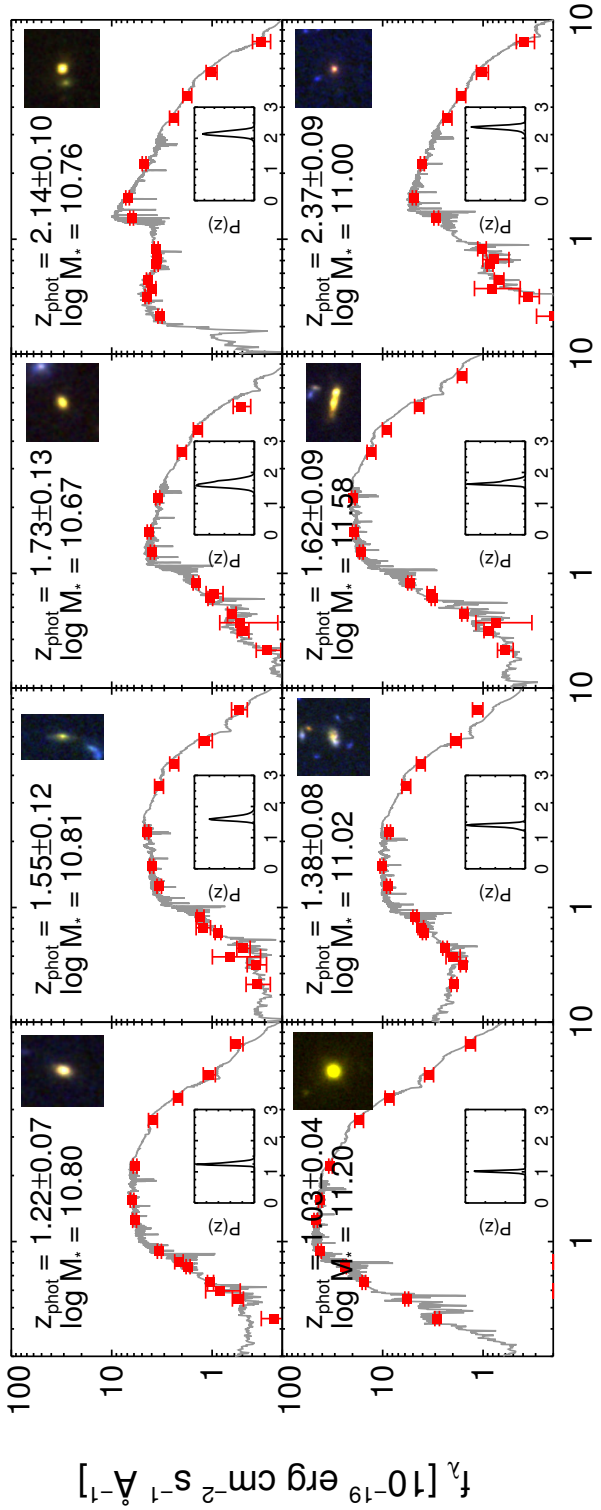

Figure 8.1: Montage of representative massive galaxies at $1 < z < 2.5$. High-precision photometry spanning 0.4 to 8 μm is plotted along with the best-fit spectral synthesis model as described in the text. Composite *HST* images in the *IJH* filters (where *I* is F814W or F775W) are inset along with EAZY photometric redshift distributions.

Figure 8.1 displays photometry, SED fits, redshift constraints, and color composite images for several representative massive galaxies at $1 < z < 2.5$. Note that the signal-to-noise ratio is very high, even at $z \simeq 2$, reflecting the high quality of the photometric data.

8.2.4 Survey mass limit and completeness

We define a limiting stellar mass for our galaxy sample, motivated by the desire to obtain a complete census of satellites with stellar mass ratios $\mu_* = M_{\rm sat}/M_{\rm host} > 0.1$ at $z < 2$ as well as our desire to track evolution in the sizes of mass-selected hosts to $z \simeq 2.5$.

The completeness of our catalog was assessed by inserting synthetic objects into blank sections of the UDS WFC3 H image, blurring by the empirical PSF and binning to the same pixel scale. These were then detected using the same `SExtractor` configuration. The 90% photometric completeness limits are $H_{\rm auto} = 26.5$ for point sources and $H_{\rm auto} = 25.6, 25.8$, and 26.1 for de Vaucouleurs profiles with $R_e = 0\farcs4, 0\farcs2$, and $0\farcs1$, respectively. For de Vaucouleurs profiles with $R_e = 0\farcs1$, which is roughly the size expected for local $\log M_* \simeq 9.7$ early-type galaxies viewed at $z \simeq 2$, the 90% completeness limit is $H_{\rm auto} = 26.1$. Figure 8.2a shows that selecting satellites with $\log M_* > 9.7$ at $z < 2$ ensures H-band fluxes above this limit, even for a maximally old population. Since we demand completeness for $\mu_* > 0.1$, this in turn implies a limit of $\log M_* > 10.7$ for the hosts.

If we are only concerned with studies of the host galaxies, i.e., without the need to detect their faint companions, they can be followed to somewhat higher redshift. We limit ourselves to $z < 2.5$ in order to retain deep detections in F160W, suitable for robust size measurements at our mass limit. Figure 8.2b shows that, in the redshift range $2 < z < 2.5$, we remain complete at $\log M_* > 10.7$ even for $R_e = 0\farcs4$, the most extended profile we tested. This size corresponds roughly to the size of a local $M_* = 10^{11}\,{\rm M}_\odot$ early-type galaxy viewed at $z = 2$.

8.2.5 Surface photometry and effective radii

We use `Galfit` (Peng et al. 2010) to fit Sérsic profiles to galaxies in our sample, using an automated procedure to fit adjacent objects simultaneously. The Sérsic index n was restricted to $0.5 < n < 8$, and the size of the fitting box was set by requiring it to enclose the Kron ellipse enlarged by a factor of 2.5. The background was measured in a rectangular annulus extending 40 pixels from the boundary of the fitting box. In order to measure structural parameters at similar rest-frame wavelengths, we selected different filters for fitting according to the redshift. In the UDS, sizes are measured in F814W for $0.4 < z < 0.9$, F125W for $0.9 < z < 1.8$, and F160W for $1.8 < z < 2.5$. In GOODS-S, F775W is used for $0.4 < z < 0.75$, F850LP for $0.75 < z < 1.1$, F125W for $1.1 < z < 1.8$, and F160W for $1.8 < z < 2.5$. This ensures that the wavelength at which sizes are measured always falls in the rest-frame interval 4240–6570 Å. Based on the mean difference between the Sérsic and

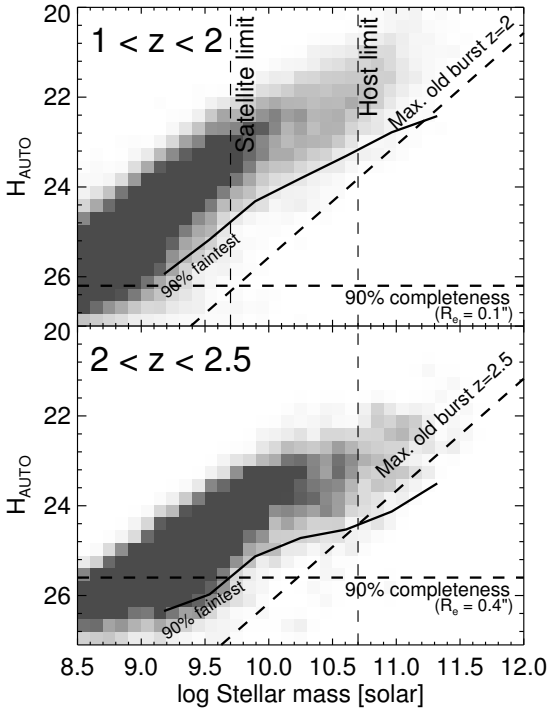

Figure 8.2: Our sample is designed to ensure a complete census of satellites with mass ratios $\mu_* = M_{\rm sat}/M_{\rm host} > 0.1$ at $z < 2$. The relation for a maximally old, dust-free stellar population using the Charlot & Bruzual (2007) models is shown as a dashed line, while the solid line indicates the 90th percentile in faintness at a given stellar mass. These are compared to completeness levels (horizontal) to set appropriate stellar mass limits. The top panel demonstrates that restricting hosts to $\log M_* > 10.7$ ensures strong detections in H for $\mu_* > 0.1$ satellites at $z < 2$. The bottom panel demonstrates the hosts themselves can be reliably studied to a higher redshift of $z = 2.5$.

AUTO magnitudes in the H band, we applied slight adjustments of $\Delta \log M_* = 0.014n$ to account for light outside of the AUTO aperture.

An extensive suite of tests performed by randomly inserting synthetic Sérsic profiles into the F814W, J, and H-band images showed that we are able to recover radii with a typical accuracy of 5%–10%, consistent with other studies (van der Wel et al. 2008; Newman et al. 2010). This procedure automatically incorporates errors arising from background misestimation and blending with neighboring objects, but applies strictly only to symmetric, Sérsic-like profiles. In the H-band image, we additionally tested for possible errors caused by PSF variations by convolving the synthetic profiles with stellar images selected from throughout the mosaic. These were then fitted using the empirical stacked PSF used to analyze the real data. We found that radii as small as $0\farcs05$ (0.4 kpc at $z = 2$) can be reliably recovered.

All galaxies with stellar masses exceeding $10^{10.7}\,\mathrm{M}_\odot$ were fit. For our study of size evolution presented in Section 3, we exclude galaxies for which *HST* imaging in the appropriate filter is not available due to imperfect overlap among the observations (5.7% of the sample), as well as those whose proximity to the image border or to a bright foreground star or galaxy precluded a reliable measurement (2.8%). Note that these cuts are uncorrelated with any galaxy property. We also exclude the 5.7% of remaining galaxies that are fit with a Sérsic index $n = 0.5$ or 8, i.e., the boundaries of the allowed range of n. These size measurements are likely to be unreliable. Although excluding them may slightly bias our mean size measurements, we expect any effect to be minor owing to the small fraction of the sample that they represent.

Effective (half-light) radii are typically reported in a circularized form defined by $R_{e,\mathrm{circ}} \equiv a\sqrt{q}$, where a is the semi-major axis of the half-light ellipse and $q = b/a$ is the axis ratio. We adopt a slightly different definition: $R_h \equiv a(1 + q)/2$. Physically, R_h closely approximates the half-light radius obtained from a classical curve of growth analysis on the intrinsic (PSF-deconvolved) Sérsic profile, i.e., the radius of the circle containing half of the total light, as we verified numerically. This definition differs appreciably from the more common $R_{e,\mathrm{circ}}$ only for small q, for which the latter diverges from a curve of growth measurement. For our mass-selected sample, the mean (median) difference between R_h and $R_{e,\mathrm{circ}}$ is only 5% (2%) and has no impact on the evolutionary trends that are the main subject of this paper.

8.2.6 Comparison to the Sloan Digital Sky Survey

The total area covered by our UDS and GOODS-S catalogs is 311 arcmin^2. At $z < 0.4$, too little volume is probed to provide reasonably large and representative samples of galaxies. In the following analysis, we therefore supplement our catalogs by comparing to $z \sim 0$ galaxies in the Sloan Digital Sky Survey (SDSS DR7, Abazajian et al. 2009). We selected galaxies from the spectroscopic survey in the redshift interval $0.05 < z < 0.07$. These were matched to stellar mass and star formation rate

estimates from the MPA-JHU DR7 catalog (Kauffmann et al. 2003a)[2] and to Sérsic fits from the NYU Value Added Catalog (Blanton et al. 2005). The stellar masses were shifted by +0.19 dex to convert from a Kroupa to a Salpeter IMF.

There may be substantial systematic differences between the derived measurements in the SDSS and CANDELS. For example, our SED fits include NIR photometry, while the SDSS does not. Comparisons of effective radii are also uncertain. Guo et al. (2009) fit Sérsic profiles to SDSS images of representative massive galaxies. Around $10^{11}\,\mathrm{M}_{\odot}$, their effective radii are on average 0.2 dex larger than the Blanton et al. (2005) values. Since none of the results in this paper rely on the SDSS data, we simply adopt the MPA-JHU stellar masses and Blanton et al. (2005) radii and, where appropriate, we caution how uncertainties in these affect the analysis.

8.3 Size Evolution of Massive Galaxies

The unique depth, resolution, and area of the CANDELS near-infrared images provides an opportunity to freshly examine the rate of size growth for various categories of galaxies within our mass-selected sample over $0.4 < z < 2.5$. Below we will focus on evolution in the stellar mass – size plane:

$$R_h = \gamma \left(\frac{M_*}{10^{11}\,\mathrm{M}_{\odot}} \right)^{\beta} = \gamma M_{11}^{\beta}. \tag{8.1}$$

In the nomenclature of early-type galaxies, this is the Kormendy projection of the stellar mass fundamental plane (relating M_*, R_h, and σ; e.g., Auger et al. 2010a). It has been extensively studied, particularly at high redshift where it is the most observationally accessible projection (e.g., Trujillo et al. 2006; Toft et al. 2007; Trujillo et al. 2007; Zirm et al. 2007; Buitrago et al. 2008; Cimatti et al. 2008; van Dokkum et al. 2008; van der Wel et al. 2008; Damjanov et al. 2009; Toft et al. 2009; Mancini et al. 2010; Ryan et al. 2010; Saracco et al. 2011; Damjanov et al. 2011). The mass-size plane provides some of the most powerful constraints on the merger histories of galaxies (e.g., Nipoti et al. 2003), which we exploit in Section 5.

Our sample contains 935 galaxies in the interval $0.4 < z < 2.5$ with stellar masses exceeding $\log M_* = 10.7$. Figure 8.3a demonstrates a strong correlation between size and the specific star-formation rate (SSFR, the star formation rate per unit stellar mass), such that the most compact galaxies are the most quiescent. The lower envelope of points delineates an evolving "compactness" limit. This figure confirms the results of many previous studies (e.g., Trujillo et al. 2006; Franx et al. 2008; Williams et al. 2010; Weinzirl et al. 2011) but represents an important advance, since it is based on a large, homogeneous sample with space-based sizes uniformly measured in the rest-frame optical to $z = 2.5$. The advantage of space-based imaging is particularly evident for lower-mass galaxies with $\log M_* < 11$. Most of these that are quiescent at $z \gtrsim 1.4$ have radii comparable

[2] `http://www.mpa-garching.mpg.de/SDSS/DR7/`

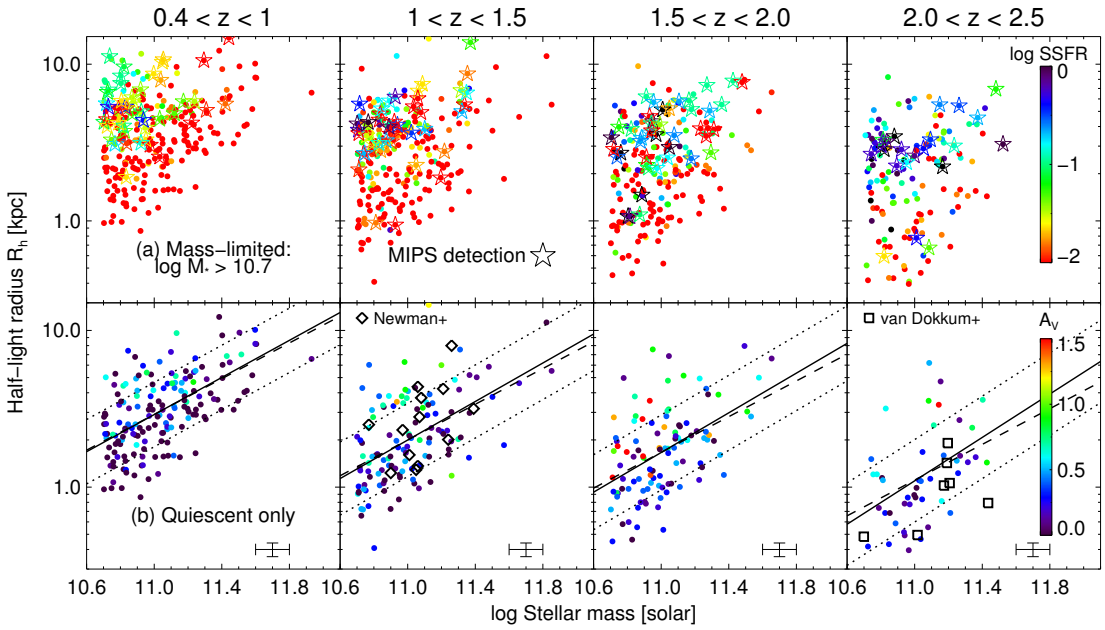

Figure 8.3: Size evolution of massive galaxies over $0.4 < z < 2.5$. **(a)** All galaxies with $\log M_* > 10.7$, with color encoding the SSFR. At each redshift there is a strong relationship between SSFR and size, with the most quiescent galaxies being the most compact. **(b)** The quiescent subsample, with color now encoding the extinction A_V. Linear fits show the best fit to $R_h \propto M_*^{\beta}$ with β as a free parameter (solid line) or fixed to the slope $\beta = 0.57$ (dashed). Dotted lines indicate the 1σ vertical scatter. Spectroscopic samples from Newman et al. (2010) and van Dokkum et al. (2008) (using CB07 fits from Muzzin et al. 2009a) that pass our selection criteria are plotted as diamonds and squares. Sizes represent Sérsic effective radii measured at rest-frame ~ 5000 Å as described in Section 2.

to or smaller than 0.″1–0.″2, which is generally taken as the limit for reliable size measurements in seeing-limited data (Bezanson et al. 2011; Williams et al. 2011).

We expect the appearance of the mass-size plane to change with time both through the evolution of existing galaxies and the continued emergence of new systems (e.g., Robertson et al. 2006; Hopkins et al. 2010a). Nevertheless, the evolution of the compactness threshold is strong enough that by $z \sim 2.5$, the most compact galaxies are typically smaller than any galaxy found in the lowest redshift bin. Although there may be a few compact systems persisting even to $z = 0$ (Valentinuzzi et al. 2010), their comoving number density is clearly greatly depleted (Trujillo et al. 2009; Taylor et al. 2010). This implies that individual, compact high-z systems must grow in size, and that the responsible processes must evacuate the most compact regions of the mass-size plane at a rate consistent with Figure 8.3. For this reason, in the following we concentrate foremost on quiescent galaxies, which are the most compact.

Figure 8.3b shows the trends we find for 483 quiescent galaxies, defined as the subsample with SSFR < 0.02 Gyr^{-1} and no detection in the MIPS 24μm channel, which would indicate the presence of warm dust. Several other definitions of quiescence are common in the literature. Among these,

Table 8.1. Fits of the Mass-Size Relation of Quiescent Galaxies to $\log R_h = \gamma + \beta(\log M_* - 11)$

Redshift	γ	β	$\sigma_{\log R_h}$
SDSS $z = 0.06$	0.54	0.57	0.16
$0.4 < z < 1.0$	0.46 ± 0.02	0.59 ± 0.07	0.21 ± 0.01
$1.0 < z < 1.5$	0.30 ± 0.02	0.62 ± 0.09	0.23 ± 0.02
$1.5 < z < 2.0$	0.21 ± 0.02	0.63 ± 0.11	0.24 ± 0.02
$2.0 < z < 2.5$	0.04 ± 0.04	0.69 ± 0.17	0.26 ± 0.03

Note. — Fits are plotted in Figure 8.3. Errors are determined from bootstrap resampling (negligible in the SDSS). The observed scatter is measured using the standard deviation.

we note that 88% of our quiescent sample would be selected by the UVJ color cuts introduced by Williams et al. (2010). The median Sérsic index of the quiescent subsample evolves modestly, from $\langle n \rangle \simeq 3$ to 4.5 over our entire redshift baseline, while the median axis ratio is essentially constant at $\langle q \rangle = 0.66$. This is consistent with the majority of these galaxies being bulge-dominated, although some are surely disks (see Kriek et al. 2009a; van der Wel et al. 2011).

Solid lines in Figure 8.3 show fits to Equation 8.1, which are reported in Table 8.1. Interestingly, there appears to be little or no evolution in the slope β of the mass–radius relation within the present uncertainties: formally, we find $d\beta/dz = 0.05 \pm 0.10$. Further, the mean $\langle \beta \rangle = 0.61 \pm 0.05$ is consistent with the $\beta = 0.57$ we measure for galaxies selected in the SDSS using the same stellar mass and SSFR criteria. In the context of spheroids, it is known that this slope cannot be established solely by dry mergers of smaller systems (e.g., Ciotti et al. 2007), and that it must therefore be imprinted by dissipational processes during a spheroid's formation, i.e., before it becomes quiescent. From this perspective, it is perhaps expected that the mass–radius slope for quiescent systems should persist to very early epochs.

Fits to the mass-size relation are always subject to an Eddington bias arising from the steep mass function. This steepness implies that near the limiting mass threshold, lower-mass galaxies are scattered above the threshold more frequently than higher-mass galaxies are scattered below it. We estimated this bias through Monte Carlo simulations, generating mock data with errors in stellar masses and radii typical of our sample. These were fit to a linear relation using a simple least-squares regression with equal weighting, as was done for the real data. The measured β may underestimate the true slope by $0.02 - 0.05$. Since this correction is small, sensitive to the true errors in the stellar mass estimates, and similar at each redshift, we decided not to apply it.

Noting the lack of significant evolution in the *slope* of the mass–size relation of quiescent galaxies, we fix $\beta = 0.57$ (the SDSS slope) and consider the growth of the normalization γ in Figure 8.4a. This figure displays the mean size of quiescent systems normalized to a stellar mass of $10^{11}\,\mathrm{M}_\odot$. It

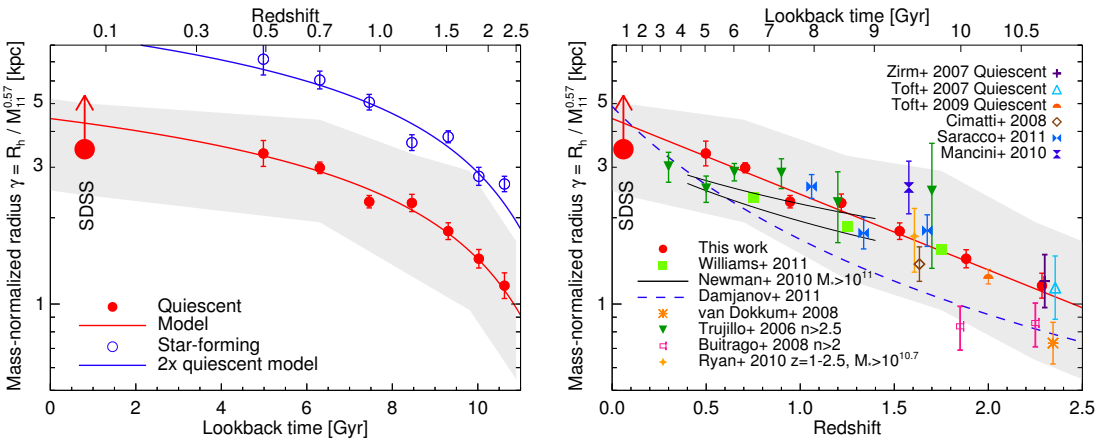

Figure 8.4: Left: Evolution in the mean size of quiescent (red) and star-forming (blue) galaxies, measured at matched rest-wavelength and normalized to $M_* = 10^{11}\,\mathrm{M}_\odot$ using the slope $R_e \propto M_*^{0.57}$. Error bars indicate the 1σ uncertainty in the mean, accounting for random sampling errors only. The shaded region shows the 1σ scatter in the quiescent population as measured in Table 1. The large red dot indicates our default SDSS relation; the arrow estimates the change if the Guo et al. (2009) sizes were used instead (Section 2.6). **Right:** Our results (red circles) are compared to other recent estimates, as indicated by the legend.

is important to recognize that the figure concerns the size evolution of the population as a whole and not necessarily the growth rate of any individual galaxy. Accordingly, we note that the growth rate at fixed mass $d\log\gamma/dt$ accelerates over this interval, remaining fairly gradual at $z \lesssim 1$ and then noticeably increasing over $z \approx 1$–2.5. We reached the same conclusion in Newman et al. (2010). Figure 8.4b shows the same data plotted against redshift; there is no apparent change in $d\log\gamma/dz$. We concentrate here on the evolution per unit time because it most directly relates to the effects of mergers. The blue points in Figure 8.4a indicate the sizes of the star-forming systems in our mass-limited sample. Interestingly, the evolution in size is similar to that for the quiescent galaxies, so that star-forming galaxies are always, on average, a factor of $\simeq 2$ larger than quiescent systems of the same mass over the entire redshift range (see Law et al. 2011).

Figure 8.4b compares our results on quiescent galaxies to several recent studies. Overall, there is a fair degree of convergence given the diverse nature of the samples, which apply various selection techniques to different types of data (e.g., sizes measured in different wavebands, from space and the ground, selection by color or morphology). In compiling these data we have harmonized all stellar masses to a Salpeter IMF and have applied an additional correction of $\Delta\log M_* = -0.05z$ for data fit with Bruzual & Charlot (2003, BC03) models.[3] We caution that direct comparisons of simple parametric fits may be misleading, since these can depend strongly on the redshift interval that is fit.

[3]This accounts for the average difference between BC03 and CB07 stellar mass estimates in our quiescent sample. The redshift dependence is expected, since the TP-AGB phase that distinguishes these models is predominant at ages of ~ 1 Gyr.

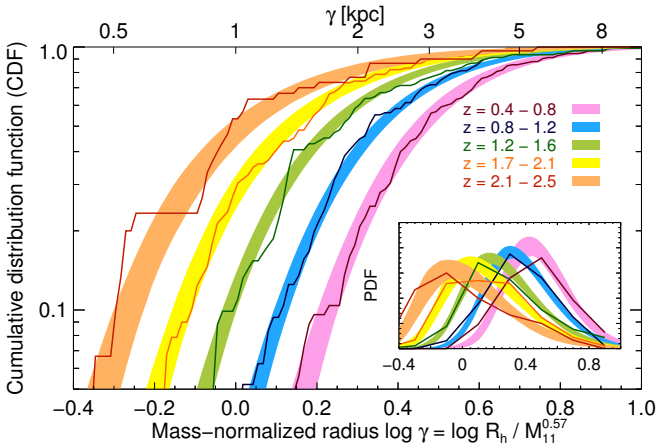

Figure 8.5: Cumulative distribution of the mass-normalized radius $\gamma = R_h/M_{11}^{0.57}$ in several redshift bins. The model described in the text is overlaid in bands with widths indicating the 90% confidence interval. Differential distributions are inset.

The primary conclusion from the high-quality CANDELS data now in hand is a factor of 3.5 ± 0.3 growth in size at fixed stellar mass for quiescent sources over the redshift interval $0.4 < z < 2.5$, with evidence for accelerated growth at earlier times (Figure 8.4a). Our challenge in the remainder of the paper will be to attempt to explain this growth rate. Although most workers have focused on the growth of the *mean size at a given epoch* (Figure 4), there is valuable information in the *distribution of sizes* which can be used to discriminate between the growth of individual systems over time and the arrival of new members of the population. Although we will discuss this model in more detail in Section 5, it is helpful to describe the data in terms of the evolving size distribution at this juncture.

Figure 8.5 shows the cumulative and differential (inset) distributions of the mass-normalized radius γ for quiescent galaxies in several redshift bins. The distribution is positively skewed in the higher redshift bins, i.e., it exhibits an excess of galaxies with large γ, which is mostly clearly visible in the inset. The largest quiescent galaxies at a given mass frequently show signs of dust (see coloring in Figure 8.3b), suggesting that their rest-optical sizes are impacted by central attenuation.[4] For our study in Section 5, the driving quantity is the declining abundance of compact galaxies. Therefore, when fitting the size distributions, it is important to adopt an asymmetric form so that the distribution at small γ is not affected by a few apparently large galaxies.

With this in mind, we describe the size distribution at a given redshift with a model in which $\log \gamma$ follows a skew normal distribution. The skew normal distribution has three parameters: the mean $\langle \log \gamma \rangle$, the standard deviation $\sigma_{\log \gamma}$, and a shape parameter s that is related to the skewness. Appendix A (Section 8.7) summarizes the relevant mathematical details. We parameterize the

[4] To illustrate the effect of extinction, if we restrict to the $\sim 80\%$ of quiescent galaxies with $A_V < 0.6$, the intercepts in Table 1 decrease by $\Delta \log \gamma = -0.05$ at $z > 1$, the slopes vary by $< 1\sigma$, and the scatter becomes $\sigma_{\log \gamma} = 0.20$ dex in every redshift bin.

Table 8.2. Size evolution model

Parameter	Posterior
Mean: $\langle \log \gamma \rangle (z = 1)$	0.38 ± 0.01
$d\langle \log \gamma \rangle / dz$	-0.26 ± 0.02
Standard deviation: $\sigma_{\log \gamma}(z = 1)$	0.22 ± 0.01
$d\sigma_{\log \gamma}/dz$	0.044 ± 0.017
Shape: $s(z = 1)$	2.3 ± 0.4
ds/dz	1.0 ± 1.1

Note. — Mean quantities, marginalized over all other parameters, are reported along with their 1σ uncertainty.

evolution in each parameter as linear in redshift:

$$\langle \log \gamma \rangle (z) = \langle \log \gamma \rangle_{z=1} + \frac{d\langle \log \gamma \rangle}{dz}(z - 1), \tag{8.2}$$

and similarly for $\sigma_{\log \gamma}$ and s. We then used a Markov Chain Monte Carlo procedure to sample the likelihood function. Each galaxy was weighted inversely to the number of galaxies at similar redshift to ensure that the entire redshift range contributed equally to the fit. Figure 8.5 compares the observed distribution in $\log \gamma$ to the model with parameters listed in Table 8.2.

This simple model accurately captures the observed features of the size evolution. First, $\langle \log \gamma \rangle$ evolves nearly linearly in redshift as $-0.26z$, which Figures 8.4b and 8.5 demonstrate is a good fit. Second, the scatter $\sigma_{\log \gamma}$ evolves fairly little with redshift. The mild increase is driven mostly by the increasing abundance of large, dusty systems toward higher redshifts, as discussed previously (see footnote 4). Note that we have not attempted to deconvolve errors arising from uncertainties in the stellar masses and radii of individual galaxies. Assuming the formal stellar mass uncertainties and a 10% uncertainty in the radii, the error in individual $\log \gamma$ measurements would be 0.07 dex nearly independent of redshift. Since this is much smaller than the measured width of the distribution, the intrinsic widths would be only ~ 0.01 dex smaller than the measured ones. If the true errors were instead twice these estimates, the intrinsic widths would be ~ 0.05 dex smaller than the measured ones. The impact of measurement errors is developed further in Appendix B (Section 8.8).

8.4 Satellites of Quiescent Galaxies at $0.4 < z < 2$

The most frequently invoked and well motivated physical processes behind the strong, regular size evolution presented in Section 3 is merging (e.g., van der Wel et al. 2008; Bezanson et al. 2009; Naab et al. 2009; Hopkins et al. 2010a). Most previous studies of merger rates have been confined to $z \lesssim 1.4$ or have focused on "major" mergers with stellar mass ratios $\mu_* \gtrsim 0.25$. This is partly

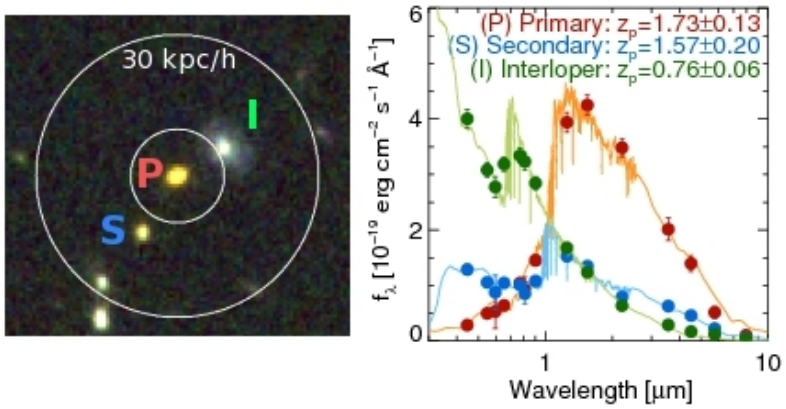

Figure 8.6: Demonstration of the pair counting procedure. The left panel displays a composite F160W/F125W/F814W image around a $10^{10.7}\,M_\odot$ quiescent "primary" galaxy at $z_p = 1.73$. The $10 < R < 30h^{-1}$ kpc search annulus is outlined. One $\mu_* \simeq 1:8$ secondary "S" is identified as a possible physical association based on its consistent photometric redshift (right panel). A blue galaxy "I" within the search aperture is excluded based on its low photometric redshift. The right panel shows the SEDs and best-fitting `FAST` models. For clarity, the models have been smoothed and the fluxes of the interloper reduced by a factor of 2.5.

due to observational limitations, since probing higher redshifts and lower-mass companions requires deep near-infrared data, and also because major mergers are of special interest for studies tracking morphological transformations.

Size growth, as well as spheroid formation (Bundy et al. 2007), are unlikely to be explained by major merging alone. Major mergers are rare: Bundy et al. (2009) estimate a rate of only $0.03 - 0.08$ Gyr^{-1} for $> 10^{10.5}\,M_\odot$ galaxies over $0.4 < z < 1.4$. If such low rates persist to $z = 2$, then $\lesssim 15\%$ of galaxies present at $z = 2$ will experience *any* major mergers by $z = 1$, whereas substantial size growth must occur over the same period. "Minor" mergers involving lower mass ratios may be crucial.

In this section, we measure the incidence of close companions to the same set of massive, quiescent galaxies at $0.4 < z < 2$ whose rate of growth was charted in Section 3. As discussed in Section 2, we here limit ourselves to $z < 2$ in order to maintain completeness for stellar mass ratios $\mu_* > 0.1$. Below, we refer to this quiescent sample as the *primary* sample, while the population of potential satellites is called the *secondary* sample. We search for secondaries around each primary galaxy at projected separations of $10 < R < 30\ h^{-1}$ proper kpc with stellar mass ratios $0.1 < \mu_* < 1$. Note that the upper limit avoids double counting. In principle, the size of the search annulus should not matter for measuring merger rates, since the merger timescales increase with the search area. In practice, the inner radius avoids searching for secondaries buried within the light of the primary at low redshift, while the outer radius strikes a reasonable balance of finding useful numbers of pairs without being dominated by chance alignments.

Since many galaxies that are close in projection lie at different redshifts, we attempt to secure

physical associations by additionally requiring that secondaries have a photometric redshift consistent with the primary, as detailed below. An example of this is given in Figure 8.6. However, due to the coarseness of photometric redshift estimates, some galaxies selected by this method will still be chance alignments not physically associated with the primary. This contamination rate is estimated simply by randomizing the positions of the primaries throughout the imaging area, maintaining all their other properties, and repeating the search for secondaries using the same criteria. This procedure is repeated many times to improve the statistical accuracy. Below we distinguish *projected* secondaries, which comprise all secondaries found within the search apertures, from the statistical secondary population that remains *after* chance contaminants are corrected for as just described, which we term *physical* secondaries. As we discuss in Section 5, it is important to realize that some fraction of these physical secondaries will not be bound to their primary host and therefore only represent candidate satellites or future mergers.

Below we measure the mean number of physical secondaries per primary host and assess the stellar mass content and colors of these systems. To examine the redshift dependence of these quantities, we break the primary sample into three redshift bins of $z = 0.4$–1, $z = 1$–1.5, and $z = 1.5$–2. In Section 5, we turn to the question of whether the size growth measured in Section 3 is consistent with the merger rates inferred here.

8.4.1 Photometric redshift accuracy

The secondary galaxy sample is selected to have stellar mass ratios $0.1 < \mu_* = M_2/M_1 < 1$ and photometric redshift differences $\delta_z = (z_2 - z_1)/(1 + z_1)$ less than a fixed threshold, where the subscripts 1 and 2 refer to the primary and secondary galaxies. Determining an appropriate threshold for δ_z requires knowledge of the accuracy of the photometric redshifts. At $0.4 < z < 1$, 327 of 1244 galaxies with $\log M_* > 9.7$ (the lowest secondary mass we might consider) have spectroscopic redshifts from the sources described in Section 2. Figure 8.7a compares these to photometric redshifts, demonstrating a small scatter of $\sigma_{\delta z} = 0.024$.[5] We verified that the redshifts, colors, and masses of the spectroscopic subsample at $z < 1$ are reasonably representative of the parent population, so the measured scatter should reflect the true photometric redshift uncertainties. Based on this result, we adopt a threshold of $|\delta_z| < 0.1$. In 2.8% of cases, the photometric estimates differ "catastrophically" by $|\delta_z| > 0.1$.

At $z > 1$ the availability of spectroscopic redshifts ($z_{\rm spec}$) declines rapidly. Of the massive, quiescent galaxy sample, 40 galaxies at $z = 1-2.3$ have measured $z_{\rm spec}$, of which only four are $z > 1.4$. The corresponding photometric redshifts display a small scatter $\sigma_{\delta z} = 0.023$ with only one outlier.[6]

[5]Throughout, we measure this scatter using the normalized median absolute deviation; see, e.g., Brammer et al. (2008).

[6]This single $z_{\rm spec}$ also disagrees with the photometric redshifts in the MUSYC (Cardamone et al. 2010) and FIREWORKS (Wuyts et al. 2008) catalogs.

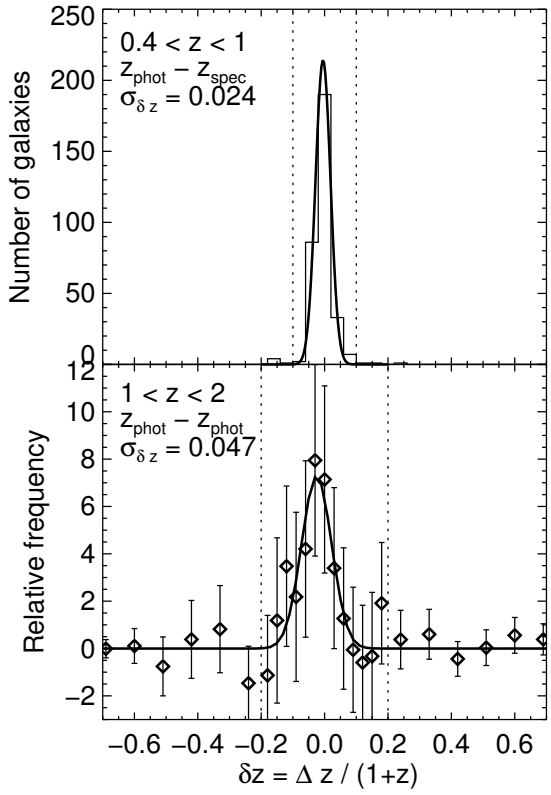

Figure 8.7: Photometric redshift errors in two redshift bins. **Top:** Comparison with spectroscopic redshifts for $\log M_* > 9.7$ galaxies at $0.4 < z < 1$ indicating a small scatter $\sigma_{\Delta z/(1+z)} = 0.024$. **Bottom:** Excess probability of a given redshift difference $\Delta z_{\rm phot}/(1+z_1)$ for secondaries within 30 h^{-1} kpc of the primary quiescent galaxy sample at $1 < z < 2$. Here secondaries are selected based on H flux ratios as described in the text. The quoted uncertainty refers to the difference in two photometric redshifts. In both panels, the dotted lines indicate the adopted δ_z threshold.

For the full mass-limited sample with $\log M_* > 9.7$ at $z = 1$–1.5, the 152 available $z_{\rm spec}$ indicate a scatter of $\sigma_{\delta z} = 0.021$, while at $z = 1.5$–2 the 32 available $z_{\rm spec}$ indicate $\sigma_{\delta z} = 0.058$. We have excluded X-ray sources in these comparisons, since they are over-represented in the spectroscopic data. We also note that the vast majority of $z_{\rm spec}$ at $z \gtrsim 1$ are in GOODS-S, so we must assume that similar techniques produce similar results in the UDS. Since $\sigma_{\delta z}$ appears to increase toward $z = 2$, we adopt a wider selection $|\delta_z| < 0.2$ for selecting secondaries at $z = 1$–2. With this selection, the catastrophic error rate ($|\delta_z| > 0.2$) is $3 \pm 1\%$ and $6 \pm 4\%$ at $z = 1$–1.5 and 1.5–2, respectively, based on the available spectroscopic data.

Since the spectroscopic samples are not representative of the full massive galaxy population at $z \gtrsim 1$, it is useful to assess the accuracy of photometric redshifts by other means. We use the empirical technique proposed by Quadri & Williams (2010). Their method is an application of the general procedure employed throughout this section: determine the distribution of δ_z for well defined primary and secondary samples, and subtract the distribution obtained with scrambled galaxy positions. In this situation, it is preferable to define a secondary sample based on flux rather than stellar mass, since errors in z_p and stellar mass are correlated. To determine a limiting flux ratio that best mimics a mass-based selection $0.1 < \mu_* < 1$, we examined the distribution of $\Delta H = H_2 - H_1$ between the primary quiescent sample and physical secondaries selected based on their stellar mass. In 90% of cases, $\Delta H < 2.2$ mag. This motivates a secondary sample defined by $0 < \Delta H < 2.2$ mag. Figure 8.7b shows the distribution of redshift differences δ_z for the physical secondaries.

The distribution is broader than at $z < 1$, as the spectroscopic comparison also indicated. The uncertainty $\sigma_{\delta z} = 0.047$ measured here refers to that in the *difference* between two photometric redshifts. The more important uncertainty for this study is the rate of catastrophic ($|\delta_z| > 0.2$) redshift errors. A crude estimate of this can be obtained by integrating the curve in Figure 8.7b, which yields $9 \pm 15\%$ over $z = 1$–2. Using the same technique at $z \simeq 2$, we find a possibly higher catastrophic rate of $15 \pm 20\%$, but this cannot be determined precisely with the present sample size. These noisier estimates may be higher than the 3%–6% inferred from the spectroscopic database, but that sample is biased toward bright systems. A better assessment of the catastrophic rate will require spectroscopic redshifts for larger and more representative samples of galaxies at $z = 1$–2 than is currently available.

8.4.2 Subtraction of host light

A concern in all pair studies is that the photometry of the secondary galaxies may be contaminated by light from the hosts. By inserting synthetic pairs of galaxies with 1 : 10 luminosity ratios and projected separations 10–30 h^{-1} kpc into the H-band mosaic, we found that our detection efficiency is not affected by the proximity of the host. Further, these tests indicated that the aperture colors

are less affected than the H-band AUTO magnitude used to scale the total stellar masses. To correct for this, we measure the `SExtractor` AUTO magnitudes of the secondary galaxies in images from which the light of the primary galaxy has been subtracted using our Sérsic fits (Section 8.2.5). We also compute stellar mass ratios μ_* using fits that omit the IRAC photometry, which is the most susceptible to contamination, although this has little effect on our results.

8.4.3 Abundance and stellar masses of physical secondaries

We now turn to the frequency of physical secondaries and their stellar mass content. First, we consider the pair fraction $f_{\rm pair}$. This is simply the mean number of physical secondaries per primary galaxy: $f_{\rm pair} = (N_p - N_r)/N_g$, where N_p is the number of projected secondaries, N_r is the expected number of chance alignments given the total search area, and N_g is the number of primary galaxies. Throughout our pair analysis, we exclude the shallower "Wide" section of GOODS-S and primaries for which more than 20% of the search annulus is masked (e.g., near the image edge). All results in the remainder of this section pertain to mass ratios $0.1 < \mu_* < 1$.

Table 8.3 presents the results. For quiescent primaries, we find $f_{\rm pair} = (16 \pm 3)\%$ when averaged over the entire host mass and redshift range. Moreover, the pair fraction does not appear to evolve significantly with redshift within our uncertainties: formally, we find $f_{\rm pair} \propto (1+z)^{-0.11 \pm 0.68}$. The paradoxical result that the galaxy merger rate remains flat as the halo merger rate increases with redshift has been explored in many theoretical works (e.g., Berrier et al. 2006; Kitzbichler & White 2008). Although our present sample is not large enough to be divided in both redshift and mass, we can examine possible mass-dependent trends by dividing the sample into the three mass bins listed in Table 8.3 and averaging over the full redshift range. We find that the pair fraction increases slightly with stellar mass as $f_{\rm pair} \propto M_*^{0.28 \pm 0.41}$, in agreement with Bundy et al. (2009). For later use in our models of size growth, we also tabulate the "intrasample" fraction $f_{\rm IS}$ of physical secondaries which are also members of the primary sample (i.e., are quiescent and $> 10^{10.7}\,{\rm M}_\odot$).

From the point of view of galaxy assembly, an equally useful quantity is the amount of stellar mass contained in physical companions. We estimate this simply by computing the mean total stellar mass in projected secondaries (expressed as a fraction of the host mass) and subtracting the random contribution as described previously. We denote this quantity f_M. Averaged over all masses and redshifts, we find $f_M = 0.060 \pm 0.011$. The mean mass ratio $\langle \mu_* \rangle = f_M / f_{\rm pair}$ is very nearly constant at ≈ 0.39 in all redshift and primary mass ranges. As many authors have noted, this implies that the stellar mass delivered in mergers arrives primarily in more massive secondaries (e.g., Hopkins et al. 2010b). In Section 5, we compare $\langle \mu_* \rangle$ to theoretical expectations.

Although we concentrate on the growth of quiescent galaxies for the remainder of this paper, for comparison with future work we also tabulate the corresponding quantities for star-forming galaxies in Table 8.3.

Table 8.3. Abundance and Properties of Physical Secondaries with $0.1 < \mu_* < 1$

Redshift	Primary mass range	N_p	N_r	N_g	$f_{\rm pair}(\%)$	$f_M(\%)$	$\langle\mu_*\rangle = f_M/f_{\rm pair}$	$f_{\rm Q}(\%)$ SSFR / $(U-V)_{\rm cor}$	$f_{\rm IS}(\%)$
Quiescent galaxies									
$0.4 < z < 1$	$10.7 < \log M_*$	41	9.7	177	18 ± 4	6.2 ± 1.6	0.35 ± 0.06	$71 \pm 10/91 \pm 8$	35 ± 12
$1.0 < z < 1.5$	$10.7 < \log M_*$	27	12.4	117	13 ± 5	5.3 ± 1.7	0.43 ± 0.08	$66 \pm 16/78 \pm 18$	33 ± 17
$1.5 < z < 2$	$10.7 < \log M_*$	30	11.8	100	18 ± 6	7.5 ± 2.7	0.41 ± 0.06	$33 \pm 15/38 \pm 16$	18 ± 14
$0.4 < z < 2$	$10.7 < \log M_* < 10.9$	39	18.0	141	15 ± 5	5.8 ± 1.8	0.39 ± 0.07	$52 \pm 14/71 \pm 16$	...
$0.4 < z < 2$	$10.9 < \log M_* < 11.2$	48	16.5	174	18 ± 5	6.5 ± 1.8	0.36 ± 0.05	$47 \pm 12/67 \pm 13$	...
$0.4 < z < 2$	$11.2 < \log M_*$	22	4.9	80	21 ± 6	8.6 ± 2.9	0.40 ± 0.08	$76 \pm 13/82 \pm 12$	...
Star-forming galaxies									
$0.4 < z < 1$	$10.7 < \log M_*$	15	4.3	84	13 ± 5	4.9 ± 2.2	0.39 ± 0.07	$50 \pm 23/71 \pm 21$	...
$1.0 < z < 1.5$	$10.7 < \log M_*$	30	14.5	127	12 ± 5	4.1 ± 2.0	0.34 ± 0.08	$41 \pm 20/53 \pm 21$	...
$1.5 < z < 2$	$10.7 < \log M_*$	30	12.9	108	16 ± 6	5.7 ± 2.4	0.36 ± 0.08	$29 \pm 15/59 \pm 17$	...

Note. — N_p, N_r, and N_g are the number of observed projected pairs, the expected number of these that are chance alignments, and the number of primary galaxies, respectively. $f_{\rm pair} = (N_p - N_r)/N_g$ is the number of physical secondaries per primary galaxy, of which a fraction $f_{\rm Q}$ are quiescent (as determined using the two methods described in the text) and a fraction $f_{\rm IS}$ are included in the primary sample (i.e., quiescent and massive). f_M is the mean stellar mass in physical secondaries as a fraction of the host. Uncertainties in $f_{\rm pair}$ reflect Poisson noise in N_p and N_r; for other quantities, uncertainties are determined from bootstrap resampling of the primary galaxies.

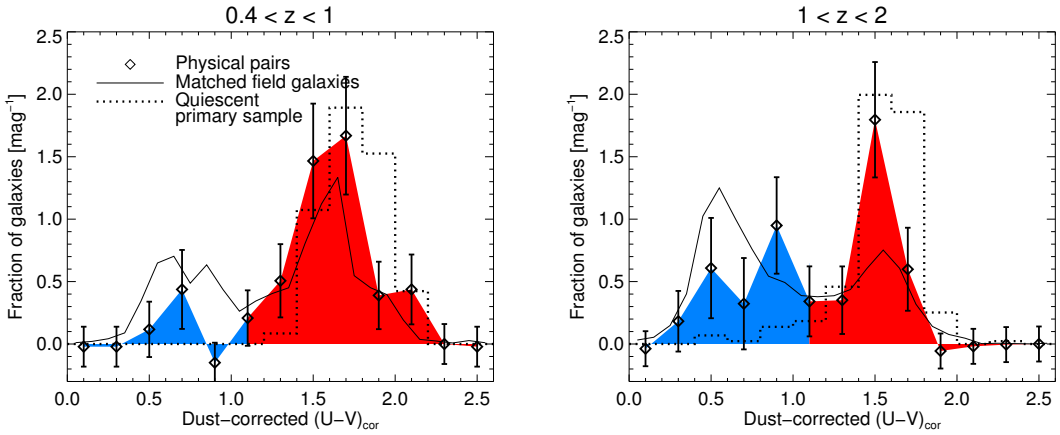

Figure 8.8: Distribution of rest-frame colors of physical secondaries around the massive, quiescent galaxy sample in two redshift bins, compared to a field sample that is matched in stellar mass and redshift (solid) and to the primary sample (dotted). At higher redshifts, a significant fraction of companions are blue.

8.4.4 Colors of physical secondaries

Since physical secondaries likely represent the "building blocks" for the future mass assembly of quiescent galaxies, particularly in their outer regions, it is interesting to consider their stellar populations in relation to those of their hosts. In particular, the fraction of mergers which are "dry" (gas-poor) versus "wet" is an important input to models of galaxy evolution. Table 8.3 presents the fraction $f_{\rm Q}$ of physical secondaries which are quiescent. We calculate this using two definitions of quiescence: the SSFR < 0.02 Gyr^{-1} threshold used throughout this paper (also excluding MIPS detections), and a color selection $(U-V)_{\rm cor} > 1.1$. Here

$$(U-V)_{\rm cor} = (U-V)_{\rm rest} - 0.47 A_V \tag{8.3}$$

represents the *extinction-corrected* rest-frame $U-V$ color (Brammer et al. 2009). Overall, the two selections are qualitatively consistent: most physical companions to quiescent galaxies are themselves quiescent at $z < 1$, and this fraction decreases with redshift.

This is illustrated in Figure 8.8, which shows the color distribution of the physical secondaries. (As throughout, we have subtracted the color distribution of similarly-selected galaxies in randomly-placed apertures.) The secondaries are compared to a field sample with matched distributions in stellar mass and redshift (solid line) and to the primary quiescent host sample (dotted). In both redshift bins, the physical secondaries are on average redder than the field comparison sample. The fraction of blue secondaries increases with redshift, suggesting that the reservoir of future merger candidates includes progressively more gas-rich galaxies at earlier times. The implications for the merger descendants are interesting but not completely clear. On the one hand, secondary bursts

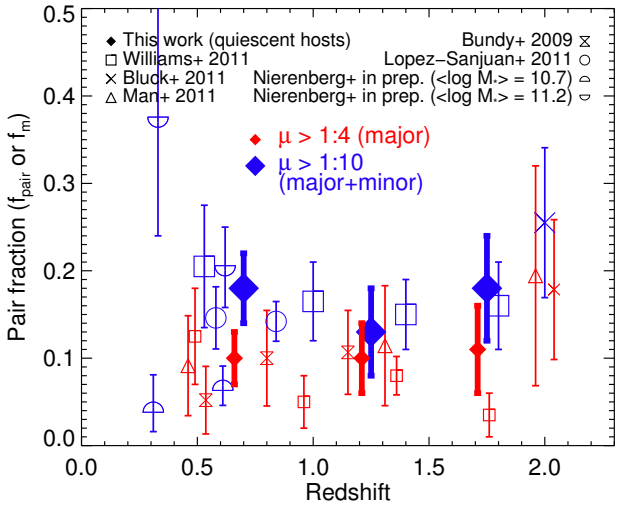

Figure 8.9: Major ($\mu > 0.25$, small red symbols) and total ($\mu > 0.1$, large blue symbols) pair fractions are compared to recent independent measurements at $z < 2$. Here μ refers to either a flux or stellar mass ratio. Overall there is reasonable consistency within the statistical uncertainties, with no clear sign of strong evolution in $f_{\rm pair}$ over $z = 0.5$–2. Expected systematic differences arising from different selection techniques are discussed in the text. Points are slightly offset in redshift for clarity.

of star-formation are observed in spectroscopic samples of early-type galaxies at $z \simeq 1$ (Treu et al. 2005). On the other hand, as we review in Section 5, merger timescales are expected to be $\gtrsim 1$ Gyr. If the processes driving satellite quenching are mostly confined to the final ∼Gyr, many of these blue secondaries may be much redder by the time of the final merger. Nevertheless, it seems likely that a significant fraction of mergers at $z \gtrsim 1$ are not completely dry, even for red hosts.

8.4.5 Comparison with previous work

Comparisons to independent estimates of the pair fraction are complicated by the intrinsic differences in samples selected by various means (stellar mass, color, luminosity). In particular, as we discuss below, samples in which satellites are selected based on their stellar mass will systematically differ from those based on luminosity, particularly in the rest-frame optical. An advantage of the present study is the characterization of the merger rate and size growth using a uniform mass-based selection. Nevertheless, it is valuable to compare our $f_{\rm pair}$ measurements to other works. In the following, we rescale published $f_{\rm pair}$ measurements to our search area by assuming that $f_{\rm pair}(R < R_{\rm max}) \propto R_{\rm max}$ (Kitzbichler & White 2008; López-Sanjuan et al. 2011). Figure 8.9 shows this comparison, focusing primarily on those studies that adopted a mass-based selection, included minor mergers, or probed to $z \simeq 2$. For comparison, we also plot the "major" pair fraction in our sample, defined by $0.25 < \mu_* < 1$.

At $z \lesssim 1$, our measurements are broadly in agreement with previous results when analogous samples are compared and search apertures are matched (e.g., Kartaltepe et al. 2007; Lin et al. 2008; Rawat et al. 2008; de Ravel et al. 2009). Of particular interest is the comparison to López-Sanjuan et al. (2011), who identified minor spectroscopic pairs. Figure 8.9 shows results for their red host sample with secondaries having rest-B luminosity ratios $\mu_B > 0.1$. Nierenberg et al (2012, in preparation, see also Nierenberg et al. 2011) identify minor companions to spheroidal hosts split into two bins of stellar mass (Chabrier IMF), identifying satellites with flux ratios $\mu_{\mathrm{F814W}} > 0.1$. The strong mass dependence they find highlights the importance of matching hosts in stellar mass when comparing pair fractions or analyzing the associated size growth. We note that Nierenberg et al. use a local background estimation that is expected to yield smaller raw pair fractions. Bundy et al. (2009) selected major pairs at $z < 1.4$ having K-band flux ratios $\mu_K > 0.25$. Their results for red hosts with $\log M_* > 10.5$ (Chabrier IMF) are shown in Figure 8.9. Several authors have inferred merger rates from morphological signatures (e.g., Lotz et al. 2008b, Conselice et al. 2009, Bridge et al. 2010). For a recent review, we refer to Lotz et al. (2011).

Few other studies have considered minor mergers at $z \gtrsim 1$. Among these, Williams et al. (2011) is the most directly comparable to our work, as their selection is based on stellar mass. Figure 8.9 shows their quiescent, $\log M_* > 10.8$ (Kroupa IMF) host galaxy sample, for which they find $f_{\mathrm{pair}} \approx 0.16$–$0.20$ ($\mu_* > 0.1$) essentially independent of redshift in encouraging agreement with our results.

Man et al. (2011) use H-band *HST*/NICMOS imaging to assess the major pair fraction for massive ($\gtrsim 10^{11}\,\mathrm{M}_\odot$) hosts, selecting secondaries with H-band flux ratios $\mu_H > 0.25$. Recently, Bluck et al. (2011) (see also Bluck et al. 2009) studied fainter companions around a similarly massive population by identifying close pairs to a limiting flux ratio of $\mu_H = 0.01$ in NICMOS imaging. As Figure 8.9 shows, our data are consistent with these flux-based selections at $z \lesssim 1.7$. There is a hint that the major and total ($\mu > 0.1$) pair fractions rise toward $z \simeq 2$, but this is not very significant at present. (Bluck et al. (2011) demonstrate stronger increases toward $z \simeq 3$.) Furthermore, samples in which secondaries are selected based on rest-optical flux will not agree in detail with stellar mass-based samples (see Bundy et al. 2004). At $z \simeq 2$, the H band probes the rest-frame V band. A significant dispersion in the stellar mass-to-light ratio M_*/L is thus expected, and the mean M_*/L declines substantially with decreasing mass. Assuming a constant M_*/L equal to that of the host and a limiting flux ratio $\mu_H > 0.1$, for example, will include bluer galaxies with lower mass ratios $\mu_* < 0.1$, likely resulting in an elevated f_{pair} compared to a mass-selected sample. This effect is expected to become stronger toward lower mass ratios and toward higher redshifts as the H band probes bluer rest wavelengths, possibly impacting trends with redshift in flux-selected samples.

Finally, van Dokkum et al. (2010) used a novel method to infer indirectly the rate at which massive galaxies assemble mass through mergers. They tracked the stellar mass growth of a sample

over $z = 0-2$ with constant comoving number density and subtracted an estimate of the *in situ* star formation. Their estimated "specific assembly rate" is $\dot{M}_*/M_* = 0.03(1+z)$ Gyr^{-1}. At $z \sim 1$ this compares well with our pair counting estimate of $f_M/\tau_e \approx 0.07/\tau_e$ for merger timescales $\tau_e \sim 1$ Gyr (see Section 5.2), although we find a weaker redshift dependence.

8.5 Connecting Size Growth with Mergers

In this section we present simple models that compare the rate of size growth measured in Section 3 with that attributable to mergers of close pairs as studied in Section 4. Sections 5.1 and 5.2 review the theoretical ingredients necessary to convert pair fractions into growth rates in mass and size. In Section 5.3 we examine the growth in the mean size of quiescent galaxies and discuss how the rate of size evolution experienced by any individual galaxy may be substantially smaller. Finally, in Section 5.4 we combine our constraints on the distribution of sizes of quiescent galaxies with the evolution of their number density to establish a minimum growth rate, which we then compare to a merger model.

8.5.1 Merger timescales and the distribution of mass ratios

Converting the observed number of physical companions into a merger rate requires us to specify the timescale during which a merger appears within our search aperture, i.e., a projected separation between 10 and 30 h^{-1} kpc. We define an effective timescale τ_e that incorporates two physical effects. The first is the mean time $T_{\rm mg}$ during which a bound, sinking satellite appears within our search aperture. As discussed in Section 4, however, not all of the physical secondaries we counted are necessarily bound to their host. By subtracting the number of pairs found in randomly placed apertures, we account for interlopers in the far fore- and background of the galaxies in our primary sample, but we can expect the remaining "physical" secondaries to include both bound satellites *and* other galaxies in the larger group-scale environment that are not bound. As is common practice in merger rate studies, we account for this by defining a factor $C_{\rm mg}$ (see also Bundy et al. 2009) to represent the fraction of physical secondaries that are bound and due to merge on a typical timescale $T_{\rm mg}$. The effective timescale is then $\tau_e = T_{\rm mg}/C_{\rm mg}$.

Patton & Atfield (2008) study projected pairs of similar luminosity in the SDSS. They assume that mergers of luminous pairs occur with a typical timescale of $T_{\rm mg} = 0.5$ Gyr. Based on tests using the Millennium simulation (Springel et al. 2005), they estimate $C_{\rm mg} \approx 0.5$ (their $f_{\rm 3D}$) for the most luminous pairs, resulting in an effective timescale $\tau_e = T_{\rm mg}/C_{\rm mg} \approx 1.0$ Gyr.

Lotz et al. (2008a, 2010b,a) investigate merger timescales for disk galaxies using high-resolution hydrodynamical simulations. For self-similar mergers of their most massive disk G3, they find a mean timescale $\langle T_{\rm mg} \rangle = 0.7$ Gyr within our adopted search annulus. Similar to Patton & Atfield

(2008), Lotz et al. (2011) allow for projection effects by setting $C_{\rm mg} = 0.6$, resulting in an effective $\tau_e = 1.2$ Gyr.

Kitzbichler & White (2008) calibrated τ_e using the Millennium simulation, coupled with a semi-analytic model of galaxy merging and evolution (de Lucia & Blaizot 2007). Considering major mergers ($0.25 < \mu_* < 4$) of $M_* = 10^{11}\,{\rm M}_\odot$ galaxies and a search aperture of $R < 30\ h^{-1}$ kpc, they find $\tau_e = 2.7$ Gyr. Since τ_e scales approximately as the outer radius of the aperture, and we exclude the inner $10\ h^{-1}$ kpc, the appropriate timescale for our study would be $\sim 2/3$ of this, or $\tau_e \approx 2$ Gyr.

Taken together, these studies imply $\tau_e = 1$–2 Gyr for major mergers. In order to make progress in the present study, we also need an estimate of τ_e for minor mergers, which will likely be larger. The outcome will depend on the relative contribution of minor mergers, i.e., the distribution of μ_* in our sample, and on how strongly the timescales vary with μ_*. Figure 8.10 breaks the observed pair fractions from Section 4 into several bins of the mass ratio μ_*. The distribution is essentially flat in $\log \mu_*$; this corresponds to a mass function that rises as μ_*^{-1}. We note that a uniform distribution over $-1 < \log \mu_* < 0$ has a mean $\langle \mu_* \rangle = 0.39$, in agreement with our measurement of $\langle \mu_* \rangle = 0.39 \pm 0.04$ (Section 4).

To understand the flat distribution in Figure 8.10, we compare the measured pair fractions to merger rates $R_{\rm mg} = f_{\rm pair}/\tau_e$ predicted by the semi-analytic model (SAM) of Hopkins et al. (2010b) under three choices of the observability timescale τ_e described in the caption. Within the uncertainties, our observations are consistent with any of these timescale scalings. At higher redshifts, the SAM predicts higher $f_{\rm pair}$ (blue curve), which we do not observe. However, the distribution in μ_* maintains the same shape nearly independently of mass or redshift. This is not particular to the Hopkins et al. (2010b) model, but is a generic feature of many SAMs (see Lotz et al. 2011). The SAM also provides an estimate of the amount of stellar mass in $\mu_* < 0.1$ mergers that we do not probe observationally. Only $\simeq 9\%$ of the predicted mass assembly rate (i.e., the rate at which stellar mass is delivered through mergers) is due to $\mu_* < 0.1$ mergers. This simply reflects the fact that for such low mass ratios, the time for a galaxy to descend from the virial radius to the center quickly exceeds a Hubble time (Taffoni et al. 2003; Boylan-Kolchin et al. 2008). By observing $\mu_* > 0.1$ pairs, therefore, we expect to account for the vast majority of the mass assembly.

In summary, the effective timescale for major mergers is likely $\tau_e = 1$–2 Gyr. For lower mass ratios, estimates are even less certain. However, since the physical secondaries are not overly dominated by the lowest mass ratio systems, consistent with the predictions of SAMs, we expect the appropriate average τ_e for our sample to be only moderately higher. In the following analysis we present results for models spanning a range of timescales.

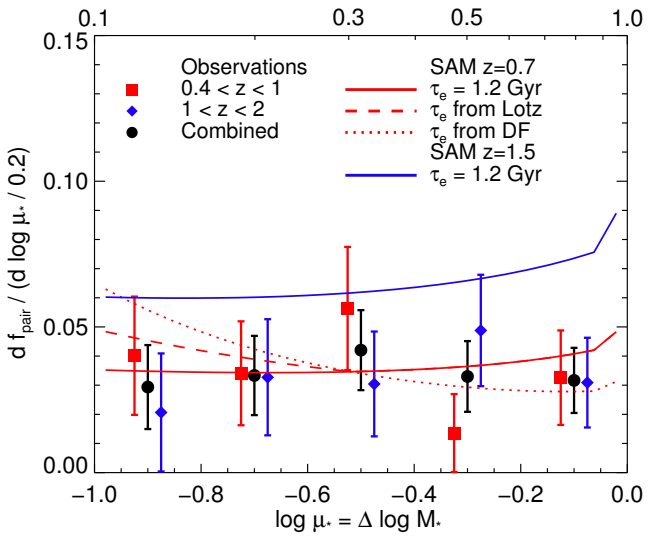

Figure 8.10: Distribution of the stellar mass ratio μ_* of physical secondaries around $\log M_* > 10.7$ quiescent galaxies in two redshift bins. Merger rate predictions of the Hopkins et al. (2010b) SAM are overlaid under several assumptions for the timescale τ_e: a constant $\tau_e = 1.2$ Gyr (solid line), $\tau_e \propto \mu_*^{-0.3}$ for $\mu_* < 0.3$, in line with the Lotz simulations (dashed), and $\tau_e \propto [\mu \log(1+\mu^{-1})]^{-1}$ (dotted) as expected from pure dynamical friction considerations.

8.5.2 Size growth efficiency

In order to address whether mergers drive the observed size growth, we need to know how the half-light radius R_h of a galaxy changes after undergoing a merger of mass ratio μ. This question has been addressed in the literature both analytically and using extensive suites of merger simulations. The growth efficiency is commonly parameterized by $\alpha = d\log R_h / d\log M_*$. For $1:1$ mergers of spheroids, both the mass and radius approximately double and $\alpha \simeq 1$ (e.g., Hernquist et al. 1993; Nipoti et al. 2003; Boylan-Kolchin et al. 2006).

Simple virial arguments based on energy conservation show that the growth efficiency can be higher for more minor mergers (Hopkins et al. 2009; Bezanson et al. 2009; Naab et al. 2009). Assuming that the orbit is parabolic, that the progenitors and merger product are structurally homologous, and that there is negligible energy transfer from the stars to the dark halo,

$$\alpha = 2 - \frac{\log(1+\mu^{2-\beta})}{\log(1+\mu)}, \tag{8.4}$$

where we have assumed the progenitors lie on a $R_h \propto M_*^{\beta}$ relation. For self-similar mergers $\mu = 1$ and we recover $\alpha = 1$. For a mass–radius slope of $\beta = 0.57$ (Section 3) and the lowest mass ratios we observe ($\mu = 0.1$), this estimate becomes $\alpha = 1.6$. We therefore expect an appropriately averaged $\langle\alpha\rangle$ over the mass ratios we consider to lie in this range.

Recognizing the assumptions entering this simple formula, it is essential to verify its predictions

with merger simulations. Nipoti et al. (2009a) simulated hierarchies of multiple dry minor mergers of spheroids and found $\langle\alpha\rangle = 1.30$. More recently, Nipoti (2011) performed a suite of $\mu = 0.2$ dry spheroid mergers and found $\langle\alpha\rangle = 1.60$ (see also Nipoti et al 2011, submitted). Oser et al. (2011) investigated the relevance of Equation 8.4 in a cosmological hydrodynamical simulation and found it to be accurate. Altogether, based on these results, we consider $\alpha \sim 1.3$–1.6 to be a reasonable average over the mass ratios we consider. We note that a higher efficiency ($\alpha > 1.6$) has not been demonstrated, when averaged over a representative set of orbits, in any N-body simulation of which we are aware.

8.5.3 Matching the observed growth of the quiescent population

With estimates for the growth efficiency α and merger timescale τ_e in hand, we can now proceed to a simple model that estimates the rates of growth in mass and size due to mergers. In a time interval Δt, the stellar mass of the average quiescent host in our sample increases by $\Delta \log M_* = \log(1 + f_M)^{\Delta t/\tau_e}$, while the radius by definition increases by $\alpha\Delta \log M_*$. Since we expect $\alpha > \beta = 0.57$, as discussed in Section 5.1, mergers will shift the mean mass-size relation:

$$\begin{aligned}\Delta \log \gamma &= \Delta \log R_h - \beta\Delta \log M_* = (\alpha - 0.57)\Delta \log M_* \\ &= (\alpha - 0.57) \log(1 + f_M)^{\Delta t/\tau_e}. \end{aligned} \tag{8.5}$$

We have neglected here the small change in the number density arising from mergers within the sample over the interval Δt. This incurs a fractional error of $\sim f_{\rm IS} f_{\rm pair} \approx 5\%$ in the mass accreted, negligible for our purposes.

Figure 8.11a reproduces the observed growth in γ from Figure 8.4. Using Equation 8.5, we overlay growth trajectories for representative values of the growth efficiency and merger timescale to illustrate the evolution of the quiescent galaxy populations in place at $z = 2$ and $z = 1$. Here we have taken f_M appropriate to $z = 0.4$–1 and $z = 1$–2 (Table 8.3) and applied a 15% correction to account for both additional satellites below our $\mu_* = 0.1$ limit and for possible catastrophic redshift errors (Section 8.4.1). We assume that all galaxies grow smoothly at this rate, i.e., we do not incorporate stochasticity in the incidence of mergers.

The primary conclusions from Figure 8.11a are twofold. First, at $z \lesssim 1$ the pairs we observe can plausibly account for most of the observed size growth if an effective timescale $\tau_e \sim 1$ Gyr, at the short end of the estimates discussed in Section 8.5.1, and an average growth efficiency $\alpha \approx 1.6$ are valid. Second, at $z \gtrsim 1$ the observed growth in $\log \gamma$ per unit time increases significantly. This enhanced growth rate cannot be matched by mergers using any reasonable choices of τ_e and α.

As discussed in Section 3, however, an important objection to the model comparisons in Figure 8.11a is that we are tracking the mean growth rate of the entire population, as if all sources are

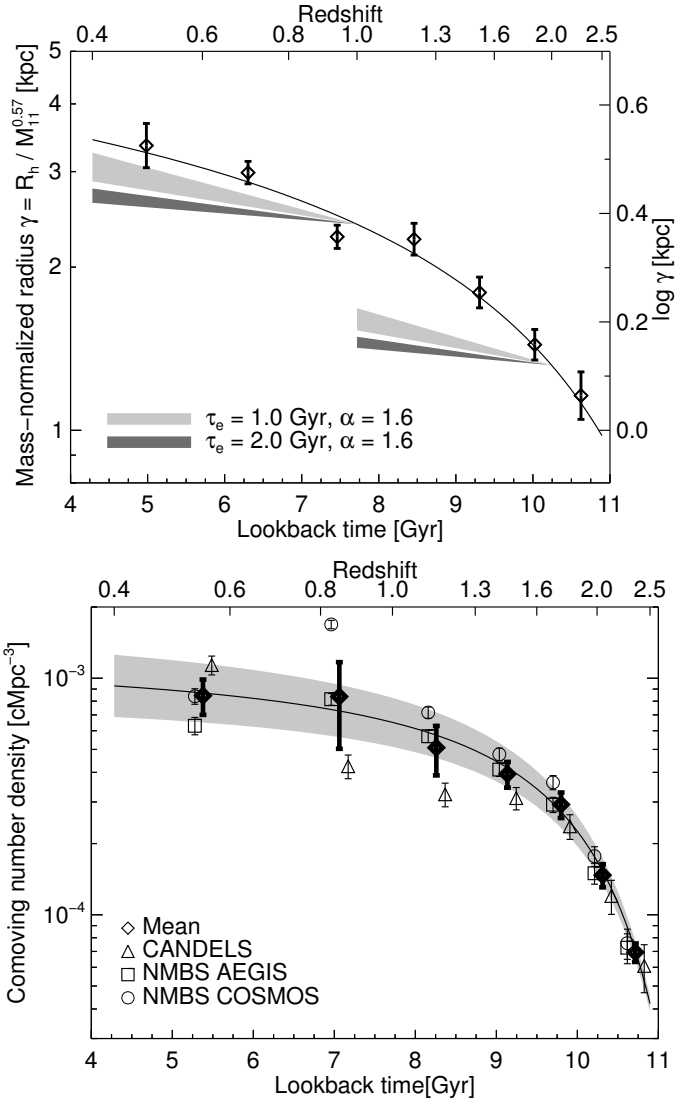

Figure 8.11: Top: Observed evolution in size measured at fixed mass for quiescent galaxies, reproduced from Figure 8.4, compared to predicted trajectories expected from the simple merging model discussed in the text. We begin with progenitors at $z = 2$ and 1 and predict their future growth. The width of the shaded bands corresponds to the uncertainty in f_M. At $z \lesssim 1$, mergers plausibly account for much of the size growth if the timescale is short, but at higher redshifts they cannot match the rapid growth of the population. **Bottom:** Comoving number density of $\log M_* > 10.7$ quiescent galaxies in CANDELS and the NMBS. Error bars for individual fields (slightly offset in redshift for clarity) reflect Poisson noise only, while the error in the mean (diamonds) is determined empirically from the scatter among the fields. The solid line and shaded region indicate the fit used in our model and its 1σ uncertainty.

enlarged in lockstep. In reality, the population at any redshift comprises both old galaxies which formed at higher redshift and which presumably are growing via mergers, *and* sources newly arriving on the quiescent sequence, whose size may reflect their epoch of formation. Galaxies appearing later are typically formed from gas-poorer progenitors. They are therefore expected theoretically to experience less dissipation in their formation, possibly leading to less compact remnants (Robertson et al. 2006; Khochfar & Silk 2006; Hopkins et al. 2010a; Shankar et al. 2011).

Figure 8.11b demonstrates that the *comoving number density* of quiescent galaxies increases very rapidly at $z \gtrsim 1.3$, exactly where the growth in mean size is most rapid. For example, only $\sim 25\%$ of the sample at $z \sim 1$ was already formed and quiescent at $z \sim 2$. These early galaxies may need only to grow marginally into the compact tail of the distribution at $z \sim 1$. They might then experience significantly less growth than the population mean tracked in Figure 8.11a. In this figure, we have combined our CANDELS catalog with those from the NEWFIRM Medium Band Survey (NMBS; Whitaker et al. 2011b) to increase the total volume. Densities in the various fields agree closely at $z \gtrsim 1.5$, where large volumes are probed, while cosmic variance dominates at $z \lesssim 1.5$.

There is observational support at $z \sim 0$ for the idea that younger early-type galaxies are larger at fixed mass (Shankar & Bernardi 2009; van der Wel et al. 2009; Bernardi et al. 2010). On the other hand, some recent studies at higher redshift have found no sign of such a correlation (Trujillo et al. 2011; Whitaker et al. 2011a; but see Saracco et al. 2011). Although the true situation remains unclear, it is interesting to consider size growth assuming that the oldest galaxies at a given redshift and stellar mass are the smallest, since this corresponds to the minimum rate of growth that individual old galaxies must undergo. We now seek to construct a test that accounts for the continual emergence of quiescent systems.

8.5.4 A minimum rate of growth for early compact galaxies

The physical processes that determine the size of a galaxy in its early history might therefore be quite different from those that drive its subsequent growth. Oser et al. (2010) described a "two phase" picture that, while obviously a simplification at some level, still provides a useful paradigm for galaxy growth. The first phase is characterized mainly by *in situ* star formation, while in the second phase, most growth occurs through accretion of stars. We wish to test whether mergers are sufficient to power size growth in this second phase. As we discussed in Section 5.3, growth in the mean size of the quiescent population (Figure 8.11a) entails processes operating in both phases which are hard to uniquely disentangle. Evolution in the population mean alone does not necessarily imply that any individual galaxy must grow in size. The key evidence for growth in the "second phase" is the declining abundance of compact systems. Observationally, we seek to explain the minimum rate at which high-z compact galaxies must evolve so as to avoid leaving too many compact remnants at later times.

To test for growth in this second phase requires the *distribution of sizes* at two redshifts and the *relative abundances* of the progenitors and candidate descendants. We focus on the redshift interval $z = 1$–2 to illustrate the method. Figure 8.12 shows the cumulative distributions of the mass-normalized radius γ at $z = 2$ and $z = 1$ using the fits presented in Section 3. These have been scaled to total number densities using the fit in Figure 8.11b. We term these *compactness functions* (CFs) in analogy to the more familiar stellar mass function (see Bezanson et al 2011 for a demonstration in terms of inferred velocity dispersion).

Mergers will shift the $z = 2$ CF in two ways in Figure 8.12. First, galaxies will expand according to Equation 8.5, which will shift the distribution rightward toward larger γ. We again assume that this growth is uniform and neglect stochasticity in mergers. A second, less important, effect is that some of these mergers will be among galaxies within the sample. This will reduce the number density of the sample over time, moving the size distribution parallel to the $\log n$ axis. In Section 4, we called these "intrasample mergers" and measured the fraction $f_{\rm IS}$ of physical secondaries they represent. The rate of intrasample mergers is then $f_{\rm IS} f_{\rm pair}/\tau_e$. Bearing in mind that $f_{\rm IS} f_{\rm pair} \approx 0.03$–$0.06$ is small (Table 8.3), we can approximate the resulting reduction in number density over an interval Δt by

$$\Delta \log n \approx \log(1 - f_{\rm IS} f_{\rm pair})^{\Delta t/\tau_e}. \tag{8.6}$$

We note that the secondaries removed from the sample in intrasample mergers will preferentially be low mass, but since γ is defined to be statistically independent of M_*, it is a good approximation to shift the CF uniformly.

The evolution of the $z = 2$ CF will thus proceed rightward and slightly downward in Figure 8.12, as indicated by the thick arrow that connects the $z = 2$ compactness function (solid red line) to that of its descendants (dashed). The length of the arrow indicates the magnitude of the size evolution and depends on $f_{\rm pair}$ and τ_e. A plausible evolutionary path must shift the $z = 2$ CF to lie below that observed at $z = 1$, otherwise too many compact descendants would remain at $z = 1$. We use this to define a minimum growth rate for $z = 2$ compact galaxies consistent with the observed depletion in the number density of similarly compact systems.

Before embarking on this task, it is necessary to define a minimum percentile $P_{\rm min}$ of the $z = 2$ CF that we wish to fit within the observed $z = 1$ distribution. For example, if we require only that the largest 30% ($P_{\rm min} = 0.7$) of the $z = 2$ descendants fit within the $z = 1$ distribution, then no size growth is necessary, as Figure 8.12 shows. At the other extreme, if we require that *all* $z = 2$ descendants are accommodated ($P_{\rm min} = 0$), the minimum necessary growth is approximately the same as the difference in the population means at the two redshifts, which we considered in Section 5.3.

In practice, some intermediate $P_{\rm min}$ must be chosen. Although smaller values of $P_{\rm min}$ provide

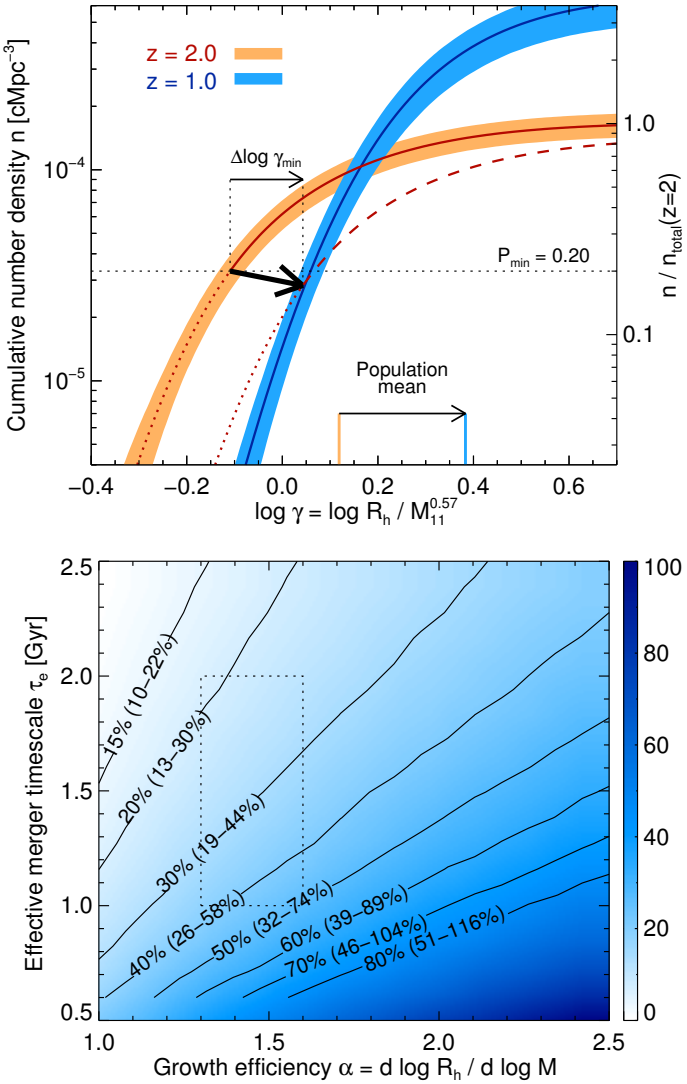

Figure 8.12: Top: Cumulative compactness functions at $z = 2$ and $z = 1$, representing the comoving number density of quiescent galaxies more compact than a given γ based on fits described in Section 3. The thick arrow indicates the minimum size expansion necessary to ensure that descendants of the $z = 2$ population can be accommodated within the $z = 1$ distribution. As discussed in the text, we do not use the lowest 20% of the $z = 2$ CF as a constraint. Bands indicate 1σ confidence regions. **Bottom:** The fraction $\Delta \log \gamma_{\rm merg} / \Delta \log \gamma_{\rm min}$ of the minimum required growth rate over $z = 1$–2 that is producible by mergers under various assumptions for the timescale and growth efficiency, with the 10–90% confidence intervals in parentheses. The dotted box outlines the range of likely parameters discussed in Sections 5.1 and 5.2.

stronger constraints, this must be balanced against our wish not to extrapolate fits of the observed γ distribution down to arbitrarily small γ, where they are poorly constrained by the finite number of galaxies. In the following we conservatively set $P_{\rm min} = 0.2$, which is large enough that the empirical CFs are fairly well constrained at $z < 2$ (see Figure 8.5). The thick arrow in Figure 8.12 has the minimum length necessary to shift the $20^{\rm th}$ percentile of the $z = 2$ CF beneath the $z = 1$ distribution. The corresponding growth $\Delta \log \gamma_{\rm min}$ can be taken as the minimum amount of growth necessary to sufficiently deplete the abundance of compact systems. Following the discussion in Section 8.5.3, this minimum growth is less than the difference in the means of the two CFs indicated at the bottom of the panel. Errors on $\Delta \log \gamma_{\rm min}$ are estimated by repeating this calculation using many samples from the Markov chains used to fit the γ distribution (Section 3). Number densities are also randomly perturbed from the mean fit as illustrated by the grey band in Figure 8.11b.

Figure 8.12a demonstrates that the minimum growth over $z = 1$–2 is $\Delta \log \gamma_{\rm min} = 0.16 \pm 0.03$, assuming a size growth efficiency of $\alpha = 1.6$. Throughout we take $\langle \mu_* \rangle = 0.39$ and also set $f_{\rm IS} = 0.18$ appropriate to $z \sim 2$ (see Table 8.3), although the results are extremely insensitive to this value. This minimum growth can now be compared to that expected from mergers via Equation 8.5: $\Delta \log \gamma_{\rm merg} = 0.08 \pm 0.02$, assuming a short timescale of $\tau_e = 1$ Gyr. Therefore, it appears that only $\Delta \log \gamma_{\rm merg} / \Delta \log \gamma_{\rm min} \approx 50\%$ of the required growth over this interval can be attributed to mergers. For longer merger timescales or lower growth efficiencies, this fraction would be less. In Figure 8.12b we show how the fraction depends on τ_e and α. The dotted line outlines the region of likely parameters discussed in Sections 5.1 and 5.2. We conclude that mergers alone are unlikely to achieve the minimum rate of expansion required between $z = 2$ and $z = 1$, even for favorable assumptions regarding these theoretical parameters.

The exercise can readily be repeated over other redshift intervals. Figure 8.13 shows the minimum growth rate that progenitors at $z = 2$ and $z = 1$ must undergo to avoid leaving too many late compact remnants. This minimum rate is compared to the mean evolution of the quiescent population, introduced in Figure 8.11, and to the merger model predictions. During the period $z = 1$–2 over which the number density is rapidly increasing, the population mean (black symbols) evolves more quickly than the minimum rate (red line). Both, however, exceed the expected growth rate from mergers (grey band), even for a favorable choice of $\tau_e = 1$ Gyr and $\alpha = 1.6$. From $z = 0.4$–1 the minimum growth rate (blue) is only slightly less than the rate at which the population mean evolves, owing to the more gradual number density increase over this period. However, this slight decrease brings the required size evolution closer to the merger model. We conclude that mergers are roughly consistent with producing the more modest size evolution at $z \lesssim 1$, assuming the same favorable choices of α and τ_e.

Broadly speaking, our more elaborate model reaches a similar conclusion to that we inferred from a naïve consideration of the mean sizes at various redshifts (Section 5.3, Figure 10). However, even

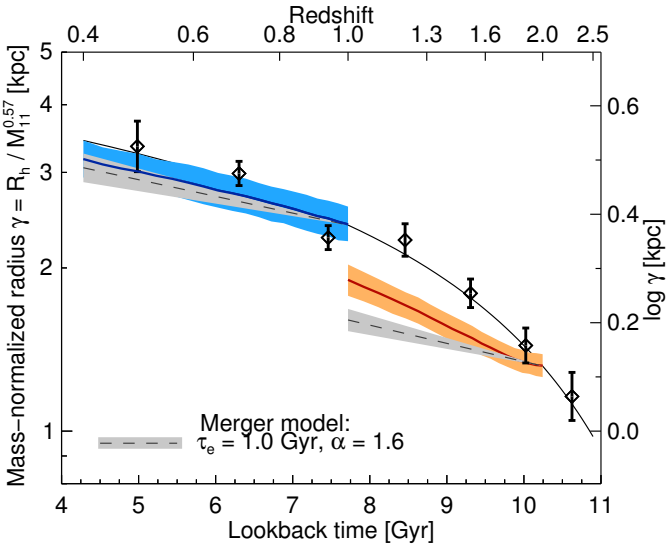

Figure 8.13: Minimum required rates of growth for quiescent populations in place at $z = 2$ and $z = 1$, indicated by the dark grey bands (colored bands in online version), are compared to the growth rates of a simple merger model (light grey) discussed in the text. Black diamonds reproduce mean sizes from Figure 8.11a. The thickness of the merger trajectories reflects the uncertainty in f_M. All indicated uncertainties are 1σ.

this refined model involves some questionable assumptions. First, we have neglected the contribution that measurement errors make to the width of the observed distribution, on the grounds that they are expected to make a small contribution. In Appendix B (Section 8.8) we discuss how our results would be impacted if the true measurement errors increase rapidly with redshift. Second, we have assumed that the descendants of quiescent galaxies are also quiescent, but some systems may be rejuvenated by secondary episodes of star formation (e.g., Treu et al. 2005). Since our results are driven by the abundance of the most compact systems, which are overwhelmingly quiescent, we expect this to be a small effect. For example, only $\simeq 15\%$ of $z > 1$ galaxies that are more compact than the median quiescent galaxy at the same redshift are classified as star-forming. Third, the lower-z CF in our comparisons applies to a constant mass threshold of $\log M_* > 10.7$. Since we expect the population in place at high-z to be continually growing in mass, an evolving mass threshold would be more appropriate. For the specific assembly rate $\dot{M}_*/M_* \approx 0.03$ dex$/\tau_e$ expected from our pair analysis, this translates to reductions in number density of $\approx$ 10–20% over the redshift intervals we considered. Since the last two effects are modest and oppose one another, neglecting them is justified.

Finally, it is important to consider the stochasticity of the merger progress. Obviously, every galaxy cannot undergo exactly 0.16 mergers with mass ratios $\mu_* > 0.1$ per timescale. In reality, since the expected number of mergers per timescale is significantly less than unity, many galaxies will experience *no* such mergers over an interval of several Gyr. This retards the movement of the compact

end of the distribution in Figure 8.12a, leaving even more late compact remnants. Accounting for stochasticity would therefore only strengthen our conclusion that additional mechanisms are necessary to explain the rate of size evolution at $z \gtrsim 1$.

In summary, our models for size growth via minor merging can reasonably account only for that observed at $z \lesssim 1$. The faster growth rate at higher redshift remains difficult to explain via merging alone, even when one accounts for the rapid buildup of the quiescent population over the same period.

8.6 Discussion and Conclusions

Using high-quality near-infrared imaging from WFC3/IR taken as part of the CANDELS survey, in conjunction with other multi-wavelength data in the UKIRT Ultra Deep Field and GOODS-South fields, we have compiled a uniform sample of 935 galaxies with stellar masses greater than $10^{10.7}\,M_\odot$ and photometric redshifts $0.4 < z < 2.5$. Within this sample, the most compact objects at a given redshift are those with quiescent stellar populations. For this subsample, the mean half-light radius measured at fixed stellar mass grows by a factor of 3.5 over this interval. The growth rate per unit time is noticeably quicker at early cosmic epochs, corresponding to the redshift range $z \approx 1.3$–2.5.

We have explored the physical origin of this size growth in 404 quiescent galaxies over $0.4 < z < 2$ by searching for close pairs whose photometric redshifts imply a likely association with their hosts. The depth of the imaging allows us to probe secondary companions whose stellar masses are only 10% of their primary hosts. Our main conclusion is that the delivery of stellar mass in mergers, estimated via the incidence of close pairs, cannot account for more than roughly half of the minimum size growth that $z = 2$ quiescent galaxies must incur to avoid leaving a greater number of late compact remnants than is observed. At $z \lesssim 1$, on the other hand, mergers may account for most or all of the size growth rate, but only if a short merger timescale (~ 1 Gyr) and fairly robust growth efficiency ($\alpha \sim 1.6$) are valid. These conclusions hold if the evolution of the mass-size relation is driven in part by the emergence of new, systematically larger quiescent galaxies. If this is not the case, then the merger rate will fall further short of that needed to drive the observed size growth.

Given the variety of theoretical and observational ingredients in this analysis, it is worthwhile to review the assumptions underlying this conclusion. Foremost is the uncertainty in the merger timescale and growth efficiency. Most of the results in Section 5 assume optimistic values for the theoretical parameters ($\tau_e = 1$ Gyr, $\alpha = 1.6$). Furthermore, all mergers in our models are dry and thus provide the maximum amount of size growth, whereas many minor mergers at high-redshift may in fact involve gas-rich secondaries (Section 4.4). We also note that our correction for unbound projected pairs ($C_{\rm mg}$, Section 5.1) is not specifically calibrated for red galaxies, which are more strongly clustered, and may therefore understate this correction and thus overstate the merger rate.

Altogether, it is therefore easy to argue that mergers produce less size growth than we have presented, but it is hard to see how the effect of mergers could be much larger.

The tension at high redshift can be viewed as a consequence of the observation that the rate of size growth per unit time is considerably larger beyond $z \simeq 1.3$, whereas the pair fraction remains nearly constant. One conceivable explanation is that the merger timescale declines with increasing redshift. However, current theoretical studies do not support this suggestion (Kitzbichler & White 2008; Lotz et al. 2011). Incompleteness due to photometric redshift errors is a concern as higher redshifts are probed, but our best estimates of the catastrophic error rate (Section 8.4.1) are not high enough to significantly alter our conclusions. We note also that although the energy arguments discussed in Section 8.5.2 are generally applicable, the details of our framework for analyzing size growth are premised on spheroid-spheroid mergers. This is true for most other observational studies to date, since the theoretical framework for such mergers has been most extensively developed. Further studies of simulated spheroid-disk minor mergers, particularly with progenitors consistent with $z \simeq 2$ observations, are needed to better assess the growth efficiency when the incoming stellar material is more loosely bound. Still, our pair fraction measurements imply that only about $50\ [\tau_e/1\ \mathrm{Gyr}]^{-1}$ percent of $z \simeq 2$ quiescent galaxies experience any $\mu_* > 0.1$ mergers over $z = 1 - 2$. This is likely to pose a challenge regardless of the particular merger physics.

An equally important assumption is that the observed half-light radii are valid proxies for half-mass radii. The former are measured observationally, but the latter are relevant when considering the mass-structural changes caused by mergers. Although a detailed study of color gradients and their evolution in our CANDELS sample is beyond the scope of this chapter, these data do confirm earlier studies that quiescent galaxies at $z \sim 2$ typically display negative color gradients (i.e., are bluer on the outside), and that these tend to flatten at lower redshift (van Dokkum et al. 2010; Guo et al. 2011; Cassata et al. 2011). The color gradients probably arise from a complex combination of age, dust, and metallicity gradients, but in any case the stellar mass-to-light ratio is lower on the outside, so that these galaxies are *more* compact in mass than in light. If anything, we therefore expect to have underestimated the rate of structural change.

Much of the early skepticism regarding the rapid size evolution of early-type galaxies focused on the possibility of severe observational errors in measuring the key parameters of size and mass. Stellar masses could be overestimated by imperfect population synthesis models, or effective radii could be underestimated in shallow imaging (e.g., Mancini et al. 2010). Subsequent observations have weakened these claims. Although substantial uncertainties remain in stellar population synthesis models (Muzzin et al. 2009a), dynamical masses measured from absorption spectra in moderate samples at $z \sim 1.3$ (Newman et al. 2010) and for a few individual galaxies or stacked spectra at $z \sim 1.6$–1.8 (Cappellari et al. 2009; van de Sande et al. 2011) have not indicated large systematic discrepancies with photometrically-determined stellar masses. Regarding size measurements, the

CANDELS survey represents a major advance as it provides the first large space-based sample that takes advantage of the improved depth and sampling of WFC3 relative to NICMOS. The radial surface brightness profile of a typical $z \sim 2$ quiescent galaxy in our sample can be traced to $\simeq 7R_e$.

Several theorists have compared the rate of galaxy size evolution in simulations to observations. Hopkins et al. (2010a), based on a suite of cosmological, hydrodynamical simulations, also conclude that mergers alone do not generate the entire rate of growth observed for quiescent galaxies. To explain the remainder, they propose a combination of several physical and observational effects. First, they assume that stellar masses and effective radii are over- and underestimated, respectively. Second, they suggest that the presence of blue cores implies that half-mass radii are larger than the measured half-light radii; as discussed above, the opposite appears more likely. Third, Hopkins et al. (2010a) model adiabatic expansion due to mass loss from stellar winds, but this effect alone expands galaxies by only $\simeq 20\%$.

Oser et al. (2011), on the other hand, present hydrodynamical "zoom" simulations in which galaxy size evolution at $z \lesssim 2$ agrees well with their compilation of observations, and they attribute the size expansion primarily to minor mergers. As these authors note, one concern is that the absence of supernova feedback in this set of simulations enhances the stellar mass formed in low-mass halos. This could overstate the effectiveness of minor mergers by substantially increasing the stellar mass they deliver. As simulations and observations at $z \simeq 2$ improve, it may be possible to test such effects through additional comparisons, such as the stellar mass–halo mass relation or the evolution of the stellar mass function.

Nipoti et al (2011, submitted) construct a ΛCDM-based analytic framework, supported by suites of N-body spheroid merger simulations, to predict the evolution of early-type galaxies undergoing dry mergers. Using a compilation of observations of early-type galaxies at $z = 1$–2.5 (including this work), they conclude that mergers alone are not consistent with the observed rate of structural evolution at $z \gtrsim 1.3$. Following on earlier work (Nipoti et al. 2009b), they also find that mergers introduce too much scatter in the scaling relations at lower redshift unless the progenitors are finely tuned to occupy a very tight region in the mass–radius plane. Such fine tuning is not consistent with the near constancy of the scatter that we observe in this plane.

Future work can extend this study in many ways. Imaging of the remaining CANDELS fields will allow possible trends of sizes and pair fractions with mass, redshift, and environment to be discerned more clearly, which may shed light on the responsible physical mechanisms. Multiplexed near-infrared spectrographs soon to be commissioned on 8–10 m telescopes will provide redshifts and confirmation of the quiescent nature for larger samples at high redshift than has previously been possible. This will provide an invaluable test of the photometric redshift and star-formation rate estimates on which the present study depends, although with current telescopes we are likely to continue to rely on photometric estimates for many of the faint companions. It should also be

possible to significantly enlarge the library of dynamical mass estimates, of which only a handful are currently available for quiescent galaxies at $z > 1.5$, and thereby test the accuracy and precision of stellar mass estimates at higher redshifts. Spectroscopic indicators of maturity and recent star-formation activity (Balmer lines, 4000 Å break) may allow tests of the "minimum growth" hypothesis considered in this work, i.e., that early quiescent galaxies remain the most compact systems in place at later epochs. If this is not the case, the challenge of accounting physically for the rapid growth of quiescent galaxies will be further heightened.

Acknowledgments

We thank Carlo Nipoti and Anna Nierenberg for fruitful conversations and useful comments, as well as the anonymous referee for a helpful report. This work is based on observations taken by the CANDELS Multi-Cycle Treasury Program with the NASA/ESA *Hubble Space Telescope*, which is operated by the Association of Universities for Research in Astronomy, Inc., under NASA contract NAS5-26555.

8.7 Appendix A: The Skew Normal Distribution

In Section 3 we fit the distribution of sizes of quiescent galaxies to skew normal distributions that evolve with redshift in order to assess changes in the mean and dispersion. The skew normal distribution has the probability density function

$$P(x) = \frac{1}{\omega\pi} e^{-\frac{(x-\psi)^2}{2\omega^2}} \int_{-\infty}^{s\left(\frac{x-\psi}{\omega}\right)} e^{-\frac{t^2}{2}} dt, \tag{8.7}$$

characterized by the parameters (ψ, ω, s). Throughput this paper, we use a parameterization in terms of the mean $\bar{x}$ and standard deviation σ, which relate to (ψ, ω, s) through the relations $\bar{x} = \psi + \omega\delta\sqrt{2/\pi}$ and $\sigma^2 = \omega^2(1 - 2\delta^2/\pi)$, where $\delta = s/\sqrt{1+s^2}$. The shape parameter s relates to the skewness, and $s = 0$ recovers a Gaussian distribution.

8.8 Appendix B: Measurement Errors in Stellar Masses and Radii

As discussed in Sections 3 and 5, the distributions in γ that we fit and compare to merger models are dominated by the intrinsic variation in γ, but also include some component of scatter arising from measurement errors in the radii and stellar masses. Random errors in stellar mass estimates are small with good photometry (typically ~ 0.1 dex in this work; see also Auger et al. 2009), but systematic

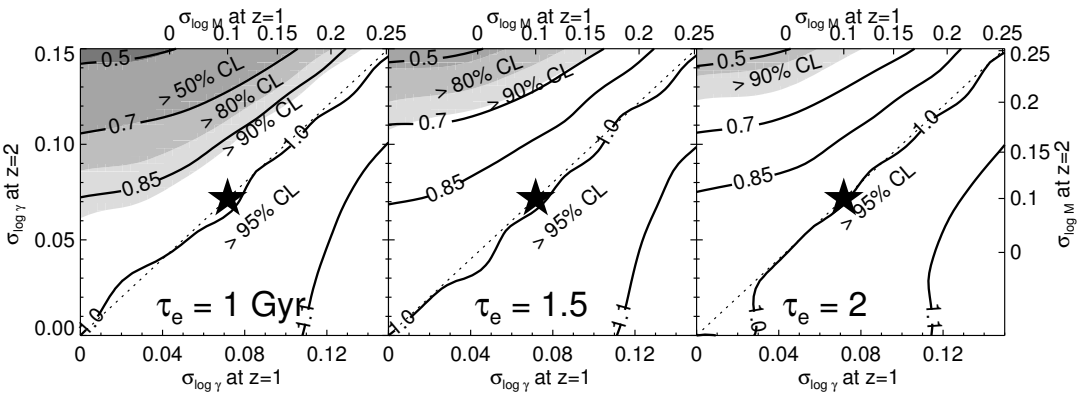

Figure 8.14: Effects of measurement errors in stellar masses and radii on our conclusions. Contours show the factor by which $\Delta \log \gamma_{\rm min}$, the minimum necessary growth for quiescent systems over $z = 1 - 2$, would change under different estimates of the measurement errors $\sigma_{\log \gamma}$ at $z = 1$ and 2. Top and right axes show the corresponding errors $\sigma_{\log M_*}$ in stellar mass, assuming 10% errors in radii. Shaded regions indicate the corresponding confidence level (CL) at which merging alone as a viable growth mechanism is rejected. The star indicates the estimated errors based on the rms formal stellar mass uncertainties from SED fitting. Panels display results for several effective merger timescales τ_e and $\alpha = 1.6$. As discussed in Appendix B, if the uncertainties on stellar mass (modulo IMF choice) are the same (dotted line) at $z = 1$ and $z = 2$, then our results are unchanged, and merging alone as a growth mechanism is rejected at $> 95\%$ CL. Only if the errors are much larger at $z = 2$ and the merger timescale is short is the CL reduced.

errors are not well understood. Comparison with independent dynamical mass measurements can place upper limits on the true scatter in stellar mass estimates. At $z \sim 0$, this limits the scatter to $\sigma_{\log M_*} \lesssim 0.15$ dex, based on the SDSS sample described in Section 2.6, while at $z \simeq 1.3$ the sample of spheroids from Newman et al. (2010) indicates a similar scatter of $\sigma_{\log M_*} \lesssim 0.1$–$0.2$ dex when spectroscopic redshifts are used. Analogous comparisons are currently not possible at higher redshift. For this study, as we describe below, the absolute uncertainties are not as important as how they may evolve with redshift.

The main sources of systematic uncertainty include the unknown IMF and the complexities of stellar population synthesis models. The former is less critical for our analysis, since in our "minimum growth" test (Section 5.4) we are tracking the same sample of massive, quiescent galaxies, so the IMF should not change. The latter uncertainty is likely more important, since younger populations may be systematically different (e.g., Maraston 2005; Conroy et al. 2009). A simple estimate of this effect can be obtained by comparing stellar mass estimates from the BC03 and CB07 models, which differ in their treatment of the TP-AGB stars that may dominate the NIR light at ages of ~ 1 Gyr. As discussed in Section 3, these models predict stellar masses systematically offset by $-0.05z$ for our quiescent sample. However, the scatter between the two models actually declines slightly from ~ 0.1 dex at $z = 1$ to ~ 0.05 dex at $z = 2$.

The main concern for our "minimum growth rate" study is the reverse: that the scatter in stellar

mass measurements for quiescent galaxies at $z = 2$ is much larger than at $z = 1$. In this scenario, the true abundance of very compact $z = 2$ galaxies would be smaller than our fits indicate, since some are simply scattered to small γ through random errors in R_h and $\log M_*$. If the $z = 1$ measurement errors are comparable, then this effect approximately cancels in our comparison of compactness functions at the two redshifts. But if the $z = 1$ measurement errors are smaller than those at $z = 2$, we expect that the minimum necessary size growth over $z = 1 - 2$ would lessen.

We can test the effects of redshift-dependent errors in our comparison of two compactness functions CF_1 and CF_2 with estimated measurement errors $\sigma_{\log\gamma,1} > \sigma_{\log\gamma,2}$ by convolving CF_2 by a Gaussian with dispersion $\sigma = \sqrt{\sigma^2_{\log\gamma,1} - \sigma^2_{\log\gamma,2}}$. Having thus matched the measurement errors, we then derive the minimum necessary growth $\Delta\log\gamma_{\rm min}$ following Section 5.4. The contours in Figure 8.14 show how this minimum growth would change for evolution over $z = 1 - 2$ assuming various measurement errors at $z = 1$ and 2. The three panels consider a range of merger timescales τ_e spanning the range discussed in Section 5.1 and a growth efficiency of $\alpha = 1.6$. As anticipated, when the measurement errors are nearly equal (dotted line), the derived minimum growth is not affected. When $\sigma_{\log\gamma}$ is much greater at $z = 2$ than at $z = 1$, however, the true minimum growth rate may be smaller and thus more comparable to the rate attainable through merging.

The shaded regions in Figure 8.14 display the confidence levels at which merging alone as a driver of size evolution is rejected. These panels indicate that the claim that merging alone is insufficient at $z \gtrsim 1$ is seriously weakened only if the measurement errors are significantly larger at $z = 2$ than at $z = 1$ *and* the effective timescale τ_e is very short ($\simeq 1$ Gyr). Given the other assumptions entering this exercise that are favorable for mergers (namely, that *all* of the most compact systems at $z = 1$ are descended from $z = 2$ quiescent galaxies, that all mergers are dry, and that there is no stochasticity in the incidence of mergers), we believe that our main results are robust.

Chapter 9

Summary and Future Directions

In Part I we concluded that the distribution of dark matter in the innermost regions of galaxy clusters is flatter than the canonical cusp of cold dark matter (CDM) halos. This result can be set alongside earlier observations at the opposite end of the mass spectrum showing that many dwarf galaxies likely have flattened or "cored" dark matter profiles. Can these results be understood by properly accounting for the impact of baryons on the underlying dark matter backbone? Do they signal dark matter microphysics that only manifests itself on small scales? Disentangling the physical origins of the small-scale dark matter distribution is clearly an urgent problem.

Our observations provide some clues toward this balance in clusters. Deviations from the canonical CDM profile occur only within the central giant elliptical. We also found signs of a correlation between the inner dark matter slope and the effective radius of the central galaxy, pointing to a link between the dark and luminous mass distributions. This suggests that baryons play an important role in flattening the dark matter cusp in clusters. On the other hand, the situation for the Milky Way satellites, where the impact of baryons is more constrained, has in some ways only become more severe (e.g., Boylan-Kolchin et al. 2012). Solutions based on modifying dark matter (e.g., introducing self-interactions) are currently enjoying renewed interest, although definitively ruling out baryonic explanations is daunting. In that case, it would be tempting to appeal to a common origin for the cusp flattening across a range of mass scales.

Progress will require advances on theoretical and observational fronts. On the theoretical side, it is important to better understand the effect on the dark matter cusp of the assembly of stars in the central galaxy. Adding stars to the centers of the progenitor halos can have a large effect on the dark matter profile in simulations; even though stars amount to only a few percent of the mass, they are tightly bound and resist stripping. There still remains some confusion in the literature regarding the net effect of dynamical friction from infalling satellites on the dark matter cusp. This may arise from numerical resolution effects, or sensitivity to the true nature of the satellites (e.g., their stellar masses and sizes; Laporte et al. 2012). Empirically, the physical properties of the galaxies that presumably merge to form the most massive ellipticals can now be measured to high redshifts. This connects

the themes of Parts I and II of this thesis, i.e., the inner dark matter profile and the assembly of stars, and suggests that the same processes that build up the stellar envelope are responsible for the depletion of dark matter in the center (although the most relevant merger mass ratio may differ). Clarifying the role of the AGN in producing dark and stellar cores, as seen in the recent simulations of Martizzi et al. (2012b), for example, is also an essential future direction. Predictions for self-interacting dark matter in simulations that incorporate baryons need to be developed, and some groups are now pursuing this. It would be especially interesting if self-interactions resist steepening (adiabatic contraction) associated with baryon loading.

Observationally, a key goal is to better quantify the dark matter distribution at intermediate mass scales between dwarf galaxies and clusters. As described in Chapter 2, disentangling baryons and dark matter is extremely difficult near $\sim L_*$, since these galaxies are the most baryon-dominated systems. Nevertheless, there is some evidence (Chapter 2) that their dark matter cusps are *steeper* than a CDM profile. Verifying this would be an important step toward understanding the effects of baryons, since it would point to a link between star-formation efficiency, which is maximal in $\sim L_*$ galaxies, and the inner dark matter profile.

One route to searching for such a mass dependence is to apply the lensing and dynamical tools developed in Part I to lower-mass systems. Using the Einstein radius $r_{\rm Ein}$ as an observational proxy for the system mass, the massive clusters studied in this thesis have $r_{\rm Ein} \gtrsim 10''$. The SLACS survey located and extensively studied elliptical galaxy lenses with $r_{\rm Ein} \lesssim 1\farcs5$, corresponding to the size of a fiber in the SDSS, but so far separating the dark and stellar distributions has been difficult (see Chapter 2) since the latter is so dominant. Intermediate-scale lenses with $1\farcs5 \lesssim r_{\rm Ein} \lesssim 10''$, likely corresponding to group-scale halos, are more dark matter-rich and so may be more amenable to such an analysis. Few of these lenses were known until recently, but now reasonable samples have been discovered (e.g., the Cassowary and SL2S samples; More et al. 2012), opening a new window on an interesting mass range. In a forthcoming DEIMOS run, we will observe several of these intriguing objects.

It is also essential to develop and refine methods for estimating the stellar mass of a galaxy from its integrated light. Our results on the dark matter profile rest on the mass-to-light ratios we derive for stars in the brightest cluster galaxies, based on models fit to lensing and kinematic data. In combination with population synthesis models, these results imply an initial mass function (IMF) that is "heavier" than that of the Milky Way. This finding agrees broadly with recent spectroscopic studies that measure photospheric absorption features sensitive to surface gravity in the integrated light of elliptical galaxies (Chapter 5). The significance of this complementary method for weighing the stars is that it is completely independent, and it makes no assumptions regarding the form of the dark matter profile (e.g., a power-law cusp, or a smooth roll-over to a core), which in some form is implicit to all lensing and dynamical studies. With Evan Kirby, we have compiled high-quality

spectroscopic data for a sample of nearby ellipticals. This work is enabled by the deep-depletion CCDs installed in DBSP at Palomar and LRIS at Keck, which reach key absorption features near ~ 1 μm with enhanced sensitivity and minimal fringing. Our aim is to verify the robustness of the spectroscopic results and their sensitivity to chemical abundance variations.

In Part II we turned to the growth of massive, quiescent galaxies since $z \simeq 2$, particularly focusing on the appearance over the last 10 Gyr of the extended stellar halos that characterize present-day ellipticals. We compared their rate of the size growth with the rate of minor mergers they undergo, both derived using *HST*/WFC3-IR imaging from the CANDELS survey. We showed that the growth of the stellar halo is consistent with being driven by observed impending mergers at $z \lesssim 1$, providing a relatively short merger timescale applies. At higher redshifts, however, a discrepancy appears: the inferred merger rate remains nearly flat, whereas the rate of size growth appears to accelerate. This implies that either the current theoretical understanding of the merger physics (timescales, size growth) is incorrect, or that additional processes contribute significantly to size growth. There are several steps that can now be taken to elucidate the physics responsible for the growth of the stellar envelopes of these systems at early epochs.

First, an important diagnostic is the evolution of velocity dispersion. This will differ depending on the physical origin of the growth, e.g., mergers or expansion from mass loss. While we made progress to $z \simeq 1.5$ in this thesis using LRIS (Chapter 7), extending dynamical studies to higher redshifts – where the most compact sources are seen and their growth appears most dramatic – requires NIR spectroscopy. Obtaining the signal-to-noise necessary for dynamics is now possible for the first time with the new generation of NIR spectrographs. Some initial observations have already been made (e.g., van de Sande et al. 2012), but samples remain small. We plan to use MOSFIRE to characterize the internal stellar kinematics of compact red galaxies to $z \simeq 2$.

At the same time, detailed spectroscopy provides valuable information on the stellar populations of quiescent galaxies. The combination of Hα emission with diagnostics of evolved stars in the Balmer line region can constrain the timescale for the quenching of star formation (e.g., Kriek et al. 2006). A key uncertainty in deciphering structural evolution is disentangling the growth of old, passive systems from the continual quenching of galaxies that adds them to the quiescent population. Because this population is not static, the mean growth observed in the population and that of any individual galaxy may differ. The question, as it is so often, is how to link progenitors and descendants. In Chapter 8, we assumed that the most compact galaxies evolve into the most compact galaxies seen later, producing a minimal estimate of the growth that early compact galaxies must undergo. The growth rate may actually be higher, if some of the evolution in the population arises from more recent arrivals being systematically less compact. This may be tested by searching for a correlation between compactness and age, as inferred through spectroscopic diagnostics of recent quenching. Sirio Belli is leading this project using spectral data from LRIS (expanded from the sample presented in this

thesis) and ultimately MOSFIRE.

Another way to discern the roles of mergers versus secular growth processes is to examine variations with environment. In a merger-driven scenario, one expects that galaxies in higher density environments will undergo (or have already undergone) more mergers. This could lead to an observable difference in the mass–size relation at different local densities. Currently, the observational literature is in disarray on this topic (Rettura et al. 2010; Cooper et al. 2012; Raichoor et al. 2012; Papovich et al. 2012). I am PI of an *HST*/WFC3 program to observe a candidate cluster at $z \approx 2$ with associated diffuse X-ray emission. The goal is to confirm the cluster and assess galaxy membership using grism spectroscopy, and then to compare the mass–size relation to that determined in the field in Chapter 8.

Our comparisons with simulations can also be improved. The analysis in Chapter 8 is based on merger timescales and size growth prescriptions derived from focused suites of isolated merger simulations. The size growth predictions, in particular, are based on spheroid–spheroid mergers. This may not be appropriate for very minor mergers. At odds with our empirical estimate of the merger rate, some, but not all, recent cosmological simulations (Oser et al. 2011, e.g.,) have found no conflict between merger-driven size growth in their simulations and size growth observations. This could reflect weak (or absent) feedback implementations, which will overproduce stars in the low-mass satellites, but differences in the merger physics could also be at play. A more direct comparison would be to "observe" satellites in simulations in a way analogous to observations, for example, by producing pair fractions measured in projected apertures and their stellar mass content.

Finally, a fascinating question is the identity of the star-forming progenitors of the compact quiescent galaxies seen at $z \gtrsim 2$. To reach their observed masses and ages at these redshifts, they must have formed stars rapidly and early in an intense starburst. Barro et al. (2012) identified a population of small *blue* galaxies with suppressed star-formation rates, which they suggest are in the process of quenching and will fade into the quiescent systems within ~ 1 Gyr. The most intense period of star formation in a merger may be highly optically obscured. Tacconi et al. (2008) argue that the compact sizes and broad line widths seen in high-redshift submillimeter galaxies in CO emission make them a very plausible progenitor population. Kinematic data from NIR or ALMA observations may provide further insight in the near future.

Appendix A

Lensing formalism

Here we review the basic mathematical formalism underlying the gravitational lensing component of this thesis, drawing upon the reviews by Treu (2010) and Kneib & Natarajan (2011). Figure A.1 illustrates the basic lensing geometry. When the thickness of the lens is much less than the distance to the lens, which is accurately true for galaxy clusters, we can treat the cluster mass as a thin sheet (the "thin lens" approximation). The lens equation

$$\vec{\beta} = \vec{\theta} - \nabla\psi = \vec{\theta} - \vec{\alpha} \tag{A.1}$$

relates the position of a background source $\vec{\beta}$ in the sky plane to that of the observed image $\vec{\theta}$ for a given mass distribution. Here $\psi = \Sigma_c^{-1} \int \Psi dz$ is a scaled, projected version of the familiar gravitational potential Ψ, and

$$\Sigma_c = \frac{c^2}{4\pi G} \frac{D_s}{D_d D_{ds}} \tag{A.2}$$

is the *critical surface density* for lensing. The lens equation defines a mapping from the image plane to the source plane that preserves surface brightness and is achromatic. The Jacobian

$$\frac{d\vec{\beta}}{d\vec{\theta}} = \mathcal{A}^{-1} = \begin{pmatrix} 1 - \partial_{xx}\psi & -\partial_{xy}\psi \\ -\partial_{xy}\psi & 1 - \partial_{yy}\psi \end{pmatrix} = \begin{pmatrix} 1 - \kappa - \gamma_1 & -\gamma_2 \\ -\gamma_2 & 1 - \kappa + \gamma_2 \end{pmatrix} \tag{A.3}$$

of this mapping defines the local distortion of an image. Here we introduce the *convergence* κ and *shear* $\vec{\gamma} = (\gamma_1, \gamma_2)$ and note that the convergence is simply the scaled surface density: $\kappa = \Sigma/\Sigma_c$. By a suitable rotation of axes the magnification matrix $\mathcal{A}^{-1}$ can be diagonalized:

$$\mathcal{A}^{-1} = (1 - \kappa) \left[\begin{pmatrix} 1 & 0 \\ 0 & 1 \end{pmatrix} + \frac{\gamma}{1 - \kappa} \begin{pmatrix} 1 & 0 \\ 0 & -1 \end{pmatrix} \right]. \tag{A.4}$$

This demonstrates that the convergence describes an isotropic magnification, whereas the shear refers to a distortion of the image shape. In the *weak lensing* limit ($\kappa, \gamma \ll 1$) the *reduced shear* $g = \gamma/(1 - \kappa)$ is proportional to the ellipticity induced in the image of a circular source. While faint

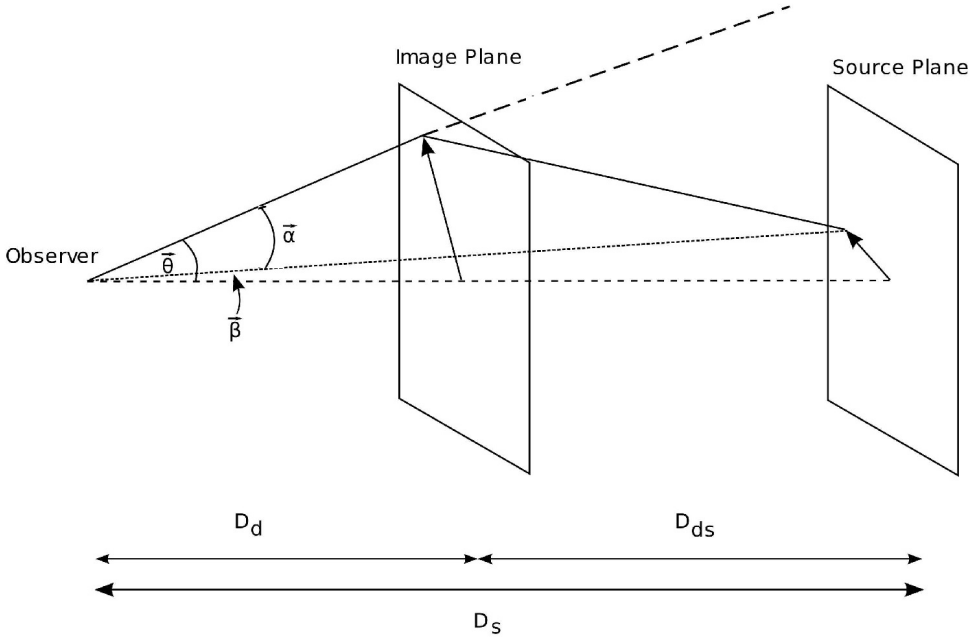

Figure A.1: Basic geometry for gravitational lensing. Note how the arrow in the source plane appears magnified in the image plane due to the deflection of light by the lens (i.e., the cluster) located between the observer and the source. The marked distances refer to angular diameter distances; in general, $D_s \neq D_d + D_{ds}$. Reproduced and adapted from Treu (2010).

background galaxies do not have intrinsically circular shapes, by averaging over many such sources with uncorrelated shapes we can recover the reduced shear. This is the basis for weak lensing as a mass probe.

Where $\mathcal{A}^{-1}$ is singular, the magnification formally diverges.[1] In the *strong lensing* regime the distortion is strong enough to produce *multiple images* of a source, which are defined by extrema of the light travel time according to Fermat's principle. It is convenient to consider an axially symmetric mass distribution to illustrate the key effects. In this situation, the magnification matrix can be expressed in polar coordinates as

$$\mathcal{A}^{-1} = \begin{pmatrix} 1 - \partial_{rr}\psi & 0 \\ 0 & 1 - \frac{1}{r}\partial_r\psi \end{pmatrix}. \tag{A.5}$$

The *tangential critical curve* is defined by the points in the image plane where $\frac{1}{r}\partial_r\psi = 1$; here the magnification diverges in the θ direction, and a strong tangential distortion is produced (see Figure 2.4). The pre-image of the critical line in the source plane is known as the *caustic*. Sources within the caustic are multiply imaged by the cluster. For an axially symmetric configuration, the tangential critical line is a circle whose radius is the *Einstein radius*, while the caustic is a

[1] For a realistic source of finite angular extent, the magnification always remains finite.

single point. (When any ellipticity is introduced, the caustic opens to enclose finite area.) For a perfectly aligned background source with $\vec{\beta} = \vec{0}$, the galaxy is imaged into a circular *Einstein ring* that traces the critical curve. The *radial* critical curve, which is interior to the tangential critical curve, corresponds to the other eigenvalue $\partial_{rr}\psi = 1$; here the magnification diverges in the radial direction. Figure 2.4 illustrates the tangential and radial critical curves and caustics for MS2137, a nearly axially-symmetric lens studied in Chapters 3 through 5.

The conditions for the critical lines can be rewritten as

$$\overline{\kappa} = 1 \qquad \text{(tangential)} \tag{A.6}$$

$$\partial_r(\overline{\kappa} r) = 1 \qquad \text{(radial)} \tag{A.7}$$

where $\overline{\kappa} = \overline{\Sigma}/\Sigma_c$ is the scaled mean surface density within a radius r. The mass enclosed within the Einstein radius $R_{\rm Ein}$ is therefore $M(< R_{\rm Ein}) = \pi R_{\rm Ein}^2 \Sigma_c$. The Einstein radius is a geometric measure of the mass enclosed within the cylinder, provided that the distances to the lens and source are known through their redshifts, and this mass can be measured at the several percent level in a nearly model-independent manner. The radial critical curve is instead sensitive to the *gradient* of the surface density at its location, i.e., the inner density slope. In the general non-axisymmetric situation, the critical curves can have more complex shapes, and misaligned sources can produce systems of multiple images that are not very strongly distorted, in contrast to the famous "giant arcs" composed of several merging images. Nonetheless, the critical curves constrain the mass profile in an analogous way, along with the ellipticity and orientation of the mass distribution.

Appendix B

Reduction and calibration of wide-field cluster imaging

Here we outline the details of the reduction and calibration of the wide-field imaging, primarily obtained using SuprimeCam at the Subaru telescope, that form the basis of the weak lensing analysis presented in Section 3.2.1. The data reduction was conducted using a series of scripts based on the `IMCAT` software. This basis of this pipeline has been described in full detail by Kaiser et al. (1999) and Donovan (2007) and was adapted for the COSMOS survey by Capak et al. (2007). Since it has been detailed more extensively elsewhere, here we summarize the most important aspects and those unique to our application.

B.1 Initial processing

The 10 SuprimeCam CCDs are processed in parallel using the `kishar` computer cluster at Caltech. One node of the cluster is responsible for each chip. After copying the raw data to the nodes, bias is subtracted from each frame using the overscan region. Additionally, a bias frame constructed from the median of 10 bias images is subtracted to account for small spatial variations. Saturated pixels, as well as neighbors within two pixels, are then masked, as is the region vignetted by the movable guider (when present).

At this stage, there are several options to create a flat field. The truest illumination pattern is produced from on sky observations, by creating a "superflat" from the median of many normalized sky frames in which the objects have been masked. However, this process requires a large number of exposures and is often impractical, especially for archival data. We therefore opted instead to use dome flats taken as nearly as possible to the observations, with flats derived from twilight sky images substituting in some cases. Comparison to "superflats" showed systematic differences in illumination of $\lesssim 2\%$, which was reached only very near the edges of the field of view. Since we are typically interested in the inner $\simeq 15'$ (corresponding to 4 Mpc at $z = 0.3$), this is acceptable.

After dividing by the flat and masking regions of chip defects, objects were detected using `hfindpeaks` (in the following, `this font` indicates routines that are part of the `IMCAT` package) and simple aperture photometry was performed. The resulting catalogs were used to derive the astrometric solution, as described below. The mode of each frame was then subtracted as a first-pass sky removal. Fringing is significant only in $z+$ band imaging. In a few cases, when many exposures were available from a single night, a fringe frame was created to correct the $z+$ data. This was scaled and subtracted to remove sky fringing from each frame.

Since SuprimeCam sits at the prime focus, scattered light is a significant problem and generates many large-scale background variations. In addition, large halos around bright stars and Galactic cirrus often produce a variable background. For these reasons, a more sophisticated background subtraction scheme is necessary and was developed by Donovan (2007). Briefly, each chip is divided into a 2×4 grid, and the mode and standard deviation are computed in each cell. Pixels deviating from the mode by more than n standard deviations are then flagged. The process is then repeated using a finer 4×8 grid. Those pixels which were flagged in both grid schemes are considered to contain flux from an object. These are recorded and masked for the rest of the sky subtraction process. Typical values of n are 1–3. Each chip is then divided into a much finer grid of $m \times 2m$ cells, and the mode is calculated for each cell in which the fraction of masked pixels does not exceed f. A continuous background image is then generated by tessellating this grid. The adopted parameters vary slightly depending on the severity of scattered light and Galactic cirrus, but $m = 32$ or 64 and $f = 0.35$–0.5 are typical. Finally, this interpolated background image is subtracted from the frame.

This process is very successful at removing scattered light gradients, halos around bright stars, and in some cases Galactic cirrus (see Figure B.1). Due to imperfect masking, halos of negative flux can be produced around bright, extended galaxies or in very high-density regions. This over-subtraction of extended objects is the price of achieving a flat background for the small galaxies relevant for the lensing analysis. In order to provide improved photometry for the BCG, a second reduction was carried out in parallel for the central $10' \times 10'$ in which much less aggressive sky-subtracted parameters were used ($n = 3$, $m = 2$, $f = 0.35$).

A potential concern is that such fine-scale sky subtraction, using boxes as small as 32×32 pixels when $m = 64$, may over-subtract light from faint sources that are not well detected – and hence not masked – in individual exposures. This could conceivably alter their measured shapes in a systematic way. We tested this by replicating the sky subtraction method on simulated STEP2 images with known applied shear (Massey et al. 2007). No bias on the measured moments of the galaxy images was detected.

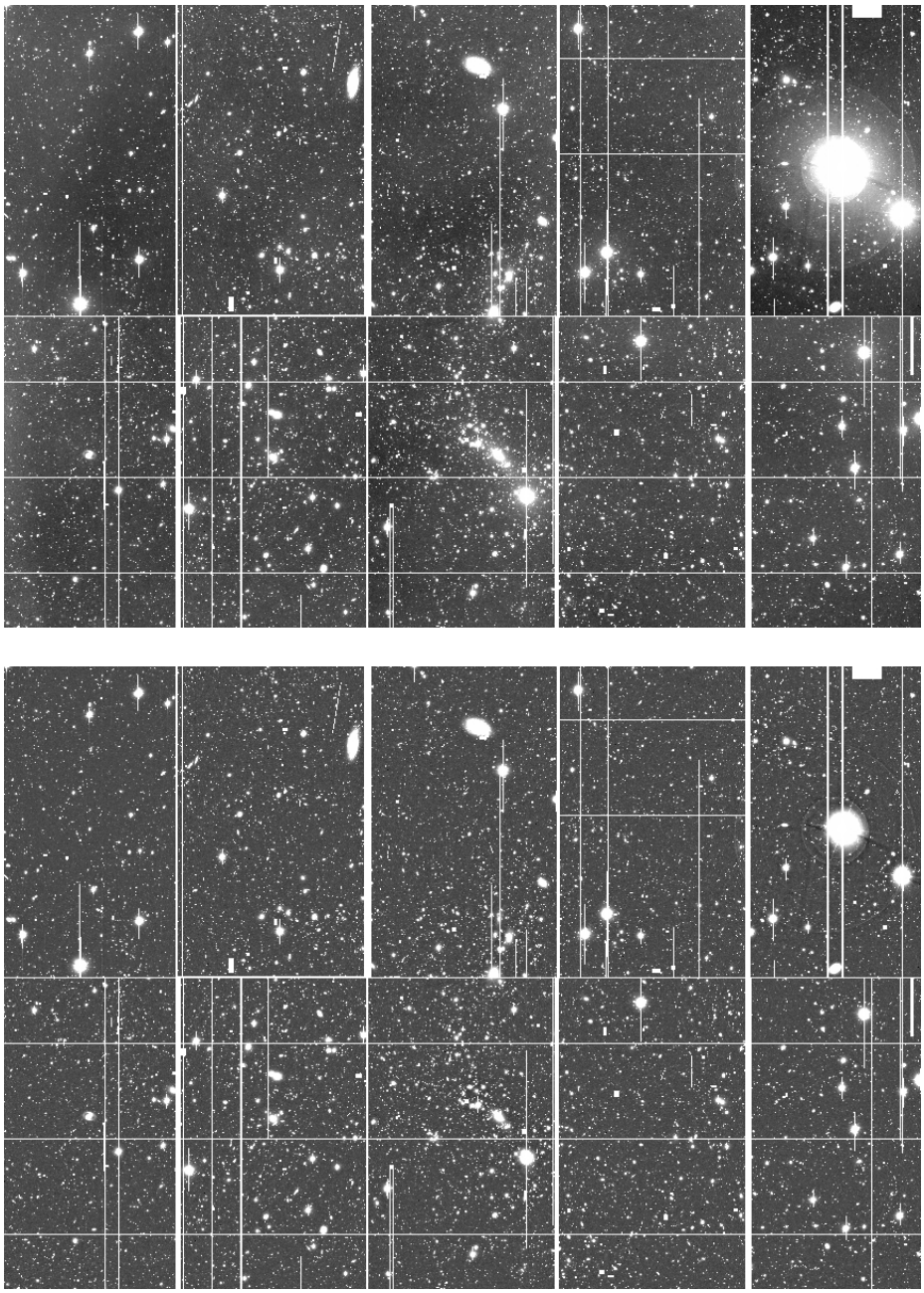

Figure B.1: Top: Single exposure in which the mode of each of the 10 chips is subtracted to remove the average sky flux level. Response variations have already been removed by flat fielding, so the large-scale background features that remain are mostly scattered light. **Bottom:** The same frame after the finer sky subtraction process described in the text. Note that the background variations have been successfully removed, including the halo around the bright star in the upper right. White regions indicate saturated pixels and regions with chip defects.

B.2 Astrometric registration

An initial astrometric solution that removes the distortion of SuprimeCam was provided by Peter Capak. Although the instrument and atmosphere are not sufficiently stable to allow this solution to be applied directly to the images, it can be used to place stars detected in each of the 10 CCDs on an initial single astrometric grid for each exposure. (Stars were selected as bright, unresolved objects in the catalog using the magnitude–half-light radius plane.) A reference catalog containing stars of known celestial coordinates was obtained for each field. Where possible, stars with pristine photometry in SDSS DR7 or DR8 were used (Abazajian et al. 2009); elsewhere, the USNO-B catalog (Monet et al. 2003) was used. While the USNO-B data are less precise and deep than the SDSS, they cover the entire sky. A stereographic projection is used to project the sky onto a plane.

Using the stellar coordinates in each exposure obtained from the initial solution, an initial estimate of the tangent point coordinates, position angle, and pixel scale were found by cross-correlation with the reference catalog. After applying these linear transformations to the stellar coordinates, stars in all of the science exposures and in the reference catalog were matched with a 25 pixel positional tolerance. The matched star coordinates were then used to establish a system of equations in which a set of two-dimensional, second-order polynomials specific to each chip and each exposure map pixel to sky coordinates. The unknowns in these equations are the coefficients of the polynomials and the true celestial positions of each star. Since the problem is overdetermined, the best solution is found by minimizing the scatter between the true and transformed stellar positions. This process ensures that the various science frames are accurately mapped onto one another, and the presence of the reference catalog anchors the results to a known plate solution.

The stellar centroids are much more accurate in the deep, CCD-based Subaru imaging than in any available external reference catalog. This is accounted for by weighting the stellar positions in the Subaru and external catalogs accordingly when solving the astrometric equations described above. In principle, weighting by the expected inverse variance of the stellar positions is sufficient, but in practice, these weights sometimes gave unstable solutions with systematic deviations from the reference catalog. By refining the weights, the solutions could be significantly improved and systematic differences relative to the reference catalog eliminated or reduced to the level of known systematic errors.

After the first astrometric solution is found, it is iteratively refined by graphically identifying and rejecting outlier stars in each exposure. Third-order polynomial mappings are used following the first pass described above. In most cases, all available bands of imaging were used simultaneously to derive the astrometric solution. The typical rms residuals are 3–5 mas per coordinate between stellar positions in individual Subaru frames and the solution position. The typical rms residuals between the SDSS and solution coordinates are 40–60 mas (per coordinate), based on 340–860 reference stars,

Table B.1. Filter information

Instrument	Filter	λ_c (Å)	Atmospheric extinction coeff.	$A_\lambda/E(B-V)$
SuprimeCam	B	4480	0.21	3.97
	V	5499	0.12	3.10
	R	6537	0.093	2.54
	$i+$	7665	0.040	1.97
	I	7984	0.027	1.85
	$z+$	9054	0.021	1.47
IMACS	Bessell B	4456	0.19	3.99
	CTIO I	8020	0.04	1.84
CFHT 12K	B	4437		4.03
MegaPrime	u^*	3835	0.35	4.66

Note. — SuprimeCam, CFHT 12K, and MegaPrime transmission curves include the total system response of the telescope and instrument, as well as the Mauna Kea atmosphere at 1.2 airmasses, while the IMACS transmission curves are derived from the filter transmission provided by the Magellan Observatory and the QE curve for the E2V chips. The central wavelength is defined as $\lambda_c = \int \lambda^2 R_\lambda d\lambda / \int \lambda R_\lambda d\lambda$. Galactic extinction coefficients are calculated using the Cardelli et al. (1989) extinction law with $R_V = 3.1$ and a source spectrum that is flat in f_λ.

while the rms residuals are 170–200 mas, based on 430–490 reference stars, when the less precise USNO-B coordinates are used. This scatter is consistent with the quoted positional uncertainties in these reference catalogs.

B.3 Photometric registration

Before coadding the images, each must be normalized so that an object has the same flux regardless of the exposure or chip in which it is measured. The flat field was normalized to have a median of unity on *each chip*; thus, differences in gain, quantum efficiency, and overall illumination remain among the chips. Likewise, the number of counts will vary from exposure to exposure according the airmass and, if the conditions are not photometric, the transparency.

A first-pass photometric calibration is made by correcting chip-to-chip variations using band-dependent calibration factors provided by the SuprimeCam team. (These cannot be derived directly from the flat field illumination pattern, primarily due to the presence of scattered light.) Likewise, exposures are normalized to an airmass of unity using the atmospheric extinction coefficients in Table B.1, which lists basic information about the filters used in this survey.

At this stage, some manual masking of the individual exposures is necessary to eliminate satellite trails, charge collection along chip edges, ghosts, areas of poor sky subtraction, and other defects. Aperture photometry is then performed on the masked images, and stars are matched between exposures using the known astrometric solution. The `fitmagshifts` routine then solves for the

chips offsets c_i and exposure offsets e_j that minimize the scatter among $m_{ij} - c_i - e_j$, where m_{ij} is the stellar flux measured on chip i in exposure j. The m_{ij} used here are corrected for field distortion (i.e., variations in the solid angle of sky viewed per pixel).

If the fiducial chip-to-chip offsets are valid and conditions are photometric, then we expect $c_i = 0$ and $e_j = 0$ for all i, j. For most of the observations, the exposure offsets are indeed $|e_j| < 0.01$ mag, but they are sometimes larger in archival data taken in non-photometric conditions. Thus, the exposure offsets were applied in all cases. In order to measure the chip-to-chip offsets c_i reliably, a large number of exposures with wide dither patterns and various rotation angles are needed, so that the same star appears on many chips. This is generally unavailable on a night-by-night basis. Therefore, no corrections to the fiducial offsets were applied. As a check on the fiducial offsets, we compared the c_i derived for different cluster observations in the R filter on 2007 November 13–14, which ideally should give identical offsets. A field-to-field dispersion of 0.03 mag was seen, and no significant mean offset was detected for any chip, with one exception: chip 9 (upper right in Figure B.1) may require a +0.04 mag offset over the fiducial value, but this is uncertain since scattered light is maximal in this chip. We conclude that the chip offsets derived using `fitmagshifts` are consistent with zero and that the fiducial offsets are sufficient to flatten the chip-to-chip variations.

B.4 Image warping and stacking

In order to combine the individual exposures, each was warped onto the final astrometric grid with a $0\farcs2$ pixel scale. For the band in which shear is measured, the sum-over-triangles option of `warpimage` was used; for the other bands, the quicker linear interpolation method was generally adopted. Before warping, the standard deviation of each chip in each exposure was recorded, in order to estimate the noise before correlations are introduced by resampling. The flat field was scaled by the measured inverse variance to produce a weight map. For the shear band, chip 5 (upper left in Figure B.1) was masked at this point, since its poor charge transfer efficiency (CTE) makes it unsuitable for shape measurements.

Exposures were combined using a weighted average based on the weight maps described above, using a 3σ clip about the median m. The weight maps are propagated to produce a final inverse variance map. The coadded "quilt" is produced in 10 patches, each 2400×4575 pixels. This includes a 100 pixel margin beyond the inner 2200×4375, so that each quilt patch shares a margin in common with its neighbor. The patches are kept on the individual cluster nodes to facilitate quicker catalog creation and shear measurement. A large 11200×8950 quilt was created by "sewing together" the patches so that the whole mosaic could be viewed at once.

Accurate photometry requires accounting for the variation in the PSF between bands. In order

to maximize the fidelity of the color measures, PSF-matched quilts were produced for each cluster by convolving each band by a Gaussian chosen so that the final median stellar half-light radius (`FLUX_RADIUS` in `SExtractor`) matches that of the band with the worst image quality.[1]

B.5 Variations for other instruments

The previous description applies to SuprimeCam data taken in 2002 and later. Some variations were necessary to adapt to IMACS, CFHT 12K, and early SuprimeCam imaging using a different mosaic of CCDs. In particular, fiducial chip offset values were not available for the latter and so had to be derived from `fitmagshifts` or from dome flats. For the SuprimeCam data from November 2000 (A963), the sky and dome flats were not usable, so a superflat constructed from science observations was created. The MegaPrime data was retrieved in a detrended state from the CFHT archive and required only rescaling of exposures, astrometric registration, and stacking.

B.6 Source detection and photometry

`SExtractor` (Bertin & Arnouts 1996) was used to detect objects for our lensing analysis and perform matched aperture photometry. Table B.2 summarizes the most relevant configuration details. We used the dual image mode, in which separate images are used for source detection and photometry. The detection band was taken as the R band image in native seeing, with the exception of A963, for which the I band was used due to the poorer quality of the R data (Section B.5). The PSF-matched image in each filter (including R itself) was used for photometry. Additionally, a catalog was generated in which the R-band image in native seeing was used for both detection and photometry; this catalog forms the basis of the shear analysis.

Stellar colors were measured in $3''$ diameter apertures. Galactic extinction was removed based on the reddening maps of Schlegel et al. (1998) and the extinction coefficients in Table B.1. The primary photometric calibration sources are the SDSS DR7 and DR8, which contain five of the clusters in the sample. In order to calibrate the stellar photometry based on the SDSS, we require color conversions between the SDSS system and the native system of the instrument. These are listed in Table B.3. In several cases the relevant conversions were obtained from the literature. An alternative method is to measure synthetic magnitudes using a well calibrated stellar spectrophotometric library and the known transmission curves of the filter, instrument, telescope, and atmosphere. Pickles (1985) provides such a spectral library. We found excellent agreement between conversions from SDSS to the Subaru B band that were derived empirically (Capak et al. 2007; Yagi et al. 2010) and that

[1]The CFHT u^* image of A383 was the one exception to this scheme, since the image quality was far poorer than the Subaru data. The Subaru images were PSF-matched internally, and the CFHT image was unaltered. The photometric calibration automatically includes an aperture correction based on point sources.

Table B.2. Weak lensing `SExtractor` configuration

Parameter	Value
DETECT_MINAREA	9
DETECT_THRESH	0.75
ANALYSIS_THRESH	0.75
FILTER	Y
FILTER_NAME	gauss_3.0_5x5.conv
CLEAN	Y
CLEAN_PARAM	1
DEBLEND_NTHRESH	64
DEBLEND_MINCONT	0.00001
MASK_TYPE	CORRECT
GAIN	1e10
BACKPHOTO_TYPE	LOCAL
BACKPHOTO_THICK	40
WEIGHT_GAIN	N
WEIGHT_TYPE	MAP_RMS

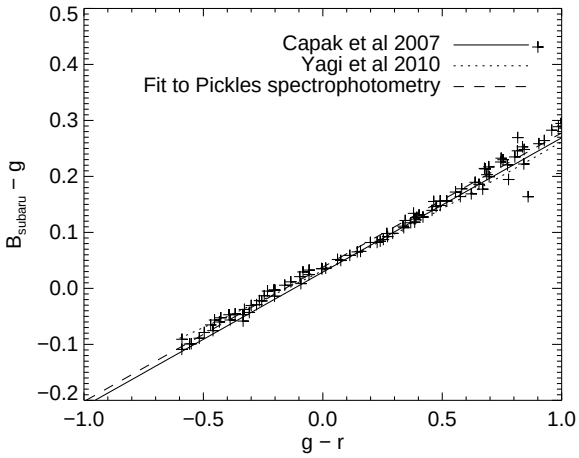

Figure B.2: Crosses show synthetic $B_{Subaru} - g_{\rm SDSS}$ and $(g-r)_{\rm SDSS}$ colors measured from the Pickles (1985) stellar spectrophotometric library. The dashed line is fit directly to these data, while the solid and dotted curves show two published conversions. The three are in close agreement.

derived directly from Pickles spectrophotometry (see Figure B.2). The agreement is better than 0.01 mag, with similar results holding in the V, R, and $i+$ filters.[2] This gives confidence that the Pickles library can be used to determine accurate color conversions when an empirical conversion between the SDSS and native photometric systems is not available.

For the five clusters contained in the SDSS, photometry of unsaturated stars was converted to the native system using these transformations, and these were used to measure the photometric zeropoint in each filter and cluster. Typically the number of suitable stars in the field of view was sufficient to render the statistical uncertainty negligible. Since the SDSS stellar magnitudes are derived from PSF-fitting, this method automatically includes a point-source aperture correction from $3''$ aperture fluxes to total fluxes. In order to measure total fluxes properly in other apertures, it is necessary

[2]The slope of the Pickles fit disagrees with the Capak et al. (2007) conversion to Subaru $z+$. The Pickles fit was adopted, but the net calibration difference remains $\lesssim 0.02$ mag.

Table B.3. Photometric conversions from SDSS

Color transformation	Valid range	Source
Subaru SuprimeCam		
$B = g + 0.240(g-r) + 0.029$	$-1 < g-r < 1$	Capak et al. (2007)
$V = g - 0.617(g-r) - 0.021$	$-1 < g-r < 1$	Capak et al. (2007)
$R = r - 0.015138(g-r) + 0.012914(g-r)^2 + 0.01919$	$-0.6 < g-r < 1.4$	Yagi et al. (2010)
$i+ = i - 0.106(r-i) + 0.007$	$-1 < r-i < 1$	Capak et al. (2007)
$I = i - 0.2654(r-i) + 0.018$	$-0.5 < r-i < 0.4$	Fit to Pickles (1985)
$z+ = z - 0.0413(i-z) - 0.002$	$-0.5 < i-z < 0.5$	Fit to Pickles (1985)
Magellan IMACS		
$B = g + 0.2915(g-r) + 0.054$	$-0.7 < g-r < 0.7$	Fit to Pickles (1985)
$I = i - 0.2817(r-i) + 0.018$	$-0.5 < r-i < 1$	Fit to Pickles (1985)
CFHT 12K		
$B = g + 0.2915(g-r) + 0.054$	$-0.7 < g-r < 0.7$	Fit to Pickles (1985)
CFHT MegaPrime		
$u^* = u - 0.238(u-g) + 0.081$	$1 < u-g < 2.5$	Shim et al. (2006)

for the zeropoint to reflect the flux actually contained within the measurement aperture. Therefore, this aperture correction was removed from the derived zeropoint by adding $\Delta m \sim 0.05$–0.10, the median difference between $3''$ and $8''$ aperture magnitudes of stars in the PSF-matched detection image, assuming that the $8''$ aperture contains virtually all of the stellar flux. (Note that this has no effect on *colors*.) For galaxy photometry, we measure colors in $2''$ diameter apertures in order to improve the signal-to-noise ratio. For each galaxy, the difference between `MAG_AUTO` and `MAG_APER` in the PSF-matched detection image was recorded and used to convert from aperture to total fluxes when necessary.

The SDSS-based calibration yielded generally stable zeropoints on photometric nights, and these further agreed with Landolt standard star observations within a few percent. MS2137 is not in the SDSS footprint, and zeropoints in this field were instead calibrated by aligning the stellar color-color locus with the $BVRI$ locus measured in A611 (which was tied to the SDSS), taking advantage of the "kink" in the $V-R$ vs. $R-I$ plane (see Figure B.3 and, e.g., High et al. 2009). The $z+$ zeropoint was then set by matching the $RIz+$ stellar locus in A2390. Since this procedure fixes only the colors, the overall flux scale was set by fixing the V zeropoint to measurements in other clusters obtained on the same photometric night. A2667 likewise lies outside the SDSS footprint; in this case, the VRI zeropoints were determined from other fields observed the same night. Small shifts (< 0.1 mag) were then made to align the stellar locus with a synthetic locus based on Pickles spectrophotometry.

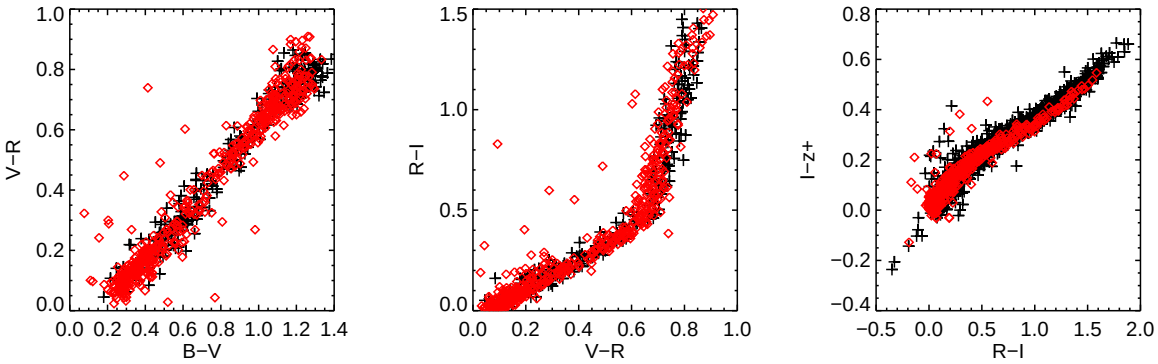

Figure B.3: Example of photometric calibration by aligning the stellar color locus to that determined in another field from an independent calibration source. In this case, the black points are tied to the SDSS, while the red points are stars in a field (outside the SDSS footprint) with zeropoints to be determined. The feature in the VRI plane allows the absolute $V-R$ and $R-I$ colors to be calibrated initially. The $B-V$ and $I-z$ colors can then be calibrated following the left and right panels. An iterative scheme was used to align the loci. Note that this method can be applied to observations regardless of the photometricity or the availability of standard star data.

Bibliography

Abadi, M. G., Navarro, J. F., Fardal, M., Babul, A., & Steinmetz, M. 2010, MNRAS, 407, 435

Abazajian, K., Fuller, G. M., & Patel, M. 2001, Phys. Rev. D, 64, 023501

Abazajian, K., & Koushiappas, S. M. 2006, Phys. Rev. D, 74, 023527

Abazajian, K. N., Adelman-McCarthy, J. K., Agüeros, M. A., et al. 2009, ApJS, 182, 543

Abdo, A. A., Ackermann, M., Ajello, M., et al. 2010, ApJ, 712, 147

Ackermann, M., Ajello, M., Allafort, A., et al. 2010, J. Astropart. Phys., 5, 25

Ahmed, Z., Akerib, D. S., Armengaud, E., et al. 2011, Phys. Rev. D, 84, 011102

Allen, S. W., Rapetti, D. A., Schmidt, R. W., et al. 2008, MNRAS, 383, 879

Allen, S. W., Schmidt, R. W., Ebeling, H., Fabian, A. C., & van Speybroeck, L. 2004, MNRAS, 353, 457

Allen, S. W., Schmidt, R. W., Fabian, A. C., & Ebeling, H. 2003, MNRAS, 342, 287

Amorisco, N. C., & Evans, N. W. 2012, MNRAS, 419, 184

Anderson, L., Aubourg, E., Bailey, S., et al. 2012, arXiv:1203.6594

Ando, S., & Nagai, D. 2012, J. Cosmol. Astropart. Phys., 7, 17

Aprile, E., Arisaka, K., Arneodo, F., et al. 2010, Physical Review Letters, 105, 131302

Auger, M. W., Treu, T., Bolton, A. S., et al. 2009, ApJ, 705, 1099

—. 2010a, ApJ, 724, 511

Auger, M. W., Treu, T., Gavazzi, R., et al. 2010b, ApJ, 721, L163

Babcock, H. W. 1939, Lick Observatory Bulletin, 19, 41

Bahcall, J. N., & Sarazin, C. L. 1977, ApJ, 213, L99

Bahcall, N. A., & Cen, R. 1992, ApJ, 398, L81

Bahcall, N. A., & Soneira, R. M. 1983, ApJ, 270, 20

Balestra, I., Mainieri, V., Popesso, P., et al. 2010, A&A, 512, A12

Barnabè, M., Dutton, A. A., Marshall, P. J., et al. 2012, MNRAS, 423, 1073

Barnes, J. E., & Hernquist, L. 1992, ARA&A, 30, 705

Barro, G., Faber, S. M., Perez-Gonzalez, P. G., et al. 2012, arXiv:1206.5000

Bartelmann, M., & Meneghetti, M. 2004, A&A, 418, 413

Barth, A. J., Ho, L. C., & Sargent, W. L. W. 2002, AJ, 124, 2607

Battaglia, G., Helmi, A., Tolstoy, E., et al. 2008, ApJ, 681, L13

Baum, W. A. 1959, PASP, 71, 106

Bell, E. F., & de Jong, R. S. 2001, ApJ, 550, 212

Bell, E. F., McIntosh, D. H., Katz, N., & Weinberg, M. D. 2003, ApJS, 149, 289

Bell, E. F., Wolf, C., Meisenheimer, K., et al. 2004, ApJ, 608, 752

Bell, E. F., Naab, T., McIntosh, D. H., et al. 2006, ApJ, 640, 241

Bender, R., Burstein, D., & Faber, S. M. 1992, ApJ, 399, 462

—. 1993, ApJ, 411, 153

Benítez, N. 2000, ApJ, 536, 571

Benson, A. J., Frenk, C. S., Lacey, C. G., Baugh, C. M., & Cole, S. 2002, MNRAS, 333, 177

Bernardi, M., Hyde, J. B., Sheth, R. K., Miller, C. J., & Nichol, R. C. 2007, AJ, 133, 1741

Bernardi, M., Shankar, F., Hyde, J. B., et al. 2010, MNRAS, 404, 2087

Bernardi, M., Sheth, R. K., Annis, J., et al. 2003a, AJ, 125, 1849

—. 2003b, AJ, 125, 1866

Berrier, J. C., Bullock, J. S., Barton, E. J., et al. 2006, ApJ, 652, 56

Bershady, M. A., Martinsson, T. P. K., Verheijen, M. A. W., et al. 2011, ApJ, 739, L47

Bershady, M. A., Verheijen, M. A. W., Swaters, R. A., et al. 2010, ApJ, 716, 198

Bertin, E., & Arnouts, S. 1996, A&AS, 117, 393

Bezanson, R., van Dokkum, P., van de Sande, J., Franx, M., & Kriek, M. 2012, arXiv:1210.7236

Bezanson, R., van Dokkum, P. G., Tal, T., et al. 2009, ApJ, 697, 1290

Bezanson, R., van Dokkum, P. G., Franx, M., et al. 2011, ApJ, 737, L31+

Bildfell, C., Hoekstra, H., Babul, A., & Mahdavi, A. 2008, MNRAS, 389, 1637

Binney, J., & Merrifield, M. 1998, Galactic Astronomy, 1st edn. (Princeton Univ. Press)

Binney, J., & Tremaine, S. 1987, Galactic Dynamics, 1st edn. (Princeton Univ. Press)

Biviano, A., & Girardi, M. 2003, ApJ, 585, 205

Blanton, M. R., & Roweis, S. 2007, AJ, 133, 734

Blanton, M. R., Schlegel, D. J., Strauss, M. A., et al. 2005, AJ, 129, 2562

Bluck, A. F. L., Conselice, C. J., Bouwens, R. J., et al. 2009, MNRAS, 394, L51

Bluck, A. F. L., Conselice, C. J., Buitrago, F., et al. 2011, arXiv:1111.5662

Blumenthal, G. R., Faber, S. M., Flores, R., & Primack, J. R. 1986, ApJ, 301, 27

Blumenthal, G. R., Faber, S. M., Primack, J. R., & Rees, M. J. 1984, Nature, 311, 517

Blumenthal, G. R., Pagels, H., & Primack, J. R. 1982, Nature, 299, 37

Bolton, A. S., Treu, T., Koopmans, L. V. E., et al. 2008, ApJ, 684, 248

Bolton, A. S., Brownstein, J. R., Kochanek, C. S., et al. 2012, arXiv:1201.2988

Bond, J. R., Szalay, A. S., & Turner, M. S. 1982, Physical Review Letters, 48, 1636

Bower, R. G., Benson, A. J., Malbon, R., et al. 2006, MNRAS, 370, 645

Bower, R. G., Lucey, J. R., & Ellis, R. S. 1992, MNRAS, 254, 601

Boyarsky, A., Ruchayskiy, O., & Shaposhnikov, M. 2009, Annual Review of Nuclear and Particle Science, 59, 191

Boylan-Kolchin, M., Bullock, J. S., & Kaplinghat, M. 2011, MNRAS, 415, L40

—. 2012, MNRAS, 422, 1203

Boylan-Kolchin, M., Ma, C.-P., & Quataert, E. 2005, MNRAS, 362, 184

—. 2006, MNRAS, 369, 1081

—. 2008, MNRAS, 383, 93

Braglia, F. G., Pierini, D., Biviano, A., & Böhringer, H. 2009, A&A, 500, 947

Brammer, G. B., van Dokkum, P. G., & Coppi, P. 2008, ApJ, 686, 1503

Brammer, G. B., Whitaker, K. E., van Dokkum, P. G., et al. 2009, ApJ, 706, L173

Bridge, C. R., Carlberg, R. G., & Sullivan, M. 2010, ApJ, 709, 1067

Brinchmann, J., & Ellis, R. S. 2000, ApJ, 536, L77

Broadhurst, T., Umetsu, K., Medezinski, E., Oguri, M., & Rephaeli, Y. 2008, ApJ, 685, L9

Broadhurst, T., Benítez, N., Coe, D., et al. 2005, ApJ, 621, 53

Brooks, A. M., & Zolotov, A. 2012, arXiv:1207.2468

Bruzual, G., & Charlot, S. 2003, MNRAS, 344, 1000

Buitrago, F., Trujillo, I., Conselice, C. J., et al. 2008, ApJ, 687, L61

Bullock, J. S., Kolatt, T. S., Sigad, Y., et al. 2001, MNRAS, 321, 559

Bullock, J. S., Kravtsov, A. V., & Weinberg, D. H. 2000, ApJ, 539, 517

Bundy, K., Ellis, R. S., & Conselice, C. J. 2005, ApJ, 625, 621

Bundy, K., Fukugita, M., Ellis, R. S., Kodama, T., & Conselice, C. J. 2004, ApJ, 601, L123

Bundy, K., Fukugita, M., Ellis, R. S., et al. 2009, ApJ, 697, 1369

Bundy, K., Treu, T., & Ellis, R. S. 2007, ApJ, 665, L5

Bundy, K., Ellis, R. S., Conselice, C. J., et al. 2006, ApJ, 651, 120

Buote, D. A., & Humphrey, P. J. 2012, in Astrophysics and Space Science Library, Vol. 378, Astrophysics and Space Science Library, ed. D.-W. Kim & S. Pellegrini, 235

Burke, C., Collins, C. A., Stott, J. P., & Hilton, M. 2012, MNRAS, 425, 2058

Burkert, A. 1995, ApJ, 447, L25

Calzetti, D., Armus, L., Bohlin, R. C., et al. 2000, ApJ, 533, 682

Capak, P., Cowie, L. L., Hu, E. M., et al. 2004, AJ, 127, 180

Capak, P., Aussel, H., Ajiki, M., et al. 2007, ApJS, 172, 99

Cappellari, M. 2008, MNRAS, 390, 71

Cappellari, M., & Emsellem, E. 2004, PASP, 116, 138

Cappellari, M., Bacon, R., Bureau, M., et al. 2006, MNRAS, 366, 1126

Cappellari, M., Emsellem, E., Bacon, R., et al. 2007, MNRAS, 379, 418

Cappellari, M., di Serego Alighieri, S., Cimatti, A., et al. 2009, ApJ, 704, L34

Cappellari, M., McDermid, R. M., Alatalo, K., et al. 2012a, Nature, 484, 485

Cappellari, M., Scott, N., Alatalo, K., et al. 2012b, arXiv:1208.3522

Cappellari, M., McDermid, R. M., Alatalo, K., et al. 2012c, arXiv:1208.3523

Cardamone, C. N., van Dokkum, P. G., Urry, C. M., et al. 2010, ApJS, 189, 270

Cardelli, J. A., Clayton, G. C., & Mathis, J. S. 1989, ApJ, 345, 245

Carollo, C. M., de Zeeuw, P. T., van der Marel, R. P., Danziger, I. J., & Qian, E. E. 1995, ApJ, 441, L25

Carter, D., Bridges, T. J., & Hau, G. K. T. 1999, MNRAS, 307, 131

Cassata, P., Giavalisco, M., Guo, Y., et al. 2010, ApJ, 714, L79

—. 2011, ApJ, 743, 96

Chabrier, G. 2003, PASP, 115, 763

Chandrasekhar, S. 1969, Ellipsoidal figures of equilibrium (Yale Univ. Press)

Cimatti, A., Daddi, E., & Renzini, A. 2006, A&A, 453, L29

Cimatti, A., Daddi, E., Renzini, A., et al. 2004, Nature, 430, 184

Cimatti, A., Cassata, P., Pozzetti, L., et al. 2008, A&A, 482, 21

Ciotti, L., Lanzoni, B., & Volonteri, M. 2007, ApJ, 658, 65

Cirasuolo, M., McLure, R. J., Dunlop, J. S., et al. 2010, MNRAS, 401, 1166

Clowe, D., Bradač, M., Gonzalez, A. H., et al. 2006, ApJ, 648, L109

Coe, D., Benítez, N., Broadhurst, T., & Moustakas, L. A. 2010, ApJ, 723, 1678

Coe, D., Umetsu, K., Zitrin, A., et al. 2012, arXiv:1201.1616

Coil, A. L., Davis, M., Madgwick, D. S., et al. 2004, ApJ, 609, 525

Colless, M., Dalton, G., Maddox, S., et al. 2001, MNRAS, 328, 1039

Collins, C. A., & Mann, R. G. 1998, MNRAS, 297, 128

Conroy, C., Gunn, J. E., & White, M. 2009, ApJ, 699, 486

Conroy, C., & van Dokkum, P. 2012, arXiv:1205.6473

Conselice, C. J., Yang, C., & Bluck, A. F. L. 2009, MNRAS, 394, 1956

Cooper, M. C., Griffith, R. L., Newman, J. A., et al. 2012, MNRAS, 419, 3018

Côté, S., Carignan, C., & Freeman, K. C. 2000, AJ, 120, 3027

Covone, G., Kneib, J.-P., Soucail, G., et al. 2006, A&A, 456, 409

Cowie, L. L., Gardner, J. P., Lilly, S. J., & McLean, I. 1990, ApJ, 360, L1

Cowie, L. L., Songaila, A., Hu, E. M., & Cohen, J. G. 1996, AJ, 112, 839

Croton, D. J., Springel, V., White, S. D. M., et al. 2006, MNRAS, 365, 11

Czoske, O., Moore, B., Kneib, J.-P., & Soucail, G. 2002, A&A, 386, 31

Daddi, E., Cimatti, A., Pozzetti, L., et al. 2000, A&A, 361, 535

Daddi, E., Cimatti, A., Renzini, A., et al. 2004, ApJ, 617, 746

Daddi, E., Röttgering, H. J. A., Labbé, I., et al. 2003, ApJ, 588, 50

Daddi, E., Renzini, A., Pirzkal, N., et al. 2005, ApJ, 626, 680

Dalcanton, J. J., & Hogan, C. J. 2001, ApJ, 561, 35

Damjanov, I., McCarthy, P. J., Abraham, R. G., et al. 2009, ApJ, 695, 101

Damjanov, I., Abraham, R. G., Glazebrook, K., et al. 2011, arXiv:1108.0656

Davé, R., Spergel, D. N., Steinhardt, P. J., & Wandelt, B. D. 2001, ApJ, 547, 574

Davis, M., Efstathiou, G., Frenk, C. S., & White, S. D. M. 1985, ApJ, 292, 371

Davis, M., & Peebles, P. J. E. 1983, ApJ, 267, 465

de Blok, W. J. G. 2010, Advances in Astronomy, 2010

de Blok, W. J. G., McGaugh, S. S., & Rubin, V. C. 2001, AJ, 122, 2396

de Blok, W. J. G., Walter, F., Brinks, E., et al. 2008, AJ, 136, 2648

de Filippis, E., Sereno, M., Bautz, M. W., & Longo, G. 2005, ApJ, 625, 108

de Lorenzi, F., Gerhard, O., Coccato, L., et al. 2009, MNRAS, 395, 76

de Lucia, G., & Blaizot, J. 2007, MNRAS, 375, 2

de Ravel, L., Le Fèvre, O., Tresse, L., et al. 2009, A&A, 498, 379

Dehnen, W. 1993, MNRAS, 265, 250

Dekel, A., Sari, R., & Ceverino, D. 2009, ApJ, 703, 785

Dekel, A., Stoehr, F., Mamon, G. A., et al. 2005, Nature, 437, 707

Del Popolo, A. 2012, MNRAS, 424, 38

Diemand, J., Moore, B., & Stadel, J. 2005a, Nature, 433, 389

Diemand, J., Zemp, M., Moore, B., Stadel, J., & Carollo, C. M. 2005b, MNRAS, 364, 665

Djorgovski, S., & Davis, M. 1987, ApJ, 313, 59

Donnarumma, A., Ettori, S., Meneghetti, M., & Moscardini, L. 2009, MNRAS, 398, 438

Donovan, D. 2007, PhD thesis, Univ. Hawai'i

Dressler, A. 1979, ApJ, 231, 659

—. 1980, ApJ, 236, 351

Dressler, A., Lynden-Bell, D., Burstein, D., et al. 1987, ApJ, 313, 42

Dubinski, J. 1998, ApJ, 502, 141

Dubinski, J., & Carlberg, R. G. 1991, ApJ, 378, 496

Duffy, A. R., Schaye, J., Kay, S. T., & Dalla Vecchia, C. 2008, MNRAS, 390, L64

Duffy, A. R., Schaye, J., Kay, S. T., et al. 2010, MNRAS, 405, 2161

Dúmet-Montoya, H. S., Caminha, G. B., & Makler, M. 2012, A&A, 544, A83

Dutton, A. A., Courteau, S., de Jong, R., & Carignan, C. 2005, ApJ, 619, 218

Dutton, A. A., Conroy, C., van den Bosch, F. C., et al. 2011, MNRAS, 416, 322

Dutton, A. A., Treu, T., Brewer, B. J., et al. 2012, MNRAS, 187

Eggen, O. J., Lynden-Bell, D., & Sandage, A. R. 1962, ApJ, 136, 748

Einasto, J. 1965, Trudy Astrofizicheskogo Instituta Alma-Ata, 5, 87

Einasto, J., Kaasik, A., & Saar, E. 1974, Nature, 250, 309

Eisenstein, D. J., Hogg, D. W., Fukugita, M., et al. 2003, ApJ, 585, 694

Eke, V. R., Cole, S., & Frenk, C. S. 1996, MNRAS, 282, 263

El-Zant, A., Shlosman, I., & Hoffman, Y. 2001, ApJ, 560, 636

El-Zant, A. A., Hoffman, Y., Primack, J., Combes, F., & Shlosman, I. 2004, ApJ, 607, L75

Elíasdóttir, Á., Limousin, M., Richard, J., et al. 2007, arXiv:0710.5636

Ellis, R., Allington-Smith, J., & Smail, I. 1991, MNRAS, 249, 184

Ellis, R. S., Smail, I., Dressler, A., et al. 1997, ApJ, 483, 582

Erben, T., Van Waerbeke, L., Bertin, E., Mellier, Y., & Schneider, P. 2001, A&A, 366, 717

Faber, S. M., & Gallagher, J. S. 1979, ARA&A, 17, 135

Faber, S. M., & Jackson, R. E. 1976, ApJ, 204, 668

Faber, S. M., Willmer, C. N. A., Wolf, C., et al. 2007, ApJ, 665, 265

Fan, L., Lapi, A., Bressan, A., et al. 2010, ApJ, 718, 1460

Fan, L., Lapi, A., De Zotti, G., & Danese, L. 2008, ApJ, 689, L101

Fedeli, C., Bartelmann, M., Meneghetti, M., & Moscardini, L. 2007, A&A, 473, 715

Feng, J. L. 2010, ARA&A, 48, 495

Feng, J. L., & Kumar, J. 2008, Physical Review Letters, 101, 231301

Fisher, D., Illingworth, G., & Franx, M. 1995, ApJ, 438, 539

Flores, R. A., & Primack, J. R. 1994, ApJ, 427, L1

Franx, M., van Dokkum, P. G., Schreiber, N. M. F., et al. 2008, ApJ, 688, 770

Franx, M., Labbé, I., Rudnick, G., et al. 2003, ApJ, 587, L79

Freedman, W. L., Madore, B. F., Gibson, B. K., et al. 2001, ApJ, 553, 47

Frenk, C. S., & White, S. D. M. 2012, Annalen der Physik, 524, 507

Frye, B., & Broadhurst, T. 1998, ApJ, 499, L115

Fukushige, T., Kawai, A., & Makino, J. 2004, ApJ, 606, 625

Fukushige, T., & Makino, J. 2001, ApJ, 557, 533

Furusawa, H., Kosugi, G., Akiyama, M., et al. 2008, ApJS, 176, 1

Gao, L., Frenk, C. S., Jenkins, A., Springel, V., & White, S. D. M. 2012a, MNRAS, 419, 1721

Gao, L., Loeb, A., Peebles, P. J. E., White, S. D. M., & Jenkins, A. 2004, ApJ, 614, 17

Gao, L., Navarro, J. F., Cole, S., et al. 2008, MNRAS, 387, 536

Gao, L., Navarro, J. F., Frenk, C. S., et al. 2012b, arXiv:1201.1940

Gavazzi, R. 2005, A&A, 443, 793

Gavazzi, R., Fort, B., Mellier, Y., Pelló, R., & Dantel-Fort, M. 2003, A&A, 403, 11

Gavazzi, R., Treu, T., Rhodes, J. D., et al. 2007, ApJ, 667, 176

Gebhardt, K., Faber, S. M., Koo, D. C., et al. 2003, ApJ, 597, 239

Gentile, G., Burkert, A., Salucci, P., Klein, U., & Walter, F. 2005, ApJ, 634, L145

Gerhard, O., Kronawitter, A., Saglia, R. P., & Bender, R. 2001, AJ, 121, 1936

Ghigna, S., Moore, B., Governato, F., et al. 2000, ApJ, 544, 616

Giavalisco, M., Ferguson, H. C., Koekemoer, A. M., et al. 2004, ApJ, 600, L93

Gilmore, G., Wilkinson, M. I., Wyse, R. F. G., et al. 2007, ApJ, 663, 948

Glazebrook, K., Abraham, R. G., McCarthy, P. J., et al. 2004, Nature, 430, 181

Gnedin, O. Y., Ceverino, D., Gnedin, N. Y., et al. 2011, arXiv:1108.5736

Gnedin, O. Y., Kravtsov, A. V., Klypin, A. A., & Nagai, D. 2004, ApJ, 616, 16

Goerdt, T., Moore, B., Read, J. I., Stadel, J., & Zemp, M. 2006, MNRAS, 368, 1073

Golse, G., & Kneib, J.-P. 2002, A&A, 390, 821

Gonzalez, A. H., Zabludoff, A. I., & Zaritsky, D. 2005, ApJ, 618, 195

Governato, F., Brook, C., Mayer, L., et al. 2010, Nature, 463, 203

Graham, A. W., Merritt, D., Moore, B., Diemand, J., & Terzić, B. 2006, AJ, 132, 2701

Graves, G. J., Faber, S. M., & Schiavon, R. P. 2009, ApJ, 693, 486

Greene, J. E., Murphy, J. D., Comerford, J. M., Gebhardt, K., & Adams, J. J. 2012, ApJ, 750, 32

Grillo, C., Gobat, R., Lombardi, M., & Rosati, P. 2009, A&A, 501, 461

Grogin, N. A., Kocevski, D. D., Faber, S. M., et al. 2011, arXiv:1105.3753

Guo, Q., White, S., Li, C., & Boylan-Kolchin, M. 2010, MNRAS, 404, 1111

Guo, Y., McIntosh, D. H., Mo, H. J., et al. 2009, MNRAS, 398, 1129

Guo, Y., Giavalisco, M., Cassata, P., et al. 2011, ApJ, 735, 18

Gustafsson, M., Fairbairn, M., & Sommer-Larsen, J. 2006, Phys. Rev. D, 74, 123522

Hau, G. K. T., Hilker, M., Bridges, T., et al. 2004, in IAU Colloq. 195: Outskirts of Galaxy Clusters: Intense Life in the Suburbs, ed. A. Diaferio, 491–495

Hennawi, J. F., Dalal, N., Bode, P., & Ostriker, J. P. 2007, ApJ, 654, 714

Hernquist, L., Spergel, D. N., & Heyl, J. S. 1993, ApJ, 416, 415

High, F. W., Stubbs, C. W., Rest, A., Stalder, B., & Challis, P. 2009, AJ, 138, 110

Hilz, M., Naab, T., & Ostriker, J. P. 2012, arXiv:1206.5004

Hoekstra, H., Franx, M., Kuijken, K., & Squires, G. 1998, ApJ, 504, 636

Hogan, C. J., & Dalcanton, J. J. 2000, Phys. Rev. D, 62, 063511

Hogg, D. W., Blanton, M. R., Brinchmann, J., et al. 2004, ApJ, 601, L29

Holden, B. P., van der Wel, A., Franx, M., et al. 2005, ApJ, 620, L83

Holmberg, E. 1958, Meddelanden fran Lunds Astronomiska Observatorium Serie II, 136, 1

Hopkins, P. F., Bundy, K., Hernquist, L., Wuyts, S., & Cox, T. J. 2010a, MNRAS, 401, 1099

Hopkins, P. F., Cox, T. J., Younger, J. D., & Hernquist, L. 2009, ApJ, 691, 1168

Hopkins, P. F., Bundy, K., Croton, D., et al. 2010b, ApJ, 715, 202

Hu, W., Barkana, R., & Gruzinov, A. 2000, Physical Review Letters, 85, 1158

Humphrey, P. J., Buote, D. A., Gastaldello, F., et al. 2006, ApJ, 646, 899

Ilbert, O., Capak, P., Salvato, M., et al. 2009, ApJ, 690, 1236

Jaffe, A. H., Ade, P. A., Balbi, A., et al. 2001, Physical Review Letters, 86, 3475

Jaffe, W. 1983, MNRAS, 202, 995

Jardel, J. R., & Gebhardt, K. 2012, ApJ, 746, 89

Jardel, J. R., Gebhardt, K., Fabricius, M., Drory, N., & Williams, M. J. 2012, arXiv:1211.5376

Jardel, J. R., & Sellwood, J. A. 2009, ApJ, 691, 1300

Jiang, G., & Kochanek, C. S. 2007, ApJ, 671, 1568

Jing, Y. P., & Suto, Y. 2000, ApJ, 529, L69

—. 2002, ApJ, 574, 538

Johansson, P. H., Naab, T., & Ostriker, J. P. 2009, ApJ, 697, L38

Jørgensen, I., Chiboucas, K., Flint, K., et al. 2006, ApJ, 639, L9

Jorgensen, I., Franx, M., & Kjaergaard, P. 1995, MNRAS, 276, 1341

Jullo, E. 2008, PhD thesis, Université de Provence, Marseille

Jullo, E., Kneib, J.-P., Limousin, M., et al. 2007, New Journal of Physics, 9, 447

Jullo, E., Natarajan, P., Kneib, J.-P., et al. 2010, Science, 329, 924

Jungman, G., Kamionkowski, M., & Griest, K. 1996, Phys. Rep., 267, 195

Kaiser, N., & Squires, G. 1993, ApJ, 404, 441

Kaiser, N., Squires, G., & Broadhurst, T. 1995, ApJ, 449, 460

Kaiser, N., Wilson, G., Luppino, G., & Dahle, H. 1999, arXiv:astro-ph/9907229

Kaplinghat, M. 2005, Phys. Rev. D, 72, 063510

Kapteyn, J. C. 1922, ApJ, 55, 302

Kartaltepe, J. S., Sanders, D. B., Scoville, N. Z., et al. 2007, ApJS, 172, 320

Kassiola, A., Kovner, I., & Blandford, R. D. 1992, ApJ, 396, 10

Kauffmann, G., White, S. D. M., & Guiderdoni, B. 1993, MNRAS, 264, 201

Kauffmann, G., Heckman, T. M., White, S. D. M., et al. 2003a, MNRAS, 341, 33

—. 2003b, MNRAS, 341, 54

Kelson, D. D. 2003, PASP, 115, 688

Kelson, D. D., van Dokkum, P. G., Franx, M., Illingworth, G. D., & Fabricant, D. 1997, ApJ, 478, L13

Kelson, D. D., Zabludoff, A. I., Williams, K. A., et al. 2002, ApJ, 576, 720

Khochfar, S., & Silk, J. 2006, ApJ, 648, L21

Kilbinger, M., Fu, L., Heymans, C., et al. 2012, arXiv:1212.3338

Kitzbichler, M. G., & White, S. D. M. 2008, MNRAS, 391, 1489

Kleyna, J. T., Wilkinson, M. I., Gilmore, G., & Evans, N. W. 2003, ApJ, 588, L21

Klypin, A., Kravtsov, A. V., Bullock, J. S., & Primack, J. R. 2001, ApJ, 554, 903

Klypin, A., Kravtsov, A. V., Valenzuela, O., & Prada, F. 1999, ApJ, 522, 82

Kneib, J. P., Mellier, Y., Fort, B., & Mathez, G. 1993, A&A, 273, 367

Kneib, J.-P., & Natarajan, P. 2011, A&A Rev., 19, 47

Kneib, J.-P., Hudelot, P., Ellis, R. S., et al. 2003, ApJ, 598, 804

Kodama, T., & Arimoto, N. 1997, A&A, 320, 41

Koekemoer, A. M., Faber, S. M., Ferguson, H. C., et al. 2011, arXiv:1105.3754

Komatsu, E., Smith, K. M., Dunkley, J., et al. 2011, ApJS, 192, 18

Koopmans, L. V. E., Bolton, A., Treu, T., et al. 2009, ApJ, 703, L51

Kormendy, J. 1977, ApJ, 218, 333

Kravtsov, A. 2010, Advances in Astronomy, 2010

Kriek, M., van der Wel, A., van Dokkum, P. G., Franx, M., & Illingworth, G. D. 2008a, ApJ, 682, 896

Kriek, M., van Dokkum, P. G., Franx, M., Illingworth, G. D., & Magee, D. K. 2009a, ApJ, 705, L71

Kriek, M., van Dokkum, P. G., Labbé, I., et al. 2009b, ApJ, 700, 221

Kriek, M., van Dokkum, P. G., Franx, M., et al. 2006, ApJ, 649, L71

—. 2008b, ApJ, 677, 219

Kronawitter, A., Saglia, R. P., Gerhard, O., & Bender, R. 2000, A&AS, 144, 53

Kuzio de Naray, R., & Kaufmann, T. 2011, MNRAS, 414, 3617

Kuzio de Naray, R., McGaugh, S. S., & de Blok, W. J. G. 2008, ApJ, 676, 920

Kuzio de Naray, R., McGaugh, S. S., de Blok, W. J. G., & Bosma, A. 2006, ApJS, 165, 461

Lackner, C. N., & Ostriker, J. P. 2010, ApJ, 712, 88

Lagattuta, D. J., Fassnacht, C. D., Auger, M. W., et al. 2010, ApJ, 716, 1579

Lange, A. E., Ade, P. A., Bock, J. J., et al. 2001, Phys. Rev. D, 63, 042001

Laporte, C. F. P., White, S. D. M., Naab, T., Ruszkowski, M., & Springel, V. 2012, MNRAS, 424, 747

Larson, R. B. 1975, MNRAS, 173, 671

Lau, E. T., Kravtsov, A. V., & Nagai, D. 2009, ApJ, 705, 1129

Law, D. R., Steidel, C. C., Shapley, A. E., et al. 2011, arXiv:1107.3137

Lawrence, A., Warren, S. J., Almaini, O., et al. 2007, MNRAS, 379, 1599

Leauthaud, A., Tinker, J., Bundy, K., et al. 2012, ApJ, 744, 159

Lewis, A., & Bridle, S. 2002, Phys. Rev. D, 66, 103511

Lewis, A. D., Buote, D. A., & Stocke, J. T. 2003, ApJ, 586, 135

Limousin, M., Richard, J., Jullo, E., et al. 2007, ApJ, 668, 643

Limousin, M., Richard, J., Kneib, J.-P., et al. 2008, A&A, 489, 23

Lin, L., Patton, D. R., Koo, D. C., et al. 2008, ApJ, 681, 232

Loeb, A., & Peebles, P. J. E. 2003, ApJ, 589, 29

Loeb, A., & Weiner, N. 2011, Physical Review Letters, 106, 171302

Londrillo, P., Nipoti, C., & Ciotti, L. 2003, Memorie della Societa Astronomica Italiana Supplementi, 1, 18

López-Sanjuan, C., Le Fèvre, O., de Ravel, L., et al. 2011, A&A, 530, A20

Lotz, J. M., Jonsson, P., Cox, T. J., et al. 2011, arXiv:1108.2508

Lotz, J. M., Jonsson, P., Cox, T. J., & Primack, J. R. 2008a, MNRAS, 391, 1137

—. 2010a, MNRAS, 404, 590

—. 2010b, MNRAS, 404, 575

Lotz, J. M., Davis, M., Faber, S. M., et al. 2008b, ApJ, 672, 177

Loubser, S. I., Sánchez-Blázquez, P., Sansom, A. E., & Soechting, I. K. 2009, MNRAS, 398, 133

Lubimov, V. A., Novikov, E. G., Nozik, V. Z., Tretyakov, E. F., & Kosik, V. S. 1980, Physics Letters B, 94, 266

Luppino, G. A., & Kaiser, N. 1997, ApJ, 475, 20

Lupton, R., Blanton, M. R., Fekete, G., et al. 2004, PASP, 116, 133

Lynds, R., & Petrosian, V. 1986, in Bulletin of the American Astronomical Society, Vol. 18, Bulletin of the American Astronomical Society, 1014

Ma, C.-P., & Boylan-Kolchin, M. 2004, Physical Review Letters, 93, 021301

Macciò, A. V., Paduroiu, S., Anderhalden, D., Schneider, A., & Moore, B. 2012, MNRAS, 424, 1105

Macciò, A. V., Ruchayskiy, O., Boyarsky, A., & Muñoz-Cuartas, J. C. 2013, MNRAS, 428, 882

Man, A. W. S., Toft, S., Zirm, A. W., Wuyts, S., & van der Wel, A. 2011, arXiv:1109.2895

Mancini, C., Daddi, E., Renzini, A., et al. 2010, MNRAS, 401, 933

Mandelbaum, R., Seljak, U., Cool, R. J., et al. 2006, MNRAS, 372, 758

Maraston, C. 2005, MNRAS, 362, 799

Marchesini, D., van Dokkum, P. G., Förster Schreiber, N. M., et al. 2009, ApJ, 701, 1765

Martizzi, D., Teyssier, R., & Moore, B. 2012a, arXiv:1211.2648

Martizzi, D., Teyssier, R., Moore, B., & Wentz, T. 2012b, MNRAS, 422, 3081

Mashchenko, S., Couchman, H. M. P., & Wadsley, J. 2006, Nature, 442, 539

Massey, R., Heymans, C., Bergé, J., et al. 2007, MNRAS, 376, 13

Mathews, W. G. 1978, ApJ, 219, 413

McCarthy, I. G., Schaye, J., Ponman, T. J., et al. 2010, MNRAS, 406, 822

McCarthy, P. J. 2004, ARA&A, 42, 477

McCarthy, P. J., Le Borgne, D., Crampton, D., et al. 2004, ApJ, 614, L9

McConnell, N. J., Ma, C.-P., Gebhardt, K., et al. 2011, Nature, 480, 215

Mead, J. M. G., King, L. J., Sijacki, D., et al. 2010, MNRAS, 406, 434

Menci, N., Fiore, F., & Lamastra, A. 2012, MNRAS, 421, 2384

Meneghetti, M., Bartelmann, M., Jenkins, A., & Frenk, C. 2007, MNRAS, 381, 171

Meneghetti, M., Fedeli, C., Pace, F., Gottlöber, S., & Yepes, G. 2010a, A&A, 519, A90

Meneghetti, M., Rasia, E., Merten, J., et al. 2010b, A&A, 514, A93

Merritt, D., Graham, A. W., Moore, B., Diemand, J., & Terzić, B. 2006, AJ, 132, 2685

Miralda-Escude, J. 1995, ApJ, 438, 514

Miralda-Escudé, J. 2002, ApJ, 564, 60

Miyazaki, S., Komiyama, Y., Sekiguchi, M., et al. 2002, PASJ, 54, 833

Mo, H., van den Bosch, F., & White, S. 2010, Galaxy Formation and Evolution (Cambridge Univ. Press)

Monet, D. G., Levine, S. E., Canzian, B., et al. 2003, AJ, 125, 984

Moore, B. 1994, Nature, 370, 629

Moore, B., Governato, F., Quinn, T., Stadel, J., & Lake, G. 1998, ApJ, 499, L5+

Moore, B., Quinn, T., Governato, F., Stadel, J., & Lake, G. 1999, MNRAS, 310, 1147

Morandi, A., & Limousin, M. 2012, MNRAS, 421, 3147

Morandi, A., Pedersen, K., & Limousin, M. 2010, ApJ, 713, 491

—. 2011, ApJ, 729, 37

More, A., Cabanac, R., More, S., et al. 2012, ApJ, 749, 38

Murphy, J. D., Gebhardt, K., & Adams, J. J. 2011, ApJ, 729, 129

Muzzin, A., Marchesini, D., van Dokkum, P. G., et al. 2009a, ApJ, 701, 1839

Muzzin, A., van Dokkum, P., Franx, M., et al. 2009b, ApJ, 706, L188

Naab, T., Johansson, P. H., & Ostriker, J. P. 2009, ApJ, 699, L178

Nagai, D., Vikhlinin, A., & Kravtsov, A. V. 2007, ApJ, 655, 98

Nair, P. B., van den Bergh, S., & Abraham, R. G. 2010, ApJ, 715, 606

Napolitano, N. R., Romanowsky, A. J., & Tortora, C. 2010, MNRAS, 405, 2351

Natarajan, P., & Kneib, J.-P. 1996, MNRAS, 283, 1031

Natarajan, P., Kneib, J.-P., Smail, I., et al. 2009, ApJ, 693, 970

Navarro, J. F., Eke, V. R., & Frenk, C. S. 1996a, MNRAS, 283, L72

Navarro, J. F., Frenk, C. S., & White, S. D. M. 1996b, ApJ, 462, 563

—. 1997, ApJ, 490, 493

Navarro, J. F., Hayashi, E., Power, C., et al. 2004, MNRAS, 349, 1039

Navarro, J. F., Ludlow, A., Springel, V., et al. 2010, MNRAS, 402, 21

Neto, A. F., Gao, L., Bett, P., et al. 2007, MNRAS, 381, 1450

Newman, A. B., Ellis, R. S., Bundy, K., & Treu, T. 2012, ApJ, 746, 162

Newman, A. B., Ellis, R. S., Treu, T., & Bundy, K. 2010, ApJ, 717, L103

Newman, A. B., Treu, T., Ellis, R. S., & Sand, D. J. 2011, ApJ, 728, L39

Newman, A. B., Treu, T., Ellis, R. S., et al. 2009, ApJ, 706, 1078

Nierenberg, A. M., Auger, M. W., Treu, T., Marshall, P. J., & Fassnacht, C. D. 2011, ApJ, 731, 44

Nipoti, C. 2011, arXiv:1109.1669

Nipoti, C., Londrillo, P., & Ciotti, L. 2003, MNRAS, 342, 501

Nipoti, C., Treu, T., Auger, M. W., & Bolton, A. S. 2009a, ApJ, 706, L86

Nipoti, C., Treu, T., & Bolton, A. S. 2009b, ApJ, 703, 1531

Nipoti, C., Treu, T., Ciotti, L., & Stiavelli, M. 2004, MNRAS, 355, 1119

Nipoti, C., Treu, T., Leauthaud, A., et al. 2012, MNRAS, 422, 1714

Nonino, M., Dickinson, M., Rosati, P., et al. 2009, ApJS, 183, 244

Oguri, M., Bayliss, M. B., Dahle, H., et al. 2012, MNRAS, 420, 3213

Oguri, M., Hennawi, J. F., Gladders, M. D., et al. 2009, ApJ, 699, 1038

Oh, S.-H., Brook, C., Governato, F., et al. 2011, AJ, 142, 24

Okabe, N., Takada, M., Umetsu, K., Futamase, T., & Smith, G. P. 2010, PASJ, 62, 811

Oke, J. B., & Gunn, J. E. 1983, ApJ, 266, 713

Oke, J. B., Cohen, J. G., Carr, M., et al. 1995, PASP, 107, 375

Onodera, M., Daddi, E., Gobat, R., et al. 2010, ApJ, 715, L6

Oort, J. H. 1932, Bull. Astron. Inst. Netherlands, 6, 249

Oser, L., Naab, T., Ostriker, J. P., & Johansson, P. H. 2011, arXiv:1106.5490

Oser, L., Ostriker, J. P., Naab, T., Johansson, P. H., & Burkert, A. 2010, ApJ, 725, 2312

Ostriker, J. P., & Peebles, P. J. E. 1973, ApJ, 186, 467

Ostriker, J. P., Peebles, P. J. E., & Yahil, A. 1974, ApJ, 193, L1

Padmanabhan, N., Seljak, U., Strauss, M. A., et al. 2004, New Astronomy, 9, 329

Papovich, C., Bassett, R., Lotz, J. M., et al. 2012, ApJ, 750, 93

Patton, D. R., & Atfield, J. E. 2008, ApJ, 685, 235

Peñarrubia, J., Pontzen, A., Walker, M. G., & Koposov, S. E. 2012, ApJ, 759, L42

Pedrosa, S., Tissera, P. B., & Scannapieco, C. 2009, MNRAS, 395, L57

Peebles, P. J. E. 1982, ApJ, 263, L1

Peirani, S., Kay, S., & Silk, J. 2008, A&A, 479, 123

Pelló, R., Kneib, J. P., Le Borgne, J. F., et al. 1999, A&A, 346, 359

Peng, C. Y., Ho, L. C., Impey, C. D., & Rix, H.-W. 2002, AJ, 124, 266

—. 2010, AJ, 139, 2097

Perlmutter, S., Aldering, G., Goldhaber, G., et al. 1999, ApJ, 517, 565

Peter, A. H. G., Moody, C. E., & Kamionkowski, M. 2010, Phys. Rev. D, 81, 103501

Peter, A. H. G., Rocha, M., Bullock, J. S., & Kaplinghat, M. 2012, arXiv:1208.3026

Pickles, A. J. 1985, ApJS, 59, 33

Pierre, M., Le Borgne, J. F., Soucail, G., & Kneib, J. P. 1996, A&A, 311, 413

Piffaretti, R., Arnaud, M., Pratt, G. W., Pointecouteau, E., & Melin, J.-B. 2011, A&A, 534, A109

Piffaretti, R., Jetzer, P., & Schindler, S. 2003, A&A, 398, 41

Pontzen, A., & Governato, F. 2012, MNRAS, 421, 3464

Popesso, P., Dickinson, M., Nonino, M., et al. 2009, A&A, 494, 443

Postman, M., & Lauer, T. R. 1995, ApJ, 440, 28

Postman, M., Lauer, T. R., Donahue, M., et al. 2012a, arXiv:1205.3839

Postman, M., Coe, D., Benítez, N., et al. 2012b, ApJS, 199, 25

Prada, F., Klypin, A. A., Cuesta, A. J., Betancort-Rijo, J. E., & Primack, J. 2012, MNRAS, 423, 3018

Press, W. H., & Schechter, P. 1974, ApJ, 187, 425

Primack, J. R. 2009, New Journal of Physics, 11, 105029

Puchwein, E., Springel, V., Sijacki, D., & Dolag, K. 2010, MNRAS, 406, 936

Qian, E. E., de Zeeuw, P. T., van der Marel, R. P., & Hunter, C. 1995, MNRAS, 274, 602

Quadri, R. F., & Williams, R. J. 2010, ApJ, 725, 794

Ragone-Figueroa, C., & Granato, G. L. 2011, MNRAS, 414, 3690

Raichoor, A., Mei, S., Stanford, S. A., et al. 2012, ApJ, 745, 130

Randall, S. W., Markevitch, M., Clowe, D., Gonzalez, A. H., & Bradač, M. 2008, ApJ, 679, 1173

Rasia, E., Meneghetti, M., Martino, R., et al. 2012, New Journal of Physics, 14, 055018

Rawat, A., Hammer, F., Kembhavi, A. K., & Flores, H. 2008, ApJ, 681, 1089

Rawle, T. D., Edge, A. C., Egami, E., et al. 2012, ApJ, 747, 29

Reddy, N. A., Erb, D. K., Steidel, C. C., et al. 2005, ApJ, 633, 748

Reese, E. D., Kawahara, H., Kitayama, T., et al. 2010, ApJ, 721, 653

Refregier, A. 2003, ARA&A, 41, 645

Reid, B. A., Samushia, L., White, M., et al. 2012, MNRAS, 426, 2719

Renzini, A. 2006, ARA&A, 44, 141

Rettura, A., Rosati, P., Nonino, M., et al. 2010, ApJ, 709, 512

Retzlaff, J., Rosati, P., Dickinson, M., et al. 2010, A&A, 511, A50+

Richard, J., Kneib, J.-P., Ebeling, H., et al. 2011, MNRAS, 414, L31

Richard, J., Pei, L., Limousin, M., Jullo, E., & Kneib, J. P. 2009, A&A, 498, 37

Richard, J., Smith, G. P., Kneib, J.-P., et al. 2010, MNRAS, 404, 325

Richtler, T., Salinas, R., Misgeld, I., et al. 2011, A&A, 531, A119

Riess, A. G., Filippenko, A. V., Challis, P., et al. 1998, AJ, 116, 1009

Rines, K., Geller, M. J., Kurtz, M. J., & Diaferio, A. 2003, AJ, 126, 2152

Roberts, M. S. 1975, in IAU Symposium, Vol. 69, Dynamics of the Solar Systems, ed. A. Hayli, 331

Roberts, M. S., & Haynes, M. P. 1994, ARA&A, 32, 115

Robertson, B., Cox, T. J., Hernquist, L., et al. 2006, ApJ, 641, 21

Rocha, M., Peter, A. H. G., Bullock, J. S., et al. 2012, arXiv:1208.3025

Rogerson, J. B., & York, D. G. 1973, ApJ, 186, L95

Romano-Díaz, E., Shlosman, I., Hoffman, Y., & Heller, C. 2008, ApJ, 685, L105

Romanowsky, A. J., Douglas, N. G., Arnaboldi, M., et al. 2003, Science, 301, 1696

Rossetti, M., Eckert, D., Cavalleri, B. M., et al. 2011, A&A, 532, A123

Rubin, V. C., & Ford, Jr., W. K. 1970, ApJ, 159, 379

Rubin, V. C., Ford, W. K. J., & . Thonnard, N. 1980, ApJ, 238, 471

Rudnick, G., von der Linden, A., Pelló, R., et al. 2009, ApJ, 700, 1559

Ryan, Jr., R. E., McCarthy, P. J., Cohen, S. H., et al. 2010, arXiv:1007.1460

Saglia, R. P., Kronawitter, A., Gerhard, O., & Bender, R. 2000, AJ, 119, 153

Salpeter, E. E. 1955, ApJ, 121, 161

Sánchez-Blázquez, P., Peletier, R. F., Jiménez-Vicente, J., et al. 2006, MNRAS, 371, 703

Sand, D. J., Treu, T., & Ellis, R. S. 2002, ApJ, 574, L129

Sand, D. J., Treu, T., Ellis, R. S., & Smith, G. P. 2005, ApJ, 627, 32

Sand, D. J., Treu, T., Ellis, R. S., Smith, G. P., & Kneib, J.-P. 2008, ApJ, 674, 711

Sand, D. J., Treu, T., Smith, G. P., & Ellis, R. S. 2004, ApJ, 604, 88

Sandage, A. 1972, ApJ, 178, 1

Sanderson, A. J. R., Edge, A. C., & Smith, G. P. 2009, MNRAS, 398, 1698

Saracco, P., Longhetti, M., & Gargiulo, A. 2011, MNRAS, 412, 2707

Schlegel, D. J., Finkbeiner, D. P., & Davis, M. 1998, ApJ, 500, 525

Schmidt, R. W., & Allen, S. W. 2007, MNRAS, 379, 209

Schneider, P., Ehlers, J., & Falco, E. E. 1999, Gravitational Lenses, Astronomy and Astrophysics Library (Springer)

Schneider, P., Kochanek, C., & Wambsganss, J. 2006, Gravitational Lensing: Strong, Weak, and Micro, Saas Fee Advanced Course 33 (Springer)

Schulz, A. E., Mandelbaum, R., & Padmanabhan, N. 2010, MNRAS, 408, 1463

Seljak, U., & Zaldarriaga, M. 1996, ApJ, 469, 437

Seljak, U., Makarov, A., McDonald, P., et al. 2005, Phys. Rev. D, 71, 103515

Sellwood, J. A., & McGaugh, S. S. 2005, ApJ, 634, 70

Sereno, M., De Filippis, E., Longo, G., & Bautz, M. W. 2006, ApJ, 645, 170

Shankar, F., & Bernardi, M. 2009, MNRAS, 396, L76

Shankar, F., Marulli, F., Bernardi, M., et al. 2011, arXiv:1105.6043

Sheinis, A. I., Bolte, M., Epps, H. W., et al. 2002, PASP, 114, 851

Shen, S., Mo, H. J., White, S. D. M., et al. 2003, MNRAS, 343, 978

Shim, H., Im, M., Pak, S., et al. 2006, ApJS, 164, 435

Simon, J. D., Bolatto, A. D., Leroy, A., & Blitz, L. 2003, ApJ, 596, 957

Simon, J. D., Bolatto, A. D., Leroy, A., Blitz, L., & Gates, E. L. 2005, ApJ, 621, 757

Smail, I., Sharp, R., Swinbank, A. M., et al. 2008, MNRAS, 389, 407

Smith, G. P., Kneib, J.-P., Ebeling, H., Czoske, O., & Smail, I. 2001, ApJ, 552, 493

Smith, G. P., Kneib, J.-P., Smail, I., et al. 2005, MNRAS, 359, 417

Smith, G. P., Khosroshahi, H. G., Dariush, A., et al. 2010, MNRAS, 409, 169

Smith, R. J., Lucey, J. R., & Carter, D. 2012, arXiv:1206.4311

Smith, S. 1936, ApJ, 83, 23

Sommer-Larsen, J., & Limousin, M. 2010, MNRAS, 408, 1998

Songaila, A., Cowie, L. L., Hogan, C. J., & Rugers, M. 1994, Nature, 368, 599

Sonnenfeld, A., Treu, T., Gavazzi, R., et al. 2012, ApJ, 752, 163

Soucail, G., Fort, B., Mellier, Y., & Picat, J. P. 1987, A&A, 172, L14

Spergel, D. N., & Steinhardt, P. J. 2000, Physical Review Letters, 84, 3760

Spergel, D. N., Verde, L., Peiris, H. V., et al. 2003, ApJS, 148, 175

Spiniello, C., Koopmans, L. V. E., Trager, S. C., Czoske, O., & Treu, T. 2011, MNRAS, 417, 3000

Springel, V., Frenk, C. S., & White, S. D. M. 2006, Nature, 440, 1137

Springel, V., White, S. D. M., Jenkins, A., et al. 2005, Nature, 435, 629

Springel, V., Wang, J., Vogelsberger, M., et al. 2008, MNRAS, 391, 1685

Stadel, J., Potter, D., Moore, B., et al. 2009, MNRAS, 398, L21

Steidel, C. C., Giavalisco, M., Pettini, M., Dickinson, M., & Adelberger, K. L. 1996, ApJ, 462, L17

Steidel, C. C., Shapley, A. E., Pettini, M., et al. 2004, ApJ, 604, 534

Stott, J. P., Collins, C. A., Sahlén, M., et al. 2010, ApJ, 718, 23

Su, M., & Finkbeiner, D. P. 2012, arXiv:1206.1616

Swaters, R. A., Madore, B. F., van den Bosch, F. C., & Balcells, M. 2003, ApJ, 583, 732

Szomoru, D., Franx, M., van Dokkum, P. G., et al. 2012, arXiv:1208.4363

Tacconi, L. J., Genzel, R., Smail, I., et al. 2008, ApJ, 680, 246

Taffoni, G., Mayer, L., Colpi, M., & Governato, F. 2003, MNRAS, 341, 434

Tal, T., van Dokkum, P. G., Nelan, J., & Bezanson, R. 2009, AJ, 138, 1417

Taylor, E. N., Franx, M., Glazebrook, K., et al. 2010, ApJ, 720, 723

Taylor, E. N., Franx, M., van Dokkum, P. G., et al. 2009, ApJS, 183, 295

Teyssier, R., Moore, B., Martizzi, D., Dubois, Y., & Mayer, L. 2011, MNRAS, 414, 195

Thomas, J., Saglia, R. P., Bender, R., et al. 2005, MNRAS, 360, 1355

—. 2011, MNRAS, 415, 545

Toft, S., Franx, M., van Dokkum, P., et al. 2009, ApJ, 705, 255

Toft, S., Gallazzi, A., Zirm, A., et al. 2012, ApJ, 754, 3

Toft, S., van Dokkum, P., Franx, M., et al. 2007, ApJ, 671, 285

Tollerud, E. J., Bullock, J. S., Strigari, L. E., & Willman, B. 2008, ApJ, 688, 277

Toomre, A. 1977, in Evolution of Galaxies and Stellar Populations, ed. B. M. Tinsley & R. B. G. Larson, D. Campbell, 401

Tremaine, S., & Gunn, J. E. 1979, Physical Review Letters, 42, 407

Tremblay, B., & Merritt, D. 1995, AJ, 110, 1039

Treu, T. 2010, ARA&A, 48, 87

Treu, T., Auger, M. W., Koopmans, L. V. E., et al. 2010, ApJ, 709, 1195

Treu, T., Dutton, A. A., Auger, M. W., et al. 2011, MNRAS, 417, 1601

Treu, T., Koopmans, L. V., Bolton, A. S., Burles, S., & Moustakas, L. A. 2006, ApJ, 640, 662

Treu, T., & Koopmans, L. V. E. 2004, ApJ, 611, 739

Treu, T., Stiavelli, M., Bertin, G., Casertano, S., & Møller, P. 2001, MNRAS, 326, 237

Treu, T., Stiavelli, M., Casertano, S., Møller, P., & Bertin, G. 1999, MNRAS, 308, 1037

—. 2002, ApJ, 564, L13

Treu, T., Ellis, R. S., Liao, T. X., et al. 2005, ApJ, 633, 174

Trujillo, I., Cenarro, A. J., de Lorenzo-Cáceres, A., et al. 2009, ApJ, 692, L118

Trujillo, I., Conselice, C. J., Bundy, K., et al. 2007, MNRAS, 382, 109

Trujillo, I., Ferreras, I., & de La Rosa, I. G. 2011, MNRAS, 415, 3903

Trujillo, I., Förster Schreiber, N. M., Rudnick, G., et al. 2006, ApJ, 650, 18

Tyson, J. A., Kochanski, G. P., & dell'Antonio, I. P. 1998, ApJ, 498, L107

Umetsu, K., Broadhurst, T., Zitrin, A., et al. 2011, ApJ, 738, 41

Umetsu, K., Medezinski, E., Nonino, M., et al. 2012, ApJ, 755, 56

Valdes, F., Gupta, R., Rose, J. A., Singh, H. P., & Bell, D. J. 2004, ApJS, 152, 251

Valentinuzzi, T., Poggianti, B. M., Saglia, R. P., et al. 2010, ApJ, 721, L19

van Albada, T. S., & Sancisi, R. 1986, Royal Society of London Philosophical Transactions Series A, 320, 447

van de Sande, J., Kriek, M., Franx, M., et al. 2011, ApJ, 736, L9+

—. 2012, arXiv:1211.3424

van den Bergh, S. 1999, PASP, 111, 657

van den Bosch, F. C., Robertson, B. E., Dalcanton, J. J., & de Blok, W. J. G. 2000, AJ, 119, 1579

van der Marel, R. P., Magorrian, J., Carlberg, R. G., Yee, H. K. C., & Ellingson, E. 2000, AJ, 119, 2038

van der Wel, A., Bell, E. F., van den Bosch, F. C., Gallazzi, A., & Rix, H.-W. 2009, ApJ, 698, 1232

van der Wel, A., Franx, M., van Dokkum, P. G., et al. 2005, ApJ, 631, 145

van der Wel, A., Holden, B. P., Zirm, A. W., et al. 2008, ApJ, 688, 48

van der Wel, A., Rix, H.-W., Wuyts, S., et al. 2011, ApJ, 730, 38

van Dokkum, P., & Conroy, C. 2012, arXiv:1205.6471

van Dokkum, P. G., & Conroy, C. 2010, Nature, 468, 940

van Dokkum, P. G., & Ellis, R. S. 2003, ApJ, 592, L53

van Dokkum, P. G., & Franx, M. 1996, MNRAS, 281, 985

van Dokkum, P. G., Franx, M., Fabricant, D., Kelson, D. D., & Illingworth, G. D. 1999, ApJ, 520, L95

van Dokkum, P. G., Franx, M., Kelson, D. D., & Illingworth, G. D. 1998, ApJ, 504, L17

van Dokkum, P. G., Kriek, M., & Franx, M. 2009, Nature, 460, 717

van Dokkum, P. G., & Stanford, S. A. 2003, ApJ, 585, 78

van Dokkum, P. G., Quadri, R., Marchesini, D., et al. 2006, ApJ, 638, L59

van Dokkum, P. G., Franx, M., Kriek, M., et al. 2008, ApJ, 677, L5

van Dokkum, P. G., Whitaker, K. E., Brammer, G., et al. 2010, ApJ, 709, 1018

Vanzella, E., Cristiani, S., Dickinson, M., et al. 2008, A&A, 478, 83

Viel, M., Becker, G. D., Bolton, J. S., et al. 2008, Physical Review Letters, 100, 041304

Vikhlinin, A., Kravtsov, A. V., Burenin, R. A., et al. 2009, ApJ, 692, 1060

Visvanathan, N., & Sandage, A. 1977, ApJ, 216, 214

Vogelsberger, M., Zavala, J., & Loeb, A. 2012, MNRAS, 423, 3740

von der Linden, A., Best, P. N., Kauffmann, G., & White, S. D. M. 2007, MNRAS, 379, 867

Wagoner, R. V. 1973, ApJ, 179, 343

Walker, M. G., Mateo, M., Olszewski, E. W., et al. 2009, ApJ, 704, 1274

Walker, M. G., & Peñarrubia, J. 2011, ApJ, 742, 20

Wechsler, R. H., Bullock, J. S., Primack, J. R., Kravtsov, A. V., & Dekel, A. 2002, ApJ, 568, 52

Weijmans, A.-M., Cappellari, M., Bacon, R., et al. 2009, MNRAS, 398, 561

Weinzirl, T., Jogee, S., Conselice, C. J., et al. 2011, ApJ, 743, 87

Westfall, K. B., Bershady, M. A., Verheijen, M. A. W., et al. 2011, ApJ, 742, 18

Whitaker, K. E., Kriek, M., van Dokkum, P. G., et al. 2011a, arXiv:1112.0313

Whitaker, K. E., van Dokkum, P. G., Brammer, G., et al. 2010, ApJ, 719, 1715

Whitaker, K. E., Labbé, I., van Dokkum, P. G., et al. 2011b, ApJ, 735, 86

White, S. D. M. 1977, MNRAS, 179, 33

White, S. D. M., Frenk, C. S., & Davis, M. 1983, ApJ, 274, L1

White, S. D. M., Navarro, J. F., Evrard, A. E., & Frenk, C. S. 1993, Nature, 366, 429

White, S. D. M., & Rees, M. J. 1978, MNRAS, 183, 341

Williams, R. J., Quadri, R. F., & Franx, M. 2011, ApJ, 738, L25

Williams, R. J., Quadri, R. F., Franx, M., et al. 2010, ApJ, 713, 738

Wolf, J., & Bullock, J. S. 2012, arXiv:1203.4240

Woo, T.-P., & Chiueh, T. 2009, ApJ, 697, 850

Wright, E. L., Meyer, S. S., Bennett, C. L., et al. 1992, ApJ, 396, L13

Wuyts, S., Labbé, I., Schreiber, N. M. F., et al. 2008, ApJ, 682, 985

Yagi, M., Yoshida, M., Komiyama, Y., et al. 2010, AJ, 140, 1814

Yan, R., Newman, J. A., Faber, S. M., et al. 2006, ApJ, 648, 281

Yee, H. K. C., Ellingson, E., Abraham, R. G., et al. 1996, ApJS, 102, 289

Yoshida, N., Springel, V., White, S. D. M., & Tormen, G. 2000, ApJ, 544, L87

Zappacosta, L., Buote, D. A., Gastaldello, F., et al. 2006, ApJ, 650, 777

Zeldovich, I. B., Einasto, J., & Shandarin, S. F. 1982, Nature, 300, 407

Zhao, D. H., Jing, Y. P., Mo, H. J., & Börner, G. 2009, ApJ, 707, 354

Zhao, H. 1996, MNRAS, 278, 488

Zirm, A. W., van der Wel, A., Franx, M., et al. 2007, ApJ, 656, 66

Zitrin, A., & Broadhurst, T. 2009, ApJ, 703, L132

Zitrin, A., Broadhurst, T., Barkana, R., Rephaeli, Y., & Benítez, N. 2011a, MNRAS, 410, 1939

Zitrin, A., Broadhurst, T., Umetsu, K., et al. 2010, MNRAS, 408, 1916

Zitrin, A., Broadhurst, T., Coe, D., et al. 2011b, ApJ, 742, 117

Zwicky, F. 1933, Helvetica Physica Acta, 6, 110

—. 1937, ApJ, 86, 217